USC
UNIVERSIDADE DE SANTIAGO DE COMPOSTELA

ESCOLA DE DOUTORAMENTO
INTERNACIONAL DA USC

Beatriz
García Plana

Tese de doutoramento

Tests of Lepton Flavour Universality using semitauonic B decays in the LHCb experiment at CERN

Santiago de Compostela, 2022

Programa de Doutoramento en Física Nuclear e de Partículas

TESE DE DOUTORAMENTO

TESTS OF LEPTON FLAVOUR UNIVERSALITY USING SEMITAUONIC B DECAYS IN THE LHCB EXPERIMENT AT CERN

Beatriz García Plana

ESCOLA DE DOUTORAMENTO INTERNACIONAL DA UNIVERSIDADE DE SANTIAGO DE COMPOSTELA

PROGRAMA DE DOUTORAMENTO EN FÍSICA NUCLEAR E DE PARTÍCULAS

SANTIAGO DE COMPOSTELA

ANO 2022


USC
UNIVERSIDADE
DE SANTIAGO
DE COMPOSTELA

DECLARACIÓN DO AUTOR/A DA TESE

D./Dna. **Beatriz García Plana**

Título da tese: **Tests of Lepton Flavour Universality using semitauonic B decays in the LHCb Experiment at CERN**

Presento a miña tese, seguindo o procedemento axeitado ao Regulamento, e declaro que:

1) A tese abarca os resultados da elaboración do meu traballo.
2) De ser o caso, na tese faise referencia ás colaboracións que tivo este traballo.
3) Confirmo que a tese non incorre en ningún tipo de plaxio doutros autores nin de traballos presentados por min para a obtención doutros títulos.
4) A tese é a versión definitiva presentada para a súa defensa e coincide a versión impresa coa presentada en formato electrónico

E comprométome a presentar o Compromiso Documental de Supervisión no caso de que o orixinal non estea na Escola.

En **Santiago de Compostela**, **27 de Maio de 2022**.

Sinatura electrónica


USC
UNIVERSIDADE
DE SANTIAGO
DE COMPOSTELA

AUTORIZACIÓN DO DIRECTOR/TITOR DA TESE

D./Dna. **Abraham Antonio Gallas Torreira**

En condición de: **Titor e director**

Título da tese: **Tests of Lepton Flavour Universality using semitauonic B decays in the LHCb Experiment at CERN**

INFORMA:

Que a presente tese, correspóndese co traballo realizado por Dna **Beatriz García Plana**, baixo a miña dirección e titorización, e autorizo a súa presentación, considerando que reúne os requisitos esixidos no Regulamento de Estudos de Doutoramento da USC, e que como director e titor desta non incorre nas causas de abstención establecidas na Lei 40/2015.

En **Santiago de Compostela**, **27 de Maio de 2022**

Sinatura electrónica


USC
UNIVERSIDADE
DE SANTIAGO
DE COMPOSTELA

AUTORIZACIÓN DO DIRECTOR/TITOR DA TESE

D./Dna. **Antonio Romero Vidal**

En condición de: **Director**

Título da tese: **Tests of Lepton Flavour Universality using semitauonic B decays in the LHCb Experiment at CERN**

INFORMA:

Que a presente tese, correspóndese co traballo realizado por Dna **Beatriz García Plana** , baixo a miña dirección, e autorizo a súa presentación, considerando que reúne os requisitos esixidos no Regulamento de Estudos de Doutoramento da USC, e que como director desta non incorre nas causas de abstención establecidas na Lei 40/2015.

En **Santiago de Compostela**, **27 de Maio de 2022**

Sinatura electrónica


USC
UNIVERSIDADE
DE SANTIAGO
DE COMPOSTELA

Á miña mamá.


USC
UNIVERSIDADE
DE SANTIAGO
DE COMPOSTELA

E como é? Dúas partes afastadas entre si
Alumean aleacións idénticas
E como é? Atopadas nos ronseis do seu ser
Son delirios, equilibrios, enredadas no aquel

Mercedes Peón

Necesitamos una ciencia que piense en la naturaleza desde dentro, sin intentar dominarla, aliándose con ella. Unas ciencias terrícolas capaces de desacelerar los excesos cometidos por la propia ciencia.

Yayo Herrero

The women of Chipko taught me about the relationship between forests, soil and water and women's sustenance economies; quantum theory taught me the four principles that have guided my thinking and my life's work—everything is interconnected, everything is potential, everything is indeterminate, there is no excluded middle; we are interbeings.

Vandana Shiva


USC
UNIVERSIDADE
DE SANTIAGO
DE COMPOSTELA

Acknowledgements

It is difficult to summarise all the people who contribute to a process moving forward. However, what is clear to me is that the first responsible for this thesis project to get ahead are my supervisors Abraham and Antonio (Toño). I feel very grateful for all the time and energy they invested in my development as a researcher. Without your help, trust and patience, I would have never ventured and enjoyed this thesis adventure.

Looking back, I can only deeply thank María, who introduced me the LHCb detector for the very first time, and shared so many survival tips in the years that followed. Moreover, if that were not enough, she kindly accepted to write me one of the expert's reports for the International Mention of the PhD. My gratitude also for Óscar, for the unconditional support with code issues, bureaucracy and daily tragicomedies.

I feel fortunate to have lived the experience of the PhD at the LHCb group in Santiago, in which I felt heard and supported. Special thanks to the seniors (Juan, Cibrán), that helped to build a friendly environment at work. During these years, I have learned that this is key for high quality research.

I would like to thank the Semileptonic working group, in special to the conveners: Greg Ciezarek, Patrick Owen, Lucia Grillo, Michel De Cian, Marcello Rotondo, Mark Smith and Donal Hill, for the useful comments in the analysis, and for the support during my *MC liaison* time. Also, I thank the Simulation working group, where I learnt interesting aspects about the LHCb simulation process.

Special thank to Olivier Leroy, who warmly welcomed me in the CPPM in Marseille in my short stay, and to whom I am very grateful for the writing of the other expert's report of the thesis. Also, I thank all the LHCb team there, in particlar Dawid Gerstel and Adam Morris, for the help and discussions, from whom I learnt about the importance of tenacity.

Thanks to all the VELO group, in particular Victor Coco, for his support during my stay at CERN. I learned a lot about the scientific process in those debates that took place from office to office.

I thank the financial support provided by the "Programa de ayuda para contratos predoctorales para la formación de doctores", of the "Ministerio de Universidades", which founded my contract at USC and my stay at CPPM. Also, thanks to the IGFAE for founding my first year of PhD.

From a more personal side, I feel very grateful for all the people that I met on stays, schools and conferences, from which I learned and grew. I would like also to thank all the group that was part of my experience in Marseille, for making me feel part, and filling my heart with beautiful rocks to climb, new landscapes and care. I also want to thank the people who make up the most human side of CERN, which I met during my stays there. Thanks for breaking with everyday life and accompanying me on explorations. I cannot forget the Valencia group, for the welcome with open arms. Specially to Ana, who almost convinced me that theory is fun. Moreover, I keep with special affection in my memories the experiences lived in Salvador de Bahía, Saint Petersburg, Göttingen and Asiago.

Agradecementos

Se hai algunha persoa sen a cal eu non estaría aquí, é miña nai, Mª Beatriz. Grazas por tentar darme ás antes de que eu sequera soubese camiñar. Grazas polo esforzo infinito, por ser o meu exemplo. Grazas a Tino, por acompañarnos.

A Serxio polo refuxio; pola paciencia morna, a calma e o aloumiño sempre a tempo. A Miguel, Buñu e Lara, por ser as miñas persoas-boias, a referencia cando me perdo; por involucrarse nos meus procesos. Aos primos Fontaíña, Manu e Artai, por manterse preto aínda estando lonxe. A Blanca e Micho, pola certeza dos coidados e a súa enorme humanidade. A Chusqui, por ensinarme o valor da vulnerabilidade. A Sonia e Luisa, por ser un espazo seguro para desfogar. A Óscar, polo equilibrio construído. A Alessandra, pola fantasía. A Julián, pola escoita activa. Ao meu tío Fernando pola serenidade, e por compartir a paixón pola ciencia. A aqueles que xa non están, pero son: ao meu avó, a Santos. A Alba, Ana e Cintia, pola complicidade dos anos. A Carbonilla, pola intuición. Tamén, síntome especialmente agradecida ás persoas que me acompañaron nesta última etapa de escritura, e me aliviaron carga: Carlos, Antía, María, Julia e Diego.

Grazas ás persoas que me fixeron levadeira esta etapa no IGFAE, coas que compartín despacho ou conversas de pasillo, que facían a atmósfera máis amable. Estou particularmente agradecida ao grupo de xénero, polo apoio, a Berta, pola comprensión e a Marcos Seco por compartir conmigo a súa experiencia.

Grazas ao activismo, por axudarme a non perder perspectiva e manter viva a esperanza; especialmente a Ecoar pola coherencia, e a Seteportas, por poñer en valor a interdependencia. Grazas ao mundo da música tradicional galega, por manterme conectada á terra e á forza da comunidade. Grazas ao circo e as persoas que o conforman, por elevarme do chan e achegarme outros mundos. Síntome intimamente agradecida coa escalada e a montaña por ser un oco polo que respirar, e por todas as persoas que nos coidamos nesta realidade. A todas as diversas convivencias que me atopei polo camiño, destacando a Casa das Augas, por ser unha oportunidade para medrar e construir. Gardo con fondo agarimo a Noeli e Elenita.

Grazas a Compostela, polos encontros impredecibles nas ruelas empedradas, pola poesía no cotián e a cultura florecente.

Grazas a todas as persoas que me acompañaron neste proceso, formando parte da miña rede que me sostén cada día.

Beatriz

Abstract

The Standard Model (SM) is a very successful theory of particle physics, since most of experimental results can be explained within its framework. In spite of this, there are fundamental questions that remain to be answered, such as the related with the flavour sector. Several New Physics (NP) models state contributions that would involve changes in the flavour structure, leading to deviations from the expected behaviour of the processes. The LHCb experiment at CERN was primarily designed to measure parameters of Charge-Parity (CP) violation in the decays of b-hadrons produced in pp collisions at the LHC. In the last years, the detector has extended its physics program, proving to be a powerful tool to test NP effects. However, the high-precision measurements performed by LHCb remain statistically limited, motivating an upgrade of the detector.

The LHCb foresees a new era of high luminosity, with values scaling up $2{\times}10^{33}\,\mathrm{cm}^{-2}\,\mathrm{s}^{-1}$. As a direct consequence, LHCb sub-detectors will face increased occupancies and rates. Therefore, in order to access these conditions, the entire LHCb experiment has to be upgraded. It is of particular relevance the VErtex LOcator (VELO) upgrade project, since it plays a significant role in the LHCb detector, allowing the reconstruction of displaced vertices, which are a distinctive characteristic of heavy flavoured particles. The VELO upgrade implies the installation of a detector based on hybrid pixel sensors, capable of 40 MHz readout. The first part of this thesis is committed to the study of the performance of the new VELO sensors. A specific testing setup built to test the high voltage tolerance is presented. Moreover, it is reported the work done towards the characterization of the effect that different irradiation profiles have on the sensors. The structure of this first part of the work is organised as follows: the **introduction** is presented through Chap. 1, Chap. 3 and Sec. 4.1. Then, Chap. 4 addresses the core of this topic of thesis, arranged so that general **objectives** for the sensors are mentioned in Sec. 4.2 and Sec. 4.3; while the **hypotheses**, **methodology** and **results** are discussed in Sec. 4.4. Finally, the **conclusions** of the studies are provided in Sec. 4.5.

The second and most important part of this thesis is dedicated to proving Lepton Flavour Universality (LFU), a fundamental property of the Standard Model that predicts that the electroweak couplings are independent of the lepton flavour. Currently, the combined measurements of $\mathcal{R}(D)$ and $\mathcal{R}(D^*)$ and the SM prediction are in tension at the level of 3.4 standard deviations. The analysis presented in this work documents the first measurement of $\mathcal{R}(D^{(*)0}) = \frac{\mathcal{B}(B^+\to\bar{D}^{(*)0}\tau^+\nu_\tau)}{\mathcal{B}(B^+\to\bar{D}^{(*)0}\ell^+\nu_\ell)}$, with the 3-prong hadronic tau decays and $\overline{D}^0$ reconstructed in its $K\pi$ mode. The work is performed with Run 2 data recorded by LHCb during the years 2016, 2017 and 2018. The measurement is done through a binned, three-dimensional, templates-based fit to selected candidates with the visible final state

of $4\pi^{\pm}K$. Even though the final result is blinded and the systematics uncertainties need to be computed, the signal branching fractions are obtained with a precision competitive with the world average. Moreover, the $\mathcal{R}(D^{(*)0})$ ratios are computed to be:

$$\begin{aligned}\mathcal{R}(D^0) &= xx \pm 0.093\ (stat.) \pm 0.034\ (ext.),\\ \mathcal{R}(D^{*0}) &= xx \pm 0.026\ (stat.) \pm 0.029\ (ext.),\end{aligned}$$

whose precision is competitive with previous experimental measurements. The results hint that the analysis documented here will mean a sensitive test of Lepton Flavour Universality. This work will have a significant impact on the $\mathcal{R}(D^{(*)})$ world average, providing insight into the flavour puzzle.

This part of the thesis has the following structure: the **introduction** is presented through Chap. 1 and Chap. 3. The **hypotheses** are developed in detail in Chap. 2. The **objectives** are tackled in Chap. 5. The **methodology** of the analysis is addressed throughout several chapters. The main strategy is presented in Chap. 5. Then, Chap. 6 provides the selection and preparation of datasets, together with to the correction to simulation applied. Chap. 7 documents specific control samples studies. Afterwards, Chap. 8 dives into the core of this thesis, where the description of the techniques applied to extract the signal yields are given in detail, together with the first **results**. The discussion of the results continue in Chap. 9, while the systematic treatment is presented in Chap. 10. Finally, the **conclusions** and future prospects are given in Sec. 11. A **summary in Galician** is provided in Ap. C, and the **bibliography** closes the document.

Key Words: Experimental High Energy Physics, LHC, LHCb, Lepton Flavour Universality, Semileptonic B Decays, Physics Beyond the Standard Model

Resumo

O Modelo Estándar (ME) é unha teoría de física de partículas que é capaz de explicar, dentro do seu marco teórico, a meirande parte dos resultados experimentais, demostrando así a súa amplia validez. Porén, deixa cuestións sen resposta, algunhas relacionadas co sector do sabor. Isto é interesante, xa que varios modelos de Nova Física (NF) predín contribucións que cambiarían a estrutura do sabor, o que implicaría novos procesos nas transicións deste sector. Dentro deste contexto de ampliación do ME, deseñouse o experimento LHCb, no CERN, que na súa orixe tiña como obxectivo medir paramétros da violación Carga-Paridade (CP) nas desintegracións de hadróns de tipo b producidas nas colisións de protóns do LHC. Nos últimos anos de operación, o experimento estendeu notablemente o horizonte da física das súas análises, asentándose como unha potente ferramenta para levar a cabo procuras de NF. Sen embargo, as medidas de alta precisión efectuadas por LHCb atópanse limitadas estadísticamente, o que motiva levar a cabo unha actualización do detector.

O LHCb inaugurará a mediados de 2022 unha nova era de alta luminosidade, onde se prevee que se acaden valores de ata $2 \times 10^{33}\,\mathrm{cm}^{-2}\,\mathrm{s}^{-1}$. Para poder facer fronte ás novas condicións de ocupacións dos sub-detectores e as correspondentes taxas de lecturas de datos, o experimento LHCb precisa someterse a unha actualización completa. Resulta de especial relevancia o proxecto previsto para o LOcalizador de VÉrtices (*VErtex LOcator*, VELO), xa que este xoga un papel fundamental na reconstrución dos vértices onde se producen e desintegran os hadróns. A actualización deste detector consiste en sustituilo por un detector de silicio baseado na tecnoloxía píxel, con unha lectura a 40 MHz. A primeira parte da tese presentada aquí está relacionada co estudo do rendemento dos novos sensores do VELO. En primeiro lugar, preséntase un procedemento deseñado e implantado para someter a proba a tolerancia dos sensores a alta voltaxe. Aplicando este procedemento, documéntase o traballo levado a cabo para caracterizar o efecto que diferentes perfiles de irradiación teñen nos sensores. Esta parte estrutúrase da seguinte forma: a **introdución** desenvólvese nos Cap. 1, Cap. 3 e Sec. 4.1. A continuación, o Cap. 4 aborda o núcleo desta primeira parte da tese, distribuído de xeito que os **obxectivos** preséntanse na Sec. 4.2 e Sec. 4.3; mentres que as **hipóteses**, **metodoloxía** e **resultados** discútense na Sec. 4.4. Finalmente, as **conclusións** dos estudos proporciónanse na Sec. 4.5.

A segunda e principal parte desta tese adícase a poñer a proba a Universalidade Leptónica de Sabor (ULS), unha propiedade fundamental do ME que predí que os acoplamientos electrofebles son independientes do sabor do leptón. Actualmente, a combinación dos resultados experimentais de $\mathcal{R}(D)$ e $\mathcal{R}(D^*)$ e a predición do ME atopánse a un nivel de tensión que escala ata as 3,4 desviacións estándar. A análise presentada aquí documen-

ta a primeira medida de $\mathcal{R}(D^{(*)0}) = \frac{\mathcal{B}(B^+ \to \bar{D}^{(*)0}\tau^+\nu_\tau)}{\mathcal{B}(B^+ \to \bar{D}^{(*)0}\ell^+\nu_\ell)}$, co tau desintegrándose nos modos $\tau^+ \to \pi^+\pi^-\pi^+\overline{\nu}_\tau$ e $\tau^+ \to \pi^+\pi^-\pi^+\pi^0\overline{\nu}_\tau$, e o $\overline{D}^0$ reconstruído na forma $K\pi$. Para a investigación, úsase unha mostra de datos do *Run 2*, recollidos polo experimento LHCb nos anos 2016, 2017 e 2018. A medida lévase a cabo mediante un axuste de histogramas tri-dimensionais, baseadas en padróns, a eventos seleccionados que teñen o estado final visible de $4\pi^{\pm}K$. A pesar de que o resultado é *cego*, de xeito que se atopa camuflado, e además falta calcular as incertidumes sistemáticas, neste traballo determínase a fracción de ramificación das sinais cunha precisión equiparable á do promedio mundial. Además, compútanse os $\mathcal{R}(D^{(*)0})$, obtendo:

$$\begin{aligned} \mathcal{R}(D^0) &= xx \pm 0{,}093\ (stat.) \pm 0{,}034\ (ext.), \\ \mathcal{R}(D^{*0}) &= xx \pm 0{,}026\ (stat.) \pm 0{,}029\ (ext.), \end{aligned}$$

que é comparable ás anteriores medidas experimentais. Estos resultados revelan que a análise que se documenta aquí constitúe unha proba precisa da Universalidade Leptónica do Sabor. A medida provocará un impacto significativo na media mundial de $\mathcal{R}(D^{(*)})$, contribuíndo á comprensión do puzzle do sabor.

Esta parte da tese organízase de acordo coa seguinte estrutura: a **introdución** preséntase ao longo dos Cap. 1 e Cap. 3. As **hipóteses** desenvólvense ampliamente no Cap. 2. Os **obxectivos** plantéxanse no Cap. 5. A **metodoloxía** da análise abórdase ao longo de varios capítulos. A estratexia seguida no traballo preséntase en Cap. 5. A continuación, o Cap. 6 documenta a selección e preparación das mostras de datos, así como as correccións que foron aplicadas á simulación. No Cap. 7 expóñense estudos específicos de mostras de control. Seguidamente, o Cap. 8 supón o núcleo do traballo desta parte da tese, onde se recolle unha descrición detallada das técnicas aplicadas para extraer o número de eventos de sinal, así como os primeiros **resultados**. A discusión dos resultados continúa no Cap. 9, mentras que o tratamento dos sistemáticos preséntase no Cap. 10. Finalmente, as **conclusiones** e perspectivas de futuro proporciónanse no Cap. 11. Un **resumo en galego da tese** inclúese no Ap. C, e a **bibliografía** pecha o documento.

Resumen

El Modelo Estándar (ME) es una teoría de física de partículas que es capaz de explicar, dentro de su marco teórico, la mayor parte de los resultados experimentales, demostrando así su amplia validez. Sin embargo, deja cuestiones sin respuesta, algunas relacionadas con el sector del sabor. Esto es interesante, ya que varios modelos de Nueva Física (NF) predicen contribuciones que cambiarían la estructura del sabor, lo que implicaría nuevos procesos en las transiciones de este sector. Dentro deste contexto de ampliar el conocimiento del ME, se diseñó el experimento LHCb, en el CERN, que en su origen tenía como objetivo medir parámetros de la violación Carga-Paridad (CP) en las desintegraciones de hadrones de tipo b producidos en las colisiones de protones del LHC. En los últimos años de operación, el experimento ha extendido notablemente el horizonte de la física de sus análisis, asentándose como una potente herramienta para llevar a cabo búsquedas de NF. Sin embargo, las medidas de alta precisión efectuadas por LHCb se encuentran limitadas estadísticamente, lo que motiva llevar a cabo un proyecto para actualizar el detector.

El LHCb inaugurará a mediados de 2022 una nueva era de alta luminosidad, donde se espera alcanzar valores de hasta $2 \times 10^{33}\,\mathrm{cm}^{-2}\,\mathrm{s}^{-1}$. Para hacer frente a las nuevas condiciones de ocupación de los sub-detectores y las tasas de lectura de datos correspondientes, el experimento LHCb debe actualizarse por completo. Resulta de especial relevancia el proyecto previsto para el LOcalizar de Vértices (*VErtex LOcator*, VELO), ya que este juega un papel clave en la reconstrucción de los vértices donde se producen y decaen los hadrones. La actualización de este detector implica reemplazarlo por un detector de silicio basado en píxeles, con una lectura a 40 MHz. La primera parte de la tesis que se presenta aquí está relacionada con el estudio de las prestaciones de los nuevos sensores del VELO. Primero, se expone un procedimiento diseñado e implementado para someter a prueba la tolerancia de los sensores al alto voltaje. Aplicando este procedimiento, se documenta el trabajo realizado para caracterizar el efecto que tienen los diferentes perfiles de irradiación sobre los sensores. Esta primera parte de la tesis está estructurada de la siguiente manera: la **introducción** se desenvuelve en los Cap. 1, Cap. 3 y Sec. 4.1. A continuación, el Cap. 4 aborda el núcleo de esta temática de la tesis, distribuído de forma que los **objetivos** se presentan en la Sec. 4.2 y Sec. 4.3; mientras que las **hipótesis**, **metodología** y **resultados** en discuten en la Sec. 4.4. Finalmente, las **conclusiones** de los estudios se proporcionan en la Sec. 4.5.

La segunda y principal parte de esta tesis está dedicada a poner a prueba la Universalidad Leptónica de Sabor (ULS), una propiedad fundamental del ME que predice que los acoplamientos electrodébiles son independientes del sabor del leptón. Actualmente, la combinación de los resultados experimentales de $\mathcal{R}(D)$ y $\mathcal{R}(D^*)$ y la predicción del ME

se encuentran a un nivel de tensión que escala hasta las 3,4 desviaciones estándar. El análisis presentado aquí documenta la primeira medida de $\mathcal{R}(D^{(*)0}) = \frac{\mathcal{B}(B^+ \to \overline{D}^{(*)0}\tau^+\nu_\tau)}{\mathcal{B}(B^+ \to \overline{D}^{(*)0}\ell^+\nu_\ell)}$, con el tau desintegrándose en los modos $\tau^+ \to \pi^+\pi^-\pi^+\overline{\nu}_\tau$ y $\tau^+ \to \pi^+\pi^-\pi^+\pi^0\overline{\nu}_\tau$, y el $\overline{D}^0$ reconstruído en la forma $K\pi$. Para la investigación, se usa una muestra de datos del *Run 2*, recogidos por el experimento LHCb en los años 2016, 2017 y 2018. La medida se lleva a cabo mediante un ajuste de histogramas tri-dimensionales, basados en plantillas, a eventos seleccionados que tienen el estado final visible de $4\pi^\pm K$. A pesar de que el resultado es *ciego*, de forma que se encuentra camuflado, y es necesario calcular las incertidumbres sistemáticas, en este trabajo se determina la fracción de ramificación de las señales con una precisión equiparable a la del promedio mundial. Además, se computan $\mathcal{R}(D^{(*)0})$, obteniendo:

$$\begin{aligned} \mathcal{R}(D^0) &= xx \pm 0{,}093\ (stat.) \pm 0{,}034\ (ext.), \\ \mathcal{R}(D^{*0}) &= xx \pm 0{,}026\ (stat.) \pm 0{,}029\ (ext.), \end{aligned}$$

que es comparable a las anteriores medidas experimentales. Estos resultados revelan que el análisis que se documenta aquí constituye una prueba precisa de la Universalidad Leptónica da Sabor. La medida provocará un impacto significativo en la media mundial de $\mathcal{R}(D^{(*)})$, contribuyendo a la comprensión del puzzle del sabor.

Esta parte de la tesis se organiza de acuerdo con la siguiente estructura: la **introducción** se presenta a lo largo de los Cap. 1 y Cap. 3. Las **hipótesis** se desenvuelven ampliamente en el Chap. 2. Los **objetivos** se plantean en el Cap. 5. La **metodología** del análisis se aborda a lo largo de varios capítulos. La estrategia seguida en el trabajo se presenta en el Cap. 5. A continuación, el Cap. 6 documenta la selección y preparación de las muestras de datos, así como las correcciones que fueron aplicadas a la simulación. En el Cap. 7, se exponen estudios específicos de muestras de control. Seguidamente, el Cap. 8 supone el núcleo de trabajo de esta parte de la tesis, donde se encuentra una descripción detallada de las técnicas aplicadas para extraer el número de eventos de señal, así como los primeros **resultados**. La discusión de los resultados continúa en el Cap. 9, mientras que el tratamiento de los sistemáticos se presentan en el Cap. 10. Finalmente, las **conclusiones** y perspectivas de futuro se proporcionan en el Cap. 11. Un **resumen en gallego de la tesis** se incluye en el Ap. C, y la **bibliografía** cierra el documento.

INDEX

1

Introduction

The 1970s went down in the history of science as some of the most transcendental years in the study of particle physics, and therefore in the development of our understanding of the basic interactions of nature. This decade witnessed a series of experimental and theoretical breakthroughs that crystallized into a theoretical framework, entailing a remarkable insight into the fundamental structure of nature. The Standard Model (SM) of particle physics describes the basic building blocks of matter, called particles, and their interactions. Over the years, it has been extensively tested by experiments, successfully explaining most of the experimental results obtained at hadron colliders, such as the Tevatron or the LHC, or measurements from e^+e^- colliders, such as Belle or BaBar collaborations. Moreover, it has precisely predicted a great variety of phenomena. The discovery of the Higgs boson by ATLAS [1] and CMS [2] in 2012 was the last missing piece of the particle physics puzzle. Nevertheless, there are several open questions that remain unanswered, motivating the search for New Physics (NP) beyond the SM. Both the theoretical principles of the SM and its limitations are discussed in Chap. 2.

The LHCb experiment at CERN was designed primarily to measure the parameters of CP violation in the decays of b-hadrons. A description of the detector is provided in Chap. 3. In the last years, the detector has extended its physics program, proving to be a powerful tool to test Beyond the Standard Model (BSM) Physics.

High-precision measurements performed by LHCb remain statistically limited, which motivated a major upgrade of the detector that started in 2019. One fundamental part of the upgrade is the replacement of the existing VErtex LOcator, VELO, based on silicon strip sensors, with a hybrid pixel detector. Chap. 4 covers the main changes that the LHCb upgrade will undergo, in particular the upgraded VELO is described in detail, along with

my direct contributions. I worked directly on the study of the performances of the sensor prototypes. On one hand, on the study of the current-voltage (IV) characteristic curves for a non-irradiated sensor, in order to ensure a correct and safe behaviour. On the other hand, it was also relevant my contribution on the study of the dependence of the temperature breakdown with the irradiation profile, since I was the main responsible for the characterisation of the sensors that I am presenting here. A specific testing setup was built, in order to test the high voltage tolerance of the sensors up to 1000 V. I contributed directly to this testing, and I also worked on the study of the understanding the nature of the breakdown voltage that appears in some of the sensors.

Changing the topic, the main work of this thesis is focused on testing one of the fundamental assumptions of the SM: Lepton Flavour Universality (LFU). Chap. 2 presents an overview on how to test LFU, together with the state of the art from both theoretical and experimental points of view. Lepton Flavour Universality has been intensely tested, resulting in a pattern of anomalies measured by LHCb and other experiments worldwide over the past two decades. It is therefore crucial to clarify the potential existence of New Physics (NP) effects. This work focus on semileptonic decays of b-hadrons which provides a sensitive probe to such NP effects. In particular, ratios between branching fractions of semitauonic and semimuonic decays cancel out hadronic effects to a large extent, resulting in a clean observable.

This thesis documents the measurement of $\mathcal{R}(D^{(*)0}) = \frac{\mathcal{B}(B^+ \to \bar{D}^{(*)0}\tau^+\nu_\tau)}{\mathcal{B}(B^+ \to \bar{D}^{(*)0}\ell^+\nu_\ell)}$, performed with Run-2 data recorded by LHCb during the years 2016, 2017 and 2018. The methodology followed for the first observation of these observables with the 3-prong hadronic tau decays is presented in Chap. 5. The selection and preparation of data and Monte Carlo samples is detailed in Chap. 6. My direct contributions to this step of the analysis are the preliminary studies and preparation of the dec-files that determine the Monte Carlo contributions, and the build up of the multivariate algorithm, necessary to suppress doubly-charmed decays, and is used as input for the final signal extraction 3D fit. The control samples are presented in Chap. 7. The core of my thesis is found to be in the Chap. 8, where the determination of the signal branching fractions is detailed, focusing on my main contribution to this analysis: the 3-dimensional (3D) fit to extract the signal yield, which implies a thorough and optimized fit model and the study of its performance using pseudo-data samples (toys). Chap. 9 presents the preliminary result of $\mathcal{R}(D^{(*)0})$. Systematic uncertainties are discussed in Chap. 10. The impact of this novel result, together with the conclusions of the thesis presented here closes this document, in Chap. 11.

2

Theoretical principles

Contents

2.1 The Standard Model

The Standard Model (SM) of particle physics is a unified description of the fundamental constituents of matter, the *elementary particles*, and the interactions among them, the *forces*.

The particles of the SM are separated into two categories, according to their spin value: fermions and bosons. Fermions are the matter particles, which have spin 1/2, and are further divided into leptons and quarks. Bosons are the force carriers, with spin 1, with the exception of the Higgs boson, which has spin 0.

2.1.1 Symmetries

The SM is a Gauge theory based on the local symmetry groups

$$SU(3)_C \times SU(2)_L \times U(1)_Y,$$

where C is the colour charge of the strong interaction, L is the left chirality of the weak interactions and Y stands for the hypercharge of the electromagnetic group. The approach to the model can be divided into two sectors:

i $SU(2)_L \times U(1)_Y$ subgroup:

It is referred to as Glashow-Salam-Weinberg Theory, or Electro-Weak Theory. It describes electromagnetic and weak interactions via the exchange of the massless photon gauge field for the electromagnetic interaction and three massive bosons $W^{\pm}$ and Z for the weak interaction.

The gauge symmetry is broken by the vacuum, which triggers the Spontaneous Symmetry Breaking (SSB), namely the Higgs Mechanism, of the electroweak group to the electromagnetic group:

$$SU(2)_L \times U(1)_Y \xrightarrow{SSB} U(1)_{QED},$$

and introduces the Higgs boson in the model as a consequence. It also induces the masses of the $W^{\pm}$ and Z^0 bosons, as well as the fermions.

ii $SU(3)_C$ subgroup:

This term corresponds to Quantum Chromodynamics (QCD), which describes the strong interaction between quarks and gluons, via the exchange of eight massless gluon gauge fields. Because of the nature of QCD, quarks are never observed as free particles but confined in bound states, known as hadrons. The hadronic states that have been observed consist of mesons ($q\bar{q}$) and baryons (qqq). Other exotic combinations as tetraquarks ($qqqq$) and pentaquarks ($qqqqq$) have also been discovered at LHCb [3, 4].

Putting all pieces together, the symmetry group $SU(3)_C \times U(1)_{QED}$ describes strong, weak and electromagnetic interactions, via the exchange of the gauge fields. The fermionic matter content is given by leptons and quarks, as shown in Fig. 2.1 and are organised in three-fold family structure as:

$$\begin{bmatrix} \nu_e & u \\ e^- & d' \end{bmatrix} \quad , \quad \begin{bmatrix} \nu_\mu & c \\ \mu^- & s' \end{bmatrix} \quad , \quad \begin{bmatrix} \nu_\tau & t \\ \tau^- & b' \end{bmatrix}, \tag{2.1}$$

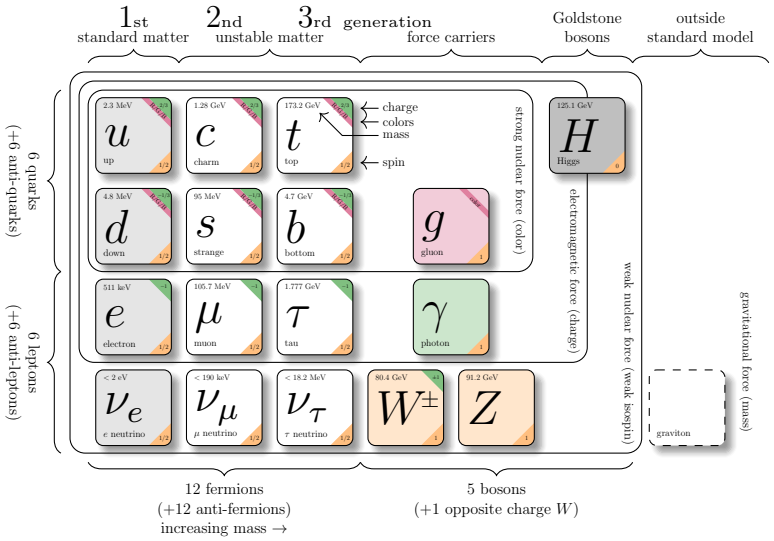

Figure 2.1: Fundamental particles in the Standard Model and the graviton. Leptons and quarks are the fermionic constituents of matter, organised in three-folds structure. The fourth columns represent the gauge bosons, which are gauge carriers. The Higgs boson is showed in the fifth column. Extracted from [6].

where,

$$\begin{bmatrix} l_e & q_u \\ l^- & q_d \end{bmatrix} \equiv \begin{pmatrix} \nu_l \\ l^- \end{pmatrix}_L , \begin{pmatrix} q_u \\ q_d \end{pmatrix}_L , l_R^-,\ q_{uR},\ q_{dR}, \tag{2.2}$$

plus the corresponding antiparticles. Therefore, The left-handed fields are $SU(2)_L$ doublets, while their right-handed partners transform as $SU(2)_L$ weak isospin singlets. The three fermionic families appear to have identical properties (gauge interactions), and they differ only by their mass and flavour quantum number [5].

2.1.2 Flavour Physics

In the SM with $SU(2)_L \times U(1)_Y$, the strenght of flavour-changing weak interaction is described by the Cabibbo-Kobayashi-Maskawa (CKM) unitary matrix [7,8]. Historically, the CKM matrix is the generalisation of the Cabibbo formalism for two families of quarks, extended for three families by Kobayashi and Maskawa. Formally, it relates the weak eigenstates of quarks to their mass eigenstates, parameterised as:

$$\begin{pmatrix} d' \\ s' \\ u' \end{pmatrix}_{\text{weak}} = \begin{pmatrix} V_{ud} & V_{us} & V_{ub} \\ V_{cd} & V_{cs} & V_{cb} \\ V_{td} & V_{ts} & V_{tb} \end{pmatrix} \begin{pmatrix} d \\ s \\ u \end{pmatrix}_{\text{mass}} . \tag{2.3}$$

The magnitude of each matrix element, $\mid V_{ij} \mid$, represents the amplitude of transition of q_i

quark into q_j quark, and therefore $\mid V_{ij} \mid^2$ gives the probability that a q_i quark turns into a q_j quark, *i.e.* the probability of transition $q_i \to q_j$. When considering the Charge-Parity (CP) conjugate process $\bar{q}_i \to \bar{q}_j$, the CKM-matrix element to consider is the complex conjugate V_{ij}^*

There are some arbitrariness in the conventions used to define this matrix. Absolute phases are not physical, and therefore 5 phases in the matrix can be reabsorbed by redefinition. By imposing unitarity conditions on top of that, the number of real parameters needed to describe the CKM-matrix is reduced from three moduli and six phases to three moduli and one phase. The resulting standard parameterisation consists of four free elements that are the three quark mixing angles θ_{ij} and one complex phase δ.

The measurements of the CKM parameters are consistent with the unitary conditions, and can be interpreted, as gathered in [9], as:

$$\begin{pmatrix} |V_{ud}| & |V_{us}| & |V_{ub}| \\ |V_{cd}| & |V_{cs}| & |V_{cb}| \\ |V_{td}| & |V_{ts}| & |V_{tb}| \end{pmatrix} \approx \begin{pmatrix} 0.974 & 0.227 & 0.004 \\ 0.226 & 0.973 & 0.041 \\ 0.009 & 0.040 & 0.999 \end{pmatrix}. \tag{2.4}$$

Therefore, according to the experimental evidence showed in Eq. 2.4, the weak interactions of quarks of different generation are suppressed with respect to that of the same generation. In particular, transitions within the same generation are characterized by V_{ii} elements of $\mathcal{O}(1)$. Those between the first and second generations are suppressed by a factor $\mathcal{O}(10^{-1})$; those between the second and third generation by a factor $\mathcal{O}(10^{-2})$; and those between the first and the third generation by a factor $\mathcal{O}(10^{-3})$ [10].

Because of the nearly diagonal shape of the CKM matrix, it is convenient to express it as an expansion of a small parameter, λ[1], that shows the CKM mixing hierarchy. A natural parameterisation that shows the strength of mixing angles of the CKM matrix was introduced by Wolfenstein [11]:

$$\begin{pmatrix} 1-\lambda^2/2 & \lambda & A\lambda^3(\rho - i\eta) \\ -\lambda & 1-\lambda^2/2 & A\lambda^2 \\ A\lambda^3(1-\rho-i\delta) & -A\lambda^2 & 1 \end{pmatrix} + \mathcal{O}(10^{-4}), \tag{2.5}$$

where:

$$\lambda = \frac{\mid V_{us} \mid}{\sqrt{\mid V_{ud} \mid^2 + \mid V_{us} \mid^2}}, \quad A\lambda^2 = \lambda \left| \frac{V_{cb}}{V_{us}} \right|, \quad A\lambda^3(\rho + i\eta) = V_{ub}^*. \tag{2.6}$$

The non-zero off-diagonal elements allow for quark mixing between generations, such as the process in flavour-changing charged currents (FCCC), like $b \to c\ell^-\bar{\nu}_\ell$ transitions[2], that occur at tree level. Processes of flavour-changing neutral currents (FCNC), such as $b \to s\ell^+\ell^-$ transitions[3] are forbidden at tree level by the GIM mechanism [12], and require a loop process involving a virtual $W^\pm$ exchange.

[1] $\lambda = 0.2265 \pm 0.0004$ [9].

[2] For more details, see Sec. 2.2.2.2.

[3] For more details, see Sec. 2.2.2.1.

2.1.3 Limitations of the Standard Model

The SM has successfully explained a wide range of precise experimental results. Despite this remarkable achievement, there are many unanswered questions that evidences that it is not the ultimate theory.

There are fundamental observed phenomena in nature that the SM is unable to explain, such as the existence of dark matter, which has been inferred through the galaxies dynamics; or the presence of dark energy, that is inferred from the speed of the expansion of the universe.

Within the SM, there are also some issues to be solved. First, the SM has 26 free parameters that are fitted experimentally: masses of the 12 fermions, the 3 coupling constants, 2 parameters that describe the Higgs potential and 8 mixing angles of the PMNS[4] and CKM matrices. The relatively large number of parameters hints that the SM would be an effective theory. Also, patterns that are not understood emerge between different parameters, suggesting a possible not-known symmetry. Moreover, gravity is not included in the SM and neutrinos are massless particles. Current neutrino experiments have shown that they actually have a mass, rising to the physical phenomena of neutrino oscillations. Also it is not clear why neutrinos masses are so tiny.

Related to the flavour sector, there are a number of fundamental questions. A transcendental issue is the observed matter-antimatter asymmetry in the universe. In the early universe, the scientific consensus is that after inflation there was a symmetric universe, *i.e.* equal abundances of matter and antimatter. Then, the excess of matter developed dynamically through a process called *baryogenesis*. This mechanism generates the asymmetry we observe today, which cannot be explained through the CP violation in the SM. Therefore, new sources of CP violation are required.

As it was motivated, physics Beyond the Standard Model is needed to explain unanswered questions in particle physics. Several searches for new particles are ongoing, that can be categorised on whether decays of new particles are studied, *direct searches*, or new physics processes are pursued through loops or additional Feynman diagrams, *indirect searches*, such as Lepton Flavour Universality tests.

2.2 Theory of semileptonic decays

The SM has been consolidated as a robust model capable of passing an enormous amount of demanding experimental tests. Its expansion through direct searches of NP in pp collision of the LHC has not yielded to any successful results, at the time of writing this document.

There is a second method for searching BSM physics, exploiting the presence of virtual states in the decay of SM particles. Semileptonic decays that involve leptons of different generations, consist of potential tests to look for NP contributions. In particular,

[4]Pontecorvo–Maki–Nakagawa–Sakata matrix [13]

semileptonic decays of a b-hadron, such as $B \to D\tau\nu$, are processes caused by the weak force in which one lepton, with each corresponding neutrino, are produced in addition to one (or more) hadron. Therefore, since leptons of different generations but with the same quark transition are involved, these decays are preferred to test the fundamental property of the SM that states that the three families of fermions are identical, except for the different mass, turning into powerful indirect searches for NP.

2.2.1 Lepton Flavour Universality

The main features of Lepton Flavour Universality (LFU) related to the SM will be discussed in the following since tests of this property constitute the main focus of this thesis.

In order to probe that the strength of the weak interaction is the same for all lepton flavours, the assumption that the coupling at each $W\ell\nu_\ell$, where $\ell = e, \mu, \tau$ is given by a non universal Fermi constant G_F^ℓ, is taken. Decays of charge leptons of Fig. 2.2, will be considered throughout the demonstration.

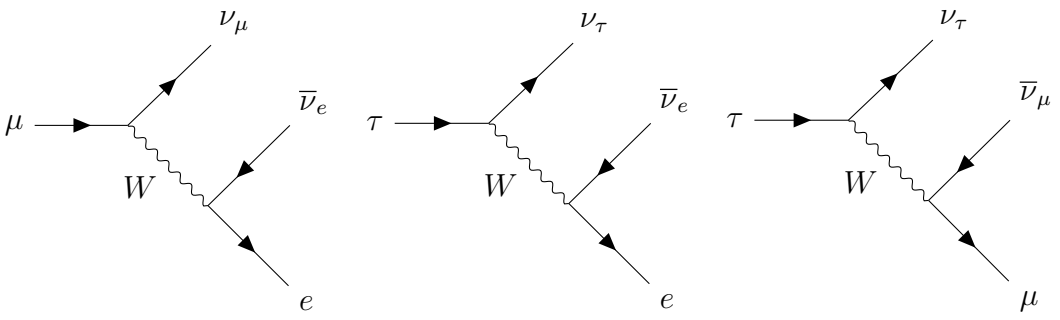

(a) $\mu \to e\overline{\nu}_e\nu_\mu$ (b) $\tau \to e\overline{\nu}_e\nu_\tau$ (c) $\tau \to \mu\overline{\nu}_\mu\nu_\tau$

Figure 2.2: Feynman diagrams of the leptonic decays of the charged leptons.

The muon decay $\mu \to e\overline{\nu}_e\nu_\mu$, Fig. 2.2(a), involves two weak-interaction vertices. Allowing the coupling of theses two vertices to be different, the decay rate can be written, to the next-to-leading order precision, as:

$$\Gamma(\mu \to e\overline{\nu}_e\nu_\mu) = \frac{G_F^e G_F^\mu m_\mu^5}{192\pi^3} \times f\left(m(e)^2/m(\mu)^2\right), \tag{2.7}$$

where $f(x) = 1 - 8x + 8x^3 - x^4 - 12x^2 \log x$ is the phase-space correction factor [14, 15]. Moreover, Eq. 2.7 can be expressed in therms of the muon lifetime, since $\mu \to e\overline{\nu}_e\nu_\mu$ is almost the sole decay of the muon, according to [9]. Therefore:

$$\Gamma(\mu \to e\overline{\nu}_e\nu_\mu) = \Gamma(\mu \to X) = \frac{1}{\tau_\mu}. \tag{2.8}$$

The same calculation for the decay rate $\tau \to e\overline{\nu}_e\nu_\tau$, Fig. 2.2(b), leads to:

$$\Gamma(\tau \to e\overline{\nu}_e\nu_\tau) = \frac{G_F^e G_F^\tau m_\mu^5}{192\pi^3} \times f\left(m(e)^2/m(\tau)^2\right). \tag{2.9}$$

Note that in some theoretical perspectives, as [15], it is included an extra term in Eq. 2.7, r_{EW}, that accounts for radiative corrections not included in the Fermi coupling constant. This contribution was already introduced in [16], and recently studies [17,18] have shown that the term was underestimated, and it may cause a bias in $\mathcal{R}(D)$ as high as 7%. However, this bias depends on individual analysis, and therefore it is required future high precision measurements from QED.

The tauon is sufficiently massive, so it can decays into a muon, $\tau \to \mu\overline{\nu}_\mu\nu_\tau$, as it is illustrated in the diagram of Fig. 2.2(c), or to mesons formed from light quarks. Therefore, the τ lifetime can be expressed as:

$$\frac{1}{\tau_\tau} = \Gamma(\tau \to X) = \sum_i \Gamma_i, \tag{2.10}$$

being Γ_i the partial decay rates for the individual decay modes. The branching fraction, in terms of the partial and total decay rate, is of the form:

$$\mathcal{B}(\tau \to e\overline{\nu}_e\nu_\tau) = \frac{\Gamma(\tau \to e\overline{\nu}_e\nu_\tau)}{\Gamma} = \Gamma(\tau \to e\overline{\nu}_e\nu_\tau) \times \tau_\tau. \tag{2.11}$$

From Eqs. 2.7 and 2.9, the τ lifetime can be written as:

$$\tau_\tau = \frac{192\pi^3}{G_F^e G_F^\tau m_\tau^5} \mathcal{B}(\tau \to e\overline{\nu}_e\nu_\tau). \tag{2.12}$$

Now, comparing the expressions for muon and tauon lifetimes, equations Eqs. 2.12 and 2.8, the ratio of non-universal Fermi constants gives:

$$\frac{G_F^\tau}{G_F^\mu} = \frac{m_\mu^5 \tau_\mu}{m_\tau^5 \tau_\tau} \mathcal{B}(\tau \to e\overline{\nu}_e\nu_\tau). \tag{2.13}$$

The ratio of the coupling can be obtained by measuring the ratio of the branching fractions. Tab. 2.1 gathers the values of the observables needed for the computation of the charged-current coupling strength, exploiting data from [9]. From these measured values and the relation of Eq. 2.13, the ratio of the muon and tauon weak charged-current coupling strength is determined to be:

$$\frac{G_F^\tau}{G_F^\mu} = 1.002 \pm 0.003. \tag{2.14}$$

Similarly, by comparing the branching fraction of tauon to the electronic and muonic decay modes, and taking into account the expected small difference due to phase space, it leads to:

$$\frac{G_F^e}{G_F^\mu} = 0.997 \pm 0.003. \tag{2.15}$$

Therefore, with high experimental accuracy, it can be concluded that $G_F^e = G_F^\mu = G_F^\tau$, providing strong experimental evidence for the lepton universality of the weak charged currents [19].

Quantity	Value
$\mathrm{m}(e)$	$(0.5109989461 \pm 0.0000000031)\,\mathrm{MeV}/c$
$\mathrm{m}(\mu)$	$(105.6583745 \pm 0.0000024)\,\mathrm{MeV}/c$
$\mathrm{m}(\tau)$	$(1776.86 \pm 0.12)\,\mathrm{MeV}/c$
$\tau(\mu)$	$(2.1969811 \pm 0.0000022) \times 10^{-6}\,\mathrm{s}$
$\tau(\tau)$	$(2.903 \pm 0.005) \times 10^{-13}\,\mathrm{s}$
$\mathcal{B}(\tau \to e\overline{\nu}_e\nu_\tau)$	$(17.82 \pm 0.04)\%$
$\mathcal{B}(\tau \to \mu\overline{\nu}_\mu\nu_\tau)$	$(17.39 \pm 0.04)\%$

Table 2.1: Input values obtained from [9] used for LFU derivation in leptonic decay of charged leptons.

Once LFU has been proved for purely leptonic decays of charged leptons, the importance of LFU tests can be highlighted by mentioning three features of the SM. Firstly, as it was presented, fermions are organized in three-fold families with the same gauge charge assignment, which lead to the same structure of coupling in all three generations, that is called *universality*. Secondly, this universality of the gauge couplings is not affected by the breakdown of the gauge coupling by the Higgs mechanism. Finally, the only difference between the three families comes from the Yukawa interaction between the Higgs field and the fermion field. The fermion mixing is described in the weak basis, where the mass matrix is diagonal, so that the mixing matrix relates weak and mass eigenstates. Then, the only source of difference between the three generations comes from the parameters of the mixing matrix: CKM matrix for the quark sector, and PMNS matrix for leptons. This last aspect is a key point in order to consider observables that test LFU, since for a given decays, quark and lepton transition depends on a different basis. [20].

2.2.2 Tests of Lepton Flavour Universality

Semileptonic decays of heavy hadrons are an excellent laboratory to test LFU, as the three generations can be accessed and compared. Since a violation of LFU symmetry would indicate the presence of NP, this symmetry can be tested by comparing observables that involve the same process differing only in the lepton flavours entering in the decay, such as the ratio of branching fraction for two decays. From the theoretical point of view, ratios provide the advantage that most of the hadronic uncertainties cancel out in the numerator and denominator. From an experimental point of view, the use of ratios is beneficial since many of the systematic uncertainties are cancelled. Two interesting sets of measurements that can be carried out to probe violation of LFU:

- Flavour Changing Neutral Currents (FCNC), in particular $b \to s\ell^+\ell^-$ transitions, which can only occur through loop diagrams in the SM.
- Flavour Changing Charged Currents (FCCC), specifically $b \to c\ell^-\bar{\nu}_\ell$, which consist of tree level processes in the SM.

2.2.2.1 $b \to s\ell^+\ell^-$ transitions

In the SM, decays of B hadrons (hadrons with a b-quark) involving a loop-level transition, like $b \to s\ell^+\ell^-$, provide a good laboratory to test LFU. Since the CKM is close to diagonal, these FCNC decays are highly suppressed in the SM, and therefore provide an increased sensitivity to NP contributions. The leading-order Feynman diagrams for $b \to s\ell^+\ell^-$ transitions proceed through the exchange of either a Z/γ penguin (Fig. 2.3 left) , or a W^+/W^- box (Fig. 2.3 right).

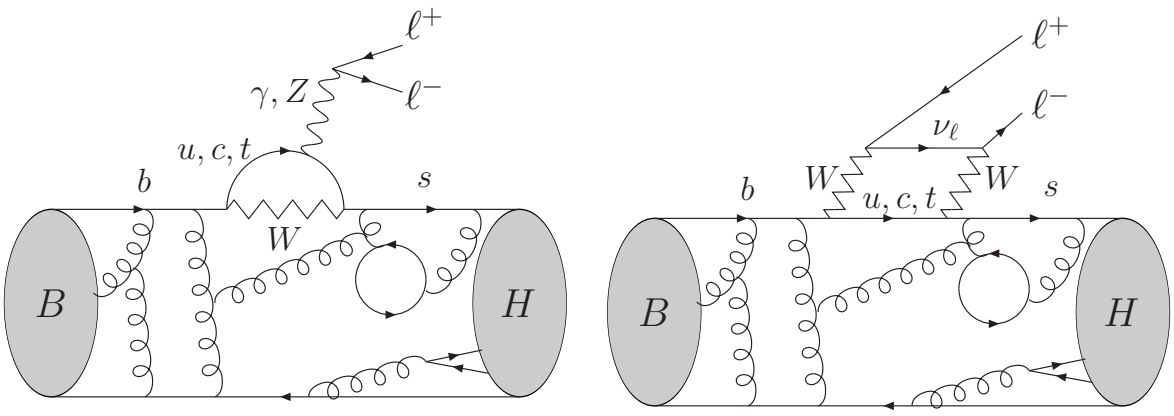

Figure 2.3: Illustration of a penguin (left) and box (right) processes of the $b \to s\ell^+\ell^-$ seen at the hadronic level, for the case of a B meson decaying in a H meson. Figures taken from [20].

Sensitive probes of particular interest to study $b \to s\ell^+\ell^-$ transitions are the ratios defined as:

$$\mathcal{R}_{H_s} = \frac{\int_{q^2_{\min}}^{q^2_{\max}} \frac{d\Gamma\left(H_b \to H_s \mu^+\mu^-\right)}{dq^2} dq^2}{\int_{q^2_{\min}}^{q^2_{\max}} \frac{d\Gamma\left(H_b \to H_s e^+e^-\right)}{dq^2} dq^2}, \tag{2.16}$$

being H_b a hadron containing a b-quark, H_s a hadron containing a s-quark, and q^2 the invariant mass squared of the dilepton system, integrated in the range between $q^2_{\min}$ and $q^2_{\max}$. Several measurements of $\mathcal{R}_{H_s}$ have been performed for experiments operating at both the B-factories and the LHC, for the particular cases of $H_s = K^+, K^*, K^0_S, K^{*0}, pK^+, K^{**}$ with $H_b = B^+, B^0, \Lambda_b$.

Theoretical predictions of the SM for $\mathcal{R}_K$ and $\mathcal{R}_{K^*}$ are extremely accurate [21,22] due to a large cancellation of hadronic uncertainties in the ratios. In Tab. 2.2, some relevant theoretical SM predictions for $\mathcal{R}_K$ and $\mathcal{R}_{K^*}$ observables are presented, where it is shown that the expectations of such ratios are very precise and found to be close to unity, with up to a per mile uncertainty.

Observable	q^2 **range**	**Ref. [23]**	**Ref. [24]**	**Ref. [25]**	**Ref. [26]**
$\mathcal{R}_K$	$1.0 - 6.0\,\text{GeV}^2/c^4$	1.00 ± 0.01	-	$1.0004^{+0.0008}_{-0.0007}$	1.00 ± 0.01
$\mathcal{R}_{K^*}$	$0.045 - 1.1\,\text{GeV}^2/c^4$	0.096 ± 0.028	0.9259 ± 0.0041	$0.920^{+0.007}_{-0.006}$	0.92 ± 0.02
$\mathcal{R}^*_K$	$1.1 - 6.0\,\text{GeV}^2/c^4$	1.00 ± 0.01	0.9965 ± 0.0006	$0.996^{+0.002}_{-0.002}$	1.00 ± 0.01

Table 2.2: SM predictions for $\mathcal{R}_{K^{(*)}}$.

2.2.2.1.1 Current experimental status

The first probes of LFU in $b \to s\ell^+\ell^-$ decays were perfomed in B-factories[5]. In particular, Belle and BaBar collaborations exploit the advantage of cleanliness in collision events at the $\Upsilon(4S)$ resonance to make the first measurements of $\mathcal{R}_K$ and $\mathcal{R}_{K^*}$ ratios [27, 28], studying two different q^2 bins in the case of BaBar and one region for Belle. All of the results have a relative precision of 20 to 50%, dominated by the statistical uncertainty, and they agree with the SM prediction within 1σ. In 2019, Belle [29] performed a measurement of the $\mathcal{R}_{K^*}$ in several q^2 bins, including the high q^2 region, up to $19\,\text{GeV}^2/c^4$. The results obtained are all consistent with the SM, being the largest deviation in the lowest q^2 bin. The last analysis performed with B-factories data was published in 2021, when a new measurement of $\mathcal{R}_K$ was presented by Belle [30], obtaining a result consistent with SM.

At a hadron collider, where the collisions are produced at high energy, measurements involving electrons are a great challenge, due to the complications that the high bremsstrahlung rate add to the reconstruction. Moreover, the high occupancy of the detector carry as a consequence low efficiency in the trigger. Specific procedures are needed in order to deal with the particular complexities, such as dedicated bremsstrahlung recovery or a trigger specifically aimed at mitigating signal loss due to low efficiency of the calorimeter hardware trigger. In 2014, the first measurement of the $\mathcal{R}_K$ ratio [31] at a hadron collider was performed by the LHCb experiment, using data from Run 1. The observable $\mathcal{R}_K$ was successfully measured in one bin with a precision of 12%, being compatible with the SM at 2.5σ level. Later, in 2017 the $\mathcal{R}_{K^*}$ ratio [32] was obtained in two q^2 bins at 17% precision each, with a SM compatibility at the $2.2 - 2.5\sigma$.

Recently last year (2021), LHCb collaboration updated the result of $\mathcal{R}_K$ [33] using the together Run 1 and Run 2 data. The new result have the same central value as the previous one presented in 2017 [34], while the statistical uncertainty has been reduced by

[5]See more details about B-factories production in Sec. 2.2.2.2.1.

a 30%. As a consequence, the tension between the experimental measurement and the SM prediction has increased from 2.5σ to 3.1σ.

From all the previous measurements listed above, it is clear that $\mathcal{R}_{K^{(*)}}$ ratios present a intriguing behaviour showing some tension with the SM that could be explained by NP contributions. Fig. 2.4(a) shows a comparison of the last $\mathcal{R}_K$ measurements of LHCb [33] together with B-factories results [28, 30], while in Fig. 2.4(b) it is shown the LHCb $\mathcal{R}_{K^{*0}}$ measurement [32] with previous experimental results of B-factories [27, 28]. After the last improvements in the $\mathcal{R}_{K^{(*)}}$ results, the measurements became statistical uncertainty dominated, and therefore more data is needed in order to solve the persistent tension.

Experiment (year)	$\boldsymbol{H_s}$ **type**	$\boldsymbol{q^2}$ **range** $[\mathbf{GeV^2/c^4}]$	**Value**	**Ref.**
Belle (2009)	K	0.0− kin. endpoint	$1.03 \pm 0.19 \pm 0.06$	[27]
Belle (2009)	K^*	0.0− kin. endpoint	$0.83 \pm 0.17 \pm 0.08$	[27]
BaBar (2012)	K	$0.10 - 8.12$	$0.74^{+0.40}_{-0.31} \pm \pm 0.06$	[28]
BaBar (2012)	K^*	> 10.11	$1.43^{0.65}_{-0.44} \pm 0.12$	[28]
BaBar (2012)	K^*	$0.10 - 8.12$	$1.06^{+0.48}_{-0.33} \pm 0.08$	[28]
BaBar (2012)	K^*	> 10.11	$1.18^{+0.55}_{-0.37} \pm 0.11$	[28]
LHCb (2014)	K^+	$1.0 - 6.0$	$0.745^{+0.090}_{0.074} \pm 0.036$	[31]
LHCb (2017)	K^{*0}	$0.045 - 1.1$	$0.66^{+0.11}_{-0.03} \pm 0.05$	[32]
LHCb (2019)	K	$1.1 - 6.0$	$0.846^{+0.060+0.016}_{-0.054-0.014}$	[34]
Belle (2019)	K^*	$0.1 - 8.0$	$0.90^{+27}_{-0.21} \pm 0.10$	[29]
Belle (2019)	K^*	$15.0 - 19.0$	$1.18^{+52}_{-0.32} \pm 0.10$	[29]
Belle (2019)	K^*	$0.1 - 8.0$	$0.90^{+27}_{-0.21} \pm 0.10$	[29]
LHCb (2021)	K	$1.1 - 6.0$	$0.846^{+0.042+0.013}_{-0.039-0.012}$	[33]
Belle (2021)	K	$1.0 - 6.0$	$1.03^{+0.28}_{-0.24} \pm 0.01$	[30]

Table 2.3: Summary of the $\mathcal{R}_{K^{(*)}}$ measurements performed at the B-factories and by the LHCb experiment. The first uncertainty contribution is the statistical source and the second represents the systematic uncertainty.

2.2.2.2 $b \to c\ell^-\bar{\nu}_\ell$ transitions

In Sec. 2.2.1, it was shown that the electroweak coupling of the gauge bosons to the leptons is independent of the lepton family. Semileptonic $b \to c\ell^-\bar{\nu}_\ell$ processes are FCCC that occur through tree-level diagrams, as shown in Fig. 2.5, and differ through the mass of the lepton ($\ell = e, \mu, \tau$).

All NP models adding coupling to the leptons proportional to their mass would couple preferentially to the tauon (17 and 3500 times heavier than the muon and the electron, respectively), thus semileptonic decays to the third-generation, namely semitauonic B decays, would be more sensitive to the presence of NP effects. Measurements of ratios

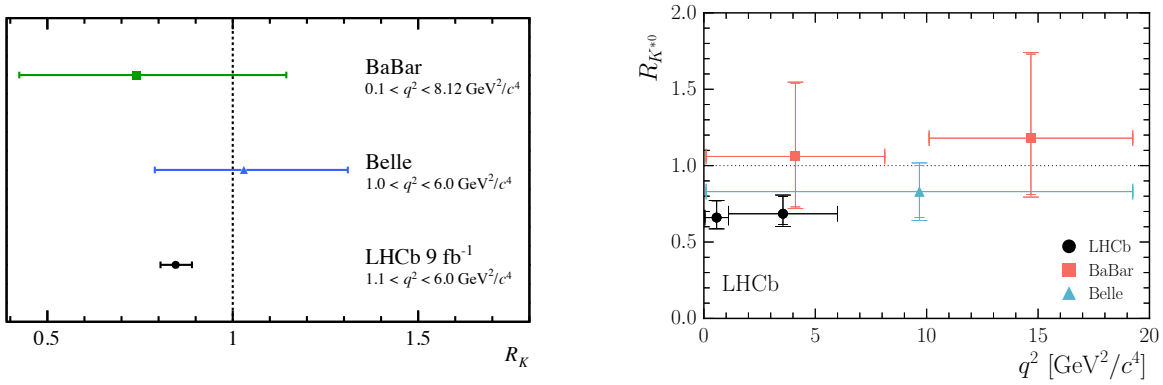

(a) (b)

Figure 2.4: (a) Comparison between $\mathcal{R}_K$ measurements of LHCb full Run 1 and Run 2 data [33] together with B-factories results [28, 30], extracted from [33]. (b) Comparison of the LHCb $\mathcal{R}_{K^{*0}}$ measurement [32] with previous experimental results of B-factories [27, 28], extracted from [32].

of branching fractions between lepton generations have been performed in order to test LFU:

$$\mathcal{R}(H_c) = \frac{\mathcal{B}(H_b \to H_c \tau^+ \nu_\tau)}{\mathcal{B}(H_b \to H_c \ell'^+ \nu_{\ell'})}, \tag{2.17}$$

where ℓ' stands for an electron or a muon in the B-factories measurements, but only for a muon at the LHCb detector, due to experimental considerations[6]. There have been performed LFU tests for the cases $H_c = D^{*+}, D^0, D^+, D^{(*)+}, \Lambda_c^{(*)+}, J/\psi$, with $H_b = B^0, B^+_{(c)}, \Lambda^0_b, B^0_s$. The inclusion of charge-conjugate modes is implied throughout. The definition of this kind of observables cancels large part of theoretical ($|V_{cb}|$ and form factors) and experimental (branching fractions and reconstruction efficiencies) uncertainties [20]. In $\mathcal{R}(H_c)$ measurements, the τ lepton can be reconstructed through different decay modes. In Tab. 2.4, the τ final states with the largest branching fractions used to perform measurements in semitauonic H_b decays are gathered.

2.2.2.2.1 Results from the B-factories

In measurements coming from B-factories, the analysis strategy is built exploiting the fact that the $\Upsilon(4S)$ resonance decays exclusively into a pair of two B mesons, either a $B^0\overline{B}^0$ or a B^+B^- pair. Tagging techniques are used to reconstruct both mesons. One

[6] In the case of LHCb measurements with $\tau \to 3\pi\nu$, it is not performed the direct measurement of $\mathcal{R}(H_c)$. Rather the value of $\mathcal{B}(H_b \to H_c \ell' \nu)$ is taken from [9], and thus the $\mathcal{R}(H_c)$ coefficient can be obtained for the case where ℓ' is a muon, an electron or a combination of both.

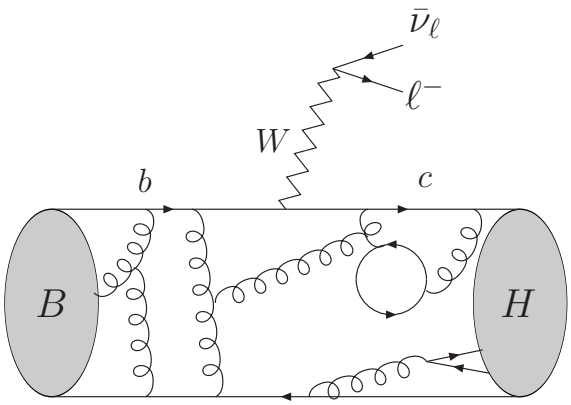

Figure 2.5: Illustration of a tree level process of the $b \to c\ell\overline{\nu}_\ell$ seen at the hadronic level, for the case of a B meson decaying into a H meson. Figure taken from [20].

Decay	$\mathcal{B}$ [%]
$\tau^- \to \mu^-\overline{\nu}_\mu\nu_\tau$	17.39 ± 0.04
$\tau^- \to e^-\overline{\nu}_e\nu_\tau$	17.82 ± 0.04
$\tau^- \to \pi^-\pi^0\nu_\tau$	25.49 ± 0.09
$\tau^- \to \pi^-\nu_\tau$	10.82 ± 0.05
$\tau^- \to \pi^-\pi^+\pi^-\nu_\tau$	9.02 ± 0.05
$\tau^- \to \pi^-\pi^+\pi^-\pi^0\nu_\tau$	4.49 ± 0.05

Table 2.4: Branching fractions of τ decays that have been used to perform measurements of $\mathcal{R}(H_c)$ observables, extracted from [35]. The 3-prong hadronic modes does not contain the K^0 contributions.

of the mesons, B_{tag}, is fully reconstructed through hadronic or partially reconstructed semileptonic B decays, where the second approach provides higher efficiency but lower kinematic constraints. Then, all the remaining particles in the rest of the event are due to signal decays coming from the other B meson, B_{signal}. At the B-factories, pure leptonic as well as hadronic decays of the τ are considered. In these decays, neutrinos that are undetected are present, and therefore there is some missing information that has to be compensated by the reconstruction of the B_{tag}.

Both BaBar and Belle collaborations have performed measurements of the $\mathcal{R}(H_c)$ observables of Eq. 2.17, for the cases $H_c = D, D^*$, where D indicates D^0 or D^+ and D^* stands for D^{*-} or D^{*0} mesons. Covering the most recent semitauonic results involving hadronic B tags, BaBar experiment published the first high-precision measurement of $R\left(D^{(*)}\right)$ with the full dataset obtained in 2012 [36, 37] , composed by $471 \times 10^6 B\overline{B}$ pairs. The Belle experiment, following a similar strategy, performed an analysis of their $772 \times 10^6 B\overline{B}$ pair dataset [38]. In both cases, the signal τ decays are $\tau \to \ell\nu\overline{\nu}$, where the light lepton $\ell = e$ or μ. These just presented results from BaBar and Belle analyses are

compatible within uncertainties.

An additional measurement of $B \to D^{(*)}\tau\nu$ decays involving hadronic tags was performed by Belle [39]. This analysis obtained the τ polarisation fraction $\mathcal{P}_\tau(D^*)$ by reconstructing the tau lepton in the hadronic $\tau \to \pi\nu$ and $\tau \to \rho\nu$ modes. The result is in good agreement with the SM expectations.

Focusing now in B-factories measurements with semileptonic tags and $\tau \to \ell\nu\overline{\nu}$ decays, the first result of $\mathcal{R}(D^*)$ was performed by Belle [40] in 2016, followed by a recent update that includes the combined measurement of $\mathcal{R}(D)$ and $\mathcal{R}(D^*)$ [41]. The last published results are in agreement with the SM prediction within 0.2σ and 1.1σ respectively, while the combined measurement agrees with the SM prediction within 0.8σ.

A summary of the reported results of $\mathcal{R}(D)$ and $\mathcal{R}(D^*)$ ratios [36–41] obtained by the B-factories experiments is shown in Tab. 2.5.

Experiment (year)	B-tag	τ decay	$\mathcal{R}(D)$	$\mathcal{R}(D^*)$	Correlation	$P_\tau(D^*)$	Ref.
BaBar (2012)	Had.	$\tau^- \to \ell'^- \overline{\nu}_{\ell'} \nu_\tau$	$0.440 \pm 0.058 \pm 0.042$	$0.032 \pm 0.024 \pm 0.018$	-0.27	–	[36, 37]
Belle (2015)	Had.	$\tau^- \to \ell'^- \overline{\nu}_{\ell'} \nu_\tau$	$0.375 \pm 0.064 \pm 0.026$	$0.293 \pm 0.038 \pm 0.015$	-0.49	–	[38]
Belle (2016)	SL	$\tau^- \to \ell'^- \overline{\nu}_{\ell'} \nu_\tau$	–	$0.302 \pm 0.030 \pm 0.011$	–	–	[40]
Belle (2017)	Had.	$\tau^- \to \pi^-(\pi^0)\nu_\tau$	–	$0.270 \pm 0.035\ ^{+0.028}_{-0.025}$	–	$-0.38 \pm 0.51\ ^{+0.21}_{-0.16}$	[39]
Belle (2019)	SL	$\tau^- \to \ell'^- \overline{\nu}_{\ell'} \nu_\tau$	$0.307 \pm 0.037\ 0.016$	$0.283 \pm 0.018 \pm 0.014$	-0.47	-	[41]

Table 2.5: Measurements of $\mathcal{R}(D^{(*)})$ and τ polarisation performed by BaBar and Belle collaborations. The tagging algorithm employed in the analysis is indicated with Had. (hadronic) or SL (semileptonic). The first uncertainty contribution is the statistical source and the second one represents the systematic uncertainty.

2.2.2.2.2 Results from the LHC

At a pp collider, such as the LHC, $b\bar{b}$ pairs are produced with a broad energy spectrum, and therefore the technique developed at B-factories cannot be applied. By taking advantage of the precise decay vertex reconstruction capabilities of the LHCb detector[7], the H_b momentum can be determined up to a discrete ambiguity in the hadronic reconstruction of the τ, *i.e.* $\tau \to \pi^+\pi^-\pi^+\nu$.

The τ can be also reconstructed through its muonic mode, *i.e.* $\tau \to \mu\nu\overline{\nu}$. In this case, the τ decay vertex cannot be reconstructed and therefore the momentum of the b-hadron is obtained via the *rest frame approximation*, which assumes that the momentum of the H_b along the beam axis is equal to the momentum of the final visible state.

The LHCb experiment has performed measurements of the ratios $\mathcal{R}(D^*)$, $\mathcal{R}(J/\psi)$ and $\mathcal{R}(\Lambda_c^+)$ using the leptonic decay $\tau^- \to \mu^-\overline{\nu}_\mu\nu_\tau$, and $\mathcal{R}(D^*)$ measurements with the hadronic 3-prong decay $\tau^- \to \pi^-\pi^+\pi^-(\pi^0)\nu_\tau$. The results [42–46] were obtained using LHCb Run 1 data collected at energies of 7 and 8 TeV, corresponding to an integrated luminosity of $3\,\text{fb}^{-1}$, summarised in Tab. 2.6.

[7] See Sec. 3.2.1.1 for more details on the LHCb vertex resolution capabilities.

Observable (year)	τ decay	Value	Ref.
$\mathcal{R}(D^*)$ (2015)	$\tau^- \to \mu^- \overline{\nu}_\mu \nu_\tau$	$0.336 \pm 0.027 \pm 0.030$	[42]
$\mathcal{R}(D^*)$ (2018)	$\tau^- \to \pi^- \pi^+ \pi^- (\pi^0) \nu_\tau$	$0.280 \pm 0.018 \pm 0.029$	[43, 44]
$\mathcal{R}(J/\psi)$ (2017)	$\tau^- \to \mu^- \overline{\nu}_\mu \nu_\tau$	$0.71 \pm 0.17 \pm 0.18$	[45]
$\mathcal{R}(\Lambda_c^+)$ (2022)	$\tau^- \to \pi^- \pi^+ \pi^- (\pi^0) \nu_\tau$	$0.242 \pm 0.026 \pm 0.040 \pm 0.059$	[46]

Table 2.6: LHCb measurements of the ratios $\mathcal{R}(D^*)$, $\mathcal{R}(J/\psi)$ and $\mathcal{R}(\Lambda_c^+)$. The first uncertainty contribution is statistical source and the second one represents the systematic uncertainty; the third one in the $\mathcal{R}(\Lambda_c^+)$ case corresponds to the external branching fraction uncertainty.

In order to make a comparison between experimental measurements and the SM prediction, the theoretical calculations are assumed to be the average performed by the HFLAV group [47], *i.e.* $\mathcal{R}(D)_{\text{SM}} = 0.299 \pm 0.003$ and $\mathcal{R}(D^*)_{\text{SM}} = 0.258 \pm 0.005$. In Sec. 2.2.2.2.3, the theoretical computation of $\mathcal{R}(D^*)$ and $\mathcal{R}(D)$ is derived. Fig. 2.6 summarises the experimental measurements, together with the SM prediction. The $\mathcal{R}(D)$ figure (left) shows an experimental-theoretical tension of 1.4σ, while the one corresponding to $\mathcal{R}(D^*)$ exhibits tension at the level of 2.9σ. Finally, plotting $\mathcal{R}(D^*)$ with respect to $\mathcal{R}(D)$, Fig. 2.7, shows a remarkable tension of 3.4σ with respect to the SM. This result motivates further analyses that could clarify the disagreement between theoretical and experimental results.

2.2.2.2.3 Effective Field Theory Computation of $\mathcal{R}(D^{(*)})$

The electroweak regime involves a large variety of energy scales, and therefore seems natural a theoretical approach that allow to separate out effects coming from different energy scales. The basic premise of an Effective Field Theory (EFT) [48, 49] is that the dynamics at low energies (large distances) does not depend of dynamics at high energies (short distances). As a result, low-energy physics can be described by means of an effective Lagrangian that contains only a few degrees of freedom, while not taking into account additional degrees that are just present at higher energies. The process of integrating the relevant degrees of freedom is performed using renormalisation group (RG) equations [50].

In the case where a hadron contains one heavy quark (such as the b-quark), the Heavy-Quark Effective Theory (HQET) essence, discussed in detail in [51], is the construction of an effective field theory starting from the QCD Lagrangian and performing a $1/m_Q$ expansion, where $m_Q = m_b, m_c$ is the mass of the heavy quark. This expansion is useful if the maximum momentum scale, k, of the process under consideration satisfies the condition $k/m_Q \ll 1$.

Following [52], the effective Hamiltonian approach can be applied to FCNC. For the $b \to c\ell^- \overline{\nu}_\ell$ transition, considering the $V-A$ structure of the weak interaction in the SM,

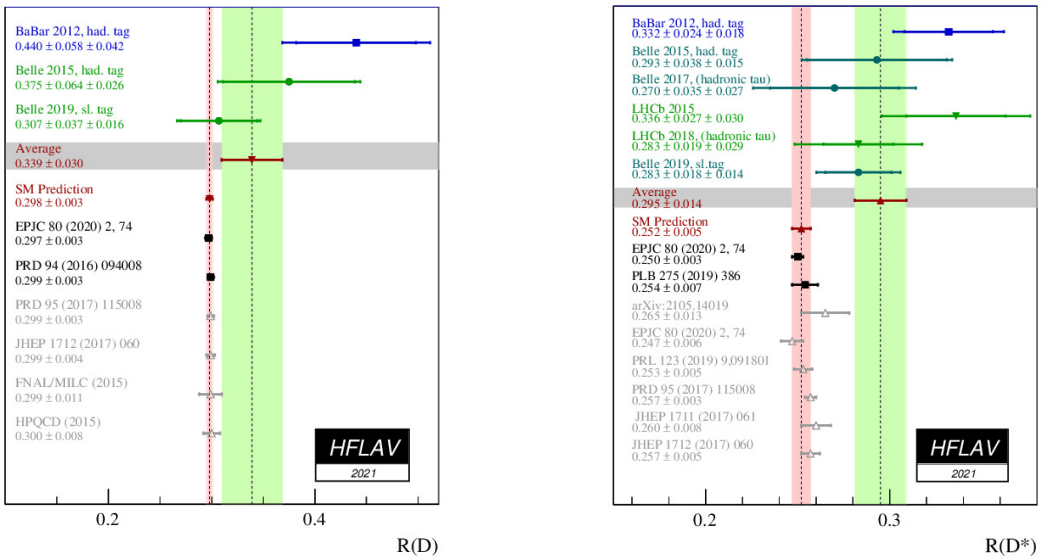

Figure 2.6: $\mathcal{R}(D)$ and $\mathcal{R}(D^*)$ world measurements, average in green, together with the SM prediction in red, by HFLAV [47].

it can be written:

$$\mathcal{H}_{eff} = \frac{4G_F V_{cb}}{\sqrt{2}} \left(\overline{c}\gamma_\mu P_L b\right) \left(\overline{\ell}\gamma^\mu P_L \nu_\ell\right) + h.c., \tag{2.18}$$

where G_F is the Fermi Constant, $G_F = 1.662787 \times 10^{-5}\,\text{GeV}^{-2}$, V_{cb} stands for the CKM matrix element, $P_{L,R} = (1 \mp \gamma_5)/2$ are the projectors on the left- (right-) handed chirality and $h.c.$ denotes the Hermitian conjugate.

The EFT ignores the W boson, and assumes a four-fermion operator $\mathcal{O}_i$. Energetic modes and massive fields that probe short distances, are encoded in the Wilson coefficients, $\mathcal{C}_i$ [20]. In Fig. 2.8, it can be seen an illustration of the $b \to c\ell^-\overline{\nu}_\ell$ process in the effective Hamiltonian approach. The Effective Hamiltonian can be expressed in terms of the local two-quark two-lepton operator, thus Eq. 2.18 can be written as:

$$\mathcal{H}_{eff} = \frac{4G_F V_{cb}}{\sqrt{2}} \sum_i \mathcal{C}_i \mathcal{O}_i. \tag{2.19}$$

Due to LFU, the SM Wilson coefficients have the same values for the three lepton families. Thus, the four-vector operator contains the dominant operator in the SM:

$$\mathcal{O}_{V\ell} = \left(\overline{c}\gamma_\mu P_L b\right) \left(\overline{\ell}\gamma^\mu P_L \nu_\ell\right), \tag{2.20}$$

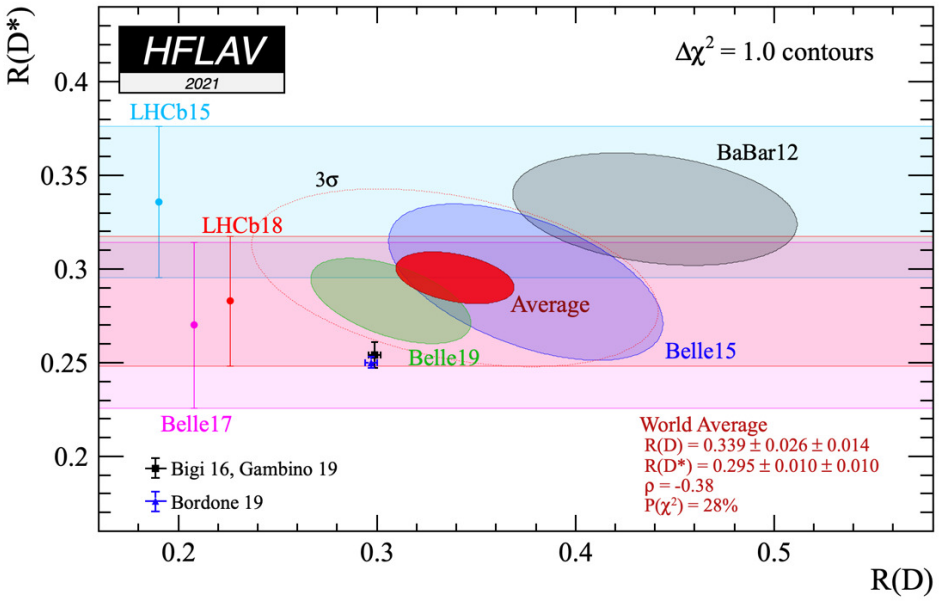

Figure 2.7: Overview of combined measurements of $\mathcal{R}(D^{(*)})$, together with the SM prediction displayed in the red ellipse, by HFLAV [47].

where the index $i = V\ell$ indicates the vector nature of the four-fermion operator, and ℓ takes account of the lepton flavour involved. The normalisation of Eq. 2.19 is chosen to have $\mathcal{C}_{V\ell}$ of order of the unity in the SM.

In [52], the detailed computation of the differential decay rate can be found. The main steps are reported in the following. Starting from the effective Hamiltonian of Eq. 2.18, the differential decay rate of $B^0 \to D^{*-}\ell^+\nu_\ell$ can be expressed as:

$$\begin{aligned}\frac{d^2\Gamma_\ell}{dq^2 d\cos\theta} =& \frac{G_F^2 |V_{cb}|^2 |\mathbf{p}|^2 q^2}{256\pi^3 m_B^2}\left(1-\frac{m_\ell^2}{q^2}\right)\times \\ & \Bigg[(1-\cos\theta)^2 |H_{++}|^2 + (1+\cos\theta)^2 |H_{--}|^2 + 2\sin^2\theta |H_{00}|^2 + \\ & \frac{m_\ell^2}{q^2}\left(\sin^2\theta\left(|H_{++}|^2+|H_{--}|^2\right)+2|H_{0t}-H_{00}\cos\theta|^2\right)\Bigg],\end{aligned} \tag{2.21}$$

where $|\mathbf{p}|$ is the 3 momentum of D^* in the B rest frame, given by: $|\mathbf{p}| = \frac{\lambda^{1/2}(m_B^2, m_{D^*}^2, q^2)}{2m_B}$, with $\lambda(a,b,c) = a^2+b^2+c^2-2(ab+bc+ca)$; q^2 corresponds to the four momentum transfer to the lepton system, expressed as $q^2 = (p_B - p_{D^*})^2$; θ stands for the angle between the D^* and the lepton in the $\ell-\nu_\ell$ rest frame and H_{mn} are the relevant (q^2 dependent) helicity amplitudes.

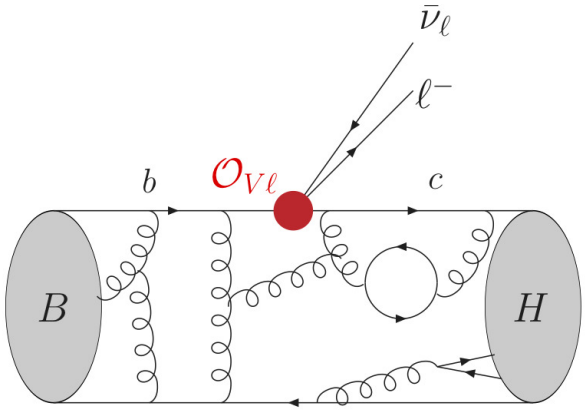

Figure 2.8: Illustration of the $b \to c\ell^-\overline{\nu}_\ell$ process in the effective Hamiltonian approach. The red dot represents a four-fermion local operator. Extracted from [20].

Performing integration over $d\cos\theta$ in Eq. 2.21 gives:

$$\frac{d\Gamma_\ell}{dq^2} = \frac{G_F^2|\mathbf{p}|q^2}{96\pi^3 m_B^2}\left(1-\frac{m_\ell^2}{q^2}\right)^2\left[\left(|H_{++}|^2+|H_{--}|^2+|H_{00}|^2\right)\left(1+\frac{m_\ell^2}{2q^2}\right)+\frac{3}{2}\frac{m_\ell^2}{q^2}|H_{0t}|^2\right]. \tag{2.22}$$

The helicity amplitudes can be expressed in terms of hadronic form factors, which depends on the spin of the decaying hadron and on the kind of quark bilinears from the effective Hamiltonian operator, like $\bar{c}\Gamma b$ of Eq. 2.20, being Γ the 4×4 matrix result of the product of the Dirac γ-matrices. The relevant form factors for $B \to H$ transitions, for H pseudoscalar or vector, for a given bilinear $\bar{q}\Gamma b$ are gathered in Tab. 2.7.

Then, the helicity amplitudes presented in Eq. 2.21 can be defined in terms of the three axial (A_0, A_1, A_2) and one vector (V) hadronic form factors depending on of q^2 as:

$$\begin{aligned}
H_{\pm\pm}^{\mathrm{SM}}(q^2) &= (m_B + m_{D^*})A_1(q^2) \mp \frac{2m_b}{m_B+m_{D^*}}|\mathbf{p}|V(q^2),\\
H_{00}^{\mathrm{SM}}(q^2) &= \frac{1}{2m_{D^*}}\sqrt{q^2}\left[\left(m_B^2 - m_{D^*}^2 - q^2\right)(m_b+m_{D^*})\,A_1(q^2) - \frac{4m_B^2|\mathbf{p}|^2}{m_B+m_{D^*}}A_2(q^2)\right],\\
H_{0t}^{\mathrm{SM}}(q^2) &= \frac{2m_B|\mathbf{p}|}{\sqrt{q^2}}A_0(q^2).
\end{aligned} \tag{2.23}$$

In order to make a prediction of the value of the $\mathcal{R}(D^{(*)})$ observable, the form factors need to be computed within the HQET framework. In this context, the form factors presented above are further expressed in terms of the universal form factor $h_{A_1}(w)$ and the ratios $R_{0,1,2}(w)$, which in turn are functions of the recoil variable w:

$$w = v_B \cdot v_{D^*} = \frac{m_B^2 + m_{D^*}^2 - q^2}{2m_B m_{D^*}}, \tag{2.24}$$

$J^P(H)$	γ	Form factors
0^-	γ_μ	f_0, f_+
0^-	$\sigma_{\mu\nu}$	f_T
1^-	γ_μ	A_0, A_1, A_2
1^-	$\gamma_\mu\gamma_5$	V
1^-	$\sigma_{\mu\nu}$	T_2, T_2
1^-	$\sigma_{\mu\nu}\gamma_5$	T_1

Table 2.7: Form factors relevant for $B \to H$ transitions as a function of the spin of the H hadron for a given bilinear $\overline{q}\Gamma b$.

where M is defined as:

$$M = \frac{2\sqrt{m_B m_{D^*}}}{(m_B + m_{D^*})}. \tag{2.25}$$

With the above definitions, the form factors are given by:

$$h_{A_1}(w) = A_1(q^2)\frac{1}{M}\frac{2}{w+1}, \tag{2.26}$$

$$A_0(q^2) = \frac{R_0(w)}{M}h_{A_1}(w), \tag{2.27}$$

$$A_2(q^2) = \frac{R_2(w)}{M}h_{A_1}(w), \tag{2.28}$$

$$V(q^2) = \frac{R_1(w)}{M}h_{A_1}(w). \tag{2.29}$$

The minimum value $w = 1$ corresponds to zero recoil of the D^* meson in the B rest frame, *i.e.* the largest kinematically allowed value of q^2.

CLN parameterisation

In the heavy quark limit, it is possible to establish approximate relations between the slope and the higher power coefficients of the reference form factors. This approximation is called Caprini-Lellouch-Neubert (CLN) parameterisation [53], and it provides simplified formulas valid within $\approx 2\%$, taking into account $1/m_Q$ (where Q stands for b or c quark) corrections near zero recoil ($w = 1$) [54]. Thus, the variation of the form factors of Eqs. 2.26, 2.27, 2.28 and 2.29 can be written as:

$$h_{A_1(w)} = h_{A_1}(1)\left[1 - 8\rho^2 z + (53\rho - 15)z^2 - (231\rho^2 - 91)z^3\right], \tag{2.30}$$

$$R_0(w) = R_0(1) - 0.11(w-1) + 0.01(w-1)^2, \tag{2.31}$$

$$R_1(w) = R_1(1) - 0,12(w-1) + 0.05(w-1)^2, \tag{2.32}$$

$$R_0(w) = R_0(1) - 0.11(w-1) + 0.01(w-1)^2, \tag{2.33}$$

being

$$z = \frac{\sqrt{w+1} - \sqrt{2}}{\sqrt{w+1} + \sqrt{2}}. \tag{2.34}$$

BGL parameterisation

Another approach to the form factors is the Boyd-Grinstein-Lebed (BGL) parameterisation, which was proposed in [55] and further developed in [56,57]. In semileptonic decays, the form factors can be parameterised as a product of known functions representing resonant poles and other nonanalytic structures, times a Taylor series in a conformal variable that tracks the momentum transfer. Therefore, the BGL parameterisations of $B \to D^* \ell \nu$ decays relies on the Taylor expansion of the form factors around $z = 0$, and depend on three functions, $f(w), g(w)$ and $\mathcal{F}_\infty(w)$:

$$h_{A_1}(w) = \frac{f(w)}{\sqrt{m_B m_{D^*}}(1+w)}, \tag{2.35}$$

$$R_0(w) = m_{D^*} \left(\frac{1+w}{1 + m_{D^*}/m_B} \right) \frac{\mathcal{F}_\in}{f}, \tag{2.36}$$

$$R_1(w) = (w+1) m_B m_{D^*} \frac{g(w)}{f(w)}, \tag{2.37}$$

$$R_2(w) = \frac{w-r}{w-1} - \frac{\mathcal{F}_1(w)}{m_B(w-1)f(w)}, \tag{2.38}$$

resulting the convergent power series of the form factor as:

$$f(z) = \frac{1}{P_{1+}(z)\phi_f(z)} \sum_{n=0}^{\infty} a_n^f z^n, \tag{2.39}$$

$$g(z) = \frac{1}{P_{1-}(z)\phi_g(z)} \sum_{n=0}^{\infty} a_n^g z^n, \tag{2.40}$$

$$\mathcal{F}_1(z) = \frac{1}{P_{1+}(z)\phi_{\mathcal{F}_1(z)}} \sum_{n=0}^{\infty} a_n^{\mathcal{F}_1} z^n, \tag{2.41}$$

$$\mathcal{F}_2(z) = \frac{1}{P_{0-}(z)\phi_{\mathcal{F}_2(z)}} \sum_{n=0}^{\infty} a_n^{\mathcal{F}_2} z^n. \tag{2.42}$$

where $P_{1\pm}(z)$ are Blaschke factors and $\phi_{f,g,\mathcal{F}_1(z)}$ phase space factors. Note that $R_0(w)$ is neglected for decays with light leptons, and it only affects τ decays.

The BGL parameterisation using the unitarity bound allows us to extend our knowledge of the form factors to other momentum transfers, and to do so in such a way that the errors can be quantified.

The world average of the form factor parameters reported by HFLAV [47] are gathered in Tab. 2.8 for CLN. As it was mentioned, the $R_0(1)$ was not measured in decays to light

leptons since they are not sensitive to this parameter, and it only contributes to the helicity suppressed amplitude $H_{0,t}$. Within HQET, it value was estimated later on, as it is reported in Tab. 2.8.

Parameter	Value	Reference
ρ^2	1.122 ± 0.015 (stat) ± 0.019 (syst)	HFLAV world average [47]
$R_1(1)$	1.270 ± 0.026	HFLAV world average [47]
$R_2(1)$	0.852 ± 0.018	HFLAV world average [47]
$\eta_{\rm EW} h_{A_1} \lvert V_{cb}\rvert$	35.27 ± 0.11 (stat) ± 0.36 (syst)	FLAG average of [58] Lattice QCD results
$R_0(1)$	1.14 ± 0.11	HQET [52]
$R_0(1)$	1.17 ± 0.02	HQET [59]

Table 2.8: World average of the CLN form factors, as updated in Spring 2021 [47].

Coming back to Eq. 2.22, the ratio of decay rates for both τ and ℓ, being ℓ either μ or e, can be expressed in terms of the hadronic helicity amplitudes, giving for $\mathcal{R}(D^*)$ the expression:

$$\mathcal{R}(D^*) = \frac{d\Gamma_\tau/dq^2}{d\Gamma_\ell/dq^2} = \left(1 - \frac{m_\tau^2}{q^2}\right)\left[\left(1 + \frac{m_\tau^2}{2q^2}\right) + \frac{3m_\tau^2}{2q^2}\frac{|H_{0t}|^2}{|H_{++}|^2 + |H_{--}|^2 + |H_{00}|^2}\right], \quad (2.43)$$

where the terms with m_ℓ^2/q^2, being $\ell = \mu, e$ in Eq. 2.22 have been neglected.

Several computations of $\mathcal{R}(D^*)$ were performed, all in agreement with the approach followed in this document, based in [52]. The most relevant inputs to the new predictions are obtained fitting with the BGL parameterisation derived from Belle data [60].

The calculations present differences in the evaluation of the theoretical uncertainties, which will be untangled with the Lattice QCD calculations of the $B \to D^*$ form factors beyond the zero recoil limit. The theoretical value is assumed to be an average performed by HFLAV [47] between all the $\mathcal{R}(D^*)$ predictions presented in Tab. 2.9, resulting in:

$$\mathcal{R}(D^*)_{\rm SM} = 0.258 \pm 0.005. \quad (2.44)$$

The same logic followed in the derivation of the $\mathcal{R}(D^*)$ calculation is applied for the $\mathcal{R}(D)$ computation. The relevant inputs in this case are the form factor measurements from BaBar [61] and Belle [62], together with Lattice results inputs [63,64]. The different calculations can be found in Tab. 2.9, and the value obtained from HFLAV [47] average is:

$$\mathcal{R}(D)_{\rm SM} = 0.299 \pm 0.003 \quad (2.45)$$

Reference	$\mathcal{R}(D^*)$	$\mathcal{R}(D)$
D.Bigi, P.Gambino [54]		0.299 ± 0.003
F.Bernlochner, Z.Ligeti, M.Papucci, D.Robinson [59]	0.257 ± 0.003	0.299 ± 0.003
D.Bigi, P.Gambino, S.Schacht [65]	0.260 ± 0.008	
S.Jaiswal, S.Nandi, S.K.Patra [66]	0.257 ± 0.005	0.299 ± 0.004
Average	0.258 ± 0.005	0.299 ± 0.003

Table 2.9: Theoretical inputs for $\mathcal{R}(D^*)$ average performed by HFLAV.

2.2.3 New Physics models

The Effective Field Theory formalism allows to accommodate potential NP effects by adding extra operators to the SM effective Hamiltonian. Focusing in $b \to c\tau^-\overline{\nu}_\tau$ transitions, there are mainly three different NP contributions that could explain the data:

- W' boson: the NP would appears as a new charge-current mediated by a general W' gauge boson. The solution most often proposed involves a Right-Handed (RH) W_R, along with a RH neutrino. [67–70]. In [71], a complete recent study can be found.
- Leptoquarks: many extensions of the SM contemplate unified descriptions of quarks and leptons, predicting the existence of new scalar and vector bosons, *leptoquarks*. A relevant paper that examines leptoquarks models was [72], followed by [73–75], among others.
- Charged Higgs boson: a new tree-level exchange of a charged Higgs boson would be a possible explanation for the B anomalies. Numerous *two-Higgs-doublet model* have been proposed, [76–79], to cite some of them.

A more comprehensive review of the theoretical status of B flavour anomalies can be found in [80]. The aim here is to point out the effort being made to explain the experimental results, and the inherent need to obtain precise measurements that could clarify the road to NP.

3

The LHCb experiment

Contents

3.1 The Large Hadron Collider

The Large Hadron Collider (LHC) [81] is a two-ring superconducting proton accelerator and collider that is located at CERN (from the French *Conseil Européen pour la*

Recherche Nucléaire, European Organisation for Nuclear Research) complex, based near Geneva, in the border between France and Switzerland. The LHC is the world's most powerful particle accelerator ever built, installed in a 26.7 km tunnel, that was constructed at a mean depth of 100 m due to geological considerations, ranging between 175 m (under the Jura) and 50 m (towards Lake Geneva). The tunnel was excavated firstly for hosting the LEP (Large Electron Positron) machine, whose first beam circulated on 1989. LEP was shutdown in the early 2000's, so that the LHC construction could started, leading to its first run in the period 2010–2013.

At the LHC, both proton beams and heavy ions can be accelerated, but in the following, only proton collisions will be studied and described throughout the thesis.

The physics runs are characterised by the energy of the proton-proton collisions at the centre-of-mass. During Run 1, the delivered beam energy was $\sqrt{s} = 7\,\text{TeV}$ during a short period in 2010, and $\sqrt{s} = 8\,\text{TeV}$ in 2011. In Run 2 the energy was increased up to $\sqrt{s} = 13\,\text{TeV}$, from the period between early 2015 to late 2018. Consequently, with an increase in energy comes an increase in production cross-sections, and therefore higher rate of events. The two presented data-taking periods will be followed by Run 3, that is scheduled to start after the Long Shutdown 2 (LS2) in Summer 2022. More information about the LS2, and the LHCb upgrade that was carried out during this period can be found in Chap. 4.

The total luminosity collected at the end of Run 2 is nearly $6\,\text{fb}^{-1}$, twice the sample corresponding to Run 1 of $3\,\text{fb}^{-1}$. More details about the luminosity definition and information about the recorded luminosity over the years can be found in Appx. A.

The accelerator complex at CERN is comprised of a succession of machines that are displayed in Fig. 3.1, where the LHC is the last element of the chain, which successively accelerate particles to increasingly higher energies. Firstly, applying an electric field to a hydrogen bottle, hydrogen atoms are stripped off their electrons, giving protons. Protons are immediately injected into a linear accelerator (LINAC2 in the past, which has been replaced in the Upgrade by LINAC4 in 2020), which creates bunches of protons of 50 MeV. The beam is then injected into a chain of three circular accelerators: Proton Synchrotron Booster (PSB), the Proton Synchrotron (PS) and the Super Proton Synchrotron (SPS), that push their energy up to 1.4 GeV, 25 GeV and 450 GeV, respectively. Protons are finally injected into the two beam pipes of the LHC, clockwise and counter-clockwise.

The mechanism that allow for proton acceleration in the LHC relies on 16 radio-frequency (RF) cavities that contain an electric field. Protons injected into the field receive and electric impulse that accelerate them up to 6.5 TeV. At the same time, the trajectory of protons is driven by superconducting dipole magnets, operating at a maximum field of 8.33 T, that bend the protons within the orbit. The magnets are enclosed in a helium vessel, and are cooled via cryogenic plants, allowing to reach 1.9 K at operation condition. The cryostat, shown in Fig. 3.2, has been designed for stabilization against thermal disturbances and for heat transport. The two LHC beams are arranged into bunches, separated at a minimum time of 25 ns, which leads to a bunch-crossing rate of 40 MHz. The beams cross each other in four different locations, called Interaction Points

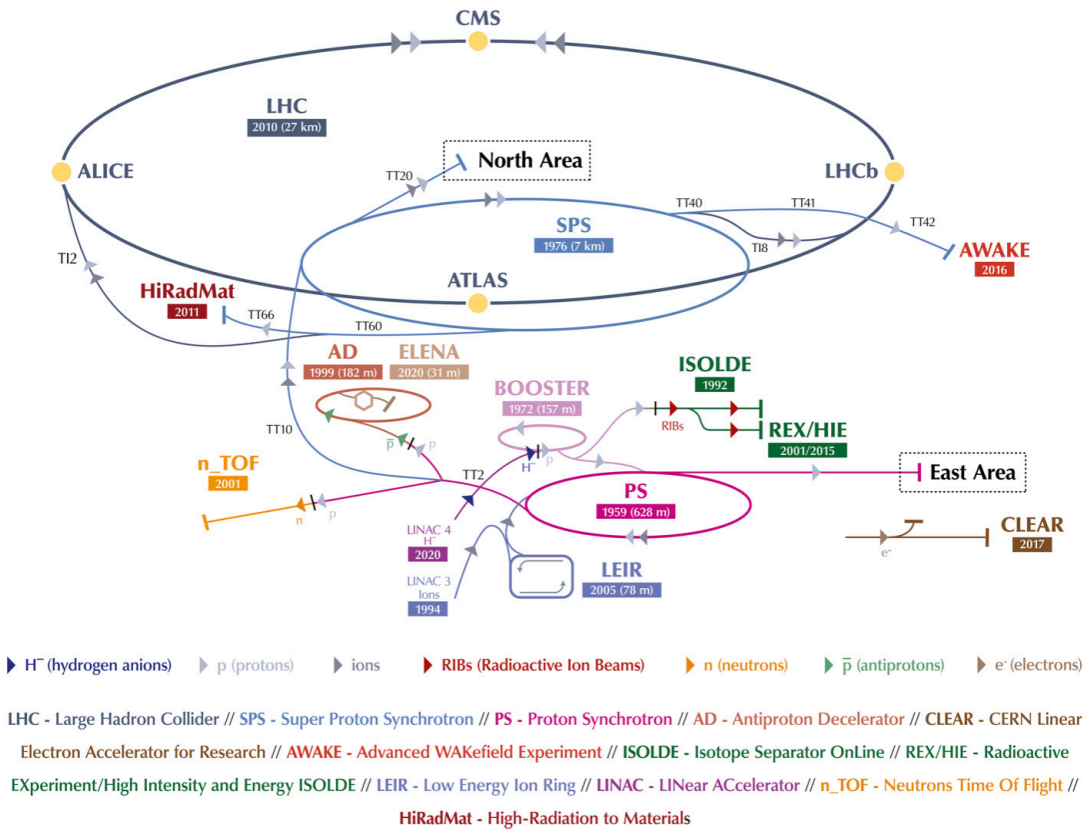

Figure 3.1: Scheme of CERN accelerator complex in 2019, with the main experiments. Extracted from [82].

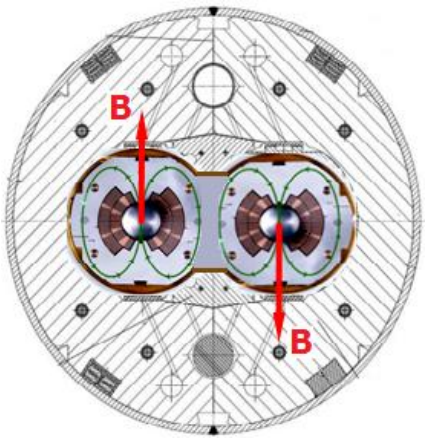

Figure 3.2: Transverse cross section of cryostat housing LHC twin dipole magnet. Extracted from [83].

(IP), where quadrupole magnets are required to act in order to focus the beams and provide stabilisation. At the IP, four main detectors are located: ATLAS (A Toroidal LHC Apparatus), CMS (Compact Muon Solenoid), ALICE (A Large Ion Collider Experiment) and LHCb (Large Hadron Collider beauty).

ATLAS [84] and CMS [85] are the two general-purpose detectors (GPD) of the LHC. Both investigate a wide range of physics, covering the broad SM physics and beyond. The Higgs boson discovery motivated the technical design of both experiments, lying the difference between the distinct magnet-system designs, which leads to the application of different technical solutions. The remarkable discovery of the Higgs goal was achieved in 2012 [1, 2]. Since then, their physics programs have been extended to study the BSM landscape. These NP programs includes extra dimensions and new particles, the Higgs sector, Supersymmetry, dark matter candidates and long-live particles.

The ALICE [86] detector has been designed to study the collisions of nuclei at the ultra-relativistic energy scale. At the LHC running conditions, the energy density is so high that it provides an excellent laboratory for studying the so called quark-gluon plasma, and therefore physics of strongly interacting matter.

The LHCb [87] detector was engineered to study B physics and it will be characterised in more detail in the following section, Sec. 3.2.

3.2 The LHCb detector

The LHCb detector [88] is a single-arm forward spectrometer that was primarily designed to perform precise measurement of the CKM matrix and its Unitary Triangle, in particular the angle γ is of special relevance. The CKM angles are related with potential CP-violation in processes containing either a b or a c-quark. Many models of NP consider contributions that would change the CP-violating phases and rare-decays branching fractions, such as heavy mesons decays highly suppressed in the SM. Thus, the core of the LHCb program also includes dedicated studies to such processes. In the last years, the LHCb detector has extended its physics reach, covering extreme energy densities, indirect searches for BSM particles, top physics or remarkable electroweak measurements, such as the W mass [89].

The detector geometry is designed based on the direction of the production of pairs $b\bar{b}$, predominately in a forward or backward cone around the collision point, as shown in Fig. 3.4(a). A comparison between LHCb acceptance with GPD is displayed in Fig. 3.4(b). The forward angular coverage range from approximately 10 mrad to 300 (250) mrad in the bending (non-bending) plane. The equivalence in units of pseudorapidity η can be derived by means of the expression:

$$\eta = -\ln\left[\tan\left(\frac{\theta}{2}\right)\right], \tag{3.1}$$

being θ the angle between the particle momentum and the beam axis. Then, it is obtained that the LHCb detector acceptance is in the $2 < \eta < 5$ region.

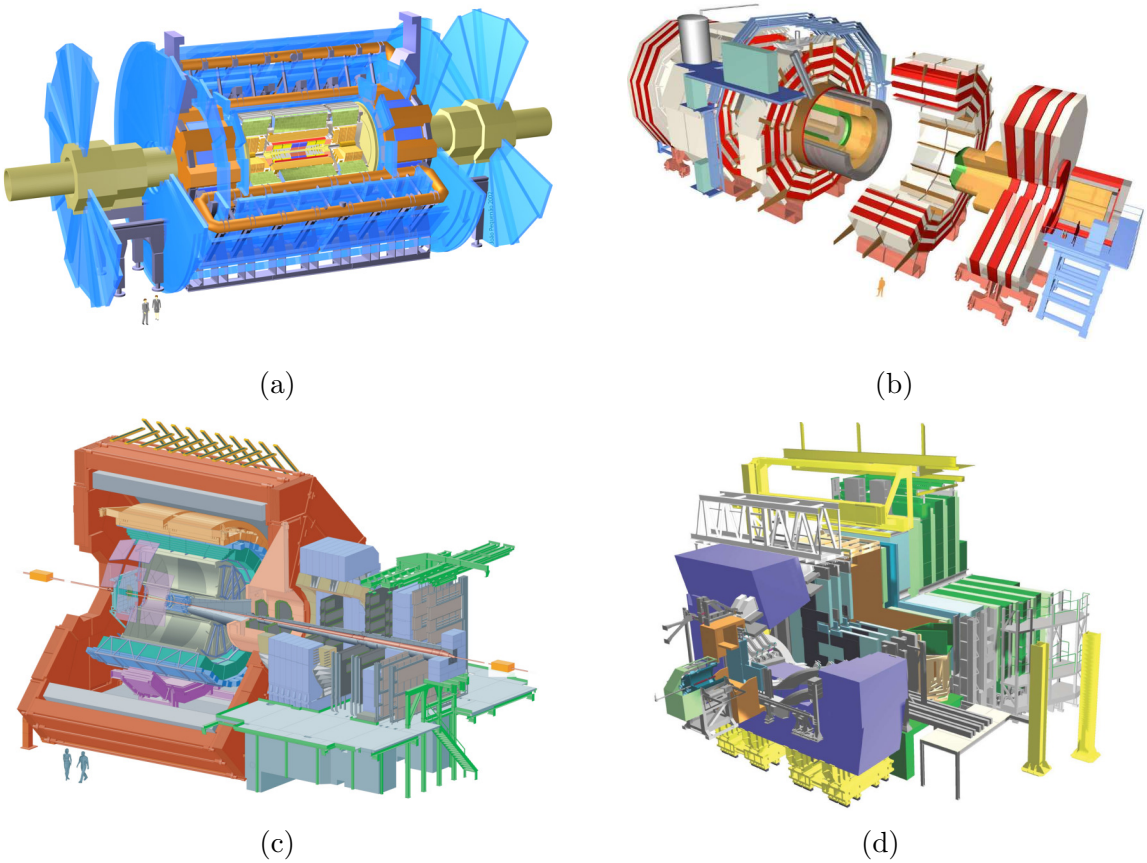

(a) (b)

(c) (d)

Figure 3.3: Schemas of the four main detectors at CERN (not at the same scale), extracted from [90]. (a) ATLAS, (b) CMS, (c) ALICE and (d) LHCb.

In addition to its particular acceptance, the luminosity of LHCb experiment needs to be tuned to meet the criteria that, on average, around one visible pp interaction is produced per bunch crossing (namely μ[1]), which would mean that the pile-up (average number of pp interactions in visible events) is around 1.5. This is essential for data quality, since flavour precision physics relies on resolving vertexes with extremely high resolution. Moreover, the trigger hardware could not be able to run on higher rates. It should be taken into account that at higher pile-up, it also increases the occupancy of the detector, condition that significantly complicates the reconstruction and increases the background. Another advantage when running at lower luminosity is that radiation damage at the detector is also reduced.

The optimal luminosity for LHCb is two orders of magnitude less than the nominal one at LHC, corresponding to $4 \times 10^{32}\,\mathrm{cm}^{-2}\,\mathrm{s}^{-1}$, so that a beam defocusing at the IP is

[1]See [92] for more information.

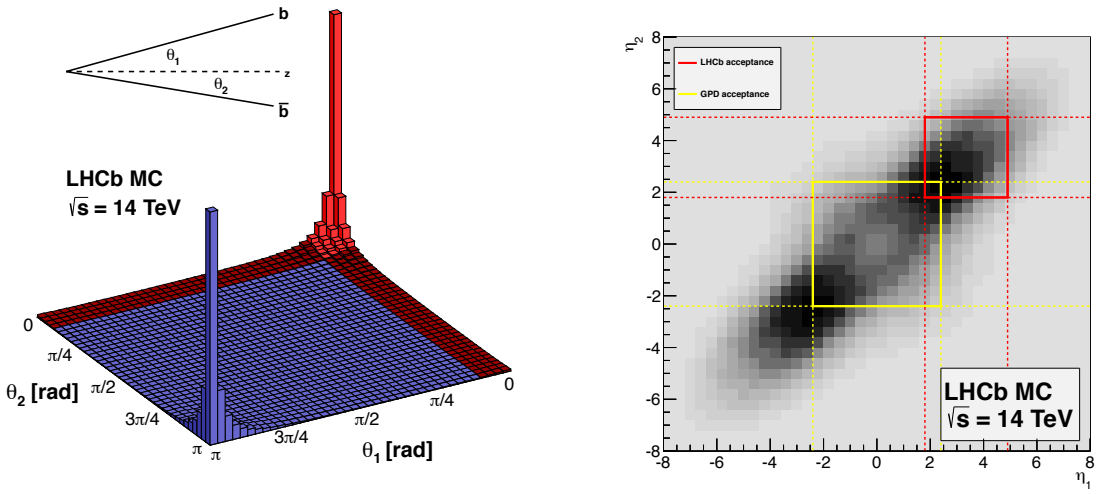

(a) (b)

Figure 3.4: (a) Distribution of $b\bar{b}$ pairs production at $\sqrt{s} = 14\,\text{TeV}$, as function of their polar angles, obtained from Pythia. In red it is shown the LHCb acceptance. (b) Comparison between LHCb (red square) and GPD acceptance (yellow square), in the pseudorapidity plane at $\sqrt{s} = 14\,\text{TeV}$. Images obtained from [91].

required. In addition to that, LHCb needs to operate at a constant pile-up. The luminosity control is guaranteed by applying the *luminosity levelling* procedure [93] during the fill, which is based on the adjustment of the two beams transversal overlap at the IP.

In Fig. 3.5 the scheme of the spectrometer and its sub-detectors are displayed. The LHCb components can be categorized in two different types: tracking stations and particle identification detectors. The tracking system, described in Sec. 3.2.1, is composed by the VErtex LOcator system (VELO) placed before the magnet and four planar tracking stations: the Tracker Turicensis (TT) upstream of the dipole magnet, and T1-T3 downstream of the magnet. Particle identification information, see Sec. 3.2.2, is provided by the following major components: two Ring-Imaging Cherenkov (RICH) detectors, electromagnetic and hadronic calorimeters and the muon chambers.

The trigger system is of crucial importance when discriminating events of interest against the dominant background. An overview of the trigger syatem can be found in Sec. 3.2.3.

The LHCb detector face many computational challenges, related how data are collected, recorded or processed efficiently, among other tasks. The specific software developed for the experiment is presented in Sec. 3.2.4.

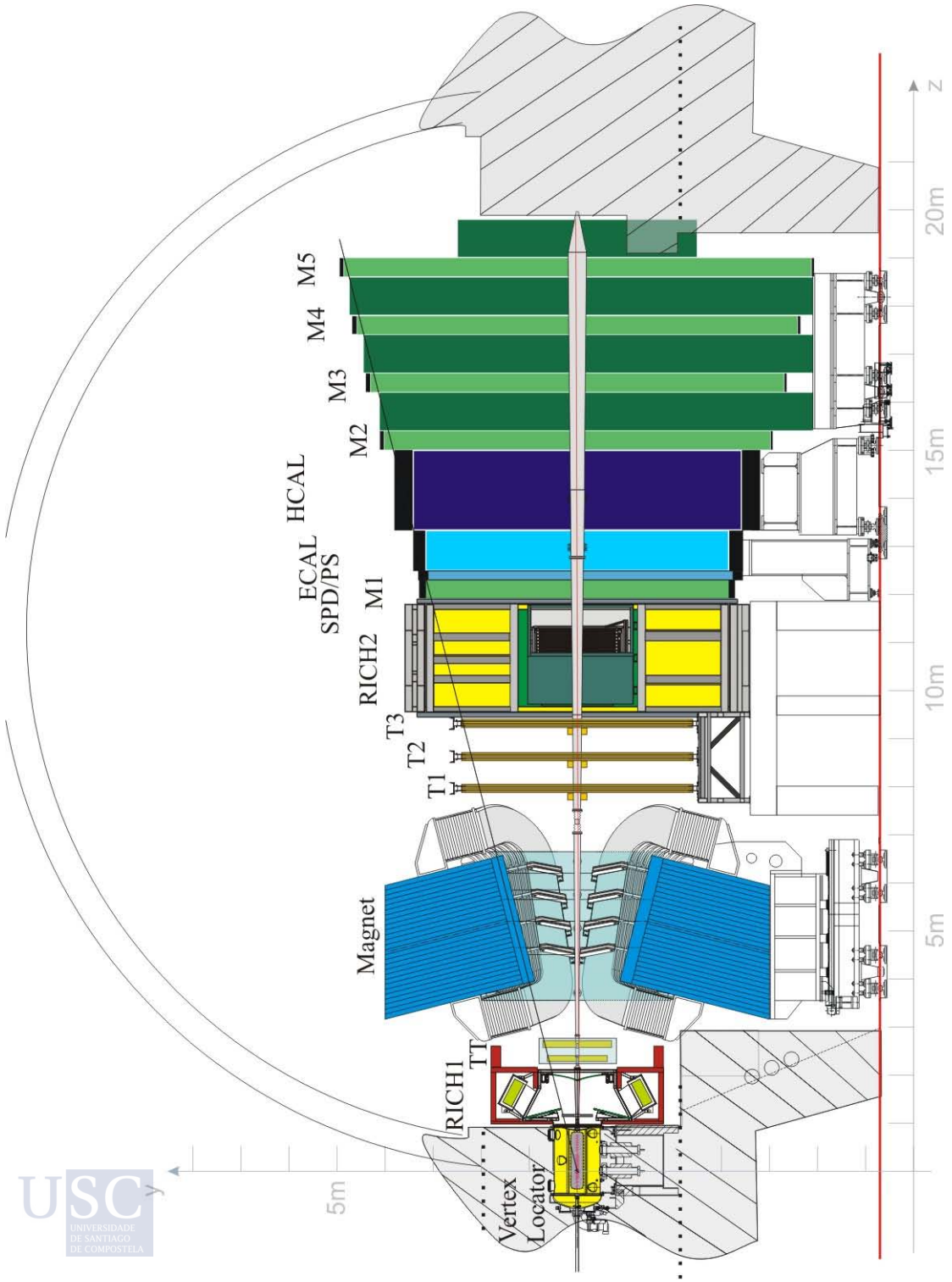

Figure 3.5: Scheme of the LHCb spectrometer and its sub-detectors. Figure from [94].

3.2.1 Tracking

3.2.1.1 The Vertex Detector

Vertex reconstruction is a crucial requirement of the LHCb experiment, since most of its physics program scope relies on the spectrometer capability to resolve production and decay vertices, which are in fact a distinctive feature of b and c-hadron decays.

Aiming for precise measurements of the primary vertices (PV), the VELO [87, 95] is located close to the interaction region. The proximity of the detector to the beam line at $\sim 7\,\text{mm}$ constrains its design. The sensors are positioned at closer distance than the aperture of the LHC during injection, and therefore the adopted layout is to mount the VELO into two retractable halves arranged perpendicular to the beam line. Both halves are not aligned, rather 1.5 cm displacement is set in order to allow them to overlap, providing full geometrical coverage around the interaction region. The two modules arrangement can be seen in Fig. 3.6 (top), with the detector in the fully closed position.

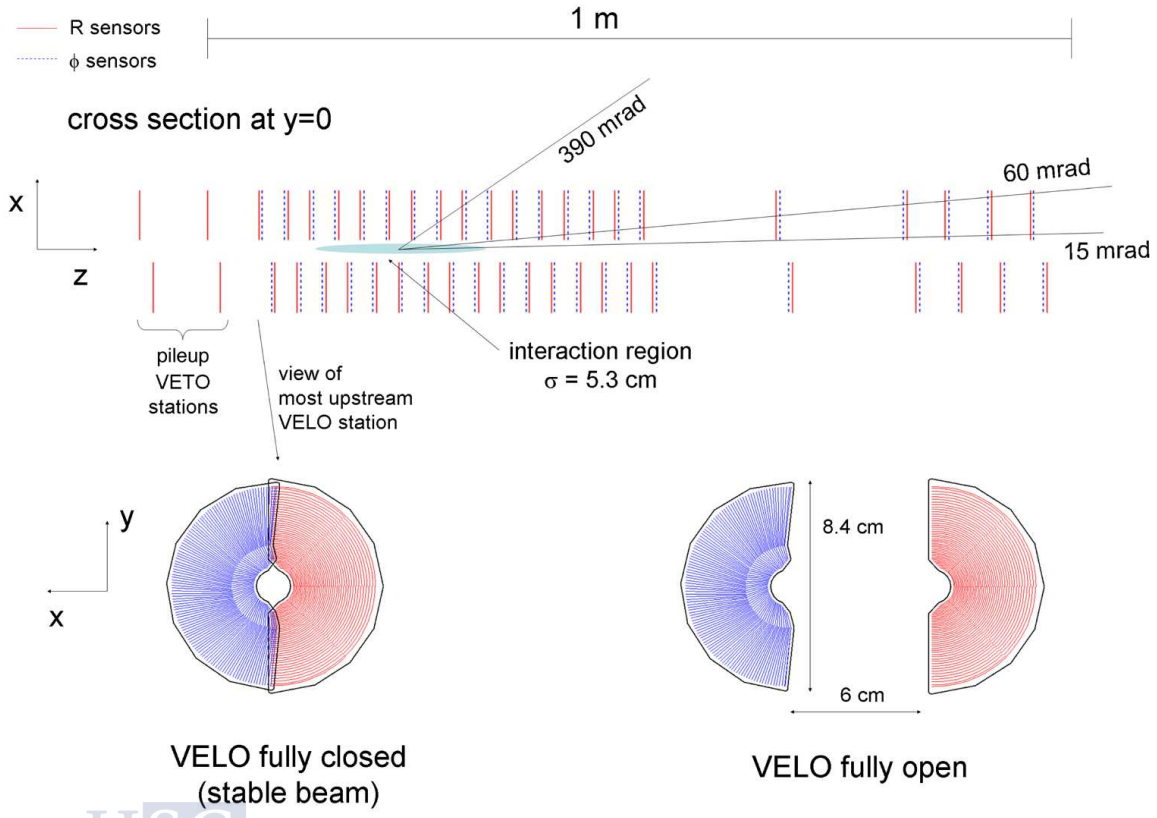

Figure 3.6: (top) Cross section of the silicon modules arrangement along the beam-direction, with the detector in the fully closed position. (bottom) Strip layout of R and ϕ sensors, in both closed and open positions. The R-measuring sensor is displayed in red, and the ϕ-measuring sensor corresponds to the blue color. Extracted from [94].

The two halves of a series of silicon modules that composed the VELO are equipped each one with 21 silicon modules that are mainly n-on-n type (except one module with n-on-p sensors placed the most upstream). Each circular-shape module consists of two 300 µm thick, and it is patterned with strips (2048) that provide R and ϕ information. The R coordinate is measured by azimuthal strips arranged in 4(2) sections in the inner (outer) regions of the sensor. The strips in the ϕ-sensor are split in an inner and an outer circular crown, in a way that the occupancy of both regions is equalized. The concept of the strip layout is illustrated in Fig. 3.6 (bottom).

The sensors must be kept at a temperature of about $-7°$C, and so it is required a sophisticated cooling system based on CO_2. VELO sensors are mounted in a vessel that maintains them in a secondary vacuum at 2×10^{-7} mb, separated from the primary vaccum one of the LHC by a thin aluminum sheet, referred to as *RF-foil*. This surface face the beam, and is only 3 mm thick, to minimise the degradation of the momentum measurement due to multiple scattering.

The intense exposure to a radiation environment strongly non-uniform leads to damage in the silicon sensors. Therefore, a dedicated prototype process was carried out in order to check that the expected performance is maintained after irradiation [88]. The main cause of bulk radiation damage is that the silicon atoms may displace from their lattice positions, leading to an increase of leakage current. Since this parameter in turn depends on the fluence, Intensity-Voltage (IV) scans provide a good quantity to measure the radiation damage. The measured leakage currents over time for the VELO are shown in Fig. 3.7, where each of the blue curves represents one VELO sensor placed at a different distance with respect to the interaction point. The green curve corresponds to the average, which is in good agreement with the predictions done with simulation, illustrated with the pink band [96]. Regarding the performance of the VELO, it has operated stably and reliably throughout the Run 1 and Run 2 of the LHC. As it was just highlighted, prototyping accurately is a fundamental part in order to ensure the correct subsequent operation of the detector. This thesis documents my contribution to the study of the upgraded VELO sensors performance, required for the new VELO silicon-pixel detector that is a crucial part of the LHCb upgrade. Both the LHCb upgrade project and the contribution to the VELO upgrade documented in this work will be presented in Chap. 4.

As mentioned above, the precise primary vertex and its subsequent decays reconstruction is a fundamental requirement of LHCb analyses. Fig. 3.8(a) shows the resolution of the reconstructed primary vertex along the beam axis versus the number of tracks associated to that PV. This leads to a PV resolution of 13 µm in the transverse plane and 71 µm along the beam-axis direction for vertices with 25 tracks.

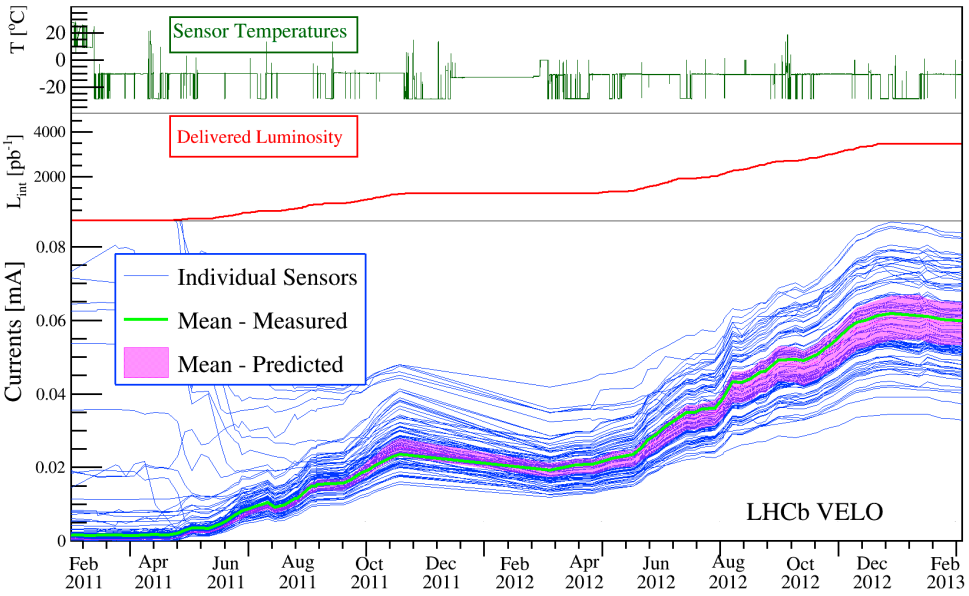

Figure 3.7: Leakage current of VELO sensors evolution with time. Above, information about the sensor temperatures and delivered luminosity. Extracted from [96].

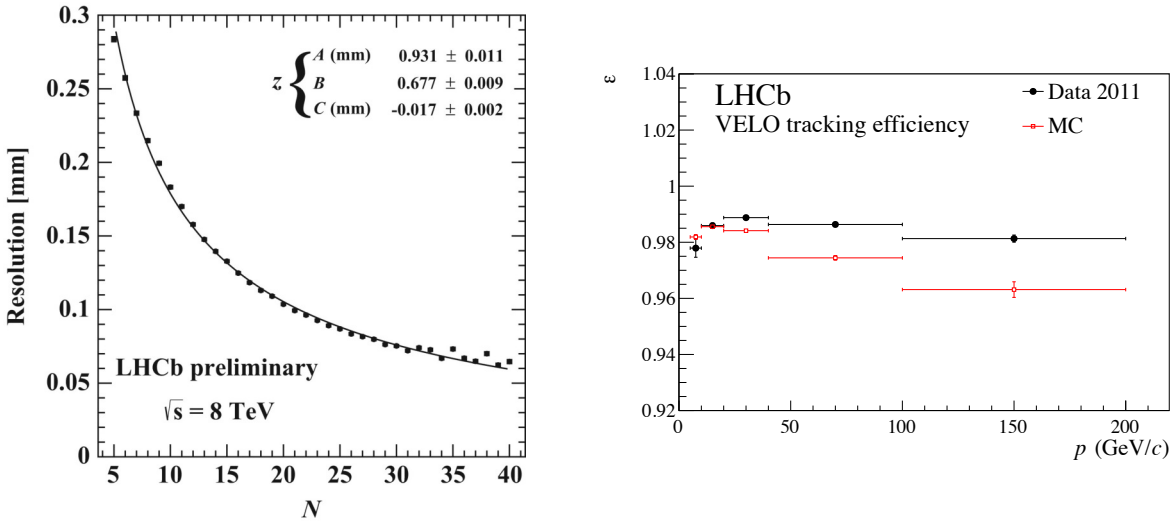

(a) (b)

Figure 3.8: (a) Resolution of the reconstructed primary vertex along the beam axis versus the number of tracks used in the reconstruction, fitted in terms of track multiplicity N as: $\sigma_{PV} = A/N^B + C$. Obtained from [97].(b) VELO tracking efficiency for the 2011 data and simulation as function of the momentum, p. Extracted from [96].

Other relevant VELO performance parameters is the signal-to-noise ratio, of about 20, leading to a best hit resolution of 4 µm at the optimal track angle. The track reconstruction efficiency is typically above 98%. Its distribution with respect to the track momentum is shown in Fig. 3.8(b). Another relevant parameter that provides a measurement of the tracking performance is the number of poor quality tracks that are produced. This kind of track is namely *ghost*, and it is defined as one in which less than 70% of the VELO clusters on the track are from the same particle. The frequency of these tracks rises with the detector occupancy, corresponding to 0.5% for randomly triggered events and 1% for HLT triggered events.

A fully characterisation of the VELO system performance can be found in [96]. A detailed description of the VELO radiation damage is given in [97], with information about methods to monitor it or the possible impact that could have on the track reconstruction performance.

3.2.1.2 The magnet

The LHCb detector includes a warm magnet [87] that deflects charged particles in the horizontal plane, allowing for its momentum measurement. In order to cover a forward acceptance of ±250 mrad vertically and ±300 mrad horizontally, the design of the magnet consists of two saddle-shaped coils placed mirror-symmetrically to each other in a magnet yoke [87, 98]. The magnet design is illustrated in Fig. 3.10.

Overall, the magnet provides an integrated magnetic field of 4 Tm, which allows the tracking detectors that are located in the field to measure the momentum of charged particles with a precision of about 0.4% for momenta up to 200 GeV/c [88]. In Fig. 3.9, it is shown the relative momentum resolution with respect to the momentum, for long tracks from data. Long tracks are the highest quality tracks, reconstructed with hits from at least the VELO and T-stations, additionally they can have hits in TT.

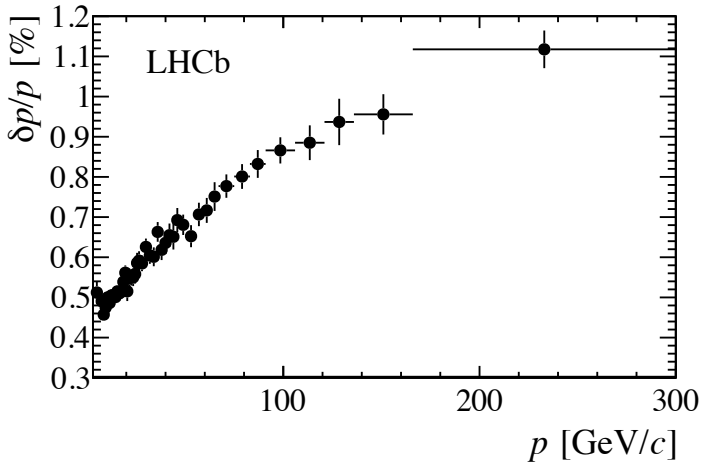

Figure 3.9: Relative momentum resolution versus momentum for long tracks in data obtained using J/ψ decays. Figure from [88].

In order to achieve the target momentum resolution, the precision of the magnetic field integral, *i.e.* $\int B\,\mathrm{d}l$, is of 10^{-4}, while the position of the B-field peak is known with a precision of few millimeters. These quantities are measured by means of an array of Hall probes (see [99] for more details).

The systematic effects of the detector are controlled by changing periodically the direction of the magnetic field, thus each year of data taking consists of two roughly equal size datasets labelled as *MagUp* and *MagDown*. This procedure leads to a precise measurement of the magnetic field in all LHCb regions that is reproducible for both polarities.

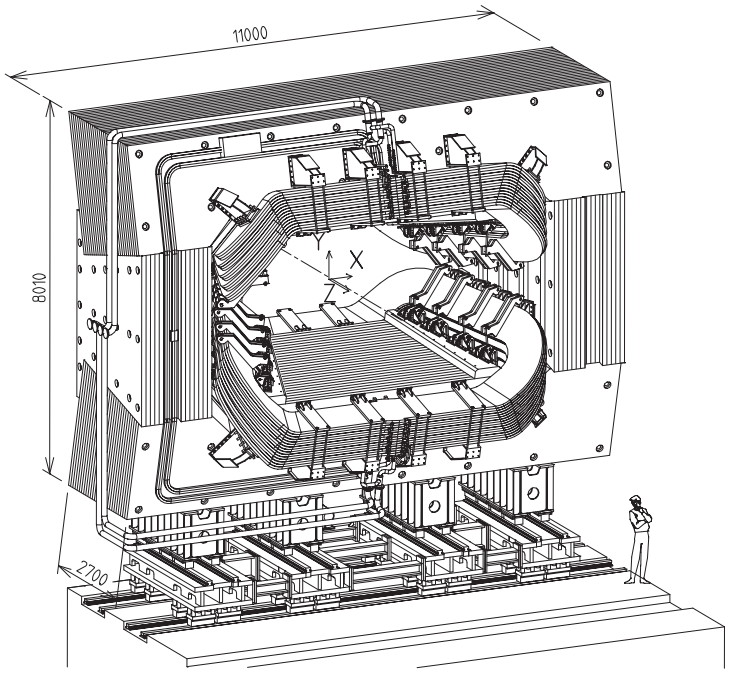

Figure 3.10: Layout of the LHCb magnet, where the interaction point lies behind it. Extracted from [94].

3.2.1.3 Tracking stations

The tracking stations consist of four planar tracking stations: the Tracker Turicensis (TT) that is located upstream of the magnet, and T1, T2 and T3, placed downstream of the magnet [87]. The stations can be categorized in two types, according to the technologies in which are based. On one hand, the Silicon Tracker (Sec. 3.2.1.3.1), composed of the TT and inner part (Inner Tracker) of the T1-T3, which uses silicon microstrip sensors. On the other hand, the outer part (Outer Tracker) of the T1-T3 (Sec. 3.2.1.3.2), which is designed as an array of drift-tubes.

3.2.1.3.1 Silicon Tracker: Tracker Turicensis and Inner Tracker

The Silicon Tracker (ST) comprises two detectors, both based on silicon microstrips: the Tracker Turicensis (TT) and the Inner Tracker (IT). The layout of the ST is displayed in Fig. 3.11 in the colour violet.

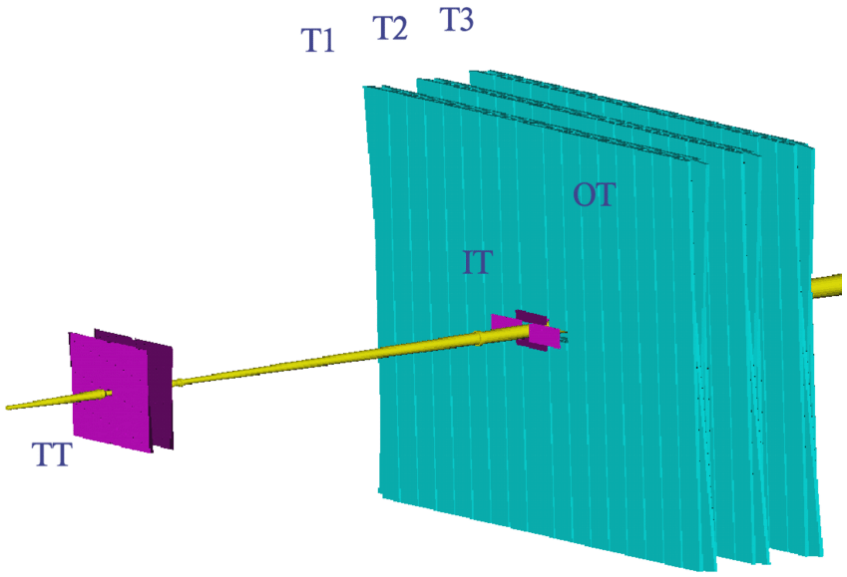

Figure 3.11: The main tracking system of LHCb: TT, IT and OT. Obtained from [100].

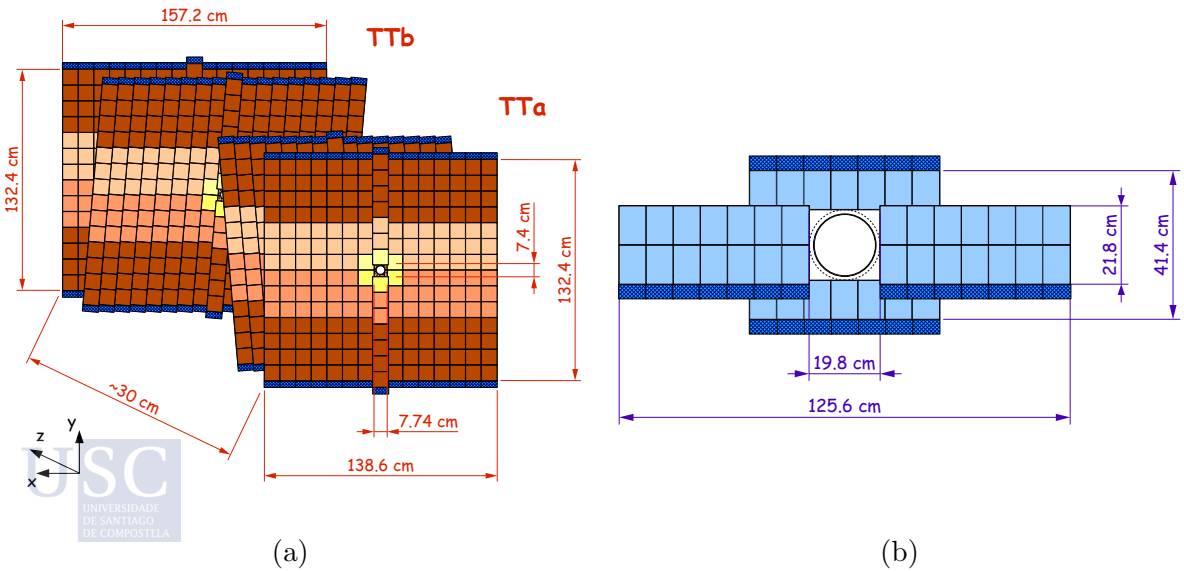

(a) (b)

Figure 3.12: (a) Layout of the TT station. (b) Scheme of an IT layer. Figures from [101].

The TT station [102] is located in front of the entrance of the magnet, covering the full acceptance of the experiment. The TT is composed of four planar detection layers arranged in two pairs, with a total size of 150 cm wide and 130 cm high. The layout of TT layers is shown in Fig. 3.12(a). The IT [103] is located downstream the magnet, and it consist of four individual detector boxes that are arranged around the beampipe, covering the inner region of the T1, T2 and T3 stations. Each detector box contains four detection layers, as the ones illustrated in Fig. 3.12(b), arranged in a way that the two internal layers have strips oriented ±5°C with respect to the external layers, with vertical strips. The overall area of the TT station is of 120 cm wide and 40 cm high.

Both the TT and IT detectors are housed in single boxes that provide electrical and thermal insulation. In order to reduce radiation damages and noise, a cooling system maintains the stations at a temperature of 5°C.

3.2.1.3.2 Outer Tracker

The Outer Tracker (OT) is a drift-time detector [104], that aims for tracking of charged particles and the measurement of their momentum in a large acceptance area [94]. It is shown in cyan in Fig. 3.11. It covers the outer part of the T1, T2 and T3 stations, that complete the IT and provides fully angular coverage. The OT is composed of layers of drift-tubes with an inner (outer) diameter of 4.9 mm (5 mm). The gas that fills the tubes is chosen so that the OT timing requirement is met, which means that all signals should arrive within 50 ns (two bunch crossing intervals). Taking into account also safety criteria, the final fast gas mixture is based on CF_4, Argon and CO_2.

3.2.2 Particle identification

In a flavour physics experiment, like LHCb, many of the b and c-hadron decays involve hadronic multi-body final states, which makes the correct hadron identification a fundamental requirement of the detector. This feature also contributes to significantly reduce the combinatorial background component.

Focusing on hadron colliders conditions, like the LHC, the b-hadrons decays studied typically contain a considerable number of pions, kaons and protons. The excellent Particle IDentification (PID) performance of LHCb relies on the RICH detectors (Sec. 3.2.2.1), two calorimeters (Sec. 3.2.2.2) and the muon chambers (Sec. 3.2.2.3) [87].

3.2.2.1 RICH detectors

The primary role of the RICH system [105] is to identify charged hadrons (π, K, p) in the full momentum range. To achieve this goal, two RICH detectors are needed: the RICH1 is placed before the magnet and it covers the low-intermediate momentum range, while the RICH2 is located after the magnet and it is design to cover the high momentum range. Both RICH, Ring Imaging Cherenkov, designs are based on Cherenkov effect.

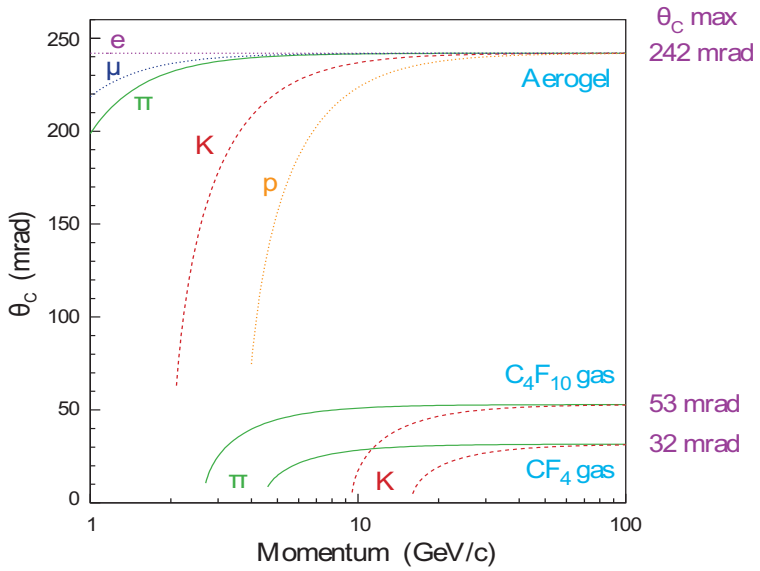

Figure 3.13: Cherenkov angle dependence with track momentum. Also the radiators that match the region are indicated. Figure from [94].

The principle of this effect can be stated as follows: when a charged particle that is propagating through a material, referred in the following as a radiator with a refractive index n, travels faster than the speed of light in this medium, its passage causes an electromagnetic radiation. This Cherenkov light that is emitted are photons distributed in a cone of angle θ around the direction of propagation of the particle. The value of the angle is directly related to the velocity of the particle, β, through the expression:

$$\cos\theta = \frac{1}{\mathrm{n}\beta}. \tag{3.2}$$

Combining the momentum estimation of the particle provided by the tracking system with the velocity information that is obtained from the θ measurement, it can be obtained the mass of the particle. Fig. 3.13 displays the dependence of the Cherenkov angle with the momentum. Also the radiators that match this region is indicated (aerogel, C_4F_{10} or CF_4 gas).

The Cherenkov photons emitted by charged particles that are passing through the RICH detectors need to be focused, aiming for reflecting the light out of the detector acceptance and collect it in Hybrid Photon Detectors (HPDs). To carry out this process, a combination of spherical and flat mirrors is installed. In the following sections, it will be presented the different optical designs that are used in RICH1 and RICH2, together with the different radiators used based on the momentum range target.

3.2.2.1.1 RICH 1

The RICH1 detector is located immediately after the VELO, and upstream the magnet. It has a wide acceptance, covering the full LHCb acceptance, which ranges from ± 25 mrad to ± 300 mrad horizontal and ± 250 mrad vertical. In order to obtain the PID of particles with the target of $1 - 60\,\mathrm{GeV}/c$ momenta, the RICH1 detector is filled with two different radiators. Silica aerogel is used for the measurement of lowest momentum tracks, whilst for the intermediate momentum region the gaseous C_4F_{10} is suitable.

As it was mentioned above, the focusing of Cherenkov light is accomplished using spherical mirrors. To bring the image out of the detector acceptance, they are tilted, and therefore the photodetectors material does not degrade the tracking. The total size of the detector results in a vessel of $2.4 \times 2.4 \times 1\,\mathrm{m}^3$, out of which there is a 5 cm thick aerogel radiator and 85 cm long C_4F_{10} gas radiator. A special effort was made in order to minimise the RICH1 physical size, and therefore the material within the detector acceptance, since the spherical mirrors are in the path of travelling charged particles and RICH1 is required to cover the full acceptance. Fig. 3.14(a) shows a side view of a scheme of the RICH1 detector.

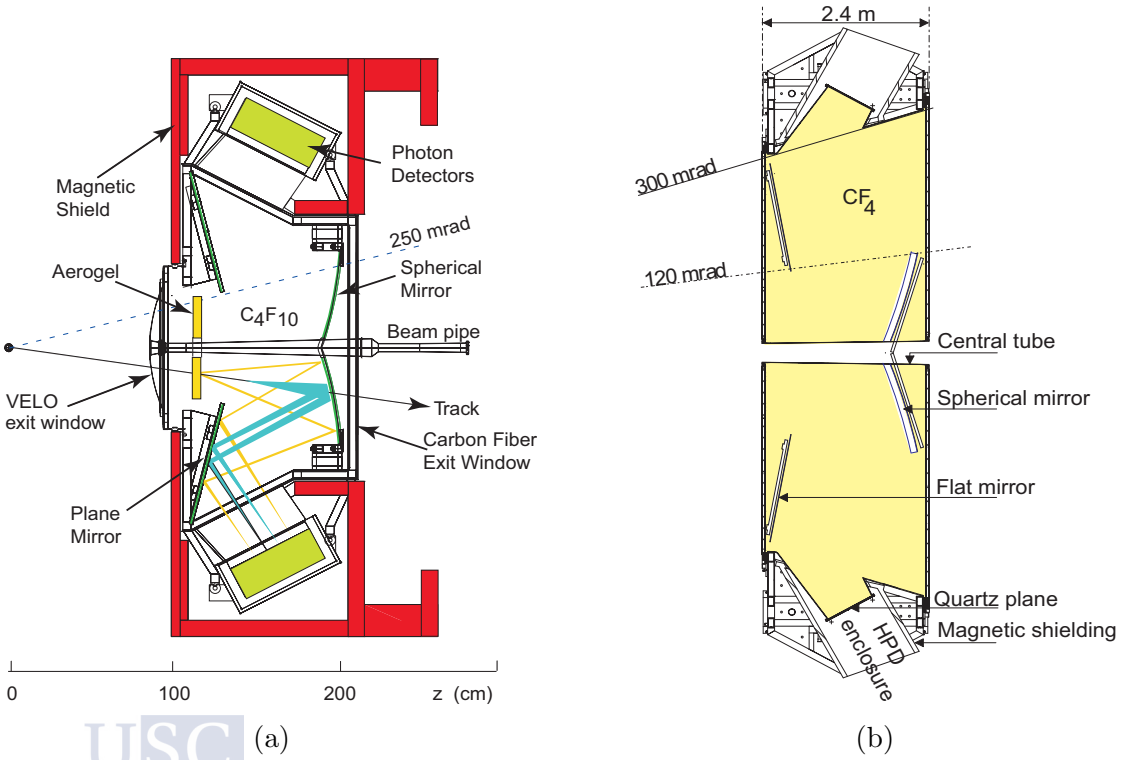

Figure 3.14: (a) Side view of the schematic layout of the RICH1 detector. (b) Top view schematic of RICH2 detector. Figures from [106].

3.2.2.1.2 RICH 2

The RICH2 detector is located right after the last tracking station and before the first muon station, downstream the magnet. It has limited angular acceptance, from ±15 mrad to ±120 mrad horizontal and ±100 mrad vertical, that is enough to cover the region where high-momentum particles are produced. The RICH2 has a CF_4 radiator, to analyse the high-momentum tracks that traverse the magnet [106]. It provides PID of particles in the range $15 - 100\,\mathrm{GeV}/c$.

It is worth mentioning the difficulty to separate pions from kaons at high energies, which required a gas with lower refactive index, and thus a reduced yield of Cherenkov photons. The overall size of the detector is $7 \times 7 \times 2\,\mathrm{m}^3$, where the CF_4 radiator has a length of 170 cm. The overall length of the detector is reduced by reflecting the image from a tilted spherical mirror by a flat secondary mirror into the detector planes [106]. The top view of the optical design is shown in Fig. 3.14(b).

3.2.2.2 Calorimeters

The main purpose of the calorimeter system [87, 107, 108] is the correct identification of hadrons, electrons and photons, which includes the measurement of their energies and positions. This information sets the basis of the first trigger level (L0), which will be described in detail in Sec. 3.2.3.

The structure of the calorimeter system is composed of an Electromagnetic CALorimeter (ECAL) followed by a Hadronic CALorimeter (HCAL). In order to cover the whole angular acceptance, also a Scintillator Pad Detector (SPD) and a PreShower (PS) detector are added to the system. In the illustration of Fig. 3.15, it is shown the showers profile that is deposited in each calorimeter layer, and how the different parts of the system complement each other. Charged particles deposit some energy in the SPD, then the electromagnetic shower start in the lead layer that is placed between the SPD and the PS. The full electromagnetic shower development happens in the ECAL. In the hadrons case, even some energy is deposited in the SPD, PS and ECAL, the main electromagnetic shower is produced in the HCAL. In the following, the different components of the calorimeter system will be described in more detail.

3.2.2.2.1 SPD and PS

SPD and the PS detector consists of detection planes of 14 mm thick scintillator pads. These detection elements are placed just before (SPD) and right after (PS) a 12 mm thick lead wall.

The lead layer is equivalent to 2.5 times the electromagnetic interaction length, corresponding to 0.06 times the hadronic one. In such configuration, incoming particles interact with the lead, creating a shower of new particles. Then, this shower interact with plastic tiles where its energy is transformed into scintillating light that is transmitted to

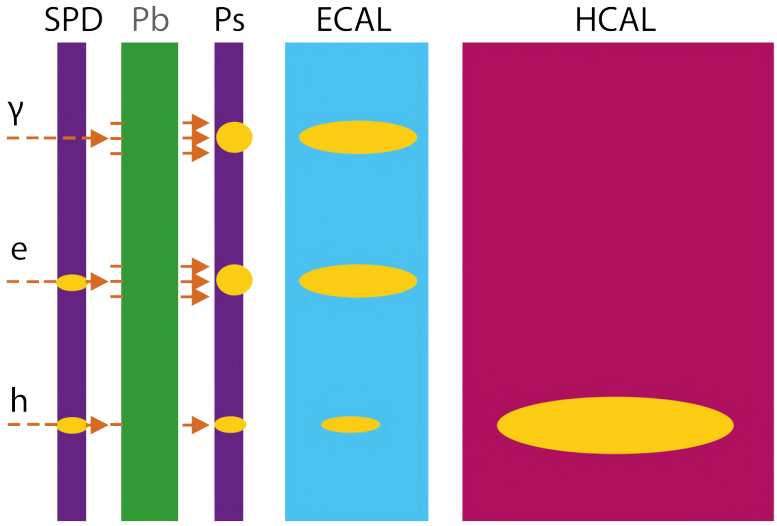

Figure 3.15: Schematic side view of the sub-detectors of the calorimeter system. Typical electromagnetic and hadronic showers are displayed.

a Photomultiplier (PMT) by wavelenght-shifting (WLS) fibres. This structure enables a clean separation between electron and hadron showers.

3.2.2.2.2 ECAL and HCAL

Both ECAL and HCAL structures consist of alternating scintillating tiles with an absorber. In the case of the ECAL, lead tiles crossed by WLS fibres are installed; while for the HCAL, iron plates are inter-spaced.

The ECAL size is 7.76 m wide and 6.30 m high, and it is placed at 12.5 m from the interaction point, covering an acceptance from 25 mrad to 300(250) mrad in the horizontal (vertical) plane. The total thickness of the ECAL is of 25 radiation lenghts, which is a compromise between containing the full electromagnetic shower while keeping an optimal energy resolution. Three different hit density regions have been defined, according to the interaction point distance, and thus three different cell size are used. An example of a ECAL cell is illustrated in Fig. 3.16(a).

The HCAL is positioned behind the ECAL, at 13.3 m from the interaction point, with dimensions 8.4 m × 6.8 m and thickness 5.6 interaction lenghts due to space limitations. Given the dimensions of the hadron showers, HCAL is segmented in an inner an outer parts with different cell size, according to the hit density. Fig. 3.16(b) shows an illustration of a HCAL cell.

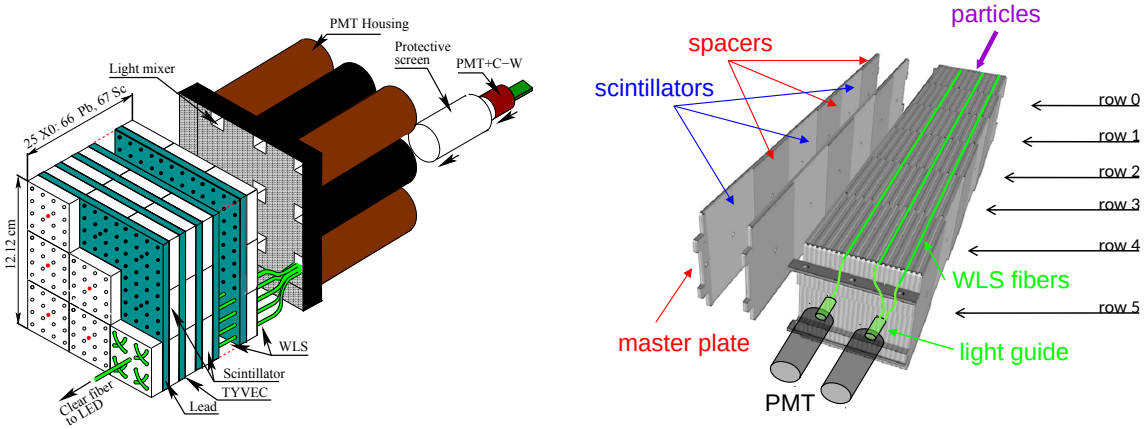

(a) (b)

Figure 3.16: (a) ECAL cell. (b) HCAL cell. Figures from [108].

3.2.2.3 Muon system

Muons are present in many of the final state decays studied in the LHCb experiment, and thus a muon system [87, 109] providing measurements of high transverse momentum muons is required. The muon system information contributes to the L0 trigger level, and also it is used in the offline reconstruction to identify muons.

The muon system is composed of five rectangular shape stations, M1-M5, place along the beam axis. Overall, the angular acceptance of the system covers 20(16) mrad and 306(258) mrad in the bending (non-bending) plane. The first station, the M1, is located upstream of the calorimeter system, it aims for the improvement of the transverse momentum measurement in the L0 trigger. The other stations, M2-M5, are placed downstream the calorimeters, and they are interspersed with each other by sheets of iron of 80 cm, that allow to select penetrating muons. The muon system together with the iron absorbers layout along the beam-axis is illustrated in Fig. 3.17. The total interaction length, including the calorimeter system, is 20 times the hadronic interaction length, which means that, in order to cross all the stations, a muon require a momentum above 6 GeV/c.

To discriminate muons against the abundant hadronic background, a muon candidate is reconstructed by aligning hits in each of the five stations. Almost the whole system is equipped with multi-wire proportional chambers (MWPC), filled with a gas that is a mixture of Ar, $C0_2$ and CF_4, in proportion 40 : 55 : 5. Overall, the system provides an efficiency for muons larger than 99%.

3.2.3 The Trigger system

The extensive program of the LHCb experiment is possible in part due to a versatile real-time reconstruction and trigger system [110]. By exploiting the fact that b-hadrons are relatively heavy and long lived, the trigger makes possible the reduction in three orders

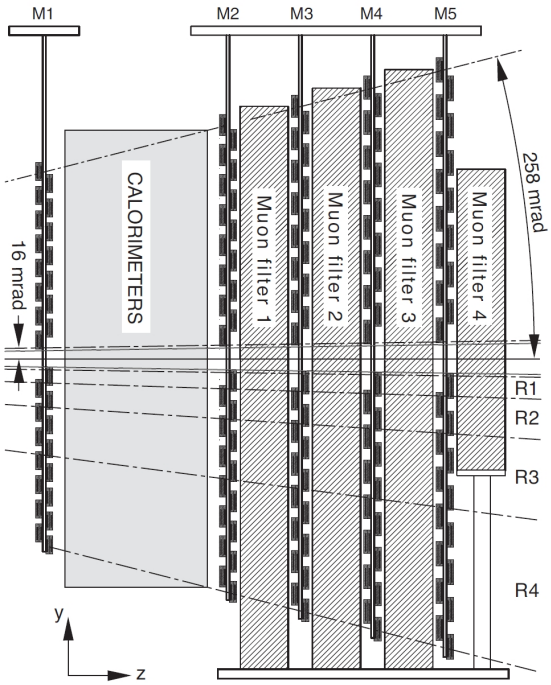

Figure 3.17: Side view of the muon system. Extracted from [109].

of magnitude of the saved collision rate needed for the offline analysis.

During the LHC Run 1, the trigger executed a simplified version of the full offline reconstruction, that lacked low-momentum charged particles and did not aim for the full particles identification. Therefore, the trigger was redesigned for the Run 2 to enable the full offline detector reconstruction to be performed in real time.

The LHCb trigger uses information from all sub-detectors, and it is based on a two level system: the first level trigger (L0) and the High Level Trigger (HLT). The trigger architecture overview is displayed in Fig. 3.18.

The first level trigger, the L0, is implemented at hardware level. It is subsequently divided in three independent triggers that use information from the calorimeters, the muon system and the PileUp system of the VELO. It aims for selecting high transverse momentum p_T muons and large transverse energy E_T deposition in the calorimeters, leading to an enormously significant reduction from the 40 MHz bunch crossing rate to below 1.1 MHz, rate at which the whole LHCb detector can be read out.

The second and last step of the LHCb trigger system is the High Level Trigger. It consists on a C++ application that runs on an Event Filter Farm (EFF), which is composed of several thousands of multi-CPU nodes. The HLT is in turn divided in two stages: HLT1 and HLT2. The former, HLT1, performs a partial event reconstruction that optimise computing time, reducing the rate to 110 kHz. The later, HLT2, performs a full event reconstruction for all tracks, operating in a similar way to the offline reconstruction

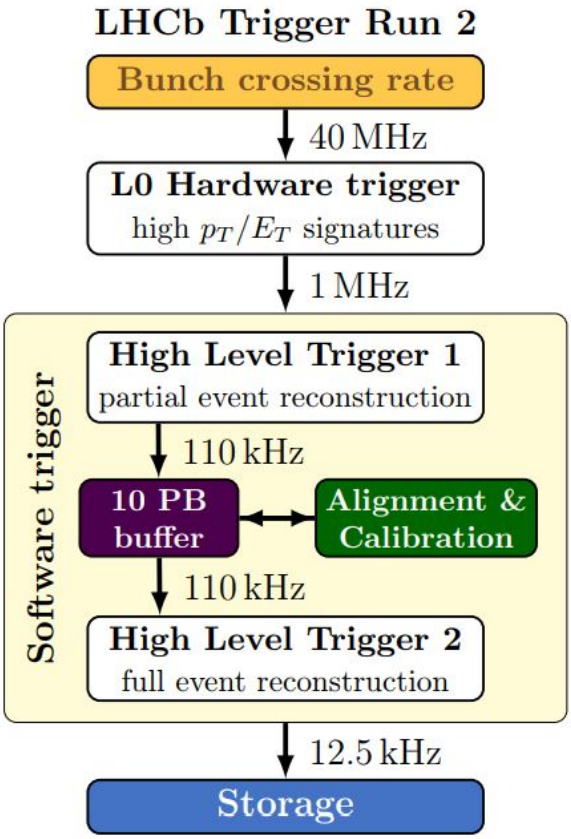

Figure 3.18: Overview of the LHCb trigger system. Figure from [110].

sequence. It reduces the event rate to 12.5 kHz, which is written to permanent storage.

The triggered events can be classified according to whether the trigger decision was due to the signal candidate (Trigger On Signal, `TOS`), due to other objects that are not associated with the signal (Trigger Independent of Signal, `TIS`) or a combination of both.

Regarding the storage, every event in the raw data is saved with its associated *Trigger Configuration Key* (TCK), that contains all the parameters that configure the trigger lines of the HLT. A more detailed description on the LHCb software is given in Sec. 3.2.4.

It is worth mentioning that in the last years of Run 2 it was implemented a new streaming strategy so-called Turbo stream [111], which allows to perform physics analyses with candidates reconstructed in the trigger. If a line is configured as Turbo line, only the information that is needed to perform the analysis is be stored in the raw event. The advantage of this method is that it allows for an increased output rate and thus higher average efficiencies. This trigger strategy is part of the evolution process towards real-time analysis, which will be fully adopted in Run 3 and later.

3.2.4 LHCb software and data flow

It is straightforward from the information given up to now that the data that reach the LHCb detector are very complex and should be processed in a specific way that optimises the data-taking efficiency and data quality. Moreover, the data must be handled very quickly, since new events information is reaching the detector immediately. The data flow is designed so that it consists of several steps, each one controlled by one application that processes the data event-by-event. The steps, which are described in [112], are the following:

1. Trigger: the data from the detector are filtered through the *trigger*, using a software package implemented in Moore. A more detailed explanation can be found in Sec. 3.2.3.

2. Reconstruction: once triggered, the raw data is reconstructed so that the detector hits information are transformed into objects, such as tracks or clusters. Brunel is the software designed to reconstruct the objects and store them in a Data Summary Tape ("DST") format[2].

3. Stripping: data are filtered further through a set of selections (*streams*) that share similar requirements. The information about this step is gathered in a *stripping line*. This step is controlled by the DaVinci application.

Simulated events will pass through a similar process, but in this case proton-proton collisions are replaced by a two simulation steps:

i Simulation: the simulation of the collision and the hadronisations are controlled by the Gauss [113] application, which in turn also depends on external libraries. The tools required in the event generation are processed in the following order:

   - Pythia [114]: it is the standard tool to generate hadron collisions. It is used to generate pp collisions with a customised configuration for LHCb.
   - EvtGen [115]: it is an event generator that simulates the decay and time evolution of a particle, once it was generated in the previous step. The Photos [116] package is interleaved with EvtGen in order to take into account final-state radiation in the simulated sample.
   - Geant4 [117]: it is a toolkit that simulates the passage of particles through matter, and therefore is able to simulate the LHCb detector response.

ii Digitisation: in order to convert the simulated samples in a way that they are as similar as possible to real data, Boole application digitise the virtual detector response, so that it enters the data processing chain described above.

[2]Root file that contains the full event information.

The data flow scheme with the associated applications for both real data and simulation is displayed in Fig. 3.19.

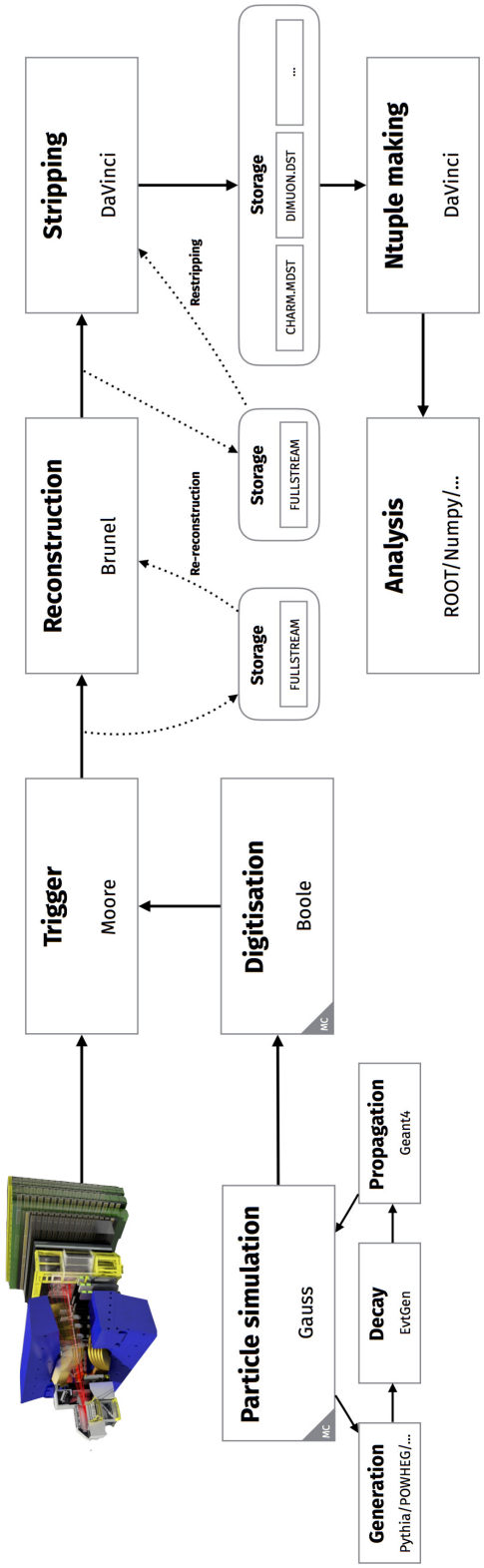

Figure 3.19: Scheme of the LHCb data flow for real and simulated data. Obtained from [112].

4

The LHCb VELO Upgrade

Contents

4.1 Overview of the LHCb upgrade

At the end of 2018, the LHC 's second run (Run 2) came to an end, after three years of successful data acquisition. Many analyses were carried out during this period, and the really precise results published have contributed to extending our knowledge of the SM. Despite achieving remarkable benchmarks, many of the LHCb measurements remain statistically dominated.

By early 2019, the Second Long Shutdown started (LS2), which was a period of three years[1] that aimed for the upgrade of the LHC, together with the main experiments at CERN. At the time of writing, the CERN Management announced the new schedule for the Second Long Shutdown, which scheduled the beginning of physics operations with stable beans of LHC Run 3 on 5th July 2022.

In the Run 3, the beam energy will reach 7 TeV, and the luminosity at LHCb will scale up to values of $2 \times 10^{33}\,\mathrm{cm}^{-2}\,\mathrm{s}^{-1}$, which means multiplying a factor of five the values of the last years of operation. As a consequence, all the LHCb sub-detectors will face increased occupancies and rates. In order to address these conditions, the entire LHCb experiment has to be upgraded, and these major changes are scheduled in two different stages. Firstly, in the Upgrade Phase I [118, 119], some sub-detectors will be replaced in order to deal with the higher granularity and radiation tolerance. Secondly, the Upgrade Phase II [120], will consist on re-designing the sub-detectors so that they can operate at higher luminosity than that of the Phase-I Upgrade detector.

The current changes are part of the LHCb Upgrade Phase I [119], that is schematised on the side view of the LHCb upgraded detector displayed in Fig. 4.2. This major upgrade will make the detector feasible to collect at least $50\,\mathrm{fb}^{-1}$ of data by 2031, allowing measurements to achieve values as precise as the theoretical predictions. In the following, the foreseen physics program and the main changes in the detector are covered.

In 2029 it will start the so-called High-Luminosity LHC (HL-LHC) phase. A LHCb upgrade Phase II is proposed in order to take full advantage of the the HL-LHC conditions, when the peak of instantaneous luminosity is expected to be ten times that of the Phase-I Upgrade detector. Its implementation will take place during Long Shutdown 4 (2033–2034), in order to prepare the detector to operate at the beginning of Run 5. The expected luminosity projection with time is shown in Fig. 4.1[2]. More information about the project can be consulted [120, 121], where the physics case is detailed in [122]. From here on, only the LHCb upgrade Phase I will be treated, and will be referred simply as LHCb upgrade.

[1] This period was extended from the original plan, due to the delay caused by the COVID-19 pandemic.
[2] In the context of the official LHC schedule of 2021.

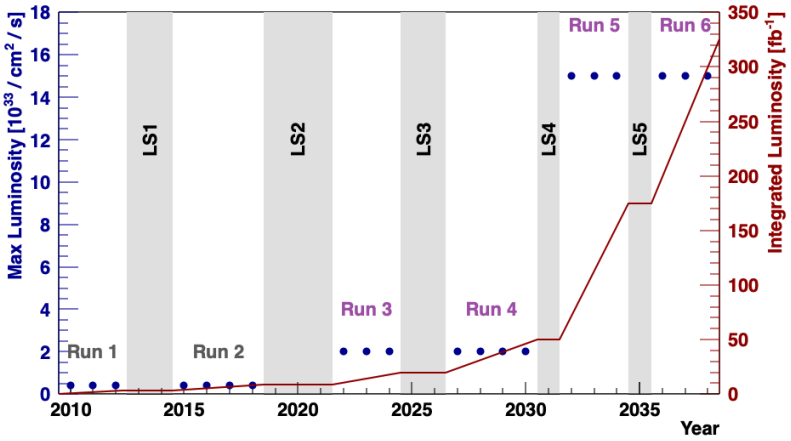

Figure 4.1: Luminosity projection for the original LHCb, Upgrade Phase I and Phase II as a function of time. The red points indicate the anticipated instantaneous luminosity during each period, while the blue line stands for the integrated luminosity accumulated. Figure from [120].

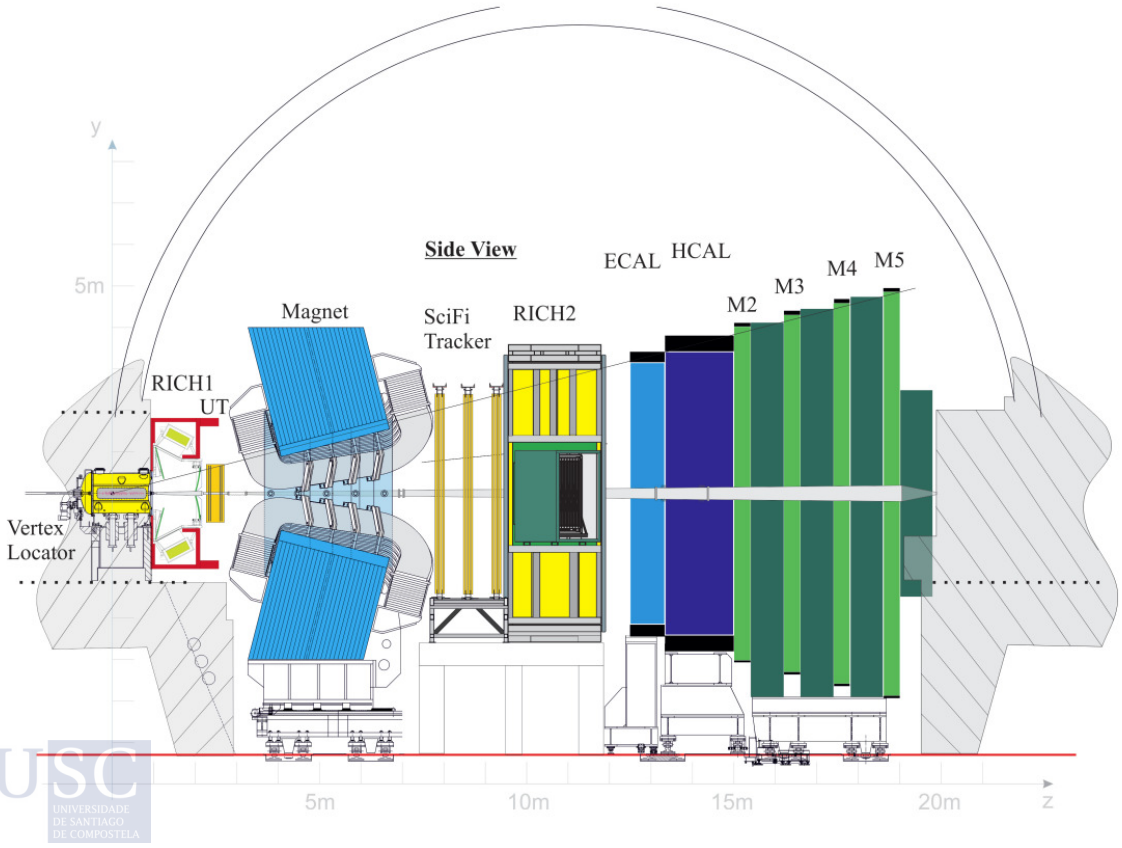

Figure 4.2: Side view of the LHCb upgrade detector, to be compared with Fig. 3.5. Figure from [123].

Physics program

The aim of the LHCb upgrade is to perform measurements that are highly sensitive to NP effects. The effectiveness of these probes depends directly on the sensitivity of the measurements [119], and therefore it is crucial to push these limits. In particular, LHCb is expected to be a fundamental piece in the flavour sector, both studying FCNC and FCCC transitions. The upgrade will also improve substantially measurements of the weak mixing phase, ϕ_s. The physics program includes as well the precise measurements of the angle γ in tree decays, the very rare decay $B_s^0 \to \mu^+\mu^-$, or the even rarer $B^0 \to \mu^+\mu^-$, among other analyses that are key to many extensions beyond the SM. The detailed physics case can be found in [124].

Trigger upgrade

The trigger upgrade [125] will be invaluable in improving the selection efficiency for hadronic final states in B and D decays. As part of the LHCb upgrade, all the sub-detectors Front-End electronics will be replaced in order to cope with up to 40 MHz bunch crossing rate (to be compared with the 1 MHz limit of the L0 trigger). The reason for this change is that at luminosity running conditions for Run 3 (around five times the Run 2 luminosity) the old trigger readout becomes a bottleneck.

With this trigger upgrade, it will conclude the project of removal the L0 hardware trigger that already started in Run 2, and the LHCb detector will become the first hadron collider experiment to apply exclusively a software trigger. The LHCb events will be then recorded and transmitted from the Front-End electronics to the readout network at the LHC bunch crossing rate. The detector operation will rely on an expanded version of the software algorithms running on the EFF that the HLT was applying, in order to select and categorise events. As a consequence, the signal efficiencies will be maximised at high event rates.

Sub-detectors upgrade

The VELO will be replaced by a new silicon-pixel detector [126], that will ensure better hit resolution and simpler track reconstruction while having higher radiation hardness. In Sec. 4.2, the VELO upgrade is presented in detail, together with the contribution of this thesis to the project.

The entire tracking system will be entirely upgraded as well. For the upstream stations, a new Upstream Tracker (UT) [123] is being installed, composed of 4 tracking layers based on silicon micro-strips, covering an area of approximately $1.5 \times 1.3\,\mathrm{m}^2$. It will present finer granularity and full coverage of the detector acceptance, while reducing thickness. The UT will aim for the reconstruction of long particles decaying after the VELO, and therefore the trigger timing and momentum resolution will be significantly improved.

The downstream tracking stations will be replaced by a Scintillating Fibre Tracker (SciFi) [123], which is structured in 12 detector modules of 5 m long. The detector aims for track reconstruction, covering the scintillating fibers the full acceptance after the magnet.

The particle identification system will be upgraded as well [127]. The optical layout of the RICH1 will be modified in order to cope with the higher particle rate conditions. A second major consequence of the upgrade strategy for the RICH system is that the readout will be replaced by Multianode PMTs [128]. The calorimeters and the muon system will replace the Front-End electronics, to be compatible with the fully triggerless readout architecture. Besides, the detectors SPD/PS detectors, which were used in the L0 trigger, will be removed.

4.2 The VELO upgrade

One fundamental part of the LHCb upgrade is the substitution of the existing Vertex Locator, VELO, based on silicon micro-strip sensors, by a hybrid pixel detector capable of 40 MHz readout at a luminosity of $2 \times 10^{33}\,\mathrm{cm}^{-2}\,\mathrm{s}^{-1}$.

As it has been emphasized throughout the present document, the VELO plays a major role in the reconstruction of displaced vertices, which are a distinctive characteristic of heavy flavoured particles. Moreover, it provides crucial information in the trigger and tracking system. To fully exploit its functionality, the VELO must cover the full momentum and angular range of the LHCb detector. The low transverse momentum range is decisive in the decay products of beauty and charm hadrons, therefore the minimisation of material in the VELO is a fundamental requirement [126].

The expected operation of the upgraded Vertex Locator is to improve the physics performance of the previous one, while operating at increased occupancies, data rates and radiation damage. The just listed requirements can only be achieved by a complete replacement of the VELO's silicon detectors together with all the electronics.

After an arduous research and a process of externally refereed review, it was decided to install a detector based on hybrid pixel sensors. In order to cope with the data rates, a new radiation hard ASIC, dubbed VeloPix, was developed. Given these new advances in the detector and the data taking conditions, it was also necessary to redesign the cooling system. The upgrade cooling will use CO_2 as coolant (as it was the case for the previous detector), but in the upgrade the gas will circulate through micro-channels in a silicon substrate. The design was made in order to protect the tip of the silicon from thermal runaway effects and to cope with the high-speed pixel ASIC power dissipation.

In the following, some VELO specific terms are defined, which are used throughout this document [126]:

- **Tiles** is the name that receives the assembly of three VeloPix ASICs in a row bump-bonded to a common silicon sensor.

- **Hybrids** are referred to as the printed boards which are mounted on both sides of

the modules and provide electronic support for the front-end ASICs and the bias voltage for the sensors.

- The VELO consists of an array of **modules** which comprise the tiles, cooling and readout inside the vacuum. Each modules comprises two hybrids.

- A pair of modules, left and right, make up a **station**.

4.3 Physics performance constraints and VELO design

The upgraded VELO was designed so that it matches a set of performance criteria. The physics performance constrains benchmarks are presented in this section, together with a description of the VELO detector design. Fig. 4.3 shows a comparison of the resolution on the impact parameter with respect to the PV for the previous and the upgraded VELO.

It is estimated that the upgraded sensors will receive during their lifetime a highly non-uniform irradiation dose up to $8 \times 10^{15} 1\,\mathrm{MeV\,n_{eq}\,cm^{-2}}$, equivalent to an integrated luminosity of $50\,\mathrm{fb}^{-1}$. At this dose, the sensors are expected to retain a 99% hit efficiency at up to 1000 V bias voltage without suffering breakdown[3] [129]. This document presents a contribution to the characterisation of the VELO prototypes performance, regarding the high voltage tolerance temperature dependence and the breakdown voltage issue, detailed in Sec. 4.4.3.

The expected integrated radiation damage at the upgrade is shown in Fig. 4.4, where contours in the $R - z$ plane are displayed, where R stands for ratio with respect to the *pp* collision point and the vertical lines in z mark the positions where the modules will be mounted. The method used for the estimation follows the same strategy than in the previous VELO case, since it has so far given a very reliable prediction.

One of the most challenging requirement on the VELO upgrade is derived from the demanding data rate constraint. The mean visible interaction rate is around 27 MHz, however it may reach a peak of 40 MHz. To meet this requirement, the readout in the VELO upgrade is done by the VeloPix ASICs, a pixel sensor which consists of a matrix of 256×256 pixels of $55 \times 55\,\mu\mathrm{m}^2$ each. The hit information is time-stamped, addressed and read out as pixels packets. Arranging the data in this way reduces the output bandwidth by $\approx 30\%$ [129].

The upgraded detector will be closer to the beam than in the current VELO, specifically at 5.1 mm (from 8.2 mm) in its closed position. Overall, the VELO upgrade consists of 52 modules that are divided into two retractable halves kept in vacuum along the beamline. The modules surrounds the interaction point. By placing them perpendicular

[3]For more information about the breakdown mechanism, see Chap. 4.4.3.2.

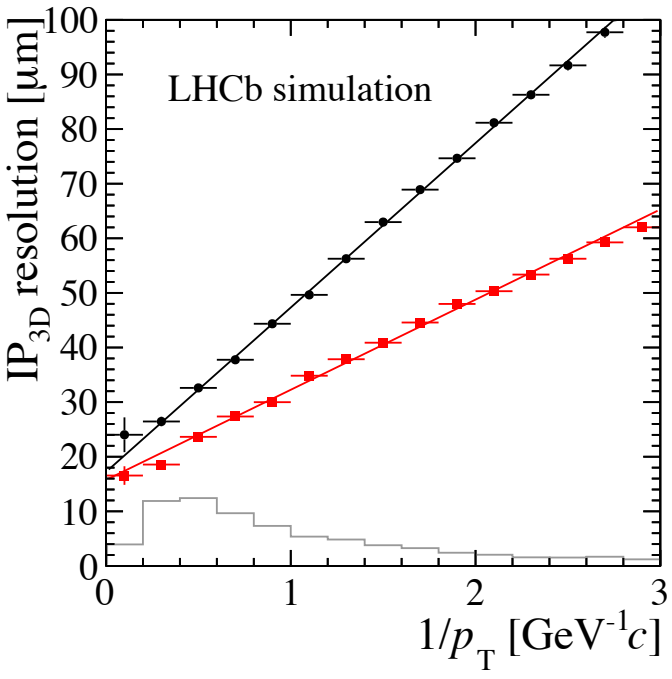

Figure 4.3: 3D Impact Parameter resolution dependence with particle inverse transverse momentum for VELO long tracks with $2 < \eta < 5$ from a primary vertex. Made with LHCb software simulation. In red the resolution is displayed for the upgrade, and in black for the current VELO [126].

to each other, gaps in the acceptance are minimised. In Fig. 4.5 (top), it can be seen one half of the detector, while Fig. 4.5 (bottom) represents two modules in the closed position.

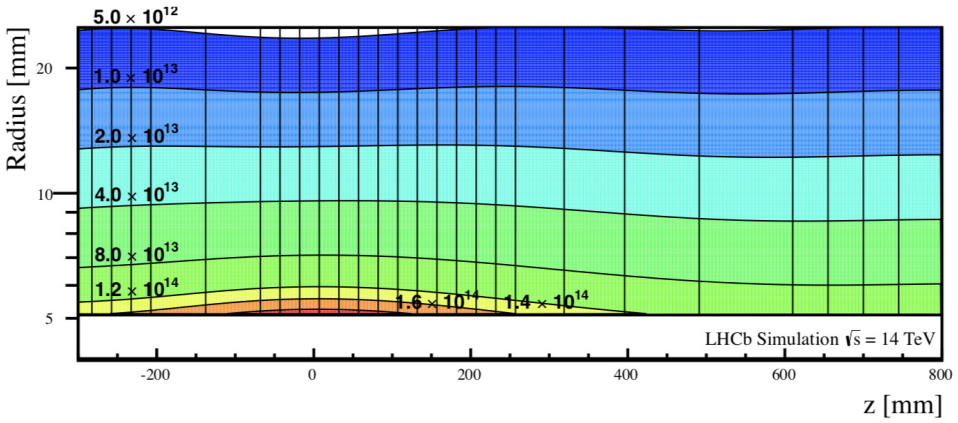

Figure 4.4: Estimated integrated radiation dose in the $R - z$ plane per fb^{-1} at upgrade conditions, expressed in units of $1\,\mathrm{MeV\,n_{eq}/\,cm^{-2}}$. The vertical axis is logarithmic, in order to highlight the behaviour around the interaction region [126].

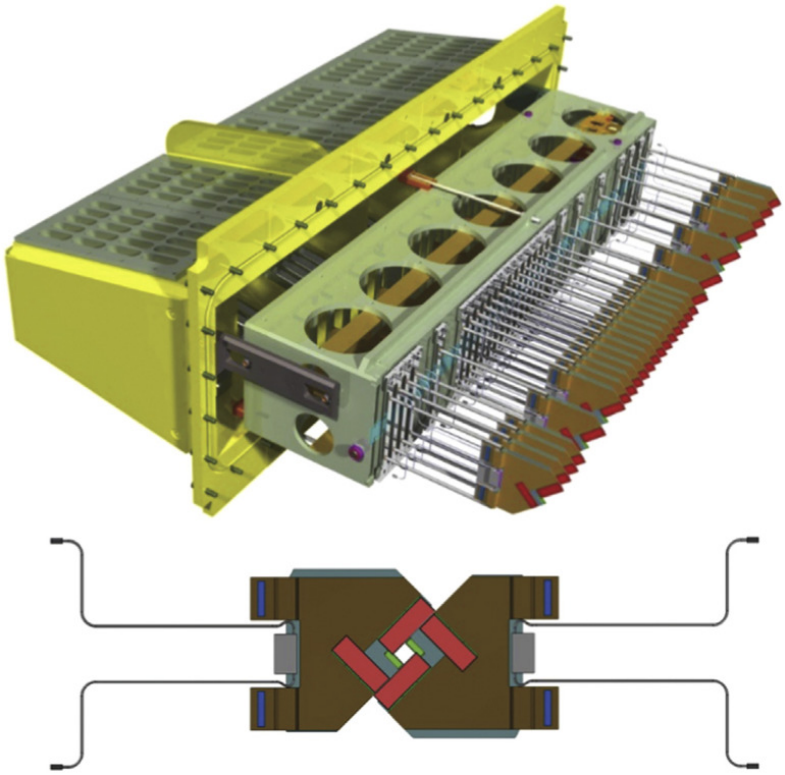

Figure 4.5: (top) Schematic of one half of the VELO upgrade detector. 26 modules are aligned along the beam direction. (bottom) Two modules in the closed position. The modules are placed in perpendicular position along the beam line, to minimise gaps in the acceptance, and there is a slight overlap between two halves, which helps detector alignment. [129].

4.4 Performance of the Prototypes

The performance of a silicon sensor can be characterized through several parameters. Firstly, in order to determine a safe operational voltage of the VeloPix sensors in the laboratory setup, the current–voltage (IV) curve is obtained in Sec. 4.4.2. Secondly, this thesis studies the radiation damage effect that the upgraded VELO is expected to face. In Sec. 4.4.3 it is documented the leakage current increase with fluence, applying the IV method presented to the sensors. Finally, in Sec. 4.4.4, research towards the characterisation of the breakdown mechanism is documented, together with a study on the modelling of this effect.

4.4.1 Testing Setup

As part of the testing procedure of the VELO sensors, it is required to study the performance of the sensors in a similar environment to the one in which the VELO will operate. All tests that enable to extract the sensor performance results were carried out in the VELO laboratory, at CERN facilities, which allows for operation under the required vacuum conditions.

On one hand, operating at low temperatures is crucial in order to prevent thermal runaway and potential sparkling that can break the sensor. On the other hand, the vacuum conditions avoid condensation forming on a cooled sensor. To meet the above requirements, tests were performed inside of a vacuum chamber, Fig. 4.6, equipped with scroll and turbo pumps. This installation allow to reach vacuum conditions of 10^{-4} to 10^{-5} mbar, similar to the operation one. The vacuum chamber is assembled inside a copper block, as it can be seen in Fig. 4.7, that made use of a water and glycol solution providing cooling conditions. Adding a Peltier element, which is mounted on top of the copper block, allows the setup to reach temperatures much colder than what would be possible just with the water cooling. Finally, sensors were mounted on top of the Peltier device.

In typical running conditions, the cold water temperature is $-15°$C, while the cold side of the Peltier could reach up to $\approx -32°$C. With the aim of expanding the research on sensors behaviour with respect to temperature, eventually a better chiller was installed on the VELO laboratory at CERN. Then, the overall running setup allows the cold side of the Peltier to reach about $-44°$C.

Regarding the prototype sensor design, it was selected based on simulations presented in the VELO TDR [126]. After a selection process from two vendors, it was chosen to go ahead with Hamamatsu (HPK) sensors. In all the studies documented in this work, VeloPix sensor n-on-p triples of HPK were employed, meaning that each sensor is connected to three independent VeloPix chips, as it is schematised in Fig. 4.8(a). Implant size of 200 µm thick on a n-on-p sensor HPK with an implant size of 39 µm and a guard ring of 450 µm, were employed, as displayed in Fig. 4.8(b). Overall, the format size of the triples are a matrix a 768×256 pixels.

A dedicated readout chain that allows to read the VeloPix chip is necessary. It is controlled using the Speedy Pixel Detector Readout (SPIDR) [130, 131] system, that was connected to a PC where data acquisition could be controlled, and data is stored.

Apart from the readout, it was needed an extra connection to provide the bias voltage. The high-voltage supply Keithley was employed, which was controlled remotely with LabView software [132].

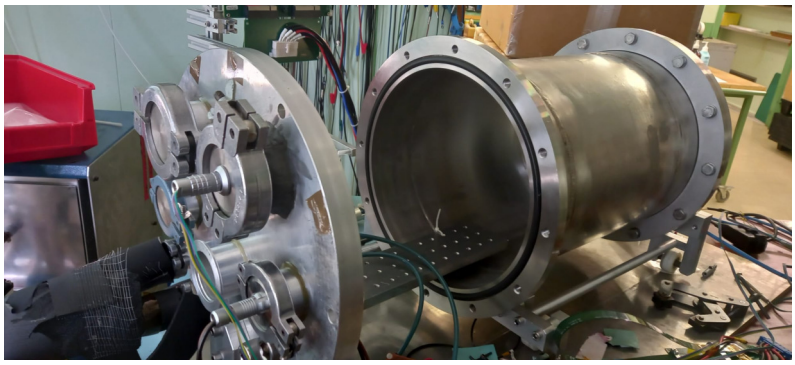

Figure 4.6: Vacuum tank, fundamental part of the testing setup.

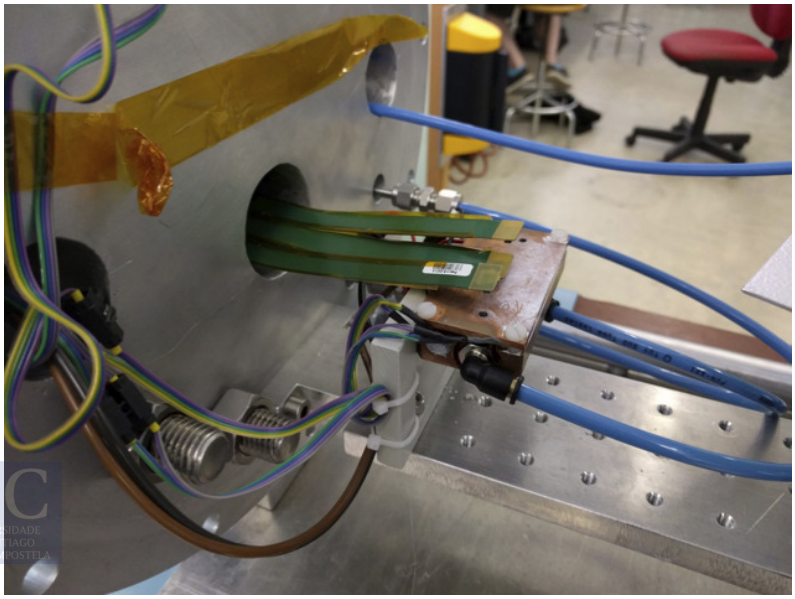

Figure 4.7: Cooling block inside the vacuum chamber.

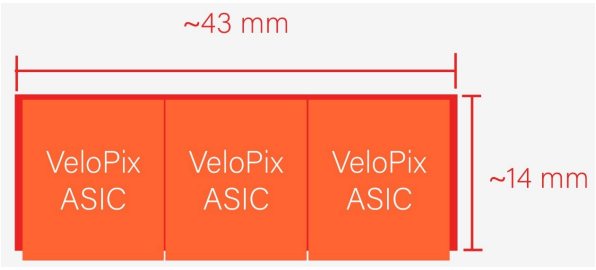

(a) Underside of a triple tile bump-bonded to VeloPix ASICs.

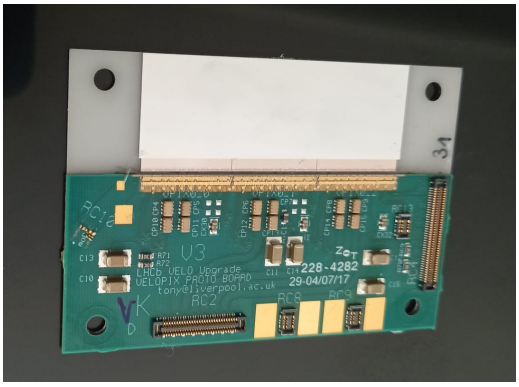

(b) Triple sensor bounded to the VeloPix.

Figure 4.8: Prototype assembly.

4.4.2 Intensity-Voltage scans

The characterisation of current versus voltage behaviour, curve IV, is a powerful tool to qualify the electrical stability and power dissipation of silicon sensors. IV scans allow tracking leakage current while looking for unusual slopes or temperature shifts, deviations that would derive in most of the problems that are seen in the production process. This step is also fundamental to guarantee the safe operational voltages of the sensors.

To avoid sparks damaging the assembly, the IV scans are performed in vacuum. The IV scan was taken in 5 V steps, with a delay of 2 s between steps to allow the current to settle. The current was measured in a range between 0 and 1000 V, corresponding to the range in which the sensors are expected to operate. In Fig. 4.9, an IV curve for a non-irradiated sensor is shown, displaying a correct behaviour in all the scan range. For low voltages, the current increases until a point where the full width of the sensor is depleted, which occurs at ≈ 100 V.

In Sec. 4.4.3, an IV scan procedure will be applied to determine the dependence of the tolerance of the high voltage concerning the temperature for different irradiation profiles.

4.4.3 High Voltage Tolerance Temperature Dependence

One of the biggest challenges that the upgrade VELO will face is radiation damage, that also affects the sensors in non-uniform way. Therefore, the second part of the work was organized with the aim of understanding the effect that different types of irradiation can have, uniform and non-uniform, and to characterize the response of the sensors once subjected to this process.

In this section it is documented the behaviour of sensors irradiated with both uniform and non-uniform fluence, in order to study the relevance of this condition. With this goal, IV scans were repeated in two different sets of tiles, which consist on HPK n-on-p sensors

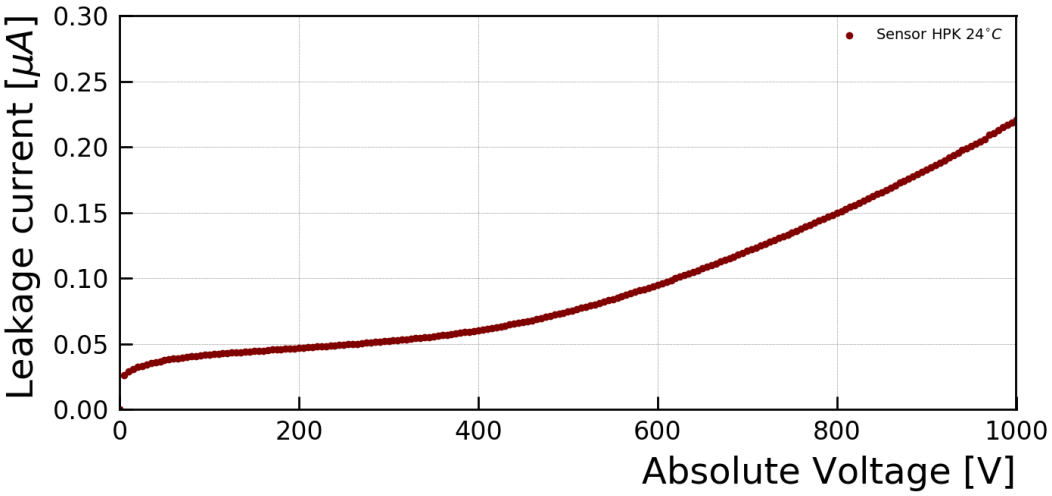

Figure 4.9: IV scan for a 200 μm thick HPK non-irradiated sensor.

bump-bonded to VeloPix ASICs. Two irradiation profiles were employed:

- IRRAD Gaussian-type for TILE 0, TILE 1, TILE 2 and TILE 3.
- Birmingham non-uniform irradiation for TILE 4, TILE 5, TILE 6 and TILE 7.

All of the sensors are them non-Parylene coated.

4.4.3.1 Leakage current

Irradiated sensors need to operate at very high bias voltages in order to collect sufficient charge. In the laboratory, a bias voltage is applied to the sensors in order to create a depleted region free of charge carriers. However, thermal excitation allows electrons to cross the band gap, even in the absence of a charged particle. The probability of thermal excitation of electrons increases strongly with the presence of impurities in the lattice. This can be explained because the impurities introduce additional energy states in the band gap. The flow of current that is produced then is called the leakage current, and it largely depends on the temperature as:

$$\mathrm{I}(T) \propto T^2 \exp^{-\left(\frac{E_g}{2kT}\right)}, \tag{4.1}$$

where T is the temperature in Kelvin, E_g is the band gap energy and k is the Boltzmann constant. Since the leakage current increases the noise, the sensors are often operated at low temperatures to decrease the probability of thermal excitations.

4.4.3.2 Breakdown mechanism

When operating with a p-on-n diode, there is a maximum reverse bias voltage that can be applied. At this point, the junction breaks down and then a rapid (exponential) increase in the current occurs. In other words, it means that the electrical field is high enough to initiate avalanche multiplications, and this avalanche process depends on both the temperature and the defects [133]. The corresponding applied voltage is referred to as the breakdown voltage. This voltage is a key parameter of power devices since operating at higher values may damage the junction.

There are mainly three breakdown mechanisms: thermal breakdown, tunneling and avalanche multiplication [134]:

(i) Thermal breakdown (thermal runaway) is the process through which, due to the heat dissipation caused by the reverse current at high reverse voltage, the junction temperature rises. This temperature increase causes, in turn, the increment of the reverse current, activating a positive feedback loop.

(ii) Tunneling breakdown takes place in diodes beyond at certain high reverse bias voltage[4], when the probability of the charge carriers of tunnelling the bandgap is almost negligible. Therefore, at some high voltage values, a significant current begins to flow by means of this tunneling process.

(iii) Avalanche multiplication happens when the field inside the junction is such that the primary current generates more free charge carriers by impact ionisation [135].

It was noticed that, during the test beam campaign of early 2017, non-uniformly irradiated sensors were having a breakdown of much lower voltage values than was expected. Further research showed that the sensors were operating at higher temperatures than the ones that the setup was expected to provide. A new cold box with a more powerful chiller was installed in the laboratory at CERN facilities, to perform a systematical study on the temperature behaviour for the VELO sensors.

4.4.3.3 IRRAD irradiated sensors

A set of sensors TILES were irradiated at the IRRAD proton facility, at CERN. This irradiation facility is located in the T8 beam-line of the East Area at the Proton Synchrotron accelerator[5]. At IRRAD, a Gaussian 24 GeV proton beam with transverse full-width half maximum of $12\,\mathrm{mm}^2$ was used to irradiate the sensors to the full fluence of $8 \times (10^{15}\,\mathrm{MeV\,n_{eq}\,cm^{-2}})$. Fig. 4.10(a) shows the IRRAD reconstructed fluence profile for full fluence sample [137]. This profile is obtained employing sensor activation and dosimetry information.

[4] Values of $10^5 \sim 10^6$ V/cm.

[5] More information about the facility can be found in [136].

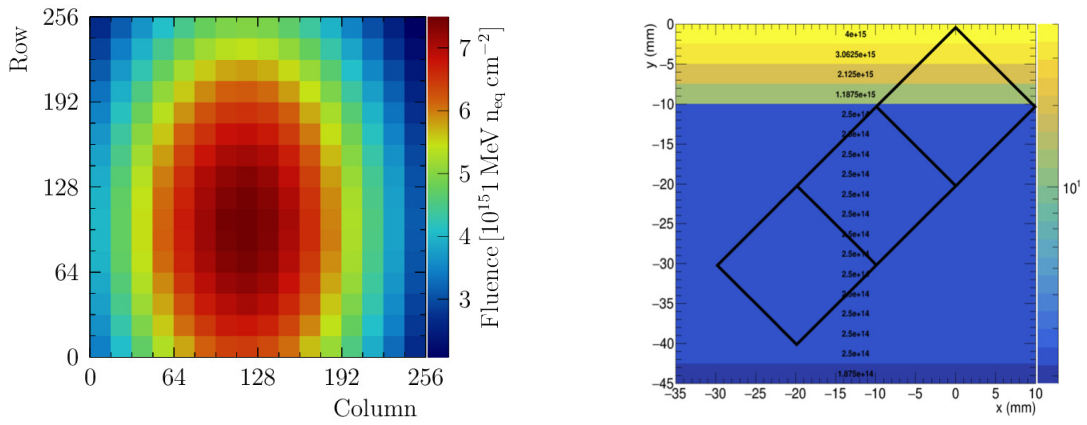

(a) (b)

Figure 4.10: (a) IRRAD fluence profile for full fluence samples, in units of 10^{15} 1 MeV $n_{eq}\,cm^{-2}$ [137]. (b) Birmingham non-uniform radiation profile for triple assemblies.

The sensors irradiated at IRRAD were the TILE 0, TILE 1, TILE 2 and TILE 3. These TILES consist of 200 µm 3×1 n-on-p HPK sensors bump-bonded to VeloPix ASICs, and glued onto a ceramic substrate. The size of the guard-ring is 450 µm and the size of the n-type implant is 39 µm. All the information about the radiation campaign for each specific sensor is displayed in Tab. 4.1.

Hybrid	Type	Implant Size (µm)	Fluence (10^{15} 1 MeV $n_{eq}\,cm^{-2}$)
TILE 0	HPK n-on-p + VeloPix ASIC	39	8
TILE 1	HPK n-on-p + VeloPix ASIC	39	8
TILE 2	HPK n-on-p + VeloPix ASIC	39	8
TILE 3	HPK n-on-p + VeloPix ASIC	39	8

Table 4.1: Sensors irradiated with 24 GeV protons at IRRAD facility.

To study the dependence of high voltage tolerance with temperature, the same presented method of IV scan was repeated after the sensors have been sent to the irradiation facilities, working again in vacuum conditions. The IV curves were documented for different sensor temperature conditions. A Peltier element allows to control and change the temperature in the cooling block just by changing the different Peltier voltages.

The IV curves for the Gaussian irradiated triplets are shown in Fig. 4.11. The IRRAD facility has a hardness factor similar to the VELO operation conditions, and therefore these tests allow us to understand the behaviour of the TILES under realistic data-taking conditions. The curves were performed for three different Peltier voltages: 1 V, 3 V and 5 V, which corresponds to a sensor temperature of −23°C, −34°C and −42°C, respectively.

In particular, it was found that when operating at $-42°$C and $-34°$C, the sensors ranged from 0 to 1000 V without showing breakdown, as it is required. When the temperature increases to $-23°$C, the sensors present a rapid increase of the current at a given voltage, namely breakdown voltage, below 1000 V. Since the test beam temperature conditions are expected to be $\approx -30°$C, the conclusion drawn from these studies was that the TILES irradiated at IRRAD were behaving as it was expected.

4.4.3.4 Birmingham irradiated sensors

The non-uniform irradiated profiles were done with a high-intensity proton beam coming from the MC40 cyclotron in Birmingham facilities [138], with an energy of 27 MeV. The irradiation profile is represented in Fig. 4.10(b). A more detailed description of the irradiation campaign can be found in Appx. B.

At Birmingham, the triplets TILE 4, TILE 5, TILE 6 and TILE 7 were irradiated. These TILES consist of 3×1 n-on-p HPK sensors of 200 µm thick with an implant size of 39 µm and a guard-ring of 450 µm, bump-bounded to VeloPix ASICs, and glued onto a ceramic substrate.

In Tab. 4.2 the irradiation characteristics for each sensor are collected. The results of the IV curves for Birmingham irradiated sensors are displayed in Fig. 4.12. All of them show a very early breakdown voltage, at values that range between 100 V when operating at high temperatures, until 700 V at normal running conditions. It was needed further research in order to understand the nature and origin of this behaviour, and this extra effort is documented in Sec. 4.4.4.

Hybrid	Type (3×1)	Implant Size (µm)	Average fluence (10^{15} 1 MeV n_{eq} cm^{-2})
TILE 4	HPK n-on-p + VeloPix ASICs	39	1.87
TILE 5	HPK n-on-p + VeloPix ASICs	39	1.48
TILE 6	HPK n-on-p + VeloPix ASICs	39	2.50
TILE 7	HPK n-on-p + VeloPix ASICs	39	1.40

Table 4.2: Sensors irradiated with 27 MeV protons at Birmingham.

4.4.3.5 Comparison of irradiated sensors

In Fig. 4.13, a comparison was done for both sets of triple assemblies. It was chosen a similar temperature range, from -34 to $-37°$C, to allow us to make an assessment of the different effects that may have each irradiation type on the sensors. While the sensors irradiated uniformly at IRRAD do not show breakdown up to 1000 V, Fig. 4.13(a), in sensors that were irradiated at Birmingham, the breakdown voltage appears before the end of the scan, Fig. 4.13(b). It was accepted in the VELO laboratory that the variance in the breakdown voltage behaviour could be due to the different types of defects that one would get from a distinct proton energy. Although both proton energy are scaled to

1 MeV neutron equivalent through the NIEL scaling [139], the types of defects generated are not necessarily the same. Still, since the early breakdown was found in VELO TILES prototypes, more research was made in order to understand the breakdown effect, which is a crucial point in the LHCb upgrade operation. It will be described in the following section.

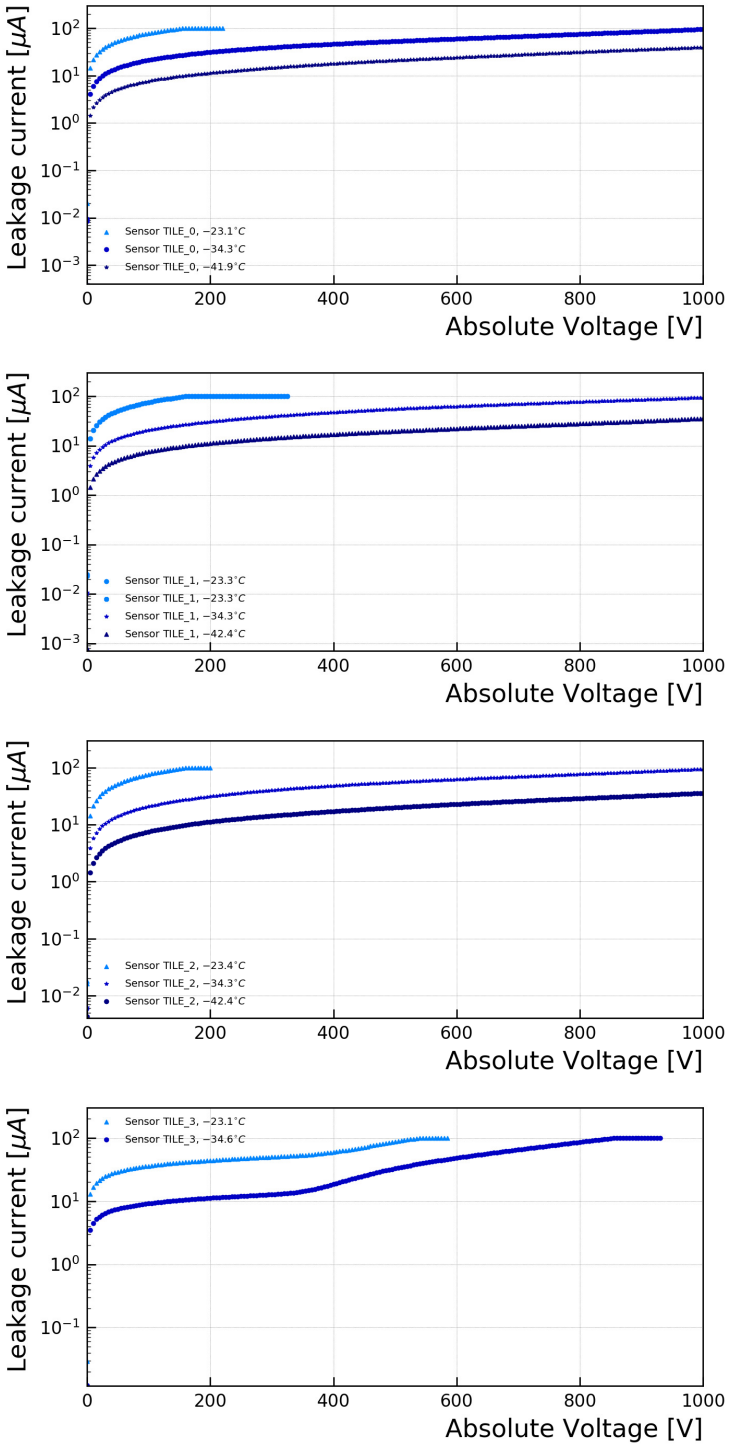

Figure 4.11: IV temperature dependence for the IRRAD sensors: TILE 0, TILE 1, TILE 2 and TILE 3

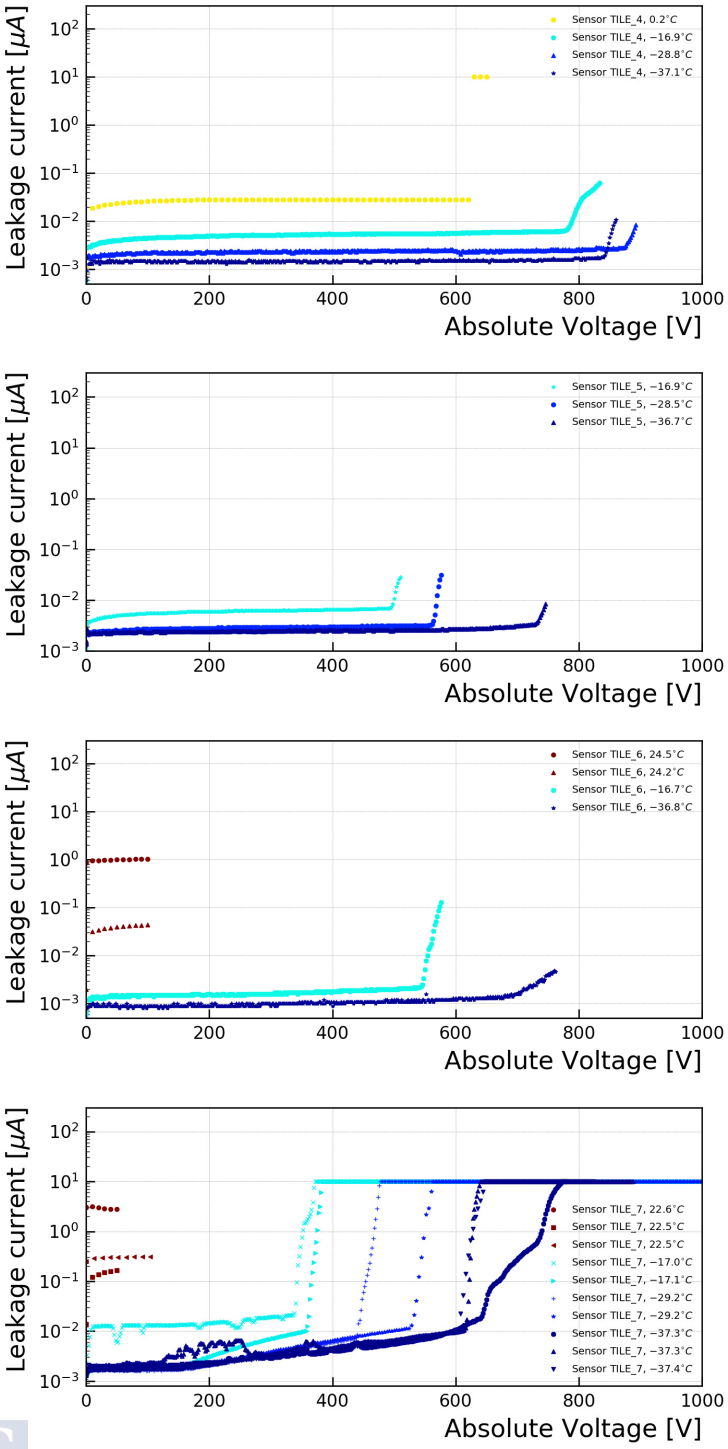

Figure 4.12: IV temperature dependence for the Birmingham sensors: TILE 4, TILE 5, TILE 6 and TILE 7.

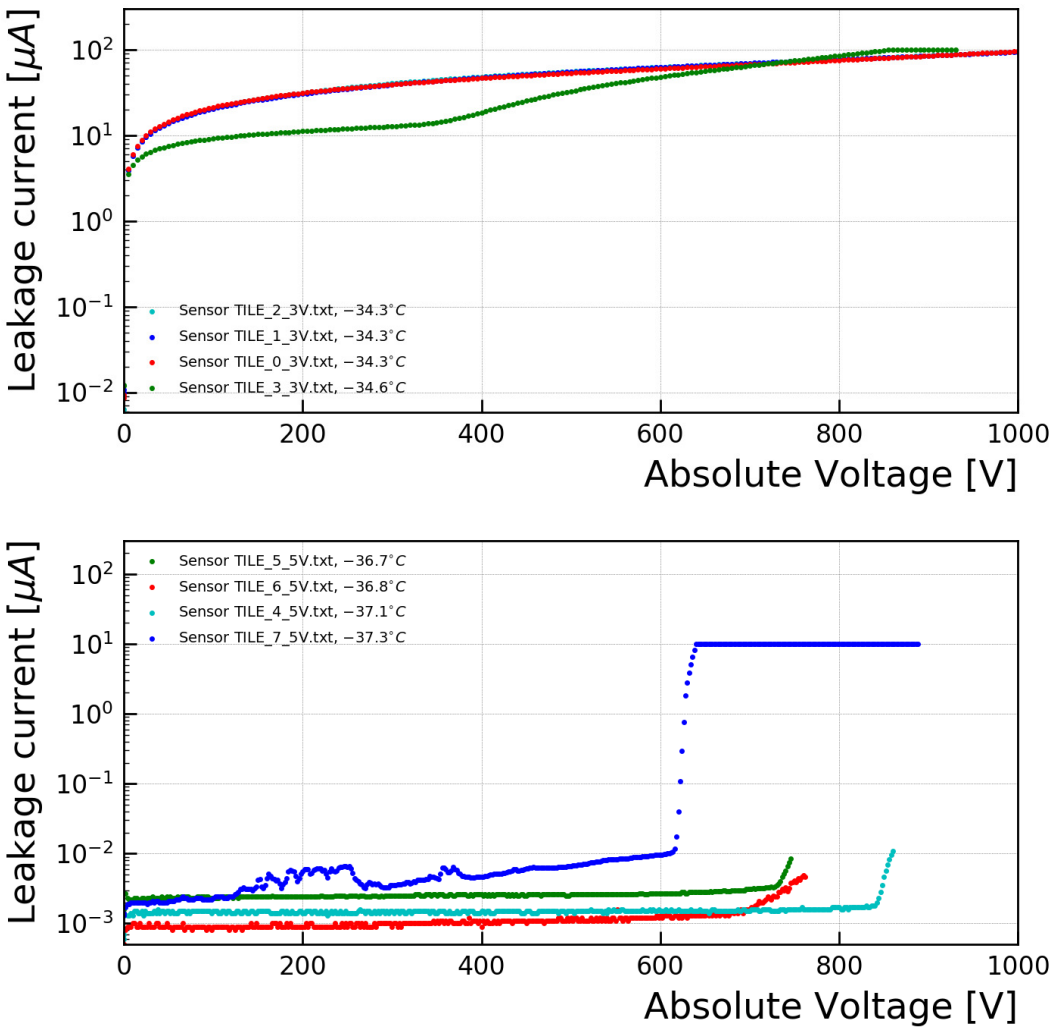

(a)

Figure 4.13: Comparison at similar temperatures of IV curves of triple assemblies irradiated at (a) IRRAD and (b) Birmingham.

4.4.4 Breakdown behaviour

From Fig. 4.12, it was found that, for all the IV curves, the breakdown mechanism presented a clear temperature dependence in the breakdown point. The most plausible hypothesis that would explain this behaviour was that the heating of the sensor itself was causing the increase of the leakage current, and vice-versa, *i.e.* thermal runaway mechanism. If this would be the case, the heat generated in the most irradiated area of the sensor would not be dissipating properly, which would impact the measurements to a great extent. Therefore, further research was done in order to test this premise.

4.4.4.1 Check of sensor temperature

In all previous measurements, the temperature was recorded in the cold and warm sides of the Peltier element, assuming that it was stable during the data-taking. In order to understand the temperature spectrum along the sensor during the voltage increase, a PT100 readout module was placed directly on the sensor TILE 5 with thermal paste. In this way, the temperature could be recorded during the IV curve scan, and it could be checked if the breakdown voltage change. The IV scan was made attaching the PT100 in the region of the sensor on top of each of the three ASICs that compose the TILE, namely chip 0, chip 1 and chip 2, being the chip 2 the one that had received more irradiation.

Fig. 4.14 shows the results of the three IV scans at $-38°$C. It can be seen that the curve in which the breakdown occurred before is the case in which the PT100 is placed in the chip with less radiation damage. Then, the effect of attaching the PT100 in the chip that received more irradiation is that the breakdown voltage is displaced towards higher values. The breakdown voltage for the case without PT100 paste on it remains in the middle of the previous cases.

It was found that the temperature was the same in all chips during the data taking, between $-28°$C and $-29°$C. However, even if the temperature was the same, placing the PT100 on the chips had a remarkable impact in the IV curve. A hypothesis that would explained this situation is that the PT100 was provoking the current to leak. If this was the case, the decrease of current in the overall sensor would be higher when the PT100 is pasted in the point in which the current is higher, *i.e.* chip 2. This is consistent with the measurements observed in Fig. 4.14.

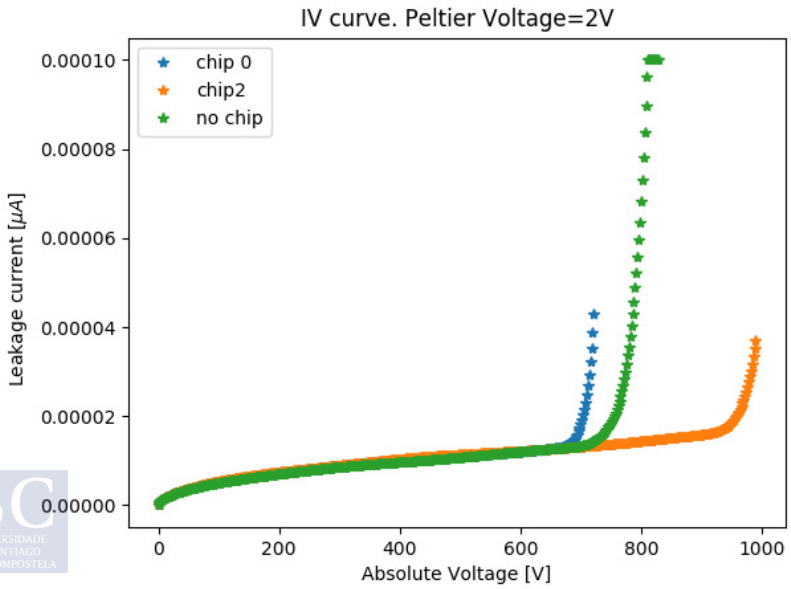

Figure 4.14: IV curves with PT100 attached in different chips of the TILE 5 at $-38°$C.

4.4.4.2 Breakdown parameterisation

Modelling the breakdown behaviour would help to understand the different components that contribute to this effect. Hence, with the objective of analysing the IV behaviour as a function of the temperature, the following functional form for the IV curve is employed:

$$\mathrm{I}_{\mathrm{leak}}(V) = \mathrm{I}_s(1 - e^{(-\alpha V)}) + \kappa V + \beta e^{\gamma(V - \mathrm{V}_{th})}, \tag{4.2}$$

where the first term of the equation is the Shockley diode equation for bias voltage, I_s stands for the diode saturation current and α is a parameter that controls how fast it reaches saturation value. The second term of the Eq. 4.2 is a linear increase due to irradiation effect, that has been identified as result of avalanche generation [140,141]. The last term models the Breakdown contribution, in which β has been set to 10^{-6}, in order to guarantee that no contributions from this term affect the non-breakdown components of the IV curve, the δ term takes into account the breakdown steepness and V_{th} is the breakdown threshold voltage. For sensors that do not show breakdown, the Eq. 4.2 is simplified as:

$$\mathrm{I}_{\mathrm{leak}}(V) = \mathrm{I}_s(1 - e^{(-\alpha V)}) + \kappa V. \tag{4.3}$$

The fit to expression Eq. 4.2 was already tested in the T25 sensor, and documented in [135]. The T25 sensor is a HPK n-on-p that was irradiated at KIT cyclotron[6], with low energy proton of 23 MeV. The irradiation fluence was $8 \times 10^{15} 1\,\mathrm{MeV\,n_{eq}\,cm^{-2}}$. The fit is shown in Fig. 4.15.

While the behaviour of the IV curve was parameterised and tested for sensors that showed breakdown, the Eq. 4.3 was not yet tested in sensors that reached 1000 V without breakdown. Therefore, this document aims for the first fit of the IV curve for a sensor without breakdown, in particular the TILE 0 with a temperature of −42°C. In Fig. 4.16 it is shown the fit to Eq. 4.3, while the fit results are gathered in Tab. 4.3.

Parameter	value
I_s	4.0824 ± 0.0050
α	0.043855 ± 0.000022
κ	$0.034310671 \pm 0.000000014$

Table 4.3: Fit result of the IV curve of the TILE 0 at −42°C to the Eq. 4.3.

By the time that the Eq. 4.3 model was fitted, in the VELO laboratory there was an interest in checking if the curve could also accommodate another term due to avalanche generation. This could mean that there was more than one component due to irradiation effects, obtaining from Eq. 4.3, the following expression:

$$\mathrm{I}_{\mathrm{leak}}(V) = \mathrm{I}_s(1 - e^{(-\alpha V)}) + \kappa_1 V + \kappa_2 V. \tag{4.4}$$

[6]In the Karlsruhe Institute of Technology, more information about the cyclotron can be found in [142].

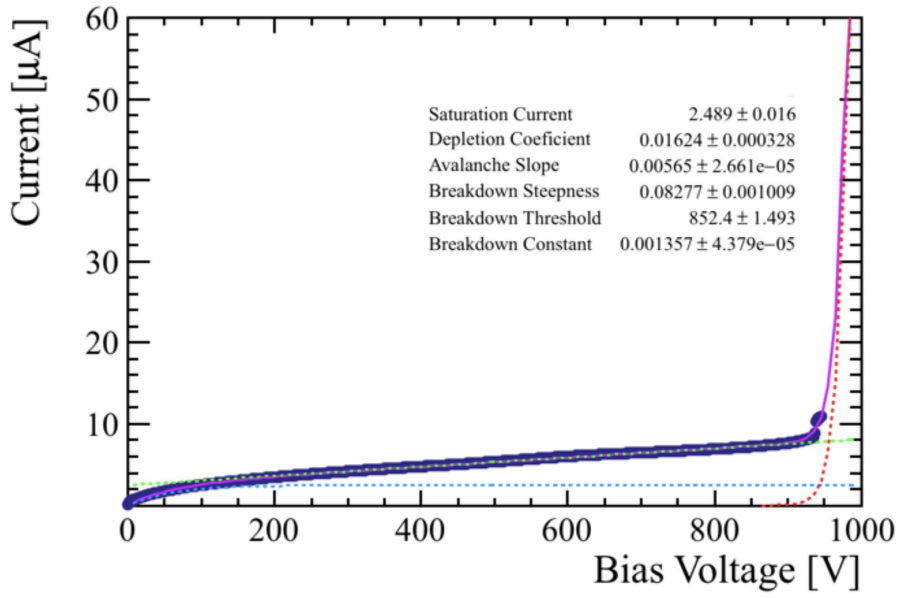

Figure 4.15: T25 at −35°C IV Curve (black dots) fitted with Eq. 4.2, plotted in violet. The blue dashed line corresponds to the diode saturation current, the green curve is the sum of the first two terms and the breakdown term appears independently in red. Obtained from [135].

This hypothesis can be found in the fit that is shown in Fig. 4.17, while the results are presented in Tab. 4.4. Both parameterisations results compatible among them, as it can be extracted from the values of the parameters of Tabs. 4.3 and 4.4.

Parameter	**value**
I_s	4.0824 ± 0.0050
α	0.043855 ± 0.000022
κ_1	$0.0079877911 \pm 0.0000000034$
κ_2	$0.0263228799 \pm 0.0000000034$

Table 4.4: Fit result of the IV curve of the TILE 0 at −42°C to the Eq. 4.4.

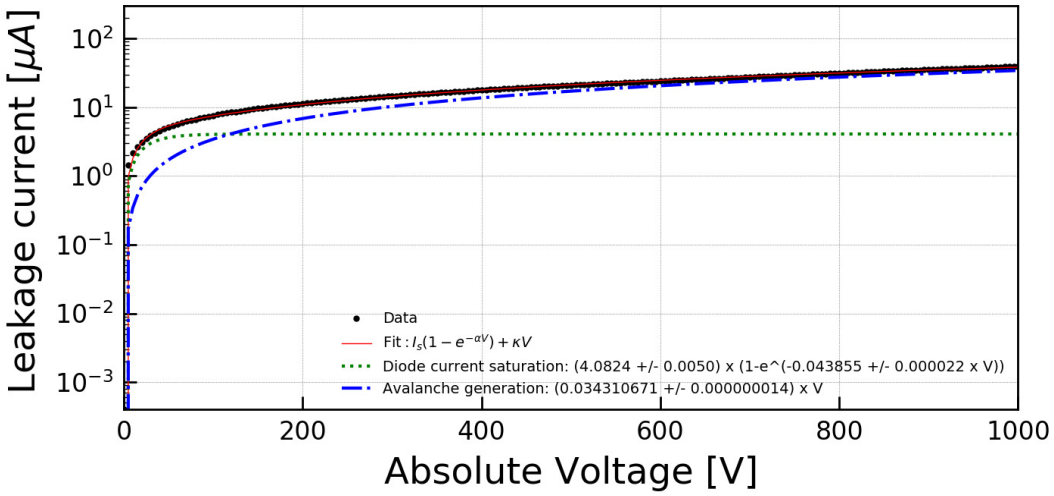

Figure 4.16: TILE 0 at −42°C IV curve (black dots) fitted with Eq. 4.3, plotted in red. The green dashed line corresponds to the diode saturation current and the blue curve is the avalanche generation term.

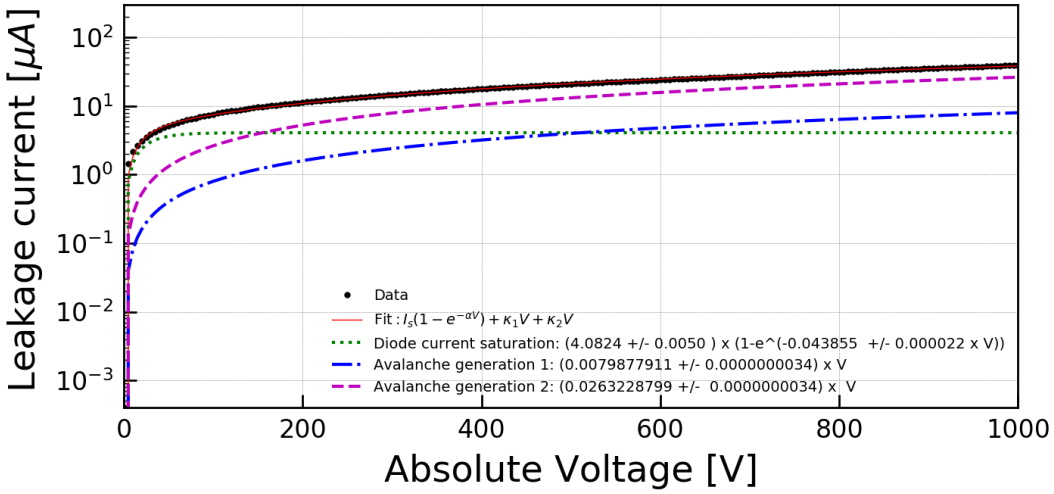

Figure 4.17: TILE 0 at −42°C IV Curve (black dots) fitted with Eq. 4.3, plotted in red. The green dashed line corresponds to the diode saturation current and the blue and magenta curves are the avalanche generation terms.

4.5 Conclusions

As a fundamental part of the LHCb upgrade, the VELO detector is being replaced by a new silicon pixel detector, which will allow the experiment to operate at higher luminosities. It is therefore of crucial importance systematize and evaluate the performance of the sensor prototypes. As part of this work, VeloPix sensor performance of n-on-p triples HPK of 200 µm thick, $55 \times 55\,\mu m^2$ pixels and 39 µm implant size were characterised.

Firstly, the IV behaviour was documented for a non-irradiated sensor, in running conditions that simulate the operational ones. The behaviour of the sensor in the range $0 - 1000\,V$ was documented, showing no breakdown voltage and proving to be safe operational voltages for the sensors.

Secondly, the dependence of the high-voltage tolerance with the temperature has been studied, by documenting the behaviour of sensors irradiated with different fluence profiles.

On one hand, sensors with uniform fluence were irradiated at the IRRAD facilities. Then, the IV procedure was applied to obtain the dependence of the curves with temperature. For all the measurements taken, the sensors were behaving as expecting, showing no breakdown behaviour.

On the other hand, a different set of triples were irradiated at Birmingham with a non-uniform fluence profile. The IV curves showed, in all cases, early breakdown voltage before the end of the scan, behaviour that motivated further research. In order to understand the nature of this phenomena, it was proceeded with a check on the sensor temperature that would clarify if the breakdown voltage was an effect of the thermal runaway of the sensor. A PT100 was pasted on a single sensor in different positions, that correspond to areas with a different irradiated fluence. The effect of attaching the PT100 was noticeable, since it would provoke the current to leak. This procedure could not finally explain the breakdown voltage, since the temperature read by the PT100 would not justify the increase of the leakage current as an effect of thermal runaway of the sensor.

In the VELO laboratory, several hypothesis raised to explain the early breakdown voltage appearance. It could happened that the sensors surface were damage, as it occurred previously with the observed Parylene damage[7] in some sensors irradiated at KIT. Also, due to the difficulty of maintaining the cold chain, it could be that the sensors were at room temperature for too long, causing irreversible damage. It was also accepted that the breakdown was due to the different type of defects that one would get from a not well documented proton energy. However, even if this effect was not fully understood, it is absolutely necessary to remark that the breakdown voltage issue was not observed in further IV curves done in different set of sensors, not even in the ones irradiated with the same fluence characteristics of the Birmingham ones. Moreover, IV tests were performed in all the sensors that will be part of the VELO upgrade detector, showing all of them the expected behaviour.

As a final contribution to the VELO upgrade project, the leakage current was pa-

[7] See [135] for more details.

rameterised, in order to complete the research that was started in the VELO laboratory. The modelling was done with two different functions, finding no relevant difference among them, since the parameters obtained from both fits are compatible.

To sum up, relevant contributions are documented regarding the procedure to test the new VELO triples. Most of the work was developed to, firstly, correct reproduce the expected IV behaviour of VELO sensors; and secondly, try to understand the breakdown voltage effect, as a disturbing issue found in the VELO laboratory by the time that I was working there. The fact that the breakdown effect was no later seen in any sensor closed the issue, categorising it as a bug at some manufacturing stage.

5

Methodology of the $\mathcal{R}(D^{(*)0})$ measurement

After expounding on the contribution of this thesis to the characterisation of the upgraded VELO prototypes (Chap. 4), I switch to a totally different topic, the analysis of data. In particular Lepton Flavour Universality tests are presented.

Contents

5.1 Introduction

As it was discussed in Sec. 2.2, the current combination of experimental measurements of $\mathcal{R}(\mathcal{D})$ and $\mathcal{R}(\mathcal{D}^*)$ is in tension with the SM prediction at the remarkable level of 3.4σ [47]. This strongly motivates new precise measurements that could clarify the tension, paving the road to NP.

In this document, a new hadronic measurement of the lepton universality ratios[1]:

$$\mathcal{R}(D^0) = \frac{\mathcal{B}(B^+ \to \overline{D}^0 \tau^+ \nu_\tau)}{\mathcal{B}(B^+ \to \overline{D}^0 \ell^+ \nu_\ell)}, \tag{5.1}$$

[1]The inclusion of charge-conjugate modes is implied throughout.

$$\mathcal{R}(D^{*0}) = \frac{\mathcal{B}(B^+ \to \overline{D}^{*0}\tau^+\nu_\tau)}{\mathcal{B}(B^+ \to \overline{D}^{*0}\ell^+\nu_\ell)}, \tag{5.2}$$

is presented, where ℓ represents either an electron or a muon. In this analysis, the decay chain of each involved particle is chosen of the form:

- The τ lepton is reconstructed using the $\tau^+ \to \pi^+\pi^-\pi^+\overline{\nu}_\tau$ and $\tau^+ \to \pi^+\pi^-\pi^+\pi^0\overline{\nu}_\tau$ decay modes.
- $\overline{D}^0$ is chosen in its $K^+\pi^-$ decay channel.
- The $\overline{D}^{*0}$ decays either into $\overline{D}^0\pi^0$ (64.7±0.9% [9] of the cases) or $\overline{D}^0\gamma$ (35.3±0.9% [9]), where the additional neutral particle is not reconstructed.

Furthermore, neutrinos are not detected, and therefore a specific strategy must be applied in order to reconstruct the B and τ four-momenta. Overall, the visible final state of the signal consists of $4\pi^\pm$ and one K^+. In Fig. 5.1, the topologies of both signals are gathered. The measurements are performed using Run 2 dataset collected by the LHCb detector.

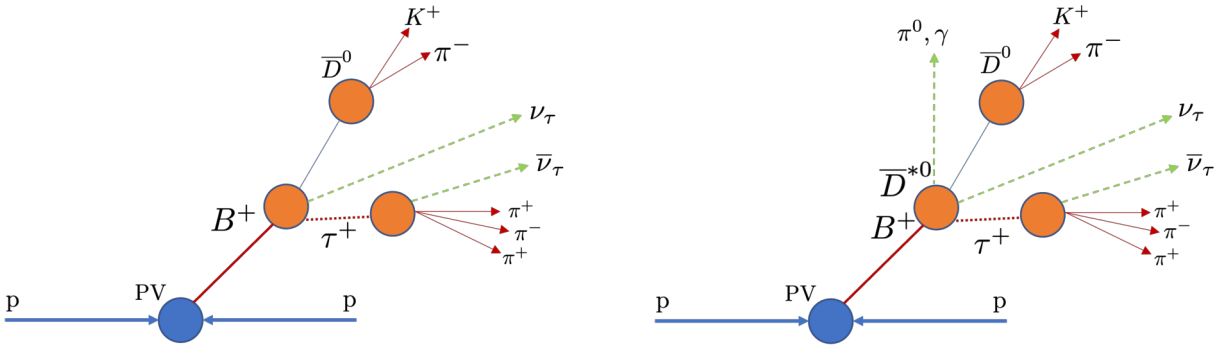

Figure 5.1: Topology of signal decays corresponding to the $\overline{D}^0$ decay chain (left) and $\overline{D}^{*0}$ (right).

The observable $\mathcal{R}(D^{(*)0})$ can be divided into two differentiated parts, the numerator and the denominator. The methods to obtain them are presented in the following.

The denominator of Eqs. 5.1 and 5.2, $\mathcal{B}(B^+ \to \bar{D}^{(*)0}\ell^+\nu_\ell)$, are obtained from external inputs that have been measured by CLEO, BaBar and Belle with good precision, as it can be seen from Tab. 5.1. Therefore, no further work is required towards this direction.

Regarding the numerator of Eqs. 5.1 and 5.2, $\mathcal{B}(B^+ \to \bar{D}^{(*)0}\tau^+\nu_\tau)$, a normalisation mode that share the same visible final states than the signal, four pions and one kaon, is introduced, so that systematics due to reconstruction effects are partially cancel out in the ratio. It is chosen the $B^+ \to \overline{D}^0 D_s^+$, with $D_s^+ \to 3\pi^\pm$. The branching fraction value for the $B^+ \to \overline{D}^0 D_s^+$ if found to be $(9.9 \pm 0.1) \times 10^{-3}$ [9], which corresponds to a precision of 10%; while for the $D_s^+ \to 3\pi^\pm$, the measured branching fraction value is (1.08±0.04)% [9], *i.e* a precision of about 4%. This strategy differs from the previous LHCb measurements

Decay	Experiment	$\mathcal{B}$ (rescaled)	Reference
$B^+ \to \overline{D}^0 \ell\nu$	CLEO	$2.13 \pm 0.13 \pm 0.17$	[143]
	BaBar	$2.16 \pm 0.08 \pm 0.12$	[61]
	Belle	$2.46 \pm 0.04 \pm 0.12$	[62]
	HFLAV average	$2.30 \pm 0.03 \pm 0.08$	[9]
$B^+ \to \overline{D}^{*0} \ell\nu$	CLEO	$6.20 \pm 0.20 \pm 0.26$	[144]
	BaBar tagged	$5.30 \pm 0.15 \pm 0.33$	[145]
	BaBar untagged	$5.00 \pm 0.08 \pm 0.31$	[146]
	HFLAV average	$5.58 \pm 0.07 \pm 0.21$	[9]

Table 5.1: Measurements from exclusive $B^+ \to \overline{D}^0 \ell\nu$ and $B^+ \to \overline{D}^{*0} \ell\nu$ braching fractions, and HFLAV average.

of hadronic $\mathcal{R}(D^{*-})$, where the $B^0 \to D^{*-} 3\pi^{\pm}$ was used. In this analysis, the similar $B^+ \to D^0 3\pi$ decay was discarded since its branching fraction is measured with very poor precision, with an uncertainty of almost 40% [9].

Taking into account the introduced measurement method, the target of the analysis become the coefficients:

$$\mathcal{K}(D^{(*)0}) = \frac{\mathcal{B}(B^+ \to \bar{D}^{(*)0} \tau^+ \nu_\tau)}{\mathcal{B}(B^+ \to \overline{D}^0 D_s^+) \times \mathcal{B}(D_s^+ \to \pi^+\pi^-\pi^+)}, \tag{5.3}$$

that can be expressed in terms of the signal and normalisation yields. These are obtained by performing separate fits to data, and further corrected by the relative efficiencies, considering as well the sum of the branching fractions of the τ^+ decay modes. This equivalence leads to:

$$\begin{aligned} \mathcal{K}(D^{(*)0}) &= \frac{N(B^+ \to \bar{D}^{(*)0} \tau^+ \nu_\tau)}{N(B^+ \to \overline{D}^0 D_s^+)} \\ &\times \frac{\varepsilon_{B^+ \to \bar{D}^0 D_s^+}}{\varepsilon^{\tau \to 3\pi\nu}_{B^+ \to \bar{D}^{(*)0}\tau^+\nu_\tau} \mathcal{B}(\tau \to 3\pi\nu) + \varepsilon^{\tau \to 3\pi\pi^0\nu}_{B^+ \to \bar{D}^{(*)0}\tau^+\nu_\tau} \mathcal{B}(\tau \to 3\pi\pi^0\nu)}, \end{aligned} \tag{5.4}$$

where $\mathcal{B}(\tau \to 3\pi\nu)$ and $\mathcal{B}(\tau \to 3\pi\pi^0\nu)$ are external inputs taken from [9].

Different strategies are followed in order to obtain the number of signal and normalisation candidates. On one hand, the signal candidates, $N(B^+ \to \bar{D}^{(*)0}\tau^+\nu_\tau)$, are extracted from a three dimensional template fit, and represents one of my fundamental contribution to the analysis. On the other hand, the number of normalisation candidates, $N(B^+ \to \overline{D}^0 D_s^+)$, is obtained from a one-dimensional unbinned fit to the $\overline{D}^0 D_s^+$ invariant mass, $m(\overline{D}^0 D_s^+)$.

Once the required yields are obtained, the $\mathcal{R}(D^{(*)0})$ ratios can be determined as:

$$\mathcal{R}(D^{(*)0}) = \mathcal{K}(D^{(*)0}) \left(\frac{\mathcal{B}(B^+ \to \overline{D}^0 D_s^+) \times \mathcal{B}(D_s^+ \to 3\pi^{\pm})}{\mathcal{B}(B^+ \to \bar{D}^{(*)0} \ell^+ \nu_\ell)} \right)_{ext.}, \tag{5.5}$$

where the branching fractions label with *ext.*, are taken from external inputs [9, 47].

In the succeeding, the structure in a nutshell of the present work is introduced. The methodology followed in this work is presented in Chap. 5. The selection and preparation of the real data and Monte Carlo samples used and its preparation are described in Chap. 6, where the events selection and and the corrections applied to the Monte Carlo samples are discussed. The studies of control samples are detailed in Chap. 7. Chap. 8 represents the main bulk of this work. It is presented the determination of the yield for the normalisation mode, the signal yield determination together with the fit model used for the extraction of the signal yields and the measurements of the signal branching fractions. Finally, $\mathcal{R}(D)$ and $\mathcal{R}(D^*)$ ratios, and therefore the main results, are given in Chap. 9. Systematic uncertainties are discussed in Chap. 10 and the final remarks and conclusions are summarised in Chap. 11.

5.2 Analysis workflow

The main strategy steps followed in the analysis are schematised in the workflow of Fig. 5.2. A description of the sequence is given in the following:

- **Selection** (Sec. 6.2). Inclusive $B \to \overline{D}^0\pi^+\pi^-\pi^+X$ events, with $\overline{D}^0 \to K^+\pi^-$, are selected using the `StrippingBu2D0TauNuForB2XTauNuAllLines` stripping line. In this line, three charged pions are required to form a good vertex (the τ vertex). It is also required a good vertex quality of the 3 pions and the $\overline{D}^0$, forming the B vertex. On top of that, two off-line selections are applied: a signal selection and a normalisation selection, optimised to select signal ($B^+ \to \overline{D}^0\tau^+\nu_\tau$ with $\tau^+ \to \pi^+\pi^-\pi^+\overline{\nu}_\tau$) and normalisation events, respectively. For normalisation, the $B^+ \to \overline{D}^0 D_s^+ (\to \pi^+\pi^-\pi^+)$ is chosen. As it was already introduced, this B^+ decay mode shares the same topology as the signal (both τ and $\overline{D}^0$ have a non-negligible lifetime) and its branching fraction is measured with much better precision than the other possible candidate, the $B^+ \to \overline{D}^0\pi^+\pi^-\pi^+$ decay mode:
  - $\mathcal{B}(B^+ \to \overline{D}^0 D_s^+) = 0.0090 \pm 0.0009$ [9]
  - $\mathcal{B}(D_s^+ \to \pi^+\pi^-\pi^+) = 0.0108 \pm 0.0004$ [9]
  - $\mathcal{B}(B^+ \to \overline{D}^0\pi^+\pi^-\pi^+) = 0.0056 \pm 0.0021$ [9]
- **Monte Carlo optimisation** (Sec. 6.3). After processing the Monte Carlo samples, and with the goal of describing the data as accurate as possible, some corrections need to be applied to the simulation. These include the re-weighting of PID, a correction on the resolution of the B and 3π vertices, B kinematics, event multiplicity, trigger efficiency and $B \to D^{(*)}$ form factors.
- **Computation of signal and normalisation efficiencies** (Sec. 6.4). The signal and normalisation efficiencies are computed using Monte Carlo simulation.

- **Study of control samples** (Chap. 7). Samples enriched in background events are produced by applying dedicated selections. These control samples are used to implement corrections to the simulation to improve the description of the data. Moreover, the correct understanding of the different components provide important help in constraining the final fits. In particular, control samples for the $B \to \overline{D}^0 D_s^+(X)$, and prompt $B \to \overline{D}^0 \pi^+\pi^-\pi^+ X$ events are studied, where X stands for possible unreconstructed particles.

- **Determination of the normalisation yield** (Sec. 8.1). The normalisation $B^+ \to \overline{D}^0 D_s^+$ yield is obtained from a fit to the $M(\overline{D}^0 D_s^+)$ invariant mass.

- **Determination of the signal yields** (Sec. 8.2). The $B^+ \to \overline{D}^0 \tau^+ \nu_\tau$ and $B^+ \to \overline{D}^{*0} \tau^+ \nu_\tau$ yields are determined from a 3-dimensional template fit on the q^2, tau decay time and the output of a multivariate algorithm distributions. The fit model is described in Sec. 8.2.1. This step is my main constribution to the analysis.

- **Measurement of signals branching fractions** (Sec. 8.3). Once the signals and normalisation yields are extracted, the $\mathcal{B}(B^+ \to \overline{D}^0 \tau^+ \nu_\tau)$ and $\mathcal{B}(B^+ \to \overline{D}^{*0} \tau^+ \nu_\tau)$ branching fractions can be determined. In order to obtain them, it is necessary to introduce the $\mathcal{B}(\tau^+ \to \pi^+\pi^-\pi^+\overline{\nu}_\tau)$,
$\mathcal{B}(\tau^+ \to \pi^+\pi^-\pi^+\pi^0\overline{\nu}_\tau)$, $\mathcal{B}(B^+ \to \overline{D}^0 D_s^+)$ and $\mathcal{B}(D_s^+ \to \pi^+\pi^-\pi^+)$ as external inputs.

- **Measurement of $\mathcal{R}(D^0)$ and $\mathcal{R}(D^{*0})$** (Chap. 9). The measured signals branching fractions are used to compute the LFU ratios $\mathcal{R}(D^0)$ and $\mathcal{R}(D^{*0})$ using the $\mathcal{B}(B^+ \to \overline{D}^0 \ell^+ \nu_\ell)$ and $\mathcal{B}(B^+ \to \overline{D}^{*0} \ell^+ \nu_\ell)$ branching fractions as external inputs.

- **Systematics** (Chap. 10). The main systematic uncertainties of this analysis are studied.

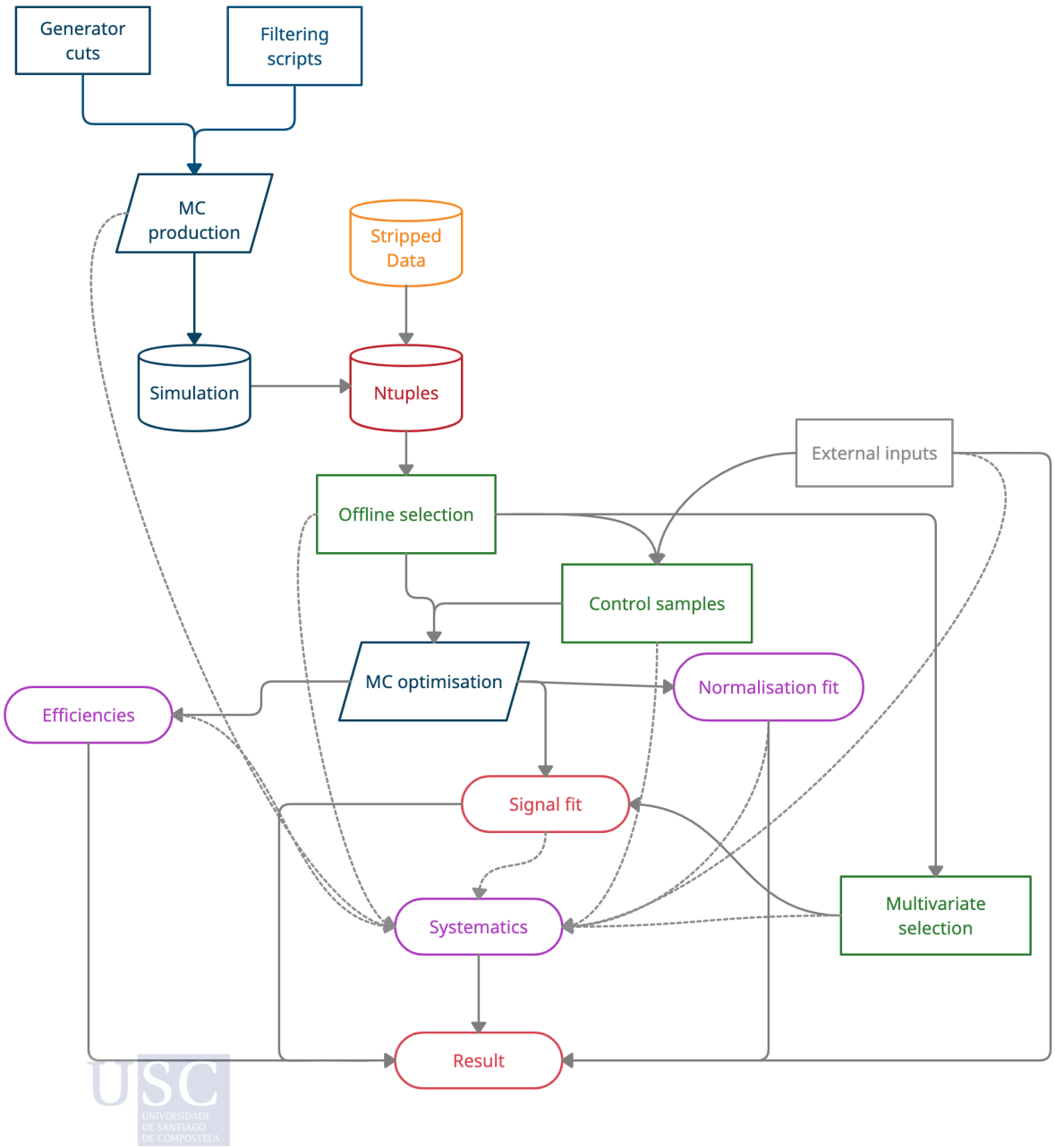

Figure 5.2: Workflow of the analysis.

6

Selection and preparation of data and Monte Carlo samples

Contents

6.1 Data and MC samples

This section describes the data and Monte Carlo samples used in this analysis.

6.1.1 Data samples

The analysis presented in this thesis makes use of a LHC Run 2 data sample of proton-proton collisions collected by the LHCb detector, during the years 2016, 2017 and 2018, at a centre-of-mass energy of 13 TeV, corresponding to an integrated luminosity of $5.4\,\text{fb}^{-1}$.

6.1.2 Monte Carlo samples

A large number of MC samples are needed in order to understand and model correctly the background composition present in the final sample (the one passing all selection requirements). Moreover, simulated events are used to compute efficiencies, or as input for MultiVariate Analysis (MVA) algorithms.

In order to produce the large number of events required, several simulation options were applied depending on the amount of events needed and the type of simulated decay (signal, background...). On one hand, filtered Monte Carlo decay productions save disk space by only writing out events that pass particular trigger/stripping decisions. On the other hand, in some large productions the ReDecay algorithm [147] is used. It speeds up the simulation by re-using the underlying event that does not participate in the simulated decay.

It took several years to gather all simulated samples needed to carry out analysis documented here. The full list of simulation samples is given in Tab. 6.1.

6.2 Selection of events

The selection of signal and normalisation events is divided in several stages:

1. Events are obtained from a specific stripping line.
2. Cleaning pre-selection and trigger requirements are applied.
3. Events are required to pass either the signal or the normalisation selection criteria.

In the following, the cuts applied at the different selection stages are detailed.

Decay(s)	**Simulation option**	$\mathbf{N_{sim.}}$ (magUp/magDown)
$B^+ \to \overline{D}^0\tau^+(\to \pi^+\pi^\pm\pi^+\overline{\nu}_\tau)\nu_\tau$	Sim09i filtered	1001755 / 10121572
$B^+ \to \overline{D}^0\tau^+(\to \pi^+\pi^-\pi^+\pi^0\overline{\nu}_\tau)\nu_\tau$	Sim09i filtered	754189 / 773537
$B^+ \to \overline{D}^{*0}\tau^+(\to \pi^+\pi^-\pi^+\pi^0\overline{\nu}_\tau)\nu_\tau$	Sim09i filtered	1001245 / 1007497
$B^+ \to \overline{D}^{*0}\tau^+(\to \pi^+\pi^-\pi^+\pi^0\overline{\nu}_\tau)\nu_\tau$	Sim09i filtered	756863 / 759234
$B^0 \to D^{*-}\tau^+(\to \pi^+\pi^-\pi^+\overline{\nu}_\tau)\nu_\tau$	Sim09e ReDecay filtered	687279 / 687279
$B^0 \to D^{*-}\tau^+(\to \pi^-\pi^+\pi^-\pi^0\overline{\nu}_\tau)\nu_\tau$	Sim09c Redecay	20039288 /20039288
$B^+ \to D^{**}\tau\nu_\tau$	Sim09k Redecay filtered	286712 / 288831
$\overline{B}^0 \to D^{**}\tau\nu$	Sim09k ReDecay filtered	255781 / 250003
$B_s^0 \to D^{**}\tau\nu$	Sim09k ReDecay filtered	288831 / 286712
$B^+ \to \overline{D}^0 D_s^+(\to \pi^+\pi^-\pi^+)$	Sim09i filtered	520804 / 520972
$B^+ \to \overline{D}^0\pi^+\pi^-\pi^+$	Sim09i filtered	284698 / 262503
$B^+ \to \overline{D}^0 X_c X'$	Sim09h ReDecay filtered	1288010 / 1853494
$\overline{B}^0 \to \overline{D}^0 X_c X'$	Sim09h ReDecay filtered	10754686 / 11004407
$B_s^0 \to \overline{D}^0 X_c X'$	Sim09h ReDecay filtered	2429723 / 3501039
prompt $B^+ \to \overline{D}^0\pi^+\pi^-\pi^+ X$	Sim09i ReDecay filtered	14240203 / 14230745
prompt $B^0 \to \overline{D}^0\pi^-\pi^+\pi^- X$	Sim09i ReDecay filtered	17818266 / 17890479
prompt $B_s^0 \to D^0\pi^-\pi^+\pi^- X$	Sim09i ReDecay filtered	1813758 / 1823421
$\overline{D}^0$ and 3π not from same B	Sim09i ReDecay filtered	12592113 / 12503618

Table 6.1: Simulation samples used in this analysis. The D^{**} symbol represents any of the $D_2^*(2460)$, $D_1(2420)$, $D_1'(2430)$, $D_0^*(2300)$, $D_{s1}(2536)^+$ or $D_{s2}^*(2573)^+$ mesons. $N_{sim.}$ corresponds to the number of events saved in disk.

6.2.1 Stripping selection

The first offline selection requirement that data and simulated events are forced to pass is comprised in a stripping line. In particular, this analysis emoployes the `StrippingBu2D0TauNuForB2XTauNuAllLines` stripping line, versions `28r2`, `29r2` and `34`, for the years 2016, 2017 and 2018, respectively. The stripping cuts are applied in the DaVinci framework, with the goal of forming a B^+ candidate by combining a $\overline{D}^0 \to K^+\pi^-$ and $\tau^+ \to \pi^+\pi^-\pi^+\overline{\nu}_\tau$ candidates. The complete set of cuts applied in this line is shown in Tab. 6.2, where:

- DOCA (particle$_i$, particle$_j$): the distance of closest approach between the tracks associated to particle$_i$ and particle$_j$.
- DIRA (particle, PV): the cosine of the angle between the particle momentum and the direction given by the position of the best PV and the particle decay vertex. This quantity is illustrated in Fig. 6.1.
- Vertex χ^2/DOF: the χ^2 per degrees of freedom of the fit combining the tracks to form the vertex.
- PV distance χ^2: the χ^2 separation between the particle vertex considered and the PV.
- χ^2-impact parameter: the χ^2 distance of a given particle to the PV.
- Ghost Probability: probability of a track to be reconstructed by a random combination of hits, not corresponding to a real particle passage.
- Track PROB. χ^2: the χ^2 probability of the track fit.
- Track χ^2/DOF: the χ^2 per degrees of freedom of the fit to the long track to which the particle is associated.
- PID$_\alpha(x)$: this quantity, which was introduced in Sec. 3.2.2, is given by: $\text{PID}_\alpha(x) = \log\mathcal{L}(\alpha) - \log\mathcal{L}(\pi)$. It corresponds to a measurement of the compatibility of a given track, x, to be identified as a particle α, where α is any of the particles K, μ, p or e.
- min[m($\pi^+\pi^-$)]: the minimum of the mass of the two pions with opposite sign from the 3π of the τ.

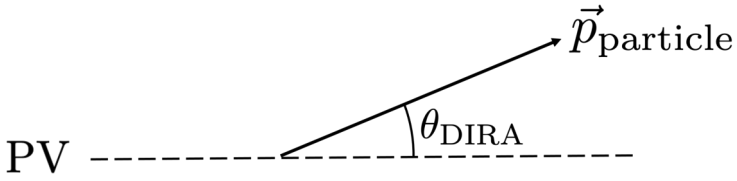

Figure 6.1: Illustration of DIRA.

Cut	**Value**
B^+	
$m(D^0 3\pi)$	2.7-5.6 GeV/c^2
DOCA	< 0.15 mm
DIRA	> 0.995
$\overline{D}^0$	
$\lvert m(K\pi) - m(D^0)_{PDG}\rvert$	< 40 MeV/c^2
Vertex χ^2/DOF	< 10
DIRA	> 0.995
PV distance χ^2	> 36
p_T	> 1.2 GeV/c
Min. $\chi^2_{\text{IP,PV}}$	> 10
DOCA$_{K\pi}$	< 0.5 mm
DOCA$_{K\pi}$ χ^2	< 15
τ	
DIRA	> 0.99
m(3π)	0.4-3.5 GeV/c^2
Max. DOCA	< 0.15 mm
min[m($\pi^+\pi^-$)]	< 1.67 GeV/c^2
At least two pions p_T	> 0.3 GeV/c^2
Vertex χ^2	< 25
At least two pions with PV χ^2_{IP}	> 5
$\overline{D}^0$ daughters	
Track p	> 2 GeV/c
Track ghost Probability	< 0.4
Track PROB. χ^2	$> 10^{-8}$
Min. $\chi^2_{\text{IP,PV}}$	> 10
$p_T(K)$	> 1.5 GeV/c
$p_T(\pi)$	> 0.25 GeV/c
K track χ^2/DOF	< 30
π track χ^2/DOF	< 3
K PIDK	> 3
π PIDK	< 50
τ daughter pions	
p_T	> 0.25 GeV/c
PV χ^2_{IP}	> 4
Track χ^2/DOF	< 4
PIDK	< 8
Ghost probability	< 0.4

Table 6.2: List of cuts included in the `StrippingBu2D0TauNuForB2XTauNuAllLines` stripping line. $m(D^0)_{PDG}$ corresponds to the best known value of the D^0 meson mass taken from the Particle Data Group (PDG) [9].

The $\overline{D}^0$ daughters are selected by applying requirements related with the transverse momentum, p_T, of both particles, small track ghost probability, distance from the PV, track quality and PID. Then, the $K^+\pi^-$ system is formed by requirements related with the vertex quality, distance to the PV, DIRA and DOCA. Finally, a $\overline{D}^0$ candidate is required to have a mass close to its best-known mass [9].

Regarding the $\tau \to 3\pi^\pm\nu$ system[1], all the daughter pions are required to have a minimum p_T, large impact parameter with respect to the PV, track quality, low ghost probability and PID requirements. Then, the τ candidate is formed by selecting a range on the reconstructed mass of the three pions, vertex quality, and applying DIRA and DOCA cuts and a requirement on the mass of the opposite-sign pions with minimum mass.

Finally, the B^+ candidate is formed by combining the aforementioned $\overline{D}^0$ and τ candidates. Cuts on the mass of $\overline{D}^0\tau$ system, DIRA and DOCA are applied.

6.2.2 Preselection

After the stripping selection, a set of cleaning cuts are applied aiming for the suppression of background events. The requirements can be summarised as follows:

- The B and 3π vertices are required to be displaced from the PV in the transverse direction.
- The impact parameter χ^2 of the pions forming the τ vertex must be incompatible with being produced at the PV.
- The PV of the $\overline{D}^0$ and τ candidates must be the same.
- A loose requirement on the momentum and pseudo-rapidity of the candidate tracks is applied to synchronise the selection with the `PIDCalib` [148] requirements.

The complete list of the offline preselection cuts is shown in Tab. 6.3, where:

- `ProbNNk`: bayesian probability of the particle of being a kaon[2]
- `ProbNNpi`: bayesian probability of the particle of being a pion.
- nSPDHits: number of hits in the SPD detector.

[1]The $3\pi^\pm$ stands for $\pi^+\pi^-\pi^-$ throughout, if nothing else is indicated.
[2]See Sec. 6.3.1 for more information about the PID variables considered in this analysis.

Cut	Value
3π vertex transverse distance to PV *	> 0.2 mm
$\chi^2_{\rm IP}$(PV) of pions from 3π vertex *	> 15
B vertex transverse distance to PV	> 0.6 mm
τ vertex χ^2	< 16
tau_pions_ProbNNpi	> 0.2
D0_K_ProbNNk	> 0.4
D0_pi_ProbNNpi	> 0.4
$\lvert z_{\rm PV}(D^0) - z_{\rm PV}(3\pi)\rvert$	< 0.0001 mm
All tracks momentum	$[2, 200]$ GeV/c
All tracks η	$[1.5, 5]$
nSPDHits	≤ 450

Table 6.3: List of cuts applied in the preselection of events. The cuts marked with * have been applied at the DaVinci stage to highly reduce the size of the output ntuples.

6.2.3 Trigger selection

The trigger selection requires the event to be selected at the three trigger levels: the hardware `L0` level and two different software High Level trigger, namely levels 1 and 2. All the trigger requirements, which are gathered in Tab. 3.18, can be briefly introduced as follows:

- `L0` level : the event is required to be triggered on signal (TOS), with the `L0` hadronic line, or independently of the signal part within the event signal (TIS).
- `Hlt1` level: the event is required to pass the `B_Hlt1TrackMVADecision_TOS` line.
- `Hlt2` level: the event must pass one of the topological lines [149].

Trigger level	Trigger lines
L0	`B_L0HadronDecision_TOS`
	`OR B_L0Global_TIS`
Hlt1	`B_Hlt1TrackMVADecision_TOS`
Hlt2	`B_Hlt2Topo2BodyDecision_TOS`
	`OR B_Hlt2Topo3BodyDecision_TOS`
	`OR B_Hlt2Topo4BodyDecision_TOS`

Table 6.4: Trigger requirements on the events used in this analysis. The total requirement corresponds to the AND of the lines at the three trigger levels.

6.2.4 The distance detachment criterion

As it was mentioned before, the reconstructed final state of the signals in this analysis consists on a D^0 meson and three charged pions. Fig. 6.2 shows the topology for both signals decays. By far, the largest background contribution is due to inclusive B decays with the same signal final state is due to inclusive $B \to \overline{D}^0\pi^+\pi^-\pi^+X$ *prompt* decays, being X any possible unreconstructed particle(s), where the three pions are produced at the B vertex, *i.e.* no mediated by any particle with non-negligible lifetime (as for instance D mesons). The topology of this kind of decays is displayed in Fig. 6.3, to be compared with Fig. 6.2, where it can be intuited how convenient it will be to introduce the distance detachment criterion.

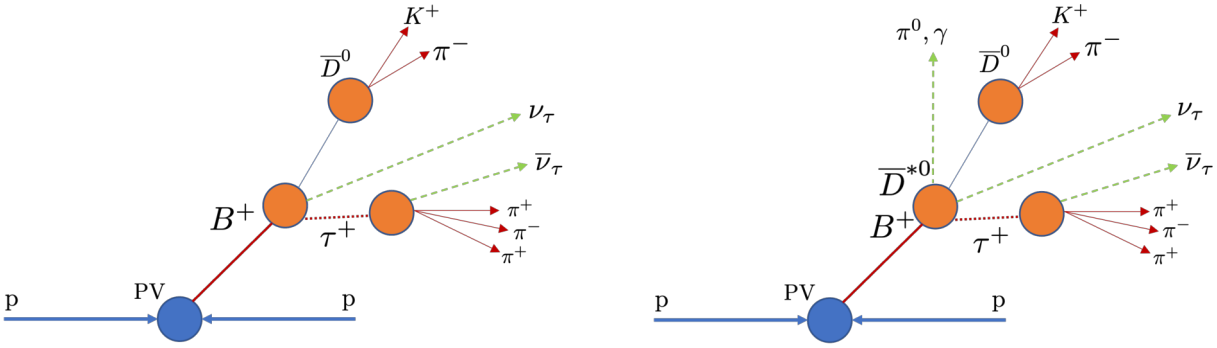

Figure 6.2: Topology of signal decays corresponding to the D^0 decay chain (left) and D^{*0} (right).

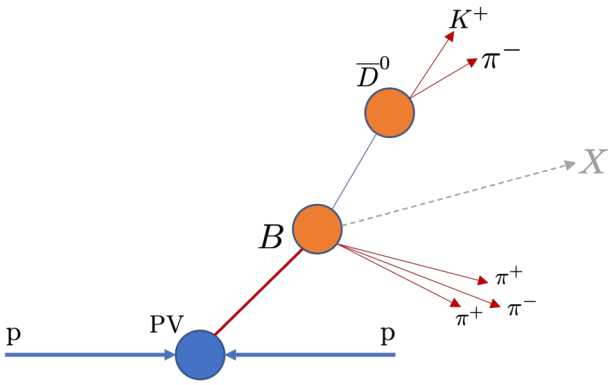

Figure 6.3: Topology of the most abundant background: the *prompt* decay, where X corresponds to possible unreconstructed particles.

This *prompt* background can be handled using information about the distance between the τ and B vertices. In particular, the excellent resolution of the VELO allows to apply a cut on this vertices distance divided by its uncertainty:

$$\Delta z/\sigma_z = \frac{z_{3\pi} - z_B}{\sqrt{\sigma_{3\pi} + \sigma_B}} \equiv \frac{z_{3\pi} - z_B}{\sigma_z}, \tag{6.1}$$

being z the direction along the beam. The cut is used to highly suppress this *prompt* contribution. In Eq. 6.1, $\sigma_{3\pi}$ (σ_B) is the uncertainty of the z-component of the 3π (B) vertex.

The distribution of $\Delta z/\sigma_z$ is shown in Fig. 6.4, for *prompt* inclusive $B^+ \to \overline{D}^0\pi^+\pi^-\pi^+X$ and signal $B^+ \to \overline{D}^0\tau^+\nu_\tau$, with $\tau^+ \to \pi^+\pi^-\pi^+\overline{\nu}_\tau$ decays. This detachment requirement has been introduced in the Run 1 hadronic $\mathcal{R}(D^*)$ measurement [43,44]. In this analysis, the same criterion, $\Delta z/\sigma_z > 4$ is applied.

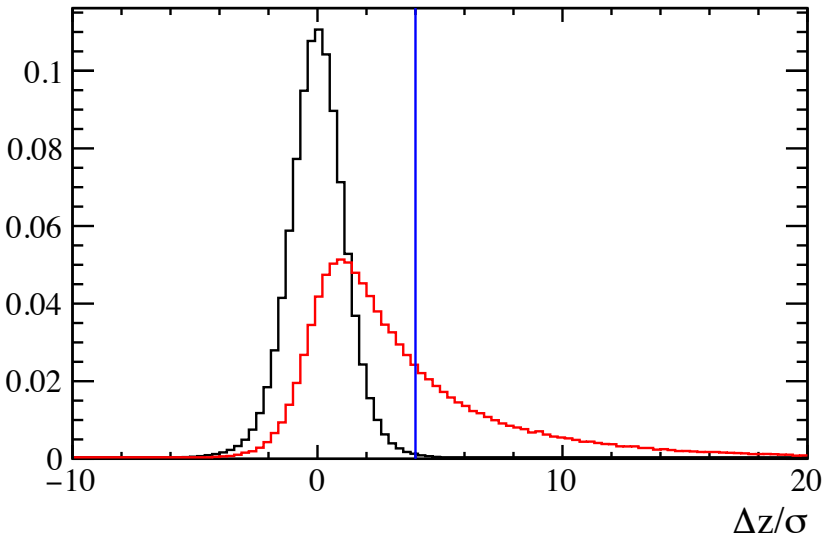

Figure 6.4: Distance between the τ and B vertices along the beam direction (z) divided by its uncertainty for inclusive *prompt* $B^- \to \overline{D}^0\pi^-\pi^+\pi^-X$ (black) and signal $B^+ \to \overline{D}^0\tau^+\nu_\tau$, with $\tau^+ \to \pi^+\pi^-\pi^+\overline{\nu}_\tau$, (red) decays. The blue vertical line indicates the $\Delta z/\sigma_z > 4$ criterion applied in this analysis. The distributions are normalised to the same area.

Once the distance detachment cut is applied, the main background contribution comes from doubly-charmed $B \to \overline{D}^0 DX$ decays, being the inclusive $B \to \overline{D}^0 D_s^+ X$ decays, by far, the main source of background in the analysis, where the D_s^+ meson decays inclusively into 3 pions. A specific control sample study will be performed in order to model this component, in Sec. 7.1.

6.2.5 Vertex Isolation

Charged particles different than the ones of a signal candidate can belong to the decay. One common case is that these extra tracks point to one of the candidate vertices, thus information on the track IP-χ^2 with respect to the vertices is used to build a vertex-isolation algorithm. Background events of this type are inclusive $B \to \overline{D}^0 DX$ decays. Here, the D symbol stands for either a D_s^+, a D^+ or a D^0 meson. Then, D_s^+ and D^+ mesons can further decay into a 5-prong final state, D_s^+ or $D^+ \to \pi^+\pi^-\pi^+\pi^-\pi^+X$. The D^0 can decay into a 4-prong final state, as for instance $K^-\pi^+\pi^-\pi^+X$ or $\pi^-\pi^+\pi^-\pi^+X$. A characteristic feature of these events is that extra tracks in these candidates must point to the τ vertex. In other background events, the extra tracks point to the B vertex, this is the case of $B \to \overline{D}^0 DK^\pm$ or $B \to \overline{D}^0 D\pi^\pm$ decays. These events can be identified and suppressed by looking at the impact parameter χ^2 of the track to the vertex, $\chi^2_{\rm IP}(\tau)$ and $\chi^2_{\rm IP}(B)$ for the τ and B vertices, respectively. For illustration, Fig. 6.5 shows the distribution of $\chi^2_{\rm IP}$ of extra tracks for signal $B^+ \to \overline{D}^0\tau^+\nu_\tau$ and background $B \to \overline{D}^0 D_s^+ X$, decays. Comparing the distributions for background and signal, it can be drawn the conclusion that the $\chi^2_{\rm IP}$ parameter of the extra track provides enough information to distinguish both kind of decays.

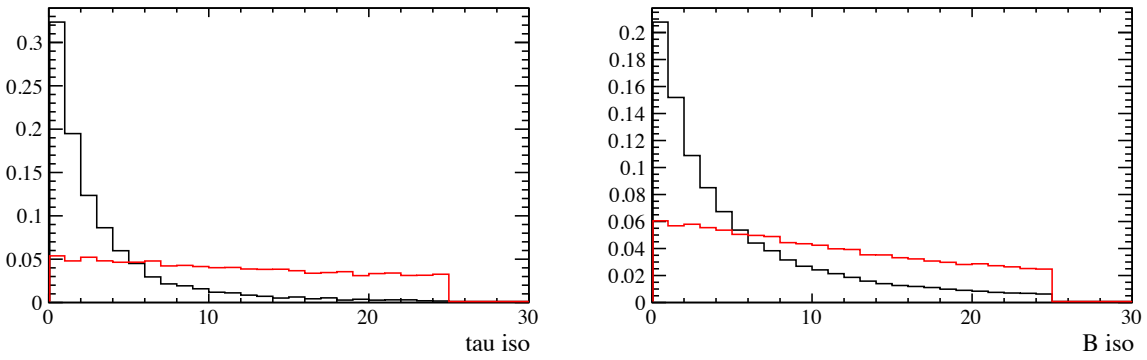

Figure 6.5: Distributions of the $\chi^2_{\rm IP}$ to the τ (left) and B (right) vertices of extra tacks for signal $B^+ \to \overline{D}^0\tau^+\nu_\tau$, with $\tau^+ \to \pi^+\pi^-\pi^+\overline{\nu}_\tau$, (red) and background $\overline{B}^0 \to \overline{D}^0 D_s^+ X$ (black) decays. On the left plot, the D_s^+ meson decays exclusively into $5\pi^\pm$. On the right plot, there is an extra charged particle produced at the B vertex in the $\overline{B}^0 \to \overline{D}^0 D_s^+ X$ decay. The extra tracks have a p_T larger than 250 MeV/c and a $\chi^2_{\rm IP}$ with respect to the candidate PV larger than 4. The distributions are normalised to the same area for comparison.

A dedicated vertex isolation algorithm has been developed for the Run 1 hadronic $\mathcal{R}(D^*)$ analysis [43, 44] that is applied in this analysis. The next two variables are introduced aiming for the suppression of background events containing additional tracks belonging to the candidate decay chain:

- $N^\tau_{iso}(p_T > 250; \chi^2_{\rm IP}({\rm PV}) > 4; \chi^2_{\rm IP}(\tau) < 25)$: Number of additional tracks with $p_T >$

250 MeV/c, an impact parameter χ^2 with respect to the PV greater than 4 and an impact parameter χ^2 with respect to the τ vertex smaller than 25.

- $N^B_{iso}(p_T > 250; \chi^2_{\rm IP}({\rm PV}) > 4; \chi^2_{\rm IP}(B) < 25)$: Number of additional tracks with $p_T >$ 250 MeV/c, an impact parameter χ^2 with respect to the PV greater than 4 and an impact parameter χ^2 with respect to the B vertex smaller than 25.

The distribution of the isolation variables $N^\tau_{iso}(p_T > 250; \chi^2_{\rm IP}({\rm PV}) > 4; \chi^2_{\rm IP}(\tau) < 25)$ and $N^B_{iso}(p_T > 250; \chi^2_{\rm IP}({\rm PV}) > 4; \chi^2_{\rm IP}(B) < 25)$ is shown in Fig. 6.6 for signal $B^+ \to \overline{D}^0\tau^+\nu_\tau$, with $\tau^+ \to \pi^+\pi^-\pi^+\overline{\nu}_\tau$, and background $B^0 \to \overline{D}^0 D_s^+ X$ events.

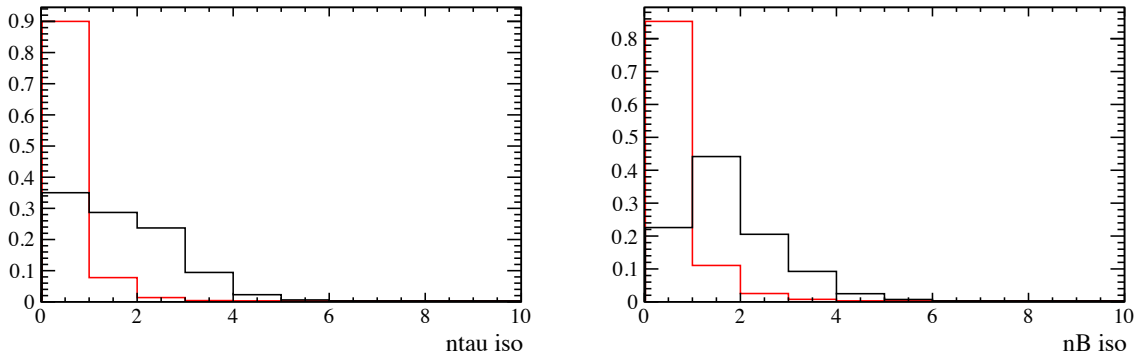

Figure 6.6: Distributions of the isolation variables $N^\tau_{iso}(p_T > 250; \chi^2_{\rm IP}({\rm PV}) > 4; \chi^2_{\rm IP}(\tau) <$ 25) (left) and $N^B_{iso}(p_T > 250; \chi^2_{\rm IP}({\rm PV}) > 4; \chi^2_{\rm IP}(B) < 25)$ (right) for signal $B^+ \to \overline{D}^0\tau^+\nu_\tau$, with $\tau^+ \to \pi^+\pi^-\pi^+\overline{\nu}_\tau$ (red), and background $B^0 \to \overline{D}^0 D_s^+ X$ events (black).

From the signal distribution of Fig. 6.6, it follows that isolated events must fulfill the requirements:

$$\begin{aligned} N^\tau_{iso}(p_T > 250; \chi^2_{\rm IP}({\rm PV}) > 4; \chi^2_{\rm IP}(\tau) < 25) &= 0 \ \text{ and} \\ N^B_{iso}(p_T > 250; \chi^2_{\rm IP}({\rm PV}) > 4; \chi^2_{\rm IP}(B) < 25) &= 0\ . \end{aligned} \tag{6.2}$$

However, an extra complication comes from the fact that, in this analysis, the $\overline{D}^0$ candidate can come from a $D^{*-} \to \overline{D}^0\pi^-$ decay, and the slow pion from the D^{*-} decay can escape the requirements of Eq. 6.2. Events of this class are removed by looking for extra tracks compatible with being a slow pion from a $D^{*-} \to \overline{D}^0\pi^-$ decay chain. Tracks with impact parameter χ^2 smaller than 25 with respect to the B vertex and without requirements on the $\chi^2_{\rm IP}({\rm PV})$ and p_T are selected. These tracks must have the correct charge. Then, the distribution of the $m(\overline{D}^0\pi^-) - m(\overline{D}^0)$ for extra tracks passing the requirements of Eq. 6.2 is shown in Fig. 6.7. A D^{*-} veto is applied by requiring the invariant mass to be out of the range [143,148] MeV/c^2. In addition, this D^{*-} reconstruction can be used to split the data into $\overline{D}^0$ and D^{*-} samples, as it is done for the $B \to \overline{D}^0 D_s^+(X)$ control sample study Sec. 7.1.

The vertex isolation criteria just presented are gathered in Tab. 6.5, and signal candidates are required to pass them.

Variable	**Requirement**
$N^{\tau}_{iso}(p_T > 250; \chi^2_{\rm IP}({\rm PV}) > 4; \chi^2_{\rm IP}(\tau) < 25)$	$= 0$
$N^{B}_{iso}(p_T > 250; \chi^2_{\rm IP}({\rm PV}) > 4; \chi^2_{\rm IP}(B) < 25)$	$= 0$
D^{*+} veto: $m(D^0\pi^+) - m(D^0)$	out of range [143,148] MeV/c^2

Table 6.5: Vertex isolation requirements applied to select signal candidates.

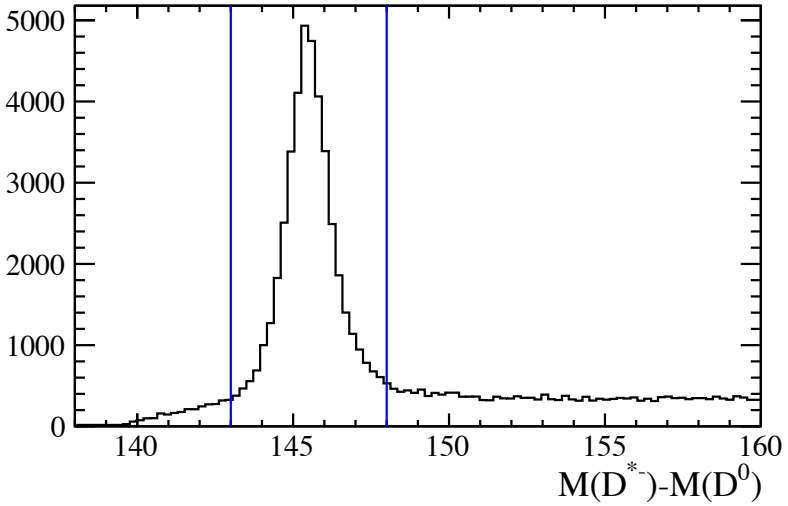

Figure 6.7: Invariant mass distribution $m(\overline{D}^0\pi^-) - m(\overline{D}^0)$ from data obtained by adding a track with the right charge to the $\overline{D}^0$ candidate. The events shown have already passed the isolation requirements of Eq. 6.2. The applied D^{*-} veto is shown by the two vertical blue lines.

6.2.6 Reconstruction of signal events

In the signal decay chain two neutrinos are present but not reconstructed, leading to a challenging signal event reconstruction. However, since the vertices of the B^+ and the τ^+ are measured, the flight direction together with the known masses make possible to obtain the momenta, in the laboratory frame, up to two 2-fold ambiguities. An illustration of the namely angles can be seen in Fig. 6.8.

Since both the τ^+ and the B^+ have a neutrino in the decays chains that is invisible to the detector, the momentum of the particle has to be reconstructed without the neutrino information. If p_τ is the 4-momenta of the original particle, p_ν is the neutrino momentum and p_x is the sum of all the other products. Following the momentum conservation

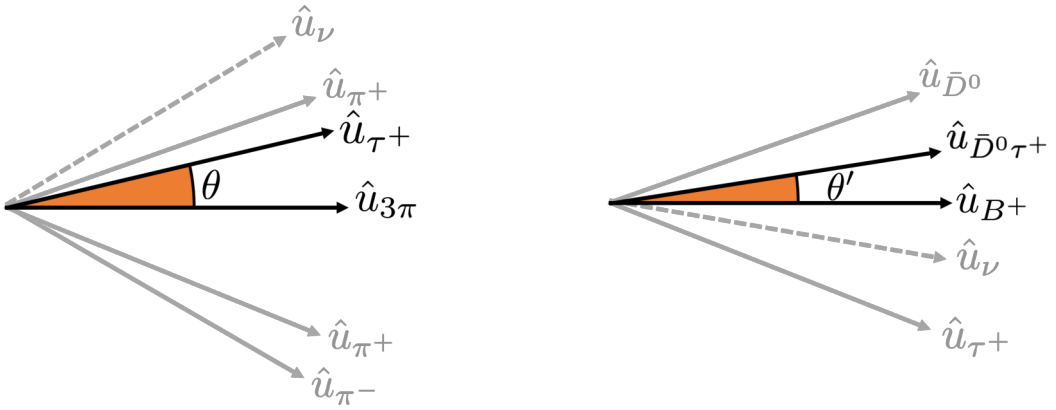

Figure 6.8: Illustration of the angles between the 3π system and the τ directions (left) and between the $D^0\tau$ system and the B^+ directions (right).

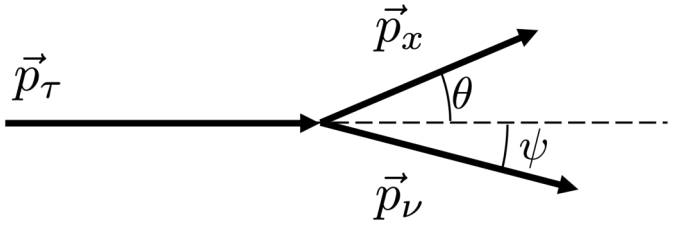

Figure 6.9: Illustration of the $\tau \to x\nu$ decay angles.

schematised in Fig. 6.9:

$$\begin{aligned} |\vec{p}_\tau| &= |\vec{p}_x|\cos\theta + |\vec{p}_\nu|\cos\psi \\ |\vec{p}_x|\sin\theta &= |\vec{p}_\nu|\sin\psi \end{aligned} \tag{6.3}$$

where θ and ψ corresponds to the angles that $|\vec{p}_\tau|$ forms with the $|\vec{p}_x|$ and $|\vec{p}_\nu|$ vectors. If now the invariant mass is introduced, together with the 4-moment equivalence $p_\tau^2 = (p_x + p_\nu)^2$:

$$m_\tau^2 = p_x^2 + p_\nu^2 + 2(p_x \cdot p_\nu) = m_x^2 + 2E_x|\vec{p_\nu}| - 2|\vec{p_x}\vec{p_\nu}|\cos(\theta+\psi). \tag{6.4}$$

Then, introducing the momenta relations of Eq. 6.3 in Eq. 6.4, the last term can be written as:

$$\begin{aligned} |\vec{p}_x||\vec{p}_\nu|\cos(\theta+\psi) &= |\vec{p}_x||\vec{p}_\nu|\cos\theta\cos\psi - |\vec{p}_x||\vec{p}_\nu|\sin\theta\sin\psi = \\ &= |\vec{p}_x|\cos\theta|\Big(|\vec{p}_\tau| - |\vec{p}_x|\cos\theta\Big) - |\vec{p}_a|^2\sin^2\theta = |\vec{p}_x||\vec{p}_\tau|\cos\theta - |\vec{p_x}|^2. \end{aligned} \tag{6.5}$$

Now, the Eq. 6.4 equivalence can be expressed as:

$$m_\tau^2 = p_x^2 + p_\nu^2 + 2(p_x \cdot p_\nu) = m_x^2 + 2E_x|\vec{p_\nu}| - 2\Big(|\vec{p_x}||\vec{p_\nu}|\cos\theta - |\vec{p_x}|^2\Big). \tag{6.6}$$

From relation $\vec{p}_\nu = \vec{p}_\tau - \vec{p}_x$, it is derived for the neutrino momenta:

$$|\vec{p}_\nu|^2 = |\vec{p}_\tau|^2 + |\vec{p}_x|^2 - 2|\vec{p}_\nu||\vec{p}_x|\cos\theta. \tag{6.7}$$

Now, the combination of the Eqs. 6.6 and 6.7 leads to a quadratic equation without information from the neutrino:

$$(E_x^2 - |\vec{p}_x|^2\cos^2\theta)|\vec{p}_\tau|^2 - (m_\tau^2 + m_x^2)|\vec{p}_x|\cos\theta|\vec{p}_\tau| + m_\tau^2|\vec{p}_x|^2 - \frac{1}{4}(m_\tau^2 - m_x^2)^2 = 0. \tag{6.8}$$

In the reconstruction of $B^+ \to \overline{D}^0\tau^+\nu$ decays, the B^+ line of flight is obtained by the unit vector joining the B^+ vertex to the PV. Subsequently, τ lepton line of flight direction is given by the line joining the 3 prong pions vertex of the τ decay and the B^+ vertex. Then, the τ momentum in the laboratory frame in obtained from Eq. 6.8, in units where $c = 1$ as:

$$|\vec{p}_\tau| = \frac{(m_{3\pi}^2 + m_\tau^2)|\vec{p}_{3\pi}|\cos\theta \pm E_{3\pi}\sqrt{(m_\tau^2 - m_{3\pi}^2)^2 - 4m_\tau^2|\vec{p}_{3\pi}|^2\sin^2\theta}}{2(E_{3\pi}^2 - |\vec{p}_{D^0\tau}|^2\cos^2\theta)}, \tag{6.9}$$

where θ is the angle between the 3π system and the τ line of flight; $m_{3\pi}$, $|\vec{p}_\tau|$ and $E_{3\pi}$ are the invariant mass, 3-momentum and energy of the 3π system, respectively; and m_τ is the known τ mass. The ambiguity is resolved by tuning the θ value, so that the argument of the square root of Eq. 6.9 is vanished. This single solution corresponds to the maximum value for the opening angle between the 3π system and the direction of the τ candidate, leading to:

$$\theta_{max} = \arcsin\left(\frac{m_\tau^2 - m_{3\pi}^2}{2m_\tau|\vec{p}_{3\pi}|}\right). \tag{6.10}$$

And subsequently, the value of the τ momentum is estimated as $|\vec{p}_\tau| = |\vec{p}_\tau(\theta_{max})|$:

$$|\vec{p}_\tau| \approx \frac{(m_{3\pi}^2 + m_\tau^2)|\vec{p}_{3\pi}|\cos\theta_{max}}{2(E_{3\pi}^2 - |\vec{p}_{3\pi}|^2\cos^2\theta_{max})}. \tag{6.11}$$

The distribution of the τ momentum and its resolution is shown in Fig. 6.10 and Fig. 6.11, respectively, for $B^+ \to \overline{D}^0\tau^+\nu_\tau$ and $B^+ \to \overline{D}^{*0}\tau^+\nu_\tau$ decays, with $\tau^+ \to \pi^+\pi^-\pi^+\overline{\nu}_\tau$.

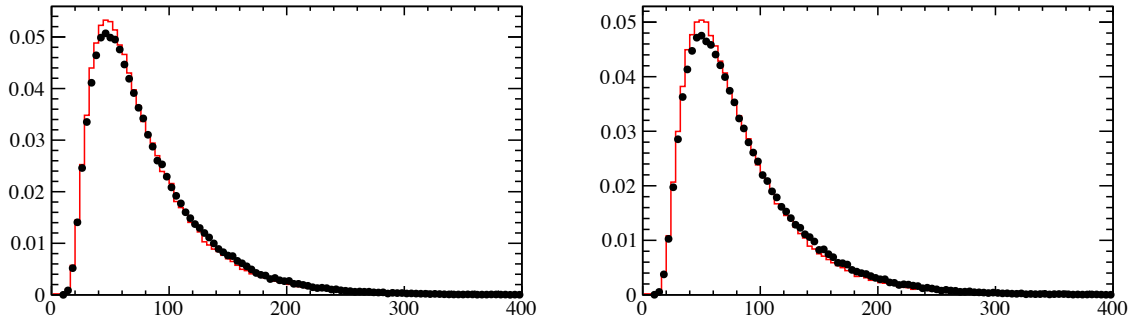

Figure 6.10: Distribution of the τ momentum estimated (black) and generated (red) for $B^+ \to \overline{D}^0\tau^+\nu_\tau$ (left) and $B^+ \to \overline{D}^{*0}\tau^+\nu_\tau$ (right) decays, with $\tau^+ \to \pi^+\pi^-\pi^+\overline{\nu}_\tau$.

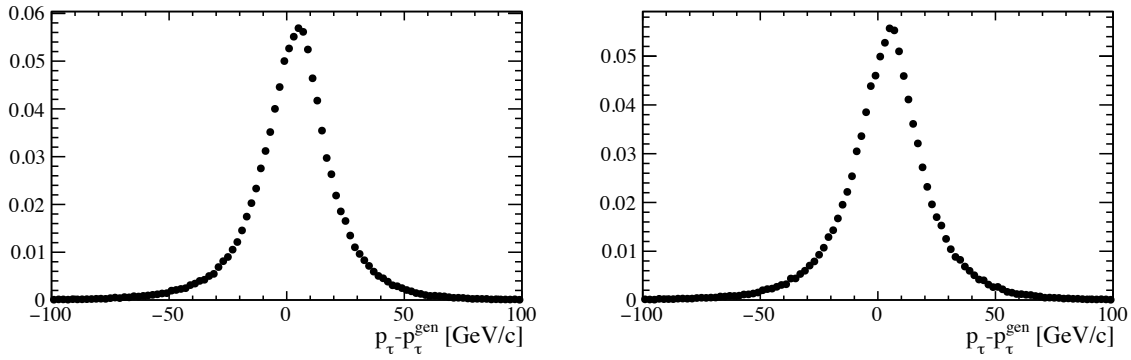

Figure 6.11: Distribution of the τ momentum resolution $p_\tau - p_\tau^{gen}$ for $B^+ \to \overline{D}^0\tau^+\nu_\tau$ (left) and $B^+ \to \overline{D}^{*0}\tau^+\nu_\tau$ (right) decays, with $\tau^+ \to \pi^+\pi^-\pi^+\overline{\nu}_\tau$.

Once the τ momentum, $|\vec{p}_\tau|$, is estimated, the same procedure can be applied to reconstruct the B^+ momentum $|\vec{p}_B| = |\vec{p}_B(\theta'_{max})|$, and so:

$$|\vec{p}_B| = \frac{(m^2_{D^0\tau} + m^2_B)|\vec{p}_{D^0\tau}|\cos\theta' \pm E_{D^0\tau}\sqrt{(m^2_B - m^2_{D^0\tau})^2 - 4m^2_B|\vec{p}_{D^0\tau}|^2\sin^2\theta'}}{2(E^2_{D^0\tau} - |\vec{p}_3\pi|^2\cos^2\theta')}, \quad (6.12)$$

where θ' is the angle between the $D^0\tau$ system and the B line of flight; $m_{D^0\tau}$, $|\vec{p}_{D^0\tau}|$ and $E_{D^0\tau}$ are the invariant mass, 3-momentum and energy of the $D^0\tau$ system, respectively; and m_B is the known B mass. The 3-momentum and mass of the $D^0\tau$ system are calculated using the τ momentum estimated previously. Denoting by p_{D^0} and $p_\tau(\theta_{\max})$ the 4-momentum of the D^0 meson and the τ lepton, respectively, it follows:

$$p_{D^0\tau} = p_{D^0} + p_\tau(\theta_{\max}). \quad (6.13)$$

Again, when the argument of the square root in Eq. 6.12 vanishes, the quadratic ambiguity disappears and the θ' angle reaches its maximum allowed value, given by

$$\theta'_{max} = \arcsin\left(\frac{m_B^2 - m_{D^0\tau}^2}{2m_B|\vec{P}_{D^0\tau}|}\right) \tag{6.14}$$

and the value of the B momentum is estimated as $|\vec{p}_B| = |\vec{p}_B(\theta'_{\rm max})|$, leading to

$$|\vec{p}_B| \approx \frac{(m_{D^0\tau}^2 + m_B^2)|\vec{p}_{D^0\tau}|\cos\theta'_{\rm max}}{2(E_{D^0\tau}^2 - |\vec{p}_{D^0\tau}|^2\cos^2\theta'_{\rm max})}. \tag{6.15}$$

The distribution of the B momentum and its resolution is shown in Figs. 6.12 and 6.13, respectively, for $B^+ \to \overline{D}^0\tau^+\nu_\tau$ and $B^+ \to \overline{D}^{*0}\tau^+\nu_\tau$ decays, with $\tau^+ \to \pi^+\pi^-\pi^+\overline{\nu}_\tau$.

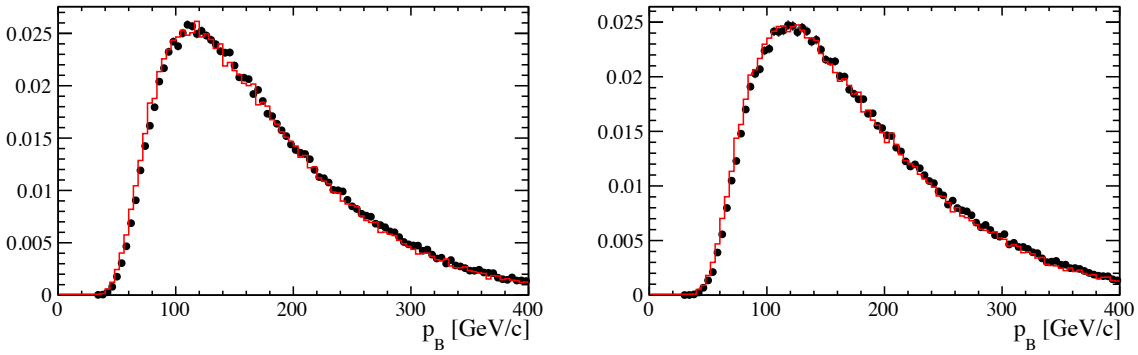

Figure 6.12: Distribution of the B momentum estimated (black) and generated (red) for $B^+ \to \overline{D}^0\tau^+\nu_\tau$ (left) and $B^+ \to \overline{D}^{*0}\tau^+\nu_\tau$ (right) decays, with $\tau^+ \to \pi^+\pi^-\pi^+\overline{\nu}_\tau$.

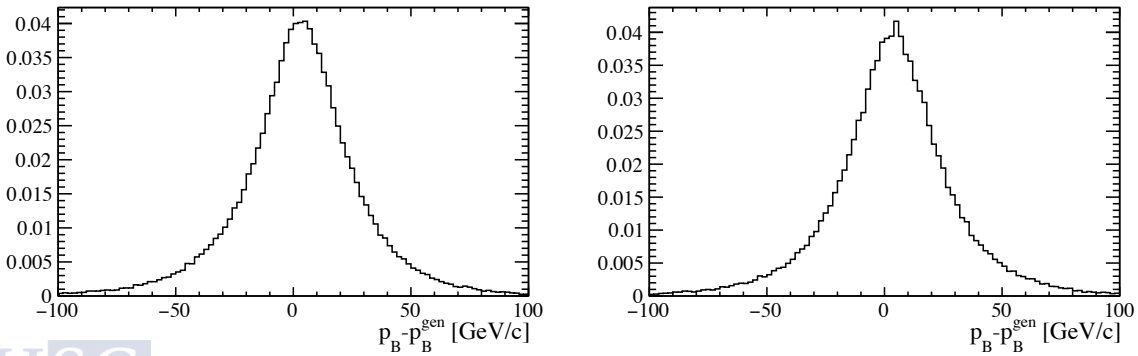

Figure 6.13: Distribution of the B^- momentum resolution $p_B - p_B^{gen}$ for $B^+ \to \overline{D}^0\tau^+\nu_\tau$ (left) and $B^+ \to \overline{D}^{*0}\tau^+\nu_\tau$ (right) decays, with $\tau^+ \to \pi^+\pi^-\pi^+\overline{\nu}_\tau$.

Following these two approximations, the B and τ 4-momenta can be estimated:

$$p_\tau = (m_\tau, |\vec{p}_\tau|\hat{\boldsymbol{u}}_\tau) \text{ and} \tag{6.16}$$
$$p_B = (m_B, |\vec{p}_B|\hat{\boldsymbol{u}}_B) \tag{6.17}$$

where $\hat{\boldsymbol{u}}_\tau$ ($\hat{\boldsymbol{u}}_B$) is the unit vector pointing from the reconstructed B vertex (PV) to the τ (B) vertex. Using the measured D^0 4-momentum:

$$p_{D^0} = (m_{D^0}, \vec{p}_{D^0}), \tag{6.18}$$

we can estimate the square of the invariant mass of (or momentum transfer to) the $\tau^+\nu_\tau$ system, $q^2 = (p_B - p_{D^0})^2$ and the τ decay time, t_τ. The q^2 distribution and its resolution are shown in Figs. 6.14 and 6.15, respectively. Note that, for $B^+ \to \overline{D}^{*0}\tau^+\nu_\tau$ decays, the q^2 is defined as $(p_B - p_{D^0})^2$ instead of $(p_B - p_{D^{*0}})^2$. The t_τ distributions and their resolution are shown in Figs. 6.16 and 6.17, respectively.

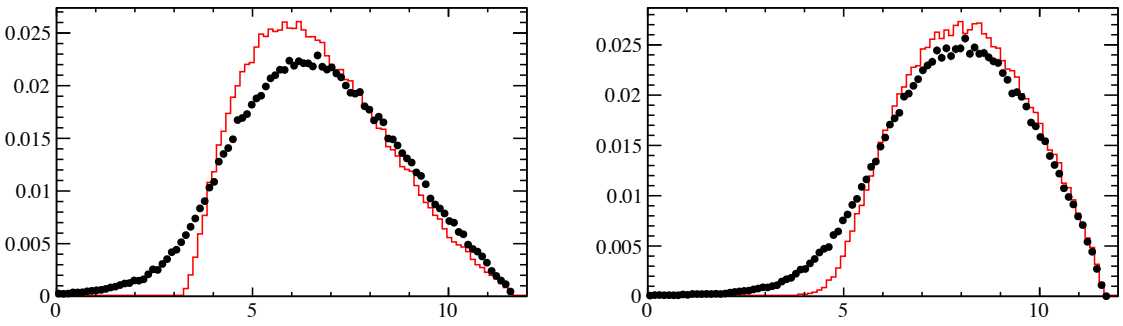

Figure 6.14: Distribution of the q^2 estimated (black) and generated (red) for $B^+ \to \overline{D}^0\tau^+\nu_\tau$ (left) and $B^+ \to \overline{D}^{*0}\tau^+\nu_\tau$ (right) decays, with $\tau^+ \to \pi^+\pi^-\pi^+\overline{\nu}_\tau$.

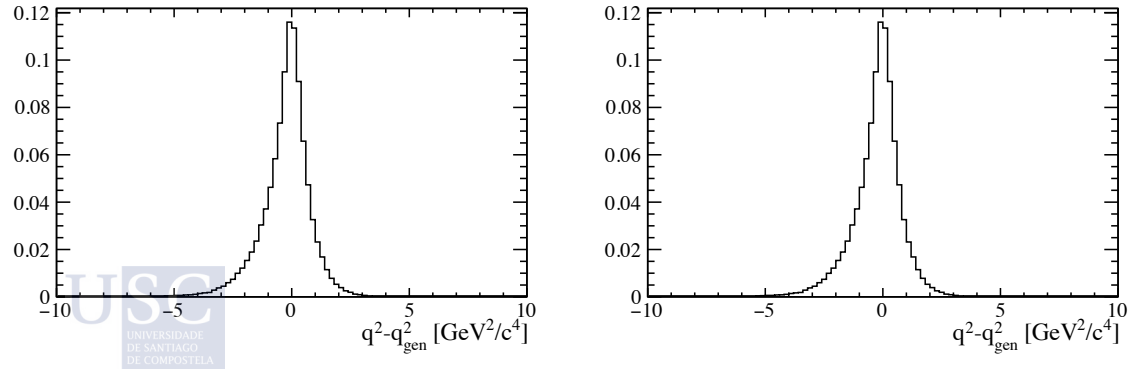

Figure 6.15: Distribution of the q^2 resolution $q^2 - q^2_{gen}$ for $B^+ \to \overline{D}^0\tau^+\nu_\tau$ (left) and $B^+ \to \overline{D}^{*0}\tau^+\nu_\tau$ (right) decays, with $\tau^+ \to \pi^+\pi^-\pi^+\overline{\nu}_\tau$.

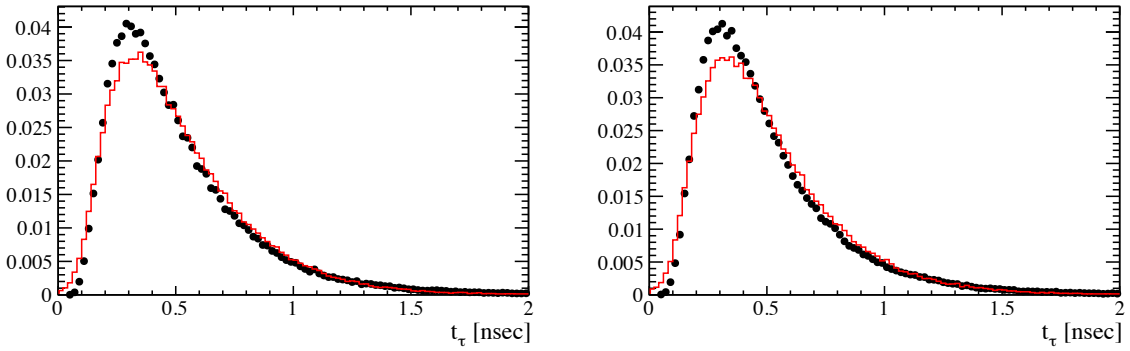

Figure 6.16: Distribution of the τ decay time, t_τ estimated (black) and generated (red) for $B^+ \to \overline{D}^0\tau^+\nu_\tau$ (left) and $B^+ \to \overline{D}^{*0}\tau^+\nu_\tau$ (right) decays, with $\tau^+ \to \pi^+\pi^-\pi^+\overline{\nu}_\tau$.

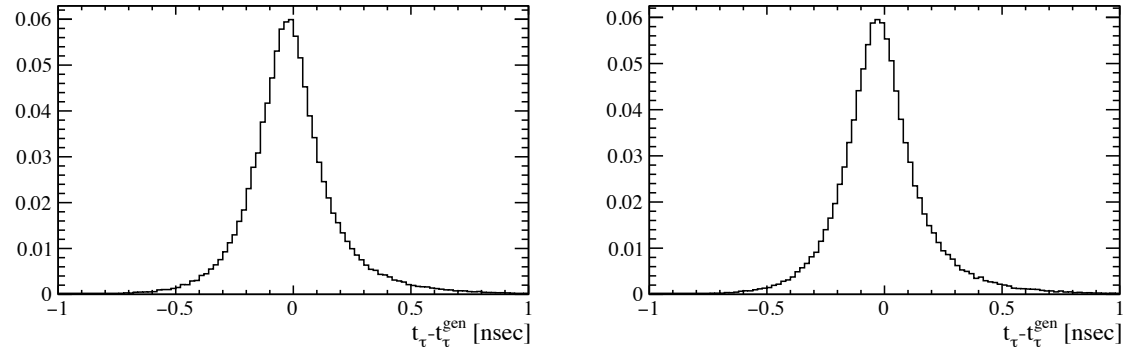

Figure 6.17: Distribution of the τ decay time resolution $t_\tau - t_\tau^{gen}$ for $B^+ \to \overline{D}^0\tau^+\nu_\tau$ (left) and $B^+ \to \overline{D}^{*0}\tau^+\nu_\tau$ (right) decays, with $\tau^+ \to \pi^+\pi^-\pi^+\overline{\nu}_\tau$.

The estimated q^2 and t_τ will be used, together with the output of a multivariate algorithm consisting on a gradient-Boosted Decision Tree (BDT), to extract the signal ($B^+ \to \overline{D}^0\tau^+\nu_\tau$ and $B^+ \to \overline{D}^{*0}\tau^+\nu_\tau$) yields from a 3-dimensional template fit.

6.2.7 Signal and normalisation selections

Two specific set of cuts are applied, depending on whether the signal or normalisation events are being selected. Both selections are shown in Tab. 6.6. In addition to the trigger, the 3π detachment cut and the isolation criteria already presented, the q^2 must be positive and the τ decay time smaller than 2 nanoseconds. The $\overline{D}^0$ mass must be in a window of $\pm 20\,\mathrm{MeV}/c^2$ around the known $\overline{D}^0$ mass, and a PID cut is applied to suppress $D^+ \to \pi^+K^-\pi^+X$ decays. An additional cut is needed to suppress events where one of the tracks of the $\overline{D}^0$ actually belongs to the 3π vertex. An example of these kind of decays is the $\overline{D}^0 \to \pi^+\pi^-\pi^+\pi^-$, where the three pions form the τ vertex and the remaining pion is used to construct the $\overline{D}^0$ candidate. The invariant mass of the 3 pions from the τ vertex

and the pion from the D^0 is shown in Fig. 6.18. Thus, requiring that the tracks forming the $\overline{D}^0$ do not point to the τ vertex removes this background. This cut corresponds to the entry "$\chi^2_{\rm IP}(\tau)$ D^0 daughters" in Tab. 6.6.

Variable	**Signal cuts**	**Normalisation cuts**
trigger	true	true
$\Delta z/\sigma$	> 4	> 4
$\chi^2_{\rm IP}(\tau)$ D^0 daughters	> 5	> 5
D^{*+} veto	true	true
$N^{\tau}_{iso}(p_T > 250; \chi^2_{\rm IP}({\rm PV}) > 4; \chi^2_{\rm IP}(\tau) < 25)$	$= 0$	$= 0$
$N^{B}_{iso}(p_T > 250; \chi^2_{\rm IP}({\rm PV}) > 4; \chi^2_{\rm IP}(B) < 25)$	$= 0$	$= 0$
q^2	> 0 GeV$^2/c^4$	> 0 GeV$^2/c^4$
t_τ	< 2 nsec	< 2 nsec
π^+ from τ^- ProbNNk	< 0.1	< 0.1
$\lvert m(D^0) - m(D^0)_{\rm PDG}\rvert$	< 20 MeV$/c^2$	< 20 MeV$/c^2$
$m(3\pi)$	< 1600 MeV$/c^2$	± 30 MeV$/c^2$ around D_s^+ mass
BDT	> -0.4	—

Table 6.6: Final selection cuts applied for signal and normalisation events. The BDT variable is defined in Sec. 6.2.8.

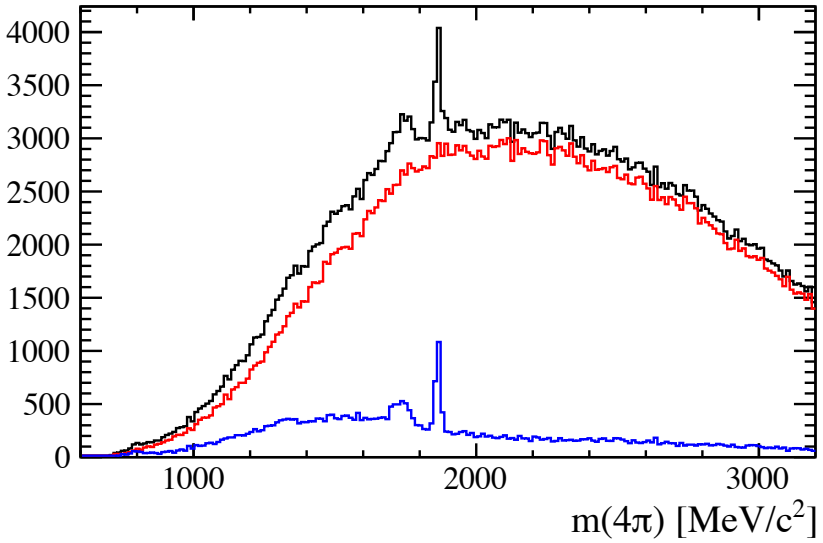

Figure 6.18: Invariant mass $m(3\pi\pi^-_{\overline{D}^0})$ distribution for events in real data (black), where $\pi^-_{\overline{D}^0}$ is the pion from the $\overline{D}^0 \to K^+\pi^-$ candidate. Events where at least one of the tracks from the $\overline{D}^0$ has in impact parameter χ^2 with respect to the τ vertex smaller than 5 is shown in blue, where a peak at the $\overline{D}^0$ mass is clearly visible. The rest of the events, that are selected for the analysis, are shown in red.

6.2.8 The BDT

By large, the dominant source of background after the final selection is due to doubly-charmed $B \to \overline{D}^0 D_s^+(X)$ decays. Aiming for the best rejection of this contribution, the TMVA toolkit [150] is used to train a Gradient Boosted Decision Tree (BDT). The BDT output is used then as a discriminating variable in the 3-dimensional template fit from which the desired signal yields are obtained.

Since the final goal of the analysis is the unbiased observation of the signals, the criteria for the input variables for the BDT is to choose those that are less correlated with the rest of 3D fit variables, in particular with the q^2 (the two signal channels differ in this distribution), while keeping those variables having the largest discriminating power for signal and background. Therefore, this limits very strongly the type and number of variables that can be uses in the BDT, leading to a BDT input composed by variables related with the 3π system. The signal sample used is the $B^+ \to \overline{D}^0 \tau^+ \nu_\tau$ Monte Carlo, with $\tau^+ \to \pi^+\pi^-\pi^+\overline{\nu}_\tau$; while for the background, the $B \to \overline{D}^0 D_s^+(X)$ Monte Carlo is employed. The signal selection is applied to both samples.

Adding neutral isolation variables contribute in background rejection, since in events where the 3π are coming from a D_s^+ decays, often extra neutral particles are produced in the decays. This neutral energy is searched for in the electromagnetic calorimeter in a cone $\sqrt{\Delta\eta^2 + \Delta\phi^2} = 0.4$ around the 3π direction, where $\Delta\eta$ ($\Delta\phi$) is a variation of pseudo-rapidity (azimuth angle) around the 3π direction.

The dynamics of the pions from the τ^+ decay is a powerful discriminator due to the dominance of the $\tau^+ \to a_1^+(\to \rho^0(\pi^+\pi^-)\pi^+)\overline{\nu}_\tau$, very different from the dynamics of D_s^+ decays. Thus, the invariant masses of 2-pions combinations are included in the training set of variables.

Identifying the pions from the τ decay as $\tau^+ \to \pi_0^+\pi_1^-\pi_2^+\overline{\nu}_\tau$, the set of variables employed in the BDT training is:

- Minimum mass of oppositely-charged pions: $\texttt{min}[m(\pi_0^+\pi_1^-), m(\pi_2^+\pi_1^-)]$.
- Maximum mass of oppositely-charged pions: $\texttt{max}[m(\pi_0^+\pi_1^-), m(\pi_2^+\pi_1^-)]$.
- Mass of the same-sign pions: $m(\pi_0^+\pi_2^+)$.
- $\frac{\texttt{tau\_0.40\_nc\_vPT}}{\texttt{tau\_PT+tau\_0.40\_nc\_vPT}}$, where `tau_PT` is the transverse momentum of the 3π system and `tau_0.40_nc_vPT` is the sum of the transverse momentum of the photons detected in the electromagnetic calorimeter contained in the cone $\sqrt{\Delta\eta^2 + \Delta\phi^2} = 0.4$ around the 3π direction.
- `tau_0.40_nc_mult`: number of photons detected in the electromagnetic calorimeter in the cone of 0.4.

The distribution of the variables used in the BDT training are shown in Fig. 6.19. The correlation matrix between variables can be seen in Fig. 6.20 for signal and background,

the signal efficiency versus the background rejection is shown in Fig. 6.21 and the BDT response is displayed in Fig. 6.22.

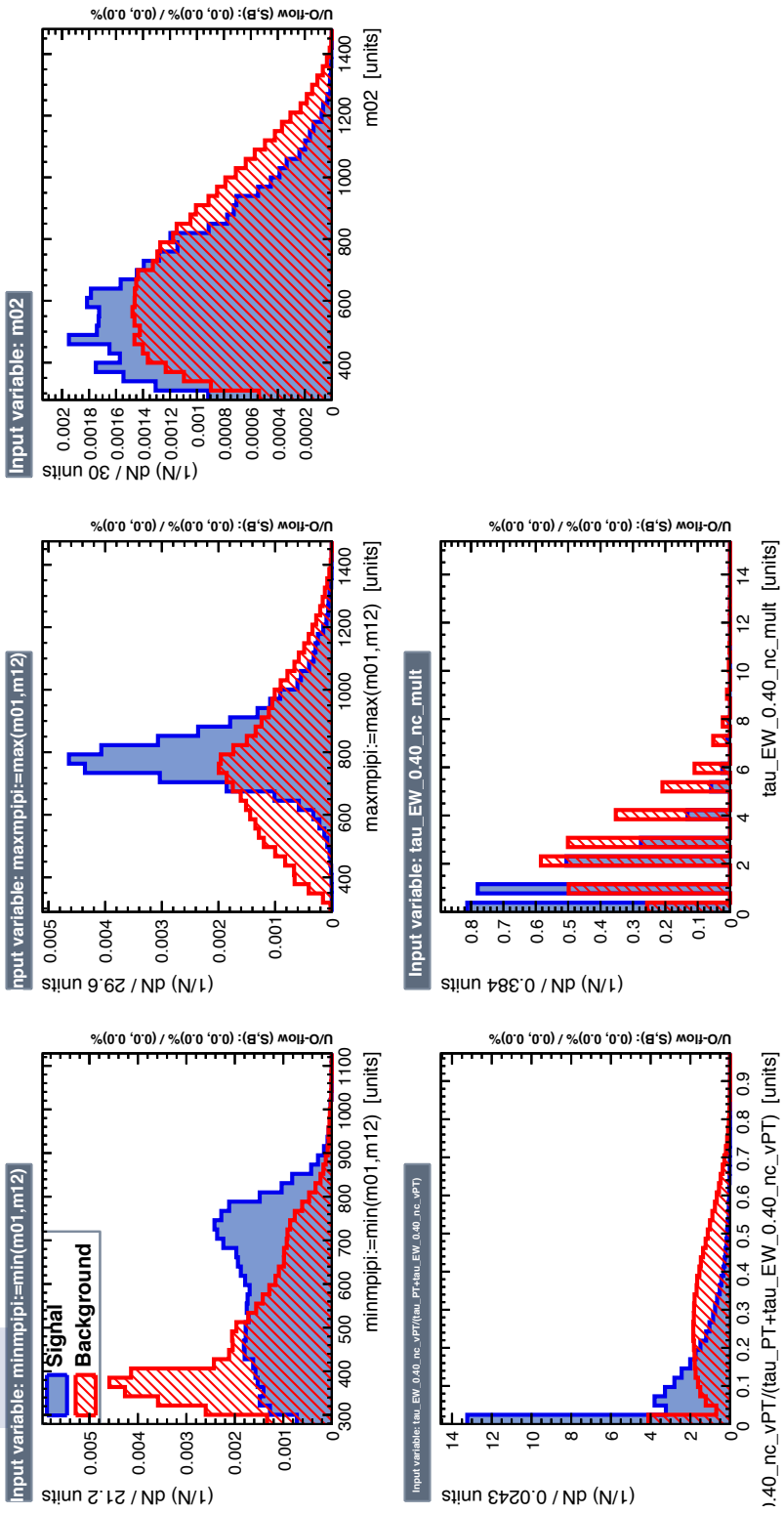

Figure 6.19: Distributions of the input variables used in the BDT training for signal (blue) and background (red).

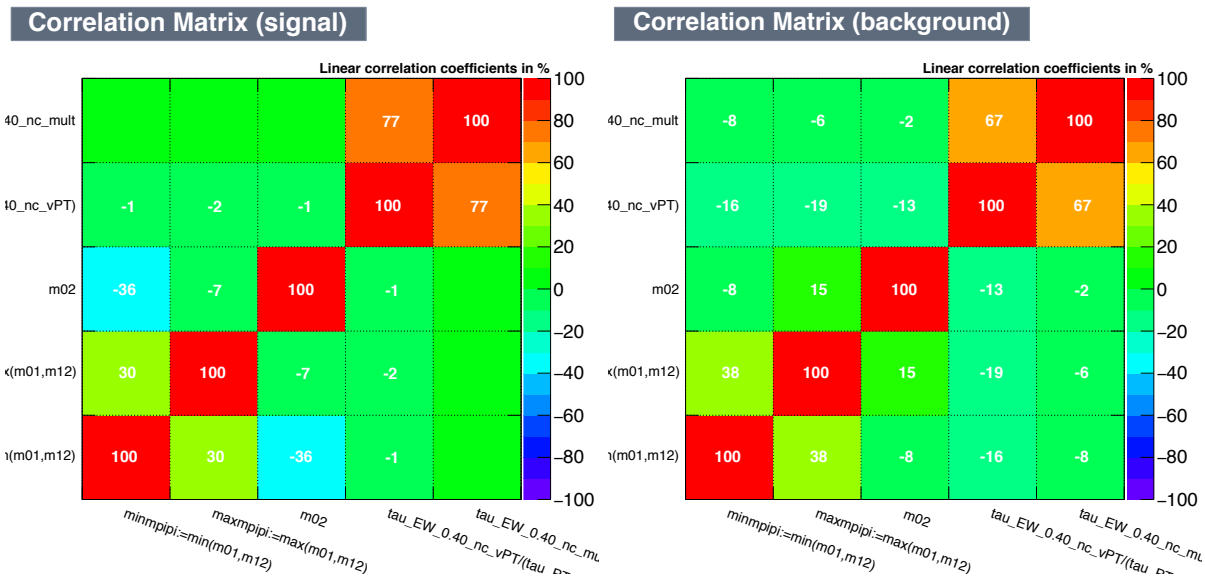

(a) (b)

Figure 6.20: Correlation matrices for input variables used in BDT training for (a) signal and (b) background.

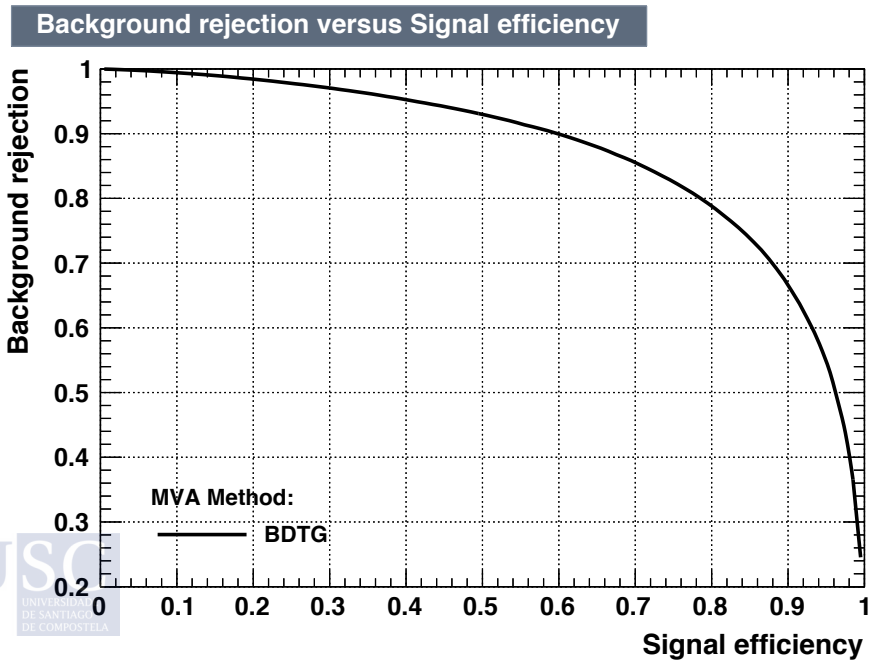

Figure 6.21: BDT background rejection vs signal efficiency.

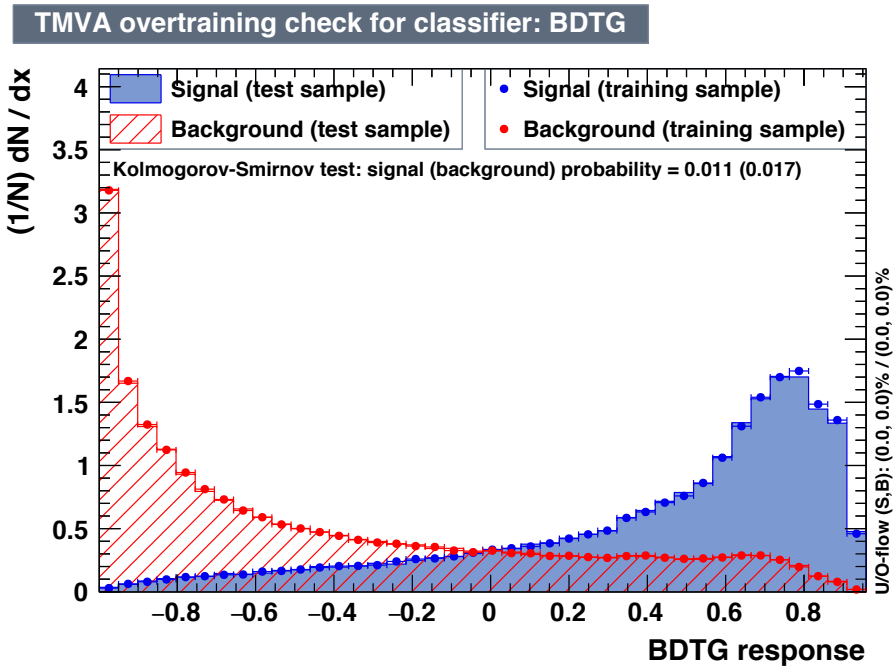

Figure 6.22: Output of the BDT training for signal (blue) and background (red).

6.2.8.1 Figure of merit

Before the fit to data is performed, the BDT cut needs to be optimised. With this goal, a figure of merit (FoM) is used. The FoM was firstly chosen as the statistical significance:

$$\text{FoM} = \frac{S}{\sqrt{S+B}}, \tag{6.19}$$

where S and B are the yields for signal and background samples, taking into account on the expected number of signal (20.000) and background (250.000). The significance as a function of the BDT cut is shown in Fig. 6.23. The maximisation of this figure of merit yields a BDT cut of 0.3 with a signal efficiency of 68% while rejecting 86% of the background.

The signal efficiency obtained by the optimisation of the significance as figure of merit provides an unacceptable low signal efficiency. In addition, the BDT output is included as a variable in the 3-dimensional signal template fit. Thus, the significance is found to be a non-optimal figure of merit for this analysis. By one hand, we want to keep a high signal efficiency and, by the other hand, to keep enough background events in the signal sample such that the fit can properly model these events with good precision. Applying the criterion just mentioned, the figure of merit is chosen such as:

$$\text{FoM} = \frac{S}{\sqrt{S+B}} \times \varepsilon_{sig}, \tag{6.20}$$

with its optimisation shown in Fig. 6.24.

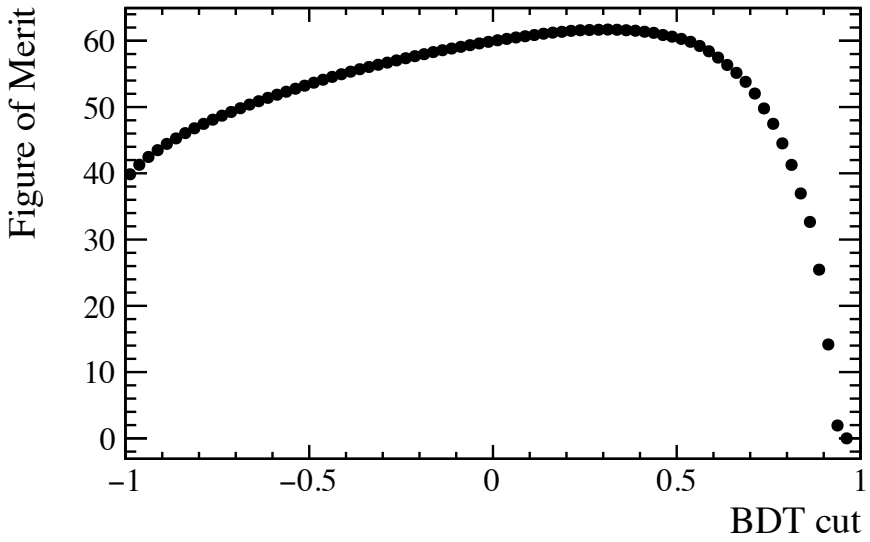

Figure 6.23: Significance as a function of the BDT cut.

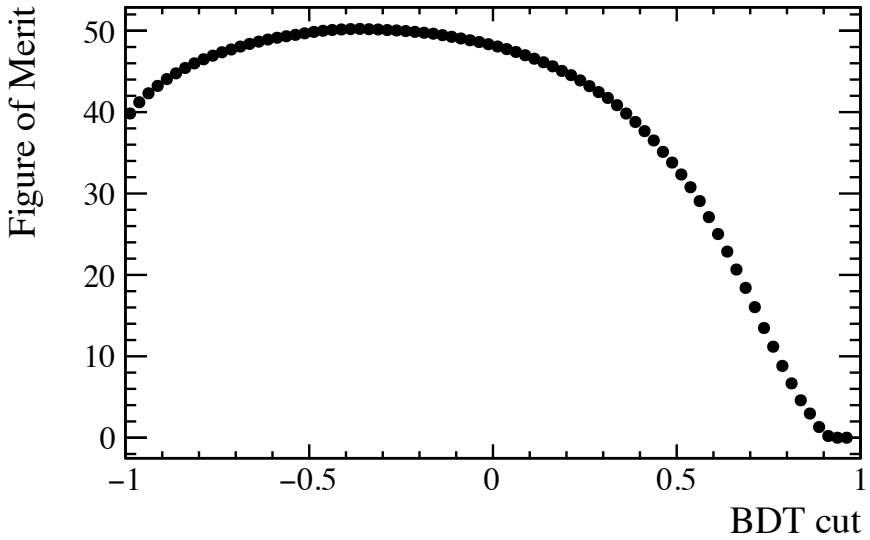

Figure 6.24: Figure of merit $\frac{S}{\sqrt{S+B}} \times \varepsilon_{sig}$ as a function of the BDT cut.

The maximisation of this figure of merit yields a BDT cut of -0.4 with a signal efficiency of 90% and a background rejection of 65%. Thus, for the signal selection, a cut BDT> -0.4 is applied in this analysis.

6.2.9 Multiple candidates

In the Run 1 hadronic $\mathcal{R}(D^*)$ analysis [43, 44], specific requirements were applied on the number of candidates in a single event. At the pre-selection stage, only events with one single candidate were kept for further analysis. In this analysis, the good performance of the selection and, in particular, the vertex isolation, leads to that only the 1.0% of events in data passing the signal selection contain multiple candidates. The percentage of simulated signal events with multiple candidates is 0.5% and for simulated doubly-charmed decays is 0.8%. Therefore, no further requirements on the event multiplicity are applied.

6.3 Corrections to simulation

In this section, the corrections to Monte Carlo samples are briefly described. These include corrections on the charged particles identification (`PIDCalib`) algorithms; vertex resolution; B kinematics, event multiplicity and trigger category; and the form-factors re-weighting for the signals $B \to D^*\tau^+\nu_\tau$ and $B \to D\tau^+\nu_\tau$.

6.3.1 Corrections on the charged particles identification

Requirements on Particle Identification (PID) variables are applied in this analysis to select charged pions and kaons forming the signal and normalisation decay candidates (and also control samples). In order to correct the Monte Carlo to match the PID performance observed in data, the `PIDCalib` tool is used [148]. The PID efficiencies are estimated following a data-driven method.

Firstly, `PIDCalib` generates calibration samples of pions and kaons, taking as input a binning on track momentum, pseudo-rapidity and number of tracks in the event; together with the PID requirements applied in the selected events. The default binning scheme was extended so that the sample can include tracks with momentum in the range $[2, 200]$ MeV/c.

The PID variables considered in this analysis are of two types: `DLLx` is a likelihood ratio of the X particle and pion hypothesis; and `ProbNNy` that is the bayesian probability of the particle of being of type y. The PID requirements applied are summarized in Tab. 6.7.

Particle	PID requirements
D0_K	DLLK> 3 && ProbNNk> 0.4
D0_pi	DLLK< 50 && ProbNNpi> 0.4
tau_pion0	DLLK< 8 && ProbNNpi> 0.2
tau_pion1	DLLK< 8 && ProbNNpi> 0.2 && ProbNNk< 0.1
tau_pion2	DLLK< 8 && ProbNNpi> 0.2

Table 6.7: PID requirements for each of the five tracks forming decay candidate.

Once the calibration histograms are produced, `PIDCalib` determines the efficiencies of a given PID requirement in data and simulation for each individual track and a weight is assigned to correct data/Monte Carlo differences. Finally, the total weight applied to each decay candidate is computed as the product of the individual weights for each track.

6.3.2 Vertex resolution

As it was introduced, *prompt* $B \to D^0 3\pi X$ events are the dominant contribution in the data sample, before it is applied the detachment $\Delta z(3\pi - B)/\sqrt{\sigma^2_{3\pi} + \sigma^2_B} > 4$ cut (see Sec. 6.2.4). In these events, the three pions are produced at the B vertex and, by consequence, the widths of the $\Delta z(3\pi - B)$ and $\Delta z(3\pi - B)/\sqrt{\sigma^2_{3\pi} + \sigma^2_B}$ distributions are due to vertex resolution effects.

Distributions for $\Delta z(3\pi - B)$ and $\Delta z(3\pi - B)/\sqrt{\sigma^2_{3\pi} + \sigma^2_B}$ are shown in Fig. 6.25 for exclusive $B^+ \to D^0 3\pi$ decays. There are evident differences between data samples (years of data taking) and simulation. Therefore, it is necessary to introduce a correction for these discrepancies. A specific correction procedure is applied to the simulation to match the data in the different data-taking periods. This is summarised as:

- Two scaling factors are applied to the $\sigma_{3\pi}$ and σ_B vertex uncertainties.
- A smearing factor is applied to the $\Delta z(3\pi - B)/\sqrt{\sigma^2_{3\pi} + \sigma^2_B}$ distribution.

The $\sigma_{3\pi}$ and σ_B uncertainties depend on the $m(3\pi)$ and $m(D^0 3\pi)$ invariant masses, respectively. Fig. 6.26 shows the dependence of the mean of the $\sigma_{3\pi}$ and σ_B distributions for data and simulation as a function of $m(3\pi)$ and $m(D^0 3\pi)$, and the corresponding ratios 2016/2017, 2016/2018 and 2016/simulation. The simulation is corrected applying first order polynomials to $\sigma_{3\pi}$ and σ_B:

$$\sigma^{'}_{3\pi} = (\alpha^{3\pi}_0 + \alpha^{3\pi}_1 \times m(3\pi)) \times \sigma_{3\pi}, \quad (6.21)$$

$$\sigma^{'}_{B} = (\alpha^{B}_0 + \alpha^{B}_1 \times m(D^0 3\pi)) \times \sigma_{B}. \quad (6.22)$$

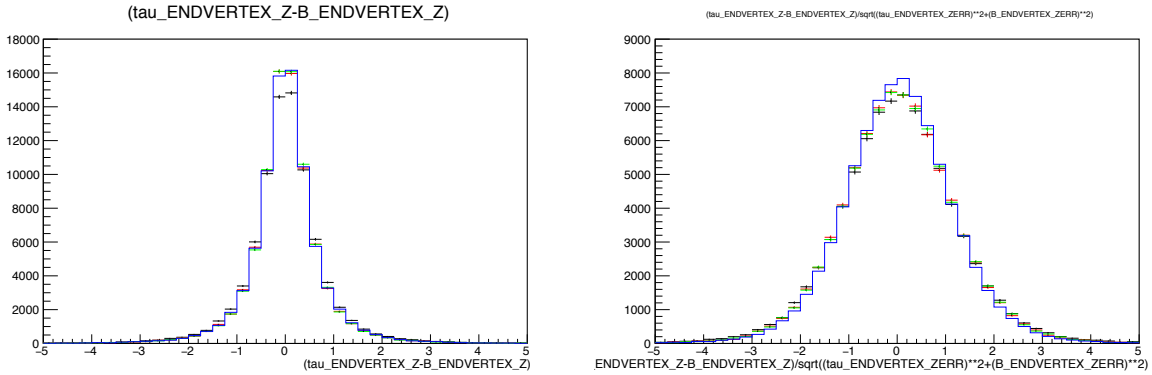

Figure 6.25: $\Delta z(3\pi - B)$ (left) and $\Delta z(3\pi - B)/\sqrt{\sigma_{3\pi}^2 + \sigma_B^2}$ (right) distributions for 2016 (black), 2017 (red), 2018 (green) data and simulation (blue) for exclusive $B^+ \to D^0 3\pi$ events. The width of the distributions is due vertex resolution effects. The resolution in 2016 data is worse than in 2017 and 2018.

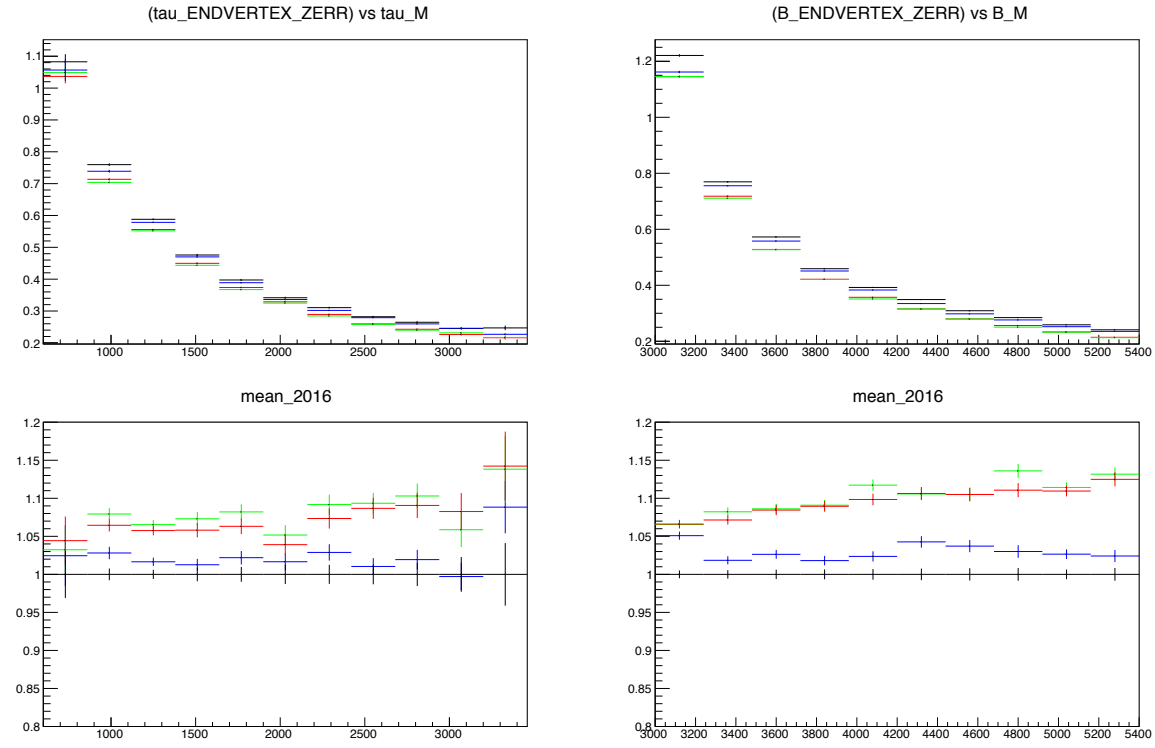

Figure 6.26: Top: mean of the $\sigma_{3\pi}$ (left) and σ_B (right) distributions as a function of $m(3\pi)$ and $m(D^0 3\pi)$, respectively. 2016, 2017 and 2018 data are shown in black, red and green, and simulation in blue. Bottom: corresponding ratios 2016/2017, 2016/2018 and 2016/simulation.

Corrections are applied separately for 2016, 2017 and 2018 data. The result of this correction is shown in Figs. 6.27, 6.28 and 6.29. An excellent agreement is observed between simulation and the data corresponding to 2017 and 2018 periods. However, to correctly describe 2016 data, an additional vertex resolution smearing is needed.The additional resolution smearing is modelled by a double-Gaussian of the form:

$$(\beta \times \text{Gaus}(0, \Delta\sigma_1) + (1-\beta) \times \text{Gaus}(0, \Delta\sigma_2)). \tag{6.23}$$

A simultaneous fit between 2016 and simulation is done to the $\Delta z(3\pi - B)/\sqrt{\sigma_{3\pi}^2 + \sigma_B^2}$ distributions, using the probability density functions (pdf):

$$\begin{aligned} \text{PDF(MC)} &= \alpha_1 \times \text{Gaus}(\mu, \sigma_1) + (1-\alpha_1) \times \alpha_2 \times \text{Gaus}(\mu, \sigma_2) \\ &+ (1-\alpha_1) \times (1-\alpha_2) \times \text{Gaus}(\mu, \sigma_3), \qquad (6.24) \\ \text{PDF(data)} &= \text{PDF(MC)} * (\beta \times \text{Gaus}(0, \Delta\sigma_1) + (1-\beta) \times \text{Gaus}(\mu, \Delta\sigma_2)), \qquad (6.25) \end{aligned}$$

where μ, α_1, α_2, σ_1, σ_2, σ_3, β, $\Delta\sigma_1$ and $\Delta\sigma_2$ are free parameters in the fit. The symbol $*$ represents the convolution of two functions. The fit results are presented in Tab. 6.8 and the corresponding projections in Fig. 6.30. The overall resolution function is used to smear the $\Delta z(3\pi - B)/\sqrt{\sigma_{3\pi}^2 + \sigma_B^2}$ variable. The simulation is corrected accounting for the relative proportion of data: 31%/32%/37% in 2016/2017/2018 conditions.

Finally, comparisons of the $\Delta z(3\pi - B)$ and $\Delta z(3\pi - B)/\sqrt{\sigma_{3\pi}^2 + \sigma_B^2}$ distributions before and after the uncertainty scaling and vertex smearing corrections are shown in Figs. 6.31, 6.32 and 6.33 for 2016, 2017 and 2018 runs., for 2016 run. The remarkable agreement between data and simulation endorses the complexity of the full vertex correction procedure.

Parameter	**Value**
α_1	0.41 ± 0.11
α_2	0.939 ± 0.009
σ_1	0.81 ± 0.04
σ_2	1.19 ± 0.06
σ_3	2.74 ± 0.25
μ	0.023 ± 0.003
β	0.89 ± 0.03
$\Delta\sigma_1$	0.26 ± 0.05
$\Delta\sigma_2$	1.50 ± 0.14

Table 6.8: Results of a simultaneous fit between 2016 data and simulation in the $\Delta z(3\pi - B)/\sqrt{\sigma_{3\pi}^2 + \sigma_B^2}$ distributions. A triple-Gaussian model is used as model, with an additional resolution model given by a double-Gaussian described by the parameters β, $\Delta\sigma_1$ and $\Delta\sigma_2$.

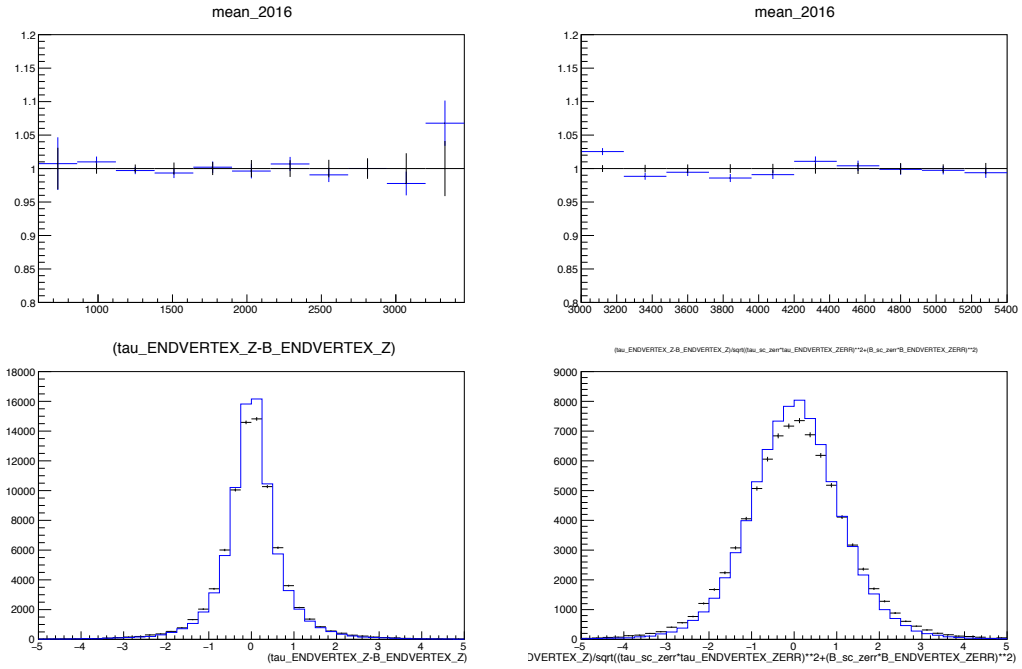

Figure 6.27: Top: ratio data(2016)/simulation for the mean of the $\sigma_{3\pi}$ (left) and σ_B (right) as a function of $m(3\pi)$ and $m(D^0 3\pi)$ after the vertex uncertainties scaling correction. Bottom: $\Delta z(3\pi - B)$ (left) and $\Delta z(3\pi - B)/\sqrt{\sigma_{3\pi}^2 + \sigma_B^2}$ (right) distributions for 2016 data (black) and simulation (blue) after the correction.

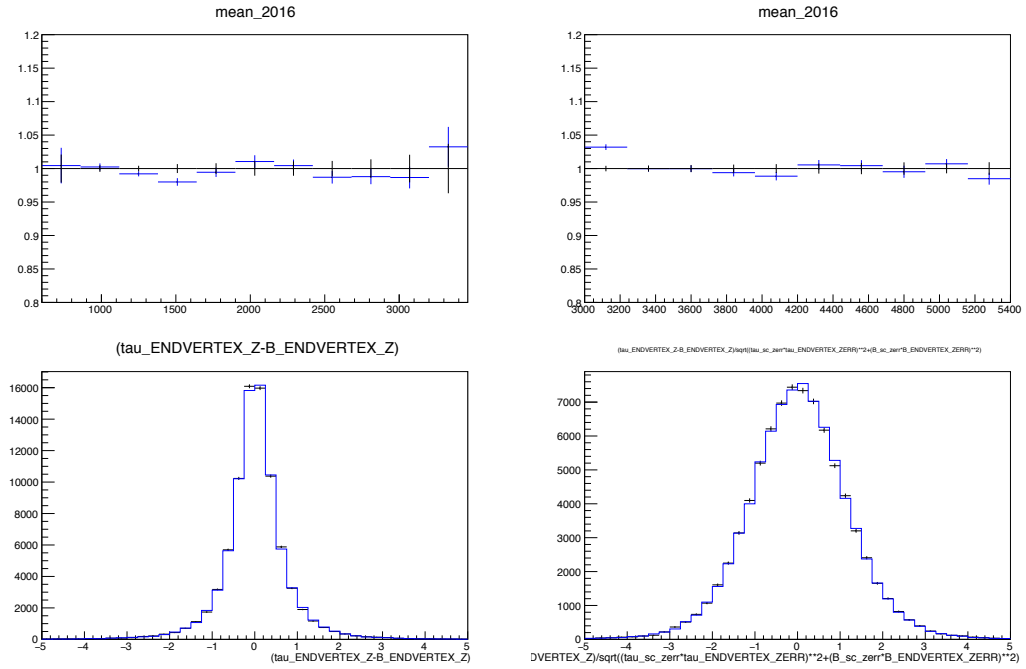

Figure 6.28: Top: ratio data(2017)/simulation for the mean of the $\sigma 3\pi$ (left) and σB (right) as a function of $m(3\pi)$ and $m(D^0 3\pi)$ after the vertex uncertainties scaling correction. Bottom: $\Delta z(3\pi - B)$ (left) and $\Delta z(3\pi - B)/\sqrt{\sigma_{3\pi}^2 + \sigma_B^2}$ (right) distributions for 2017 data (black) and simulation (blue) after the correction.

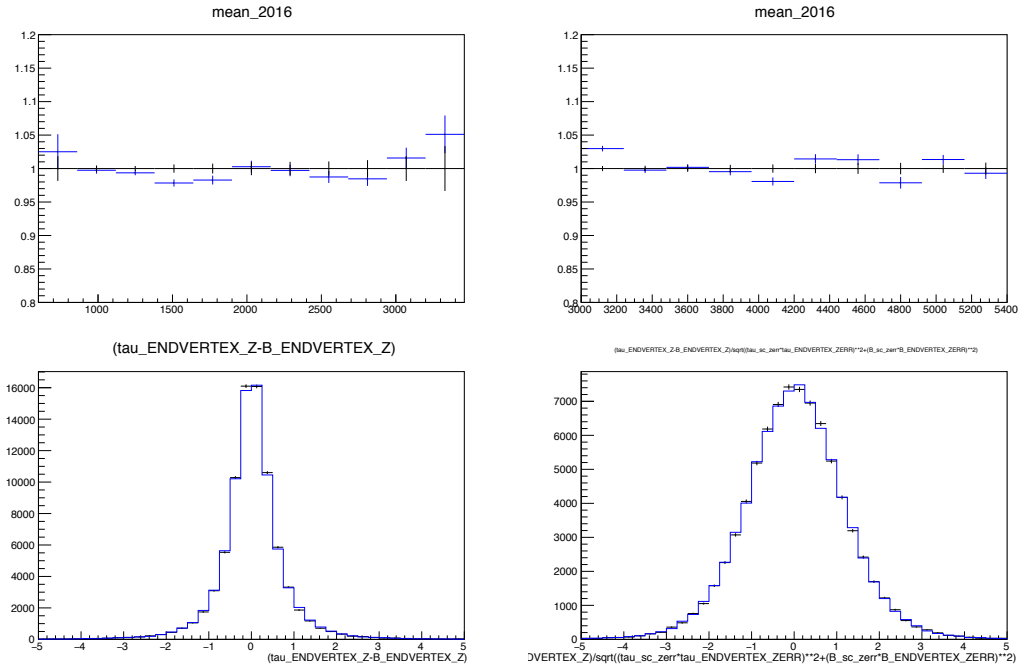

Figure 6.29: Top: ratio data(2018)/simulation for the mean of the $\sigma 3\pi$ (left) and σB (right) as a function of $m(3\pi)$ and $m(D^0 3\pi)$ after the vertex uncertainties scaling correction. Bottom: $\Delta z(3\pi - B)$ (left) and $\Delta z(3\pi - B)/\sqrt{\sigma_{3\pi}^2 + \sigma_B^2}$ (right) distributions for 2018 data (black) and simulation (blue) after the correction.

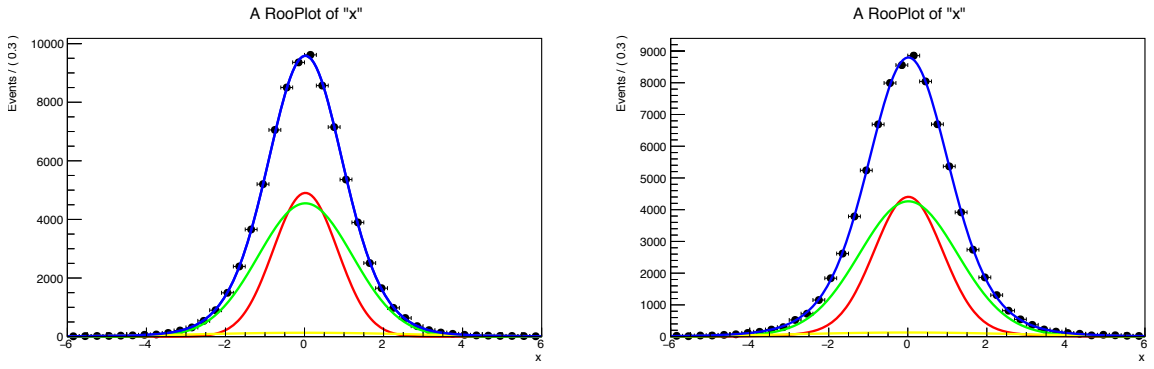

Figure 6.30: Projections of the simultaneous fit between 2016 data (right) and simulation (left) to the $\Delta z(3\pi - B)/\sqrt{\sigma_{3\pi}^2 + \sigma_B^2}$ distributions using a triple-Gaussian model with common parameters and an additional smearing factor.

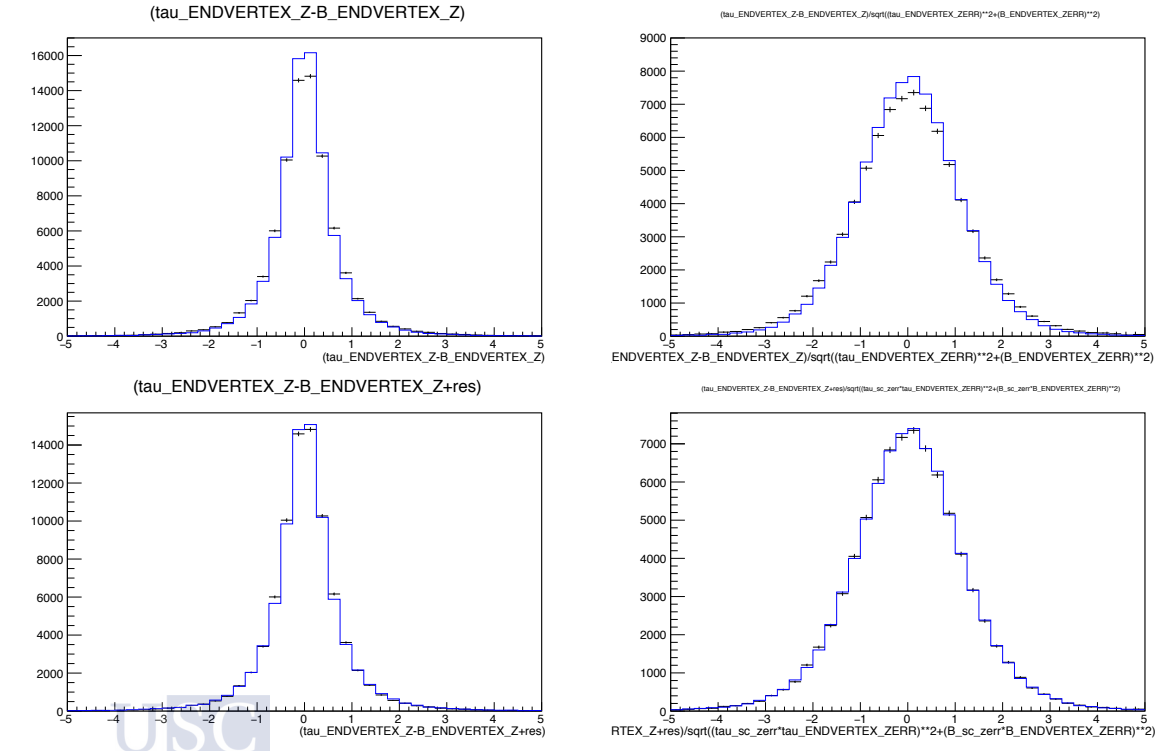

Figure 6.31: Comparison of the $\Delta z(3\pi - B)$ (left) and $\Delta z(3\pi - B)/\sqrt{\sigma_{3\pi}^2 + \sigma_B^2}$ (right) distributions before (top) and after (bottom) the uncertainties scaling correction and vertex smearing. Black points correspond to 2016 data and the blue histogram to simulation.

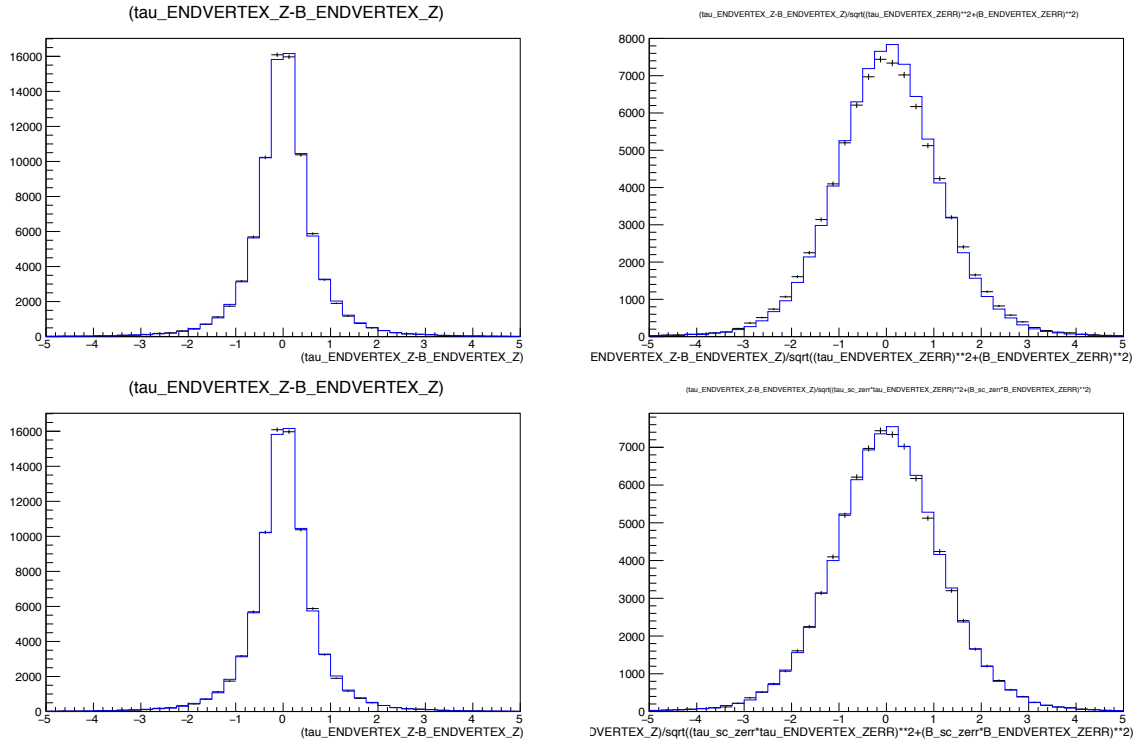

Figure 6.32: Comparison of the $\Delta z(3\pi - B)$ (left) and $\Delta z(3\pi - B)/\sqrt{\sigma_{3\pi}^2 + \sigma_B^2}$ (right) distributions before (top) and after (bottom) the uncertainties scaling correction. Black points correspond to 2017 data and the blue histogram to simulation.

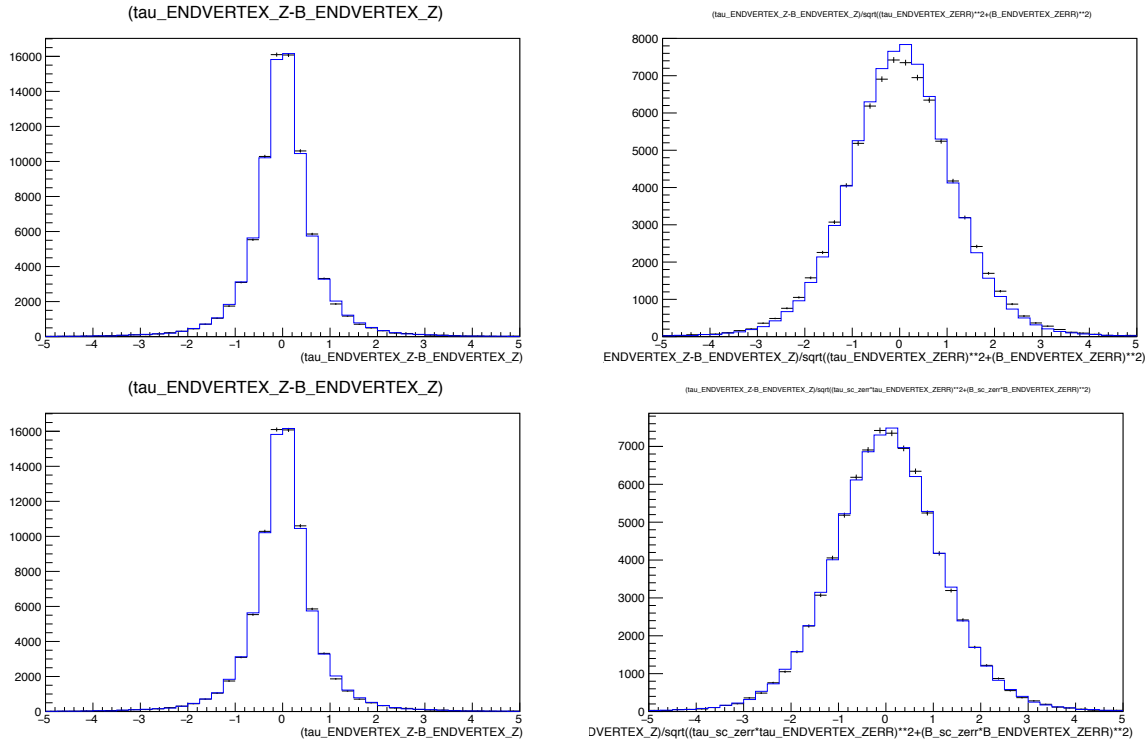

Figure 6.33: Comparison of the $\Delta z(3\pi - B)$ (left) and $\Delta z(3\pi - B)/\sqrt{\sigma_{3\pi}^2 + \sigma_B^2}$ (right) distributions before (top) and after (bottom) the uncertainties scaling correction. Black points correspond to 2018 data and the blue histogram to simulation.

6.3.3 Re-weighting on B kinematics, event multiplicity and trigger category

A sequential 2D reweighting is performed using the exclusive $B \to \overline{D}z3\pi$ peak in order to correct the B kinematics and event multiplicity. First, the reweighting is done on the `nTracks` and `B_OWNPV_NDOF` variables and, after this step, the same procedure is applied on the $p_T(B)$ and $\eta(B)$ variables. Since the full B kinematics cannot be reconstructed for signal decays, the corresponding Monte Carlo truth variables for $p_T(B)$ and $\eta(B)$ are used in this step.

This 2D re-weighting is done independently in 3 exclusive categories, which are:

- `!B_L0Global_TIS`
- `!B_L0HadronDecision_TOS`
- `B_L0Global_TIS & B_L0HadronDecision_TOS`

After the 2D reweighting, a global reweighting in the trigger variables is performed in order to make the TISTOS efficiencies in Monte Carlo and data match.

The final result of these steps is shown in Fig. 6.34, after reweighting of the kinematic and occupancy variables in the full sample without dividing by trigger category.

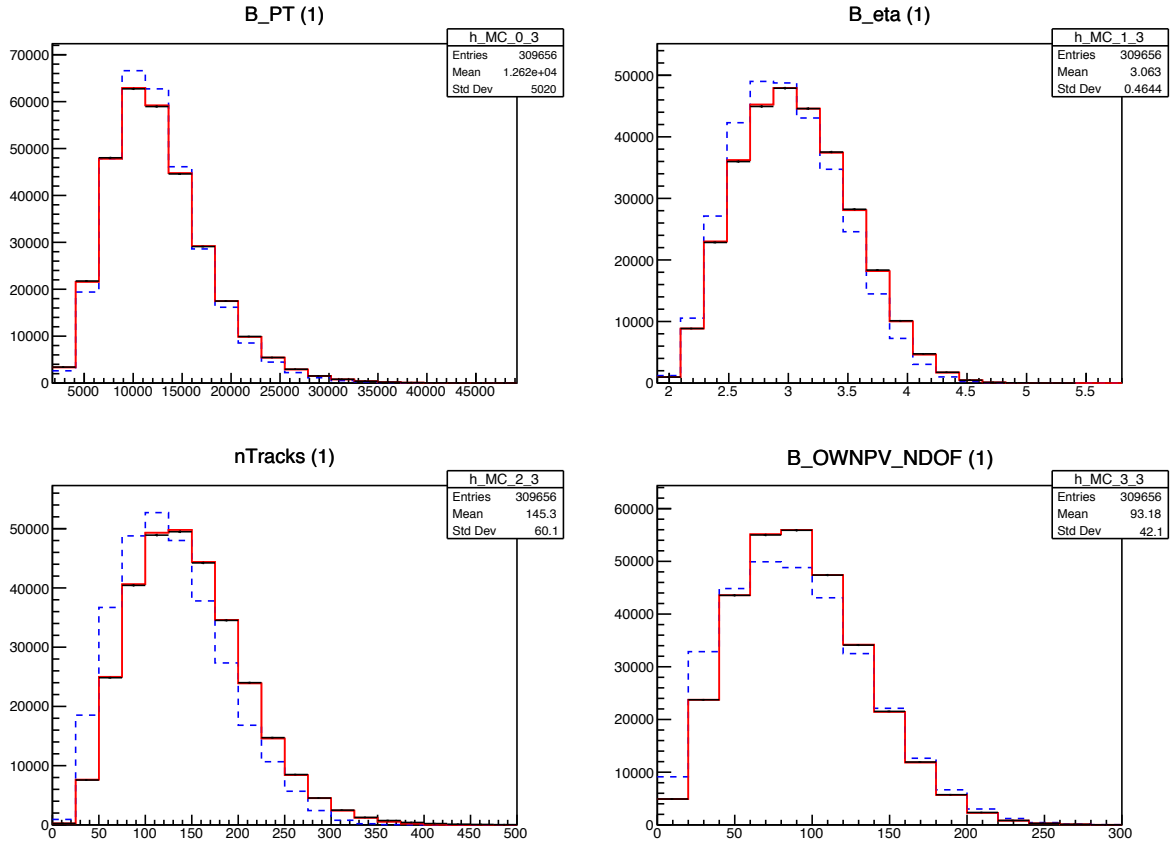

Figure 6.34: Comparison between Monte Carlo before reweighting (dashed blue), after reweighting (red) and data (black) of the kinematic and occupancy variables in the full sample (without dividing by trigger category).

For the computing of these weights, the $B \to \overline{D}^0 3\pi$ and $B \to \overline{D}^0 3\pi X$ Monte Carlo samples are used together, to maximize the statistics in the exclusive peak. Prior to the 2D reweighting, these samples are reweighted in the $m(3\pi)$ distribution, so their kinematics match with the data. To review if the reweighting procedure is working properly, a check is made by computing the weights using only the $B \to \overline{D}^0 3\pi$ sample, and then applying them to the $B \to \overline{D}^0 3\pi X$ sample. The result of this check is shown on Fig. 6.35.

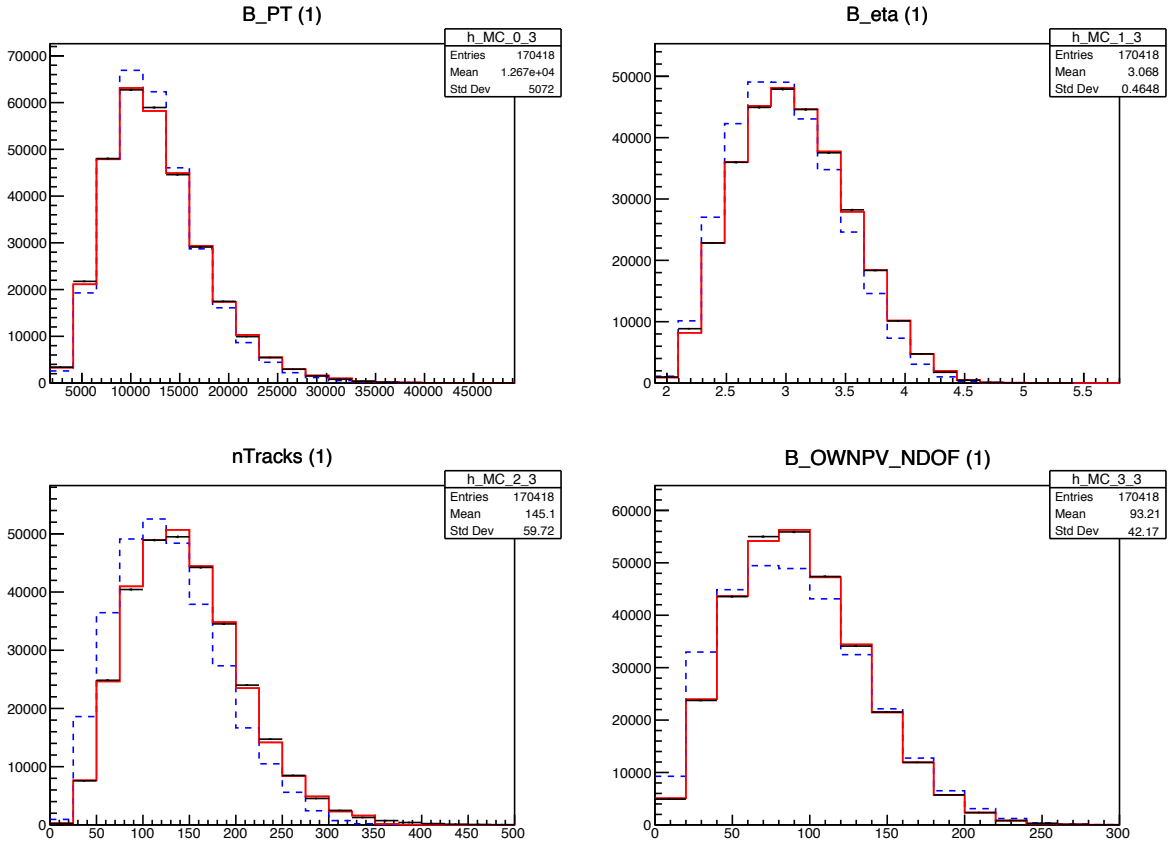

Figure 6.35: Comparison between Monte Carlo before reweighting (dashed blue), after reweighting (red) and data (black) of the kinematic and occupancy variables in the $B \to \overline{D}^0 3\pi X$ sample (without dividing by trigger category). The weights used in this reweighting were computed using only the $B \to \overline{D}^0 3\pi$ sample.

6.3.4 Form factors re-weighting

When working with MC templates in analyses of semileptonic decays, sizable biases often arise in measurements of branching fractions, so several strategies are used in order to reduce these effects. One possible approach is to completely transform the simulated data from one theoretical framework to the desired model, so as to effectively avoid biases. This type of transformation, or re-weighting, can be readily achieved with HAMMER (Helicity Amplitude Module for Matrix Element Re-weighting) [151], a dedicated software for fast and efficient transformations of large MC samples. This tool was primarily developed for $b \to c\tau\nu$ processes and might be used either for NP studies or different SM form-factor (FF) parameterisations. In Sec. 2.2.2.2.3, it was presented some FF basis that encodes the hadronic transitions for the $B^0 \to D^{*-}\ell^+\nu_\ell$ process, framed within in the EFT. In the following, it will be covered the different FF parameterisations that were used in the analysis for the $B \to D\tau^+\nu_\tau$ and $B \to D^*\tau^+\nu_\tau$, which must be explicitly specified in the code flow. We propose a z expansion for the definition of the BGL parameterisation (see Sec. 2.2.2.2.3), which will be used for both processes. Weight computations were performed with HAMMER v1.2.1, the latest available version (released in January 2022).

6.3.4.1 Form factors for $B \to D\tau^+\nu_\tau$ decays

From the power of series presented in Eqs. 2.39, 2.40, 2.41 and 2.42, truncated at $N = 3$, this construction calls for 8 free parameters, which need to be estimated. This construction calls for 8 free parameters, which need to be estimated. In Tab. 6.9 we show our choice for those parameters as presented in [54]. For that particular computation, a global fit was performed, using lattice QCD calculations from HPQCD and FNAL/MILC collaborations, as well as recent experimental data from BaBar and Belle.

Parameter	Value
a_0^0	0.07932 ± 0.00058
a_1^0	$-0.214^{+0.015}_{-0.014}$
a_2^0	$0.17^{+0.10}_{-0.24}$
a_3^0	$-0.958^{+1.060}_{-2.000}$
a_0^+	0.01565 ± 0.00011
a_1^+	-0.0353 ± 0.0031
a_2^+	$-0.043^{+0.021}_{-0.035}$
a_3^0	$0.194^{+0.019}_{-0.016}$

Table 6.9: Best determination of BGL parameters and their uncertainties for $B \to D\tau^+\nu_\tau$, performed in [54] through a global fit to lattice and experimental data.

6.3.4.2 Form factors for $B \to D^* \tau^+ \nu_\tau$ decays

In this particular case, the z expansion is truncated at order $N = 2$. This FF construction has 12 natural parameters, but it can be easily reduced to 10 free parameters. The constraints are established from relation enforced at zero recoil and in $q^2 = 0$ (see [65] for more details). In Tab. 6.10 we present an estimation for those parameters and their uncertainties, as computed in [65]. This computation includes Light Cone Sum Rules (LCSR) constraints, a procedure that may be consulted in [152].

Parameter	Value
a_0^g	$0.0299^{+0.0053}_{-0.0035}$
a_1^g	$0.04^{+0.07}_{-0.20}$
a_2^g	$-0.9^{+1.8}_{-0.0}$
a_0^f	0.01218 ± 0.00016
a_1^f	$-0.029^{+0.021}_{-0.013}$
a_2^f	$0.5^{+0.0}_{-0.3}$
$a_1^{F_1}$	$-0.0051^{+0.0049}_{-0.0013}$
$a_2^{F_1}$	$0.065^{+0.009}_{-0.089}$
$a_0^{F_2}$	0.0595 ± 0.0093
$a_1^{F_2}$	-0.318 ± 0.170

Table 6.10: Best determination of BGL parameters and their uncertainties for $B \to D^* \tau^+ \nu_\tau$, performed in [65] through a global fit to lattice and experimental data with LCSR constraints.

6.4 Efficiencies

Signal and MC efficiencies are computed using simulated events. All weights applied to simulation are applied in the calculation. The efficiencies are shown in Tab. 6.11. Signal (normalisation) efficiencies are computing applying the signal (normalisation) selection.

Decay	Generation Eff. Up/Down	Filtering Eff.	Total Eff. ($\times 10^{-5}$)
$B^+ \to \overline{D}^0 \tau^+ \nu_\tau$, $\tau^+ \to \pi^+\pi^-\pi^+\overline{\nu}_\tau$	$0.04178 \pm 0.00011 / 0.04186 \pm 0.00011$	0.0501	9.73
$B^+ \to \overline{D}^0 \tau^+ \nu_\tau$, $\tau^+ \to \pi^+\pi^-\pi^+\pi^0\overline{\nu}_\tau$	$0.037156 \pm 0.000099 / 0.037107 \pm 0.000097$	0.0494	3.83
$B^+ \to \overline{D}^{*0} \tau^+ \nu_\tau$, $\tau^+ \to \pi^+\pi^-\pi^+\overline{\nu}_\tau$	$0.04004 \pm 0.00010 / 0.04032 \pm 0.00011$	0.0493	8.40
$B^+ \to \overline{D}^{*0} \tau^+ \nu_\tau$, $\tau^+ \to \pi^+\pi^-\pi^+\pi^0\overline{\nu}_\tau$	$0.036045 \pm 0.000096 / 0.036071 \pm 0.000096$	0.0488	3.12
$\overline{B}^0 \to D^{*-} \tau^+ \nu_\tau$, $\tau^+ \to \pi^+\pi^-\pi^+\overline{\nu}_\tau$	$0.1601 \pm 0.0022 / 0.1592 \pm 0.0022$	0.0227	1.78
$\overline{B}^0 \to D^{*-} \tau^+ \nu_\tau$, $\tau^+ \to \pi^+\pi^-\pi^+\pi^0\overline{\nu}_\tau$	$0.1559 \pm 0.0021 / 0.1578 \pm 0.0022$	1.0	0.62
$B^+ \to \overline{D}^0 D_s^+$, $D_s^+ \to \pi^+\pi^-\pi^+$	$0.05980 \pm 0.00015 / 0.05992 \pm 0.00015$	0.0614	38.09

Table 6.11: Generation, filtering and total efficiencies for all signals and the normalisation mode. The signal (normalisation) efficiencies are requested to pass the signal (normalisation) selections.

These efficiencies are needed to measure the signal branching fractions and the LFU ratios. In addition, some other parameters are needed as input for the nominal fit model in Sec. 8.2.1. These are:

- $f_{3\pi}^{D^0}$: fraction of $B^+ \to \overline{D}^0\tau^+\nu_\tau$ events with $\tau^+ \to \pi^+\pi^-\pi^+\overline{\nu}_\tau$ with respect to the total number of $B^+ \to \overline{D}^0\tau^+\nu_\tau$ events (the sum of the $\tau^+ \to \pi^+\pi^-\pi^+\overline{\nu}_\tau$ and $\tau^+ \to \pi^+\pi^-\pi^+\pi^0\overline{\nu}_\tau$ events).
- $f_{3\pi}^{D^{*0}}$: fraction of $B^+ \to \overline{D}^{*0}\tau^+\nu_\tau$ events with $\tau^+ \to \pi^+\pi^-\pi^+\overline{\nu}_\tau$ with respect to the total number of $B^+ \to \overline{D}^{*0}\tau^+\nu_\tau$ events.
- $f_{3\pi}^{D^{*+}}$: fraction of $\overline{B}^0 \to D^{*-}\tau^+\nu_\tau$ events with $\tau^+ \to \pi^+\pi^-\pi^+\overline{\nu}_\tau$ with respect to the total number of $\overline{B}^0 \to D^{*-}\tau^+\nu_\tau$ events.
- $f_{D^{*+}/D^{*0}}$: ratio of $\overline{B}^0 \to D^{*-}\tau^+\nu_\tau$ events with respect to $B^+ \to \overline{D}^{*0}\tau^+\nu_\tau$ events.

They are computed using the following relations:

$$
\begin{aligned}
f_{3\pi}^{D^0} &= \frac{\mathcal{B}(\tau \to 3\pi) \times \varepsilon^{\tau\to 3\pi}_{B^+\to\overline{D}^0\tau^+\nu_\tau}}{\mathcal{B}(\tau \to 3\pi) \times \varepsilon^{\tau\to 3\pi}_{B^+\to\overline{D}^0\tau^+\nu_\tau} + \mathcal{B}(\tau \to 3\pi\pi^0) \times \varepsilon^{\tau\to 3\pi\pi^0}_{B^+\to\overline{D}^0\tau^+\nu_\tau}}\,, \\
f_{3\pi}^{D^{*0}} &= \frac{\mathcal{B}(\tau \to 3\pi) \times \varepsilon^{\tau\to 3\pi}_{B^+\to\overline{D}^{*0}\tau^+\nu_\tau}}{\mathcal{B}(\tau \to 3\pi) \times \varepsilon^{\tau\to 3\pi}_{B^+\to\overline{D}^{*0}\tau^+\nu_\tau} + \mathcal{B}(\tau \to 3\pi\pi^0) \times \varepsilon^{\tau\to 3\pi\pi^0}_{B^+\to\overline{D}^{*0}\tau^+\nu_\tau}}\,, \\
f_{3\pi}^{D^{*+}} &= \frac{\mathcal{B}(\tau \to 3\pi) \times \varepsilon^{\tau\to 3\pi}_{\overline{B}^0\to D^{*-}\tau^+\nu_\tau}}{\mathcal{B}(\tau \to 3\pi) \times \varepsilon^{\tau\to 3\pi}_{\overline{B}^0\to D^{*-}\tau^+\nu_\tau} + \mathcal{B}(\tau \to 3\pi\pi^0) \times \varepsilon^{\tau\to 3\pi\pi^0}_{\overline{B}^0\to D^{*-}\tau^+\nu_\tau}} \quad \text{and} \\
f_{D^{*+}/D^{*0}} &= \frac{\mathcal{B}(D^{*+} \to D^0X)}{\mathcal{B}(D^{*0} \to D^0X)} \times \frac{f_d}{f_u} \times \frac{\mathcal{B}(\overline{B}^0 \to D^{*-}\tau^+\nu_\tau)}{\mathcal{B}(B^+ \to \overline{D}^{*0}\tau^+\nu_\tau)} \\
&\times \frac{\mathcal{B}(\tau \to 3\pi) \times \varepsilon^{\tau\to 3\pi}_{\overline{B}^0\to D^{*-}\tau^+\nu_\tau} + \mathcal{B}(\tau \to 3\pi\pi^0) \times \varepsilon^{\tau\to 3\pi\pi^0}_{\overline{B}^0\to D^{*-}\tau^+\nu_\tau}}{\mathcal{B}(\tau \to 3\pi) \times \varepsilon^{\tau\to 3\pi}_{B^+\to\overline{D}^{*0}\tau^+\nu_\tau} + \mathcal{B}(\tau \to 3\pi\pi^0) \times \varepsilon^{\tau\to 3\pi\pi^0}_{B^+\to\overline{D}^{*0}\tau^+\nu_\tau}}\,. \qquad (6.26)
\end{aligned}
$$

Here, the B^+ and B^0 mesons productions are assumed to be the same, $f_u = f_d$. Also, the branching fractions $\mathcal{B}(B^+ \to \overline{D}^{*0}\tau^+\nu_\tau)$ and $\mathcal{B}(\overline{B}^0 \to D^{*-}\tau^+\nu_\tau)$ are assumed to be equal, based on isospin assumptions. The ratio $\mathcal{B}(D^{*+} \to D^0X)/\mathcal{B}(D^{*0} \to D^0X)$ is set to 0.677 from [9].

Parameter	Value
$f_{3\pi}^{D^0}$	0.836
$f_{3\pi}^{D^{*0}}$	0.844
$f_{3\pi}^{D^{*+}}$	0.853
$f_{D^{*+}/D^{*0}}$	0.142

Table 6.12: Values of the parameters needed as input for the nominal fit model.

7

Control samples

Contents

In the previous chapter, Chap. 6, the selections for the signals and normalisation modes have been described. However, before the fit to obtain the signal yields is performed, it is convenient to create additional control data samples that help to constrain the background contributions in the fit.

The data samples used for this end are referred to as the control samples, and by studying them, it is possible to apply data-driven corrections to simulated background samples. In this chapter, the two control samples used in this analysis are described.

7.1 The $B \to \overline{D}^0 D_s^+(X)$ decay model

By far, the main background contribution in the signal sample is due to inclusive $B \to \overline{D}^0 D_s^+(X)$ decays. Hence, it is necessary to create a control sample that allows to precisely model these decays. This control sample is produced by selecting exclusive $D_s^+ \to \pi^+\pi^-\pi^+$ events withing a $\pm 30\,\mathrm{MeV}/c^2$ mass window around the D_s^+ nominal mass.

The first step then is to divide the sample into two sub-samples:

- $\overline{D}^0 D_s^+$ sub-sample. This sample is produced by applying the same cuts as in the signal selection, except the requirement on the $m(3\pi)$ invariant mass. In particular,

the same vertex isolation requirements are applied. This highly suppresses events where the $\overline{D}^0$ comes from a $D^{*-} \to \overline{D}^0\pi^-$ decay. Thus, this sub-sample is composed by events without a D^{*-} decay and with no extra charged particles coming from the B or τ vertices.

- $D^{*-}D_s^+$ sub-sample. It is produced by requiring an additional track compatible with being a pion from a $D^{*-} \to \overline{D}^0\pi^-$ decay. Events with $m(\overline{D}^0\pi^-)$ in the range $[143, 148]\,\mathrm{MeV}/c^2$ are selected. In this sample, the pion from the D^{*-} decay is not taken into account when computing the vertex isolation variables $N^{\tau}_{iso}(p_T > 250; \chi^2_{\mathrm{IP}}(\mathrm{PV}) > 4; \chi^2_{\mathrm{IP}}(\tau) < 25)$ and $N^{B}_{iso}(p_T > 250; \chi^2_{\mathrm{IP}}(\mathrm{PV}) > 4; \chi^2_{\mathrm{IP}}(B) < 25)$. This sub-sample is thus enriched in events with a D^{*+} candidate with no additional charged particles coming from he B and τ vertices.

Then, the Monte Carlo sample is divided into multiple components and a one-dimensional simultaneous fit is performed to the $m'_{\overline{D}^0 D_s^+}$ distribution of the $\overline{D}^0 D_s^+$ sub-sample and the $m'_{D^{*-}D_s^+}$ distribution of the $D^{*-}D_s^+$ sub-sample. Here, $m'_{\overline{D}^0 D_s^+}$ ($m'_{D^{*-}D_s^+}$) is the invariant mass obtained by adding the reconstructed momenta of the $\overline{D}^0$ (D^{*-}) and of the D_s^+ candidates and then deconvoluting it by subtracting the reconstructed masses of the $\overline{D}^0$ (or D^{*-}) and of the D_s^+ mesons and adding their respective nominal masses from [9]:

$$m'_{\overline{D}^0 D_s^+} \equiv m_{\mathrm{meas.}}(\overline{D}^0 D_s^+) - m_{\mathrm{meas.}}(\overline{D}^0) - m_{\mathrm{meas.}}(D_s^+) + m_{\mathrm{PDG}}(\overline{D}^0) + m_{\mathrm{PDG}}(D_s^+). \quad (7.1)$$

$$m'_{D^{*-}D_s^+} \equiv m_{\mathrm{meas.}}(D^{*-}D_s^+) - m_{\mathrm{meas.}}(D^{*-}) - m_{\mathrm{meas.}}(D_s^+) + m_{\mathrm{PDG}}(D^{*-}) + m_{\mathrm{PDG}}(D_s^+). \quad (7.2)$$

The components used to describe the data are:

- $B^+ \to \overline{D}^0 D_s^+$,
- $B^+ \to \overline{D}^{*0} D_s^+$,
- $B^+ \to \overline{D}^0 D_s^{*+}$,
- $B^+ \to \overline{D}^{*0} D_s^{*+}$,
- $B^+ \to \overline{D}^0 D_{s1}(2460)^+$,
- $B^+ \to \overline{D}^{*0} D_{s1}(2460)^+$,
- $B^+ | B_s^0 \to \overline{D}^0 D_s^+ X$,
- $B^0 \to \overline{D}^0 D_s^+ X$,

- $B^0 \to D^{*-} D_s^+$,
- $B^0 \to D^{*-} D_s^{*+}$,
- $B^0 \to D^{*-} D_{s0}^*(2317)^+$,
- $B^0 \to D^{*-} D_{s1}(2460)^+$,
- background,

where $B^+|B_s^0 \to \overline{D}^0 D_s^+(X)$ indicates the component which contains decays originated from a B^+ or a B_s^0 that are not included in any of the other components, and $B^0 \to \overline{D}^0 D_s^+(X)$, the same but for B^0 decays.

A specific fit procedure is developed, that involve the following parameters:

- The relative yield of a component i with respect to the $B^+ \to \overline{D}^0 D_s^+$ component in the $\overline{D}^0 D_s^+$ sample,

$$F_i \equiv \frac{N_i^{(\overline{D}^0 D_s^+)}}{N_{B^+ \to \overline{D}^0 D_s^+}^{(\overline{D}^0 D_s^+)}}. \tag{7.3}$$

  In what follows, the super-index indicates the sub-sample and the sub-index the component.

- The relative yield of a component i with respect to the $B^0 \to D^{*-} D_s^+$ component in the $\overline{D}^0 D_s^+$ sample,

$$F_i^* \equiv \frac{N_i^{(\overline{D}^0 D_s^+)}}{N_{B^0 \to D^{*-} D_s^+}^{(\overline{D}^0 D_s^+)}}. \tag{7.4}$$

  By definition, these parameters are related to the first kind through the expression:

$$F_i = F_{B^0 \to D^{*-} D_s^+} F_i^*. \tag{7.5}$$

- The relative efficiency of a component i between the two sub-samples,

$$\epsilon_i \equiv \frac{N_i^{(D^{*-} D_s^+)}}{N_i^{(\overline{D}^0 D_s^+)}}. \tag{7.6}$$

For the free parameters in the fit, we will choose $N_{D_s^+}^{(\overline{D}^0 D_s^+)}$, the total number of signal events in the $\overline{D}^0 D_s^+$ sub-sample (events which are not background), and then either a F_i or a F_i^* parameter for each component. The F_i^* parameters are assigned only to three of the main components in the $D^{*-} D_s^+$ sub-sample ($B^0 \to D^{*-} D_s^{*+}$, $B^0 \to D^{*-} D_{s0}^*(2317)^+$ and $B^0 \to D^{*-} D_{s1}(2460)^+$), while a F_i free parameter is used for every other component.

The probability density functions (PDF) used to fit the data are:

$$\mathrm{PDF}^{(\overline{D}^0 D_s^+)}(m'_{\overline{D}^0 D_s^+}) = N_{\mathrm{WS}}^{(\overline{D}^0 D_s^+)} \mathrm{PDF}_{\mathrm{WS}}^{(\overline{D}^0 D_s^+)}(m'_{\overline{D}^0 D_s^+}) + \sum_i N_i^{(\overline{D}^0 D_s^+)} \mathrm{PDF}_i^{(\overline{D}^0 D_s^+)}(m'_{\overline{D}^0 D_s^+}), \tag{7.7}$$

for the $\overline{D}^0 D_s^+$ sub-sample, and

$$\mathrm{PDF}^{(D^{*-} D_s^+)}(m'_{D^{*-} D_s^+}) = \tag{7.8}$$

$$= N_{\mathrm{WS}}^{(D^{*-} D_s^+)} \mathrm{PDF}_{\mathrm{WS}}^{(D^{*-} D_s^+)}(m'_{D^{*-} D_s^+}) + \sum_i N_i^{(D^{*-} D_s^+)} \mathrm{PDF}_i^{(D^{*-} D_s^+)}(m'_{D^{*-} D_s^+}), \tag{7.9}$$

for the $D^{*-} D_s^+$ sub-sample. In these expressions, $\mathrm{PDF}_{\mathrm{WS}}^{(\overline{D}^0 D_s^+)}(m'_{\overline{D}^0 D_s^+})$ and $\mathrm{PDF}_{\mathrm{WS}}^{(D^{*-} D_s^+)}(m'_{D^{*-} D_s^+})$ are the $m'_{\overline{D}^0 D_s^+}$ and $m'_{D^{*-} D_s^+}$ PDFs, taken from the wrong-sign data sample, and $\mathrm{PDF}_i^{(\overline{D}^0 D_s^+)}(m'_{\overline{D}^0 D_s^+})$ and $\mathrm{PDF}_i^{(D^{*-} D_s^+)}(m'_{D^{*-} D_s^+})$ are the $m'_{\overline{D}^0 D_s^+}$ PDFs for the i^{th} component, taken from Monte Carlo. The wrong-sign sample is composed of D^0 and D_s^+ combinations with the incorrect charge, *i.e.* $D^0 D_s^+$ instead of the right-sign combination $\overline{D}^0 D_s^+$, and thus they are used to describe the background. The superscripts indicate to which sub-sample these quantities are referring to. The yields of each component in each sub-sample can be expressed uniquely in terms of the free parameters of the fit and the relative efficiencies, by using:

$$N_i^{(\overline{D}^0 D_s^+)} = N_{D_s^+}^{(\overline{D}^0 D_s^+)} \frac{F_i}{\sum_j F_j}, \tag{7.10}$$

and

$$N_i^{(D^{*-} D_s^+)} = N_{D_s^+}^{(\overline{D}^0 D_s^+)} \times \varepsilon_i \times \frac{F_i}{\sum_j F_j}, \tag{7.11}$$

where the relative efficiencies are calculated from Eq. 7.6 using simulation and are fixed parameters in the fit. The components of each PDF are shown in Tab. 7.1 and Tab. 7.2 for the $\overline{D}^0 D_s^+$ and $D^{*-} D_s^+$ sub-samples, respectively. In those tables, the sum of the F_i parameters is defined as:

$$\begin{aligned}
\sum_i F_i &= F_{B^+ \to \overline{D}^0 D_s^+} + F_{B^+ \to \overline{D}^{*0} D_s^+} + F_{B^+ \to \overline{D}^0 D_s^{*+}} + F_{B^+ \to \overline{D}^{*0} D_s^{*+}} \\
&+ F_{B^+ \to \overline{D}^0 D_{s1}(2460)^+} + F_{B^+ \to \overline{D}^{*0} D_{s1}(2460)^+} + F_{B^+ | B_s^0 \to \overline{D}^0 D_s^+ X} \\
&+ F_{B^0 \to \overline{D}^0 D_s^+ X} + F_{B^0 \to D^{*-} D_s^+} + F_{B^0 \to D^{*-} D_s^+} \times F^*_{B^0 \to D^{*-} D_s^{*+}} \\
&+ F_{B^0 \to D^{*-} D_s^+} \times F^*_{B^0 \to D^{*-} D^*_{s0}(2317)^+} \\
&+ F_{B^0 \to D^{*-} D_s^+} \times F^*_{B^0 \to D^{*-} D_{s1}(2460)^+},
\end{aligned} \tag{7.12}$$

where, by definition, $F_{B^+ \to \overline{D}^0 D_s^+} = 1$.

Component	**Yield**
$B^+ \to \overline{D}^0 D_s^+$	$N_{D_s^+}^{(\overline{D}^0 D_s^+)} \times F_{B^+ \to \overline{D}^0 D_s^+} / \sum_i F_i$
$B^+ \to \overline{D}^{*0} D_s^+$	$N_{D_s^+}^{(\overline{D}^0 D_s^+)} \times F_{B^+ \to \overline{D}^{*0} D_s^+} / \sum_i F_i$
$B^+ \to \overline{D}^0 D_s^{*+}$	$N_{D_s^+}^{(\overline{D}^0 D_s^+)} \times F_{B^+ \to \overline{D}^0 D_s^{*+}} / \sum_i F_i$
$B^+ \to \overline{D}^{*0} D_s^{*+}$	$N_{D_s^+}^{(\overline{D}^0 D_s^+)} \times F_{B^+ \to \overline{D}^{*0} D_s^{*+}} / \sum_i F_i$
$B^+ \to \overline{D}^0 D_{s1}(2460)^+$	$N_{D_s^+}^{(\overline{D}^0 D_s^+)} \times F_{B^+ \to \overline{D}^0 D_{s1}(2460)^+} / \sum_i F_i$
$B^+ \to \overline{D}^{*0} D_{s1}(2460)^+$	$N_{D_s^+}^{(\overline{D}^0 D_s^+)} \times F_{B^+ \to \overline{D}^{*0} D_{s1}(2460)^+} / \sum_i F_i$
$B^+ \vert B_s^0 \to \overline{D}^0 D_s^+ X$	$N_{D_s^+}^{(\overline{D}^0 D_s^+)} \times F_{B^+ \vert B_s^0 \to \overline{D}^0 D_s^+ X} / \sum_i F_i$
$B^0 \to \overline{D}^0 D_s^+ X$	$N_{D_s^+}^{(\overline{D}^0 D_s^+)} \times F_{B^0 \to \overline{D}^0 D_s^+ X} / \sum_i F_i$
$B^0 \to D^{*-} D_s^+$	$N_{D_s^+}^{(\overline{D}^0 D_s^+)} \times F_{B^0 \to D^{*-} D_s^+} / \sum_i F_i$
$B^0 \to D^{*-} D_s^{*+}$	$N_{D_s^+}^{(\overline{D}^0 D_s^+)} \times F_{B^0 \to D^{*-} D_s^+} \times F^*_{B^0 \to D^{*-} D_s^{*+}} / \sum_i F_i$
$B^0 \to D^{*-} D_{s0}^*(2317)^+$	$N_{D_s^+}^{(\overline{D}^0 D_s^+)} \times F_{B^0 \to D^{*-} D_s^+} \times F^*_{B^0 \to D^{*-} D_{s0}^*(2317)^+} / \sum_i F_i$
$B^0 \to D^{*-} D_{s1}(2460)^+$	$N_{D_s^+}^{(\overline{D}^0 D_s^+)} \times F_{B^0 \to D^{*-} D_s^+} \times F^*_{B^0 \to D^{*-} D_{s1}(2460)^+} / \sum_i F_i$
background in $\overline{D}^0 D_s^+$ sample	$N_{\mathrm{WS}}^{(\overline{D}^0 D_s^+)}$

Table 7.1: Yields for each component of $\mathrm{PDF}^{(\overline{D}^0 D_s^+)}(m'_{\overline{D}^0 D_s^+})$, the probability density function used used to fit the $\overline{D}^0 D_s^+$ control sample.

Component	**Yield**
$B^+ \to \overline{D}^0 D_s^+$	$N_{D_s^+}^{(\overline{D}^0 D_s^+)} \times \varepsilon_{B^+ \to \overline{D}^0 D_s^+} \times F_{B^+ \to \overline{D}^0 D_s^+} / \sum_i F_i$
$B^+ \to \overline{D}^{*0} D_s^+$	$N_{D_s^+}^{(\overline{D}^0 D_s^+)} \times \varepsilon_{B^+ \to \overline{D}^{*0} D_s^+} \times F_{B^+ \to \overline{D}^{*0} D_s^+} / \sum_i F_i$
$B^+ \to \overline{D}^0 D_s^{*+}$	$N_{D_s^+}^{(\overline{D}^0 D_s^+)} \times \varepsilon_{B^+ \to \overline{D}^0 D_s^{*+}} \times F_{B^+ \to \overline{D}^0 D_s^{*+}} / \sum_i F_i$
$B^+ \to \overline{D}^{*0} D_s^{*+}$	$N_{D_s^+}^{(\overline{D}^0 D_s^+)} \times \varepsilon_{B^+ \to \overline{D}^{*0} D_s^{*+}} \times F_{B^+ \to \overline{D}^{*0} D_s^{*+}} / \sum_i F_i$
$B^+ \to \overline{D}^0 D_{s1}(2460)^+$	$N_{D_s^+}^{(\overline{D}^0 D_s^+)} \times \varepsilon_{B^+ \to \overline{D}^0 D_{s1}(2460)^+} \times F_{B^+ \to \overline{D}^0 D_{s1}(2460)^+} / \sum_i F_i$
$B^+ \to \overline{D}^{*0} D_{s1}(2460)^+$	$N_{D_s^+}^{(\overline{D}^0 D_s^+)} \times \varepsilon_{B^+ \to \overline{D}^{*0} D_{s1}(2460)^+} \times F_{B^+ \to \overline{D}^{*0} D_{s1}(2460)^+} / \sum_i F_i$
$B^+ \vert B_s^0 \to \overline{D}^0 D_s^+ X$	$N_{D_s^+}^{(\overline{D}^0 D_s^+)} \times \varepsilon_{B^+ \vert B_s^0 \to \overline{D}^0 D_s^+ X} \times F_{B^+ \vert B_s^0 \to \overline{D}^0 D_s^+ X} / \sum_i F_i$
$B^0 \to \overline{D}^0 D_s^+ X$	$N_{D_s^+}^{(\overline{D}^0 D_s^+)} \times \varepsilon_{B^0 \to \overline{D}^0 D_s^+ X} \times F_{B^0 \to \overline{D}^0 D_s^+ X} / \sum_i F_i$
$B^0 \to D^{*-} D_s^+$	$N_{D_s^+}^{(\overline{D}^0 D_s^+)} \times \varepsilon_{B^0 \to D^{*-} D_s^+} \times F_{B^0 \to D^{*-} D_s^+} / \sum_i F_i$
$B^0 \to D^{*-} D_s^{*+}$	$N_{D_s^+}^{(\overline{D}^0 D_s^+)} \times \varepsilon_{B^0 \to D^{*-} D_s^{*+}} \times F_{B^0 \to D^{*-} D_s^+} \times F^*_{B^0 \to D^{*-} D_s^{*+}} / \sum_i F_i$
$B^0 \to D^{*-} D_{s0}^*(2317)^+$	$N_{D_s^+}^{(\overline{D}^0 D_s^+)} \times \varepsilon_{B^0 \to D^{*-} D_{s0}^*(2317)^+} \times F_{B^0 \to D^{*-} D_s^+} \times F^*_{B^0 \to D^{*-} D_{s0}^*(2317)^+} / \sum_i F_i$
$B^0 \to D^{*-} D_{s1}(2460)^+$	$N_{D_s^+}^{(\overline{D}^0 D_s^+)} \times \varepsilon_{B^0 \to D^{*-} D_{s1}(2460)^+} \times F_{B^0 \to D^{*-} D_s^+} \times F^*_{B^0 \to D^{*-} D_{s1}(2460)^+} / \sum_i F_i$
background in $D^{*-} D_s^+$ sample	$N_{\mathrm{WS}}^{(D^{*-} D_s^+)}$

Table 7.2: Yields for each component of $\mathrm{PDF}^{(D^{*-} D_s^+)}(m'_{D^{*-} D_s^+})$, the probability density function used to fit the $D^{*-} D_s^+$ control sample.

A simultaneous fit is done using these two PDFs, where the background yields $N_{\mathrm{WS}}^{(\overline{D}^0 D_s^+)}$ and $N_{\mathrm{WS}}^{(D^{*-} D_s^+)}$ are fixed to the number of events in the wrong-sign $\overline{D}^0 D_s^+$ and $D^{*+} D_s^+$ samples. The results are shown in Tab. 7.3 and Fig. 7.1. These results will be used to model the $B \to \overline{D}^0 D_s^+ X$ component in the signal fit (see Sec. 8.2.1).

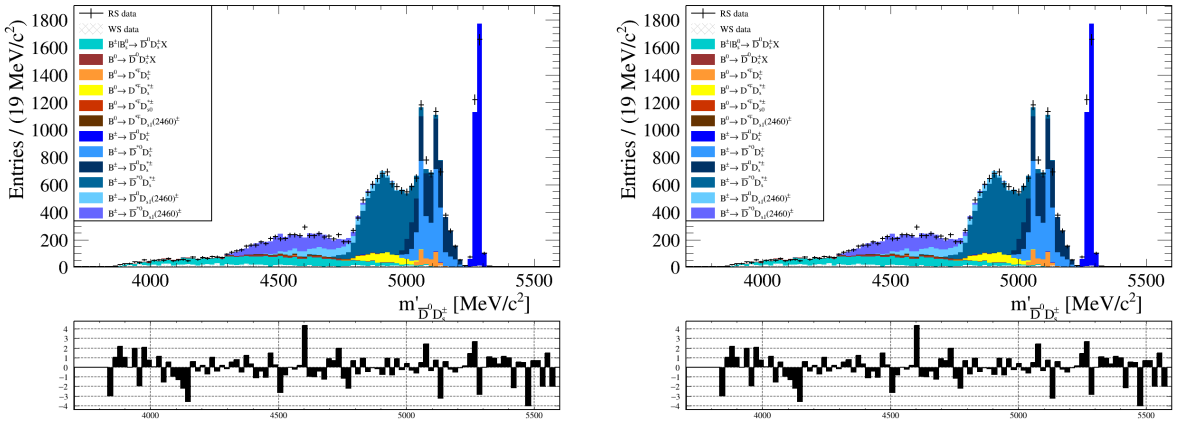

Figure 7.1: $\overline{D}^0 D_s^+$ (left) and $D^{*-} D_s^+$ (right) sub-samples invariant mass data and PDF after fitting.

Parameter	Fit result
$N_{MC}^{(\overline{D}^0 D_s^+)}$	21520 ± 150
$F_{B^+ \to \overline{D}^{*0} D_s^+}^{(\overline{D}^0 D_s^+)}$	0.915 ± 0.054
$F_{B^+ \to \overline{D}^0 D_s^{*+}}^{(\overline{D}^0 D_s^+)}$	0.935 ± 0.056
$F_{B^+ \to \overline{D}^{*0} D_s^{*+}}^{(\overline{D}^0 D_s^+)}$	1.829 ± 0.047
$F_{B^+ \to \overline{D}^0 D_{s1}(2460)^+}^{(\overline{D}^0 D_s^+)}$	0.332 ± 0.038
$F_{B^+ \to \overline{D}^{*0} D_{s1}(2460)^+}^{(\overline{D}^0 D_s^+)}$	0.710 ± 0.040
$F_{B^+ \mid B_s^0 \to \overline{D}^0 D_s^+ (X)}^{(\overline{D}^0 D_s^+)}$	0.817 ± 0.037
$F_{B^0 \to \overline{D}^0 D_s^+ (X)}^{(\overline{D}^0 D_s^+)}$	0.0991 ± 0.0092
$F_{B^0 \to D^{*-} D_s^+}^{(\overline{D}^0 D_s^+)}$	0.1205 ± 0.0041
$F_{B^0 \to D^{*-} D_s^{*+}}^{*(D^{*-} D_s^+)}$	1.763 ± 0.064
$F_{B^0 \to D^{*-} D_{s0}^*(2317)^+}^{*(D^{*-} D_s^+)}$	0.190 ± 0.046
$F_{B^0 \to D^{*-} D_{s1}(2460)^+}^{*(D^{*-} D_s^+)}$	0.443 ± 0.053

Table 7.3: Free parameters of the simultaneous fit, with their values as they are before and after the fit.

7.2 The prompt control sample

A small fraction of decays of B hadrons into a $\overline{D}^0$ meson and three pions produced at the B vertex (without the presence of a hadron with non-negligible lifetime), referred to as *prompt*, pass the distance-detachment cut and hence they are present in the signal-selection sample. They sit at the low-lifetime region, as is the case of signal events. Therefore, it is important to produce a control sample to improve the modelling of this component.

To obtain the control sample for *prompt* B decays, a cut in the distance in the z coordinate between the B and the 3π vertices divided by its uncertainty is applied. Events in the range $-3 < (z_{3\pi} - z_B)/\sigma_z < 0$ are selected. The lower cut suppresses combinatorial background, while the upper cut also suppresses contributions from decays that have the 3π vertex displaced from the B vertex. This sample is further restricted by using the decay vertex of the reconstructed $\overline{D}^0$ meson, requiring $z_{\overline{D}^0} - z_B > 0$, to further suppress combinatorial background.

As seen in Fig. 7.2, the Monte Carlo sample does not correctly reproduce the data. To correct this, a 2D histogram in the BDT and q^2 variables is used, with the same binning as the one used in the signal fit, and weights are applied to make the Monte Carlo sample match the data.

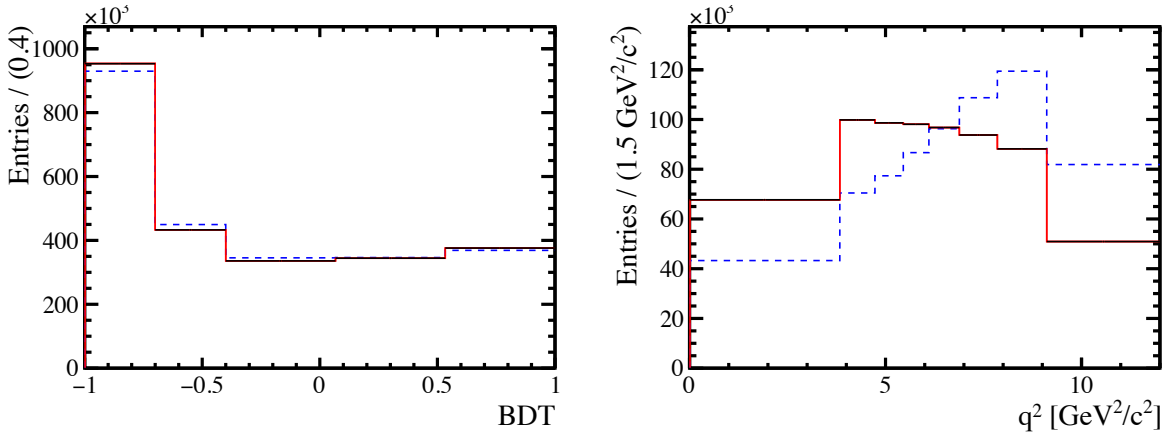

Figure 7.2: BDT output and q^2 distributions for the prompt control sample. The dashed blue line represents the original Monte Carlo sample, while the red line is the Monte Carlo sample after re-weighting in these variables. Data is shown in black. The distributions are normalised to the number of events in data.

8

Measurement of $B^+ \to \overline{D}^0 \tau^+ \nu_\tau$ and $B^+ \to \overline{D}^{*0} \tau^+ \nu_\tau$ branching fractions

Contents

8.1 Determination of the normalisation yield

In the following, the determination of the normalisation yield will be presented, according to the method introduced in Chap. 5. As normalisation channel, the $B^+ \to \overline{D}^0 D_s^+$ decay is used. Events are required to pass the normalisation selection. The normalisation yield is obtained from a one-dimensional fit to the deconvoluted mass:

$$m'_{\overline{D}^0 D_s^+} \equiv m_{\text{meas.}}(\overline{D}^0 D_s^+) - m_{\text{meas.}}(\overline{D}^0) - m_{\text{meas.}}(D_s^+) + m_{\text{PDG}}(\overline{D}^0) + m_{\text{PDG}}(D_s^+), \quad (8.1)$$

in a window mass of $\pm 60\,\text{MeV}/c^2$ around the B^+ best-known mass [9].

In order to describe this shape, a Crystal Ball (C.B.) function is used to describe the mass peak, and an exponential function to describe the background. First, a fit to the $B^+ \to \overline{D}^0 D_s^+$ Monte Carlo sample is performed using only the C.B. function. The result of this first fit is used to extract the tail parameters of the C.B. function. Then, a fit to the data sample is performed using the full model, with all parameters floating except the C.B. tail parameters, which are fixed to the result of the first fit.

The obtained yield is 3047 ± 56 events, and the fit result is shown in Fig. 8.1.

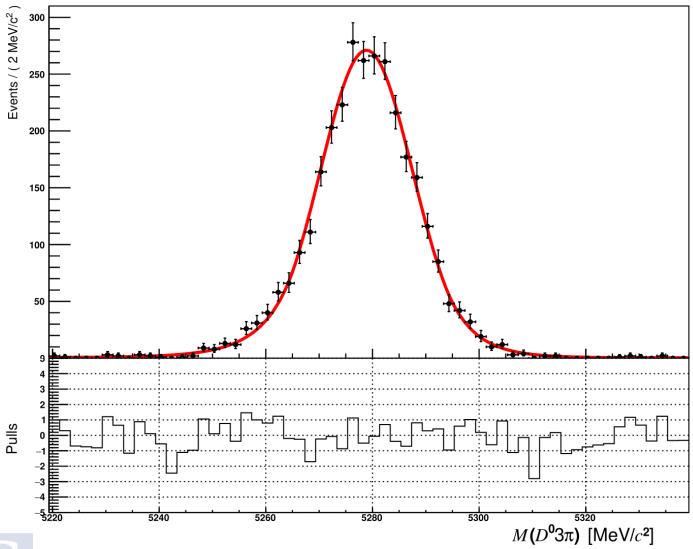

Figure 8.1: Fit to the $m'_{\overline{D}^0 D_s^+}$ distribution after the selection of the $B^+ \to \overline{D}^0 D_s^+$ mass peak. The shape is described by an exponential function and a C.B. function, with its tail parameters fixed to those obtained in a fit to the Monte Carlo sample.

8.2 Determination of the signal yields

8.2.1 Fit model

The yields of $B^+ \to \overline{D}^0 \tau^+ \nu_\tau$ and $B^+ \to \overline{D}^{*0} \tau^+ \nu_\tau$ are extracted from a 3-dimensional template fit to the τ decay time, squared dilepton mass, q^2, and BDT distributions. The templates for signals and backgrounds are produced from the corresponding Monte Carlo samples. The binning is chosen such taht each bin of each variable contains approximately the same number of events in data. The number of bins are 8 for the τ decay time, 8 for the q^2 and 3 bins for the BDT. The templates used for the signals and the main background components are shown in Figs. 8.2, 8.3, 8.4 and 8.5.

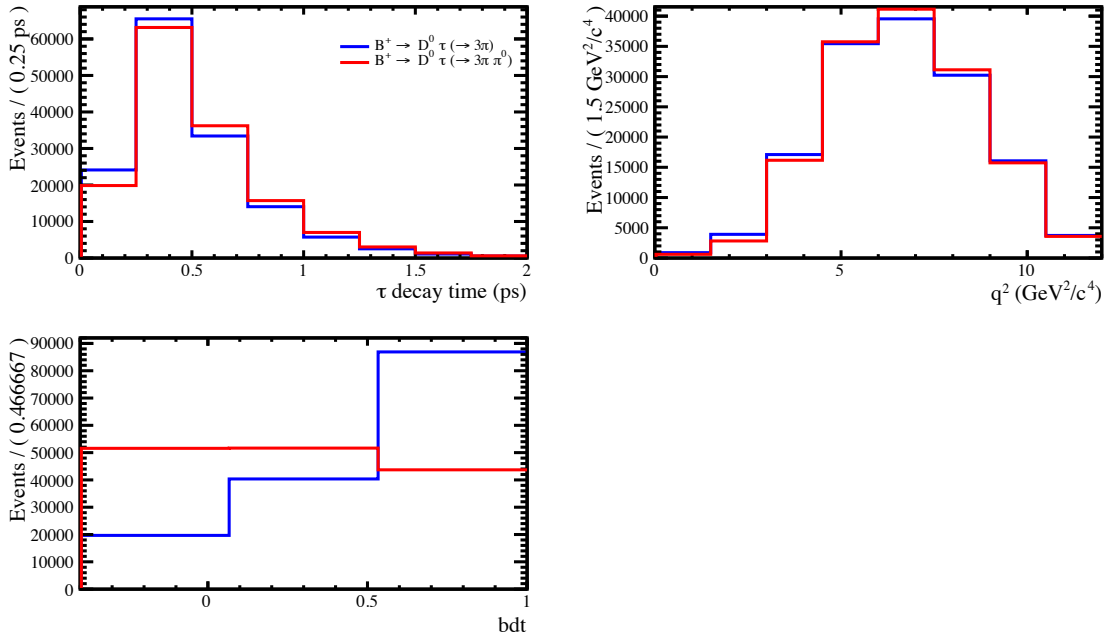

Figure 8.2: Templates used in the signal fit model for $B^+ \to D^0\tau\nu$ decays with $\tau^+ \to \pi^+\pi^-\pi^+\overline{\nu}_\tau$ (red) and $\tau^+ \to \pi^+\pi^-\pi^+\pi^0\overline{\nu}_\tau$ (blue).

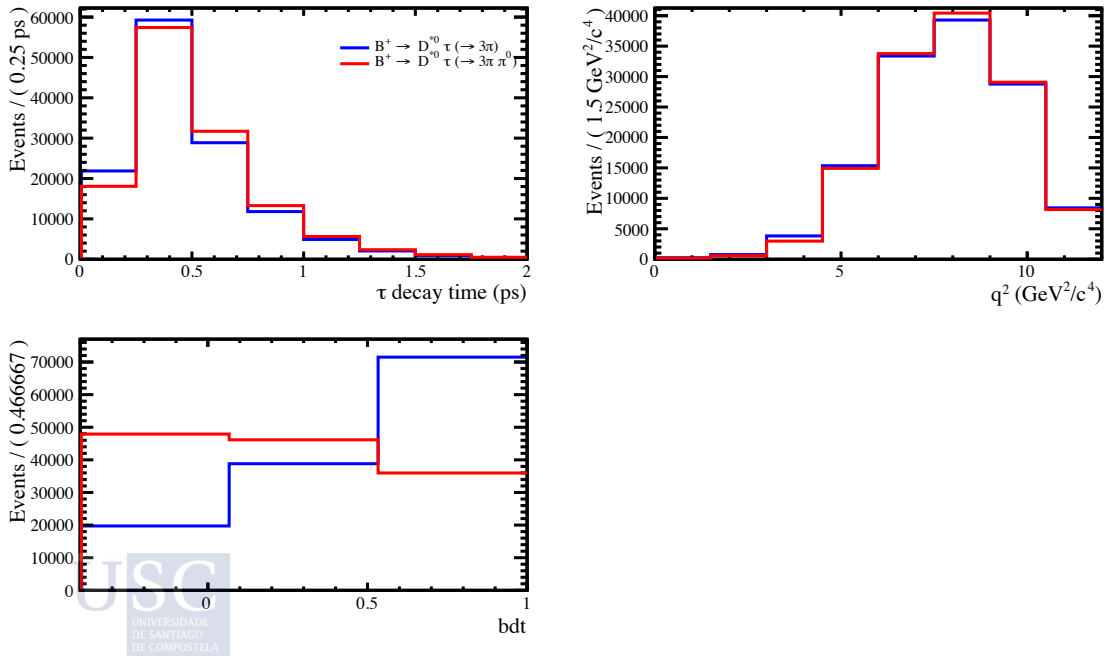

Figure 8.3: Templates used in the signal fit model for $B^+ \to D^{*0}\tau\nu$ with $\tau^+ \to \pi^+\pi^-\pi^+\overline{\nu}_\tau$ (red) and $\tau^+ \to \pi^+\pi^-\pi^+\pi^0\overline{\nu}_\tau$ (blue).

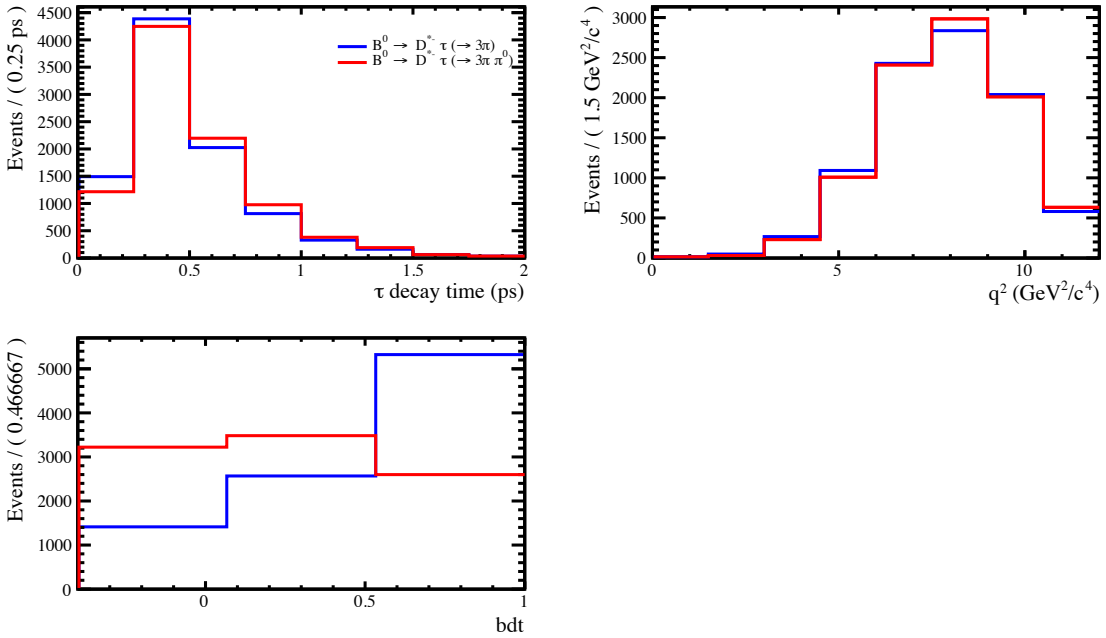

Figure 8.4: Templates used in the signal fit model for $B^0 \to D^{*-}\tau\nu$ decays with $\tau^+ \to \pi^+\pi^-\pi^+\overline{\nu}_\tau$ (red) and $\tau^+ \to \pi^+\pi^-\pi^+\pi^0\overline{\nu}_\tau$ (blue).

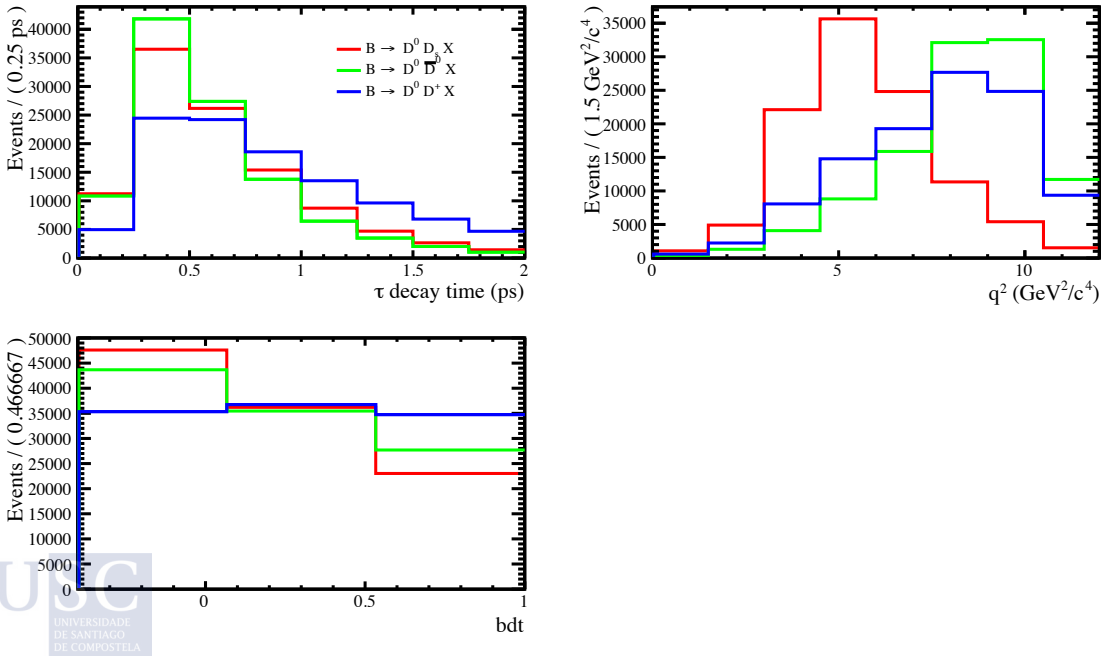

Figure 8.5: Templates used in the signal fit model for $B \to D^0 D_s^+ X$ (red), $B \to D^0 \overline{D}^0 X$ (green) and $B \to D^0 D^+ X$ (blue).

8.2.2 Feed down from $\overline{B} \to D^{**}\tau^-\overline{\nu}_\tau$ decays

Contributions from semitauonic B decays into excited charmed mesons, which will be generically referred as $B \to D^{**}\tau^-\overline{\nu}_\tau$, are a critical point in this analysis since their branching fractions have not been measured. In this work, a total of ten decays of this kind are taken into account:

- $B^- \to D_1(2420)^0\tau^-\overline{\nu}_\tau$,
- $B^- \to D_2^*(2460)^0\tau^-\overline{\nu}_\tau$,
- $B^- \to D_0^*(2300)^0\tau^-\overline{\nu}_\tau$,
- $B^- \to D_1'(2430)^0\tau^-\overline{\nu}_\tau$,
- $\overline{B}^0 \to D_1(2420)^+\tau^-\overline{\nu}_\tau$,
- $\overline{B}^0 \to D_2^*(2460)^+\tau^-\overline{\nu}_\tau$,
- $\overline{B}^0 \to D_0^*(2300)^+\tau^-\overline{\nu}_\tau$,
- $\overline{B}^0 \to D_1'(2430)^+\tau^-\overline{\nu}_\tau$,
- $\overline{B}_s^0 \to D_{s1}'(2536)^+\tau^-\overline{\nu}_\tau$ and
- $\overline{B}_s^0 \to D_{s2}^*(2573)^+\tau^-\overline{\nu}_\tau$.

The procedure to determine their their branching fractions is based on theoretical predictions of the LFU ratios:

$$\mathcal{R}(D^{**}) = \frac{\mathcal{B}(\overline{B} \to D^{**}\tau^-\overline{\nu}_\tau)}{\mathcal{B}(\overline{B} \to D^{**}\ell^-\overline{\nu}_\ell)}, \tag{8.2}$$

together with experimental measurements of $\mathcal{B}(B \to D^{**}\ell^-\overline{\nu}_\ell)$. In particular, the recent work [153]("Approximation C") is followed, from which the $\mathcal{R}(D^{**})$ ratios are predicted to be:

$$\begin{aligned}
\mathcal{R}_{\rm SM}(D_1) &= 0.10 \pm 0.01, \\
\mathcal{R}_{\rm SM}(D_2^*) &= 0.07 \pm 0.01, \\
\mathcal{R}_{\rm SM}(D_0^*) &= 0.08 \pm 0.03, \\
\mathcal{R}_{\rm SM}(D_1') &= 0.06 \pm 0.02, \\
\mathcal{R}_{\rm SM}(D_{s1}') &= 0.09 \pm 0.02, \\
\mathcal{R}_{\rm SM}(D_{s2}^*) &= 0.07 \pm 0.01,
\end{aligned} \tag{8.3}$$

where the different symbols stand for:

$$
\begin{aligned}
D_1 &\equiv D_1(2420)^+/D_1(2420)^0, && (8.4)\\
D_2^* &\equiv D_2^*(2460)^+/D_2^*(2460)^0,\\
D_0^* &\equiv D_0^*(2300)^+/D_0^*(2300)^0,\\
D_1' &\equiv D_1'(2430)^+/D_1'(2430)^0, && (8.5)\\
D_{s1}' &\equiv D_{s1}'(2536)^+,\\
D_{s2}^* &\equiv D_{s2}^*(2573)^+.
\end{aligned}
$$

Using these predictions and measurements of $\mathcal{B}(\overline{B} \to D^{**}\ell^-\overline{\nu}_\ell)$ [9], the branching fractions $\mathcal{B}(\overline{B} \to D^{**}\tau^-\overline{\nu}_\tau)$ can be estimated.

On one hand, D_2^*, D_1, D_1' and D_0^* mesons decay strongly into a charm meson and pions. Their branching fractions have been estimated using experimental measurements and isospin relations in [154] and are summarized in Tab. 8.1. On the other hand, for the $D_{s1}'^+$ (D_{s2}^{*+}) meson, it is assumed that it decays 50% of the times into $D^{*0}K^+$ (D^0K^+) and 50% into $D^{*+}K^0$ (D^+K^0).

Parent	**Final State**				
	$D^*\pi^+$	$D^*\pi^0$	$D\pi^+$	$D\pi^0$	$\sum D\pi\pi$
D_2^*	0.26	0.13	0.40	0.20	—
D_1	0.42	0.21	—	—	0.36
D_1'	0.67	0.33	—	—	—
D_0^*	—	—	0.67	0.33	—

Table 8.1: Estimates for D^{**} strong decay branching fractions to exclusive two-body decays, and the sum of non-D^*-resonant three-body decays, $\sum D\pi\pi$. Table taken from [154] (Table XVI) and based on the approach of [153] and measurements from [155].

The D_1 meson can decay through non-D^*-resonant three-body decays, $\sum D\pi\pi$. Hence, it is necessary to split these modes into $D\pi^+\pi^-$, $D\pi^0\pi^0$ and $D\pi^0\pi^+$. Approximate isospin conservation by the strong interaction can be used to estimate the value of several ratios of D^* branching fractions. The branching fractions for D_1^0 and D_1^+ mesons into three particles have been computed, and the results are Tab. 8.2.

Parent	**Final State**						
	$D^*\pi^+$	$D^*\pi^0$	$D\pi^+$	$D\pi^0$	$D\pi^+\pi^-$	$D\pi^0\pi^0$	$D\pi^0\pi^+$
D_1^0	0.42	0.21	—	—	0.24	0.04	0.08
D_1^+	0.42	0.21	—	—	0.02	0.11	0.23

Table 8.2: Estimates for D_1 strong decay branching fractions to exclusive two body decays and non-D^*-resonant three-body decays using the isospin relations.

Using the estimated D^{**} decays branching fractions and the measurements of $\mathcal{B}(\overline{B} \to D^{**}(\to D^{(*)}X)\ell^-\overline{\nu}_\ell)$ from [9], the $\overline{B} \to D^{**}\tau^-\overline{\nu}_\tau$ and $\overline{B} \to D^{**}(\to D^0X)\tau^-\overline{\nu}_\tau$ branching fractions can be estimated. The results are shown in Tab. 8.4.

As a cross-check, in Tab. 8.3, the total branching fractions $\mathcal{B}(B^- \to D^{**}\ell^-\overline{\nu}_\ell)$ and $\mathcal{B}(\overline{B}^0 \to D^{**}\ell^-\overline{\nu}_\ell)$ are compared to the experimental measurements from Ref. [9], finding an excellent agreement.

Parent	**Estimated** $\boldsymbol{\mathcal{B}(\overline{B} \to D^{**}\ell\nu)}$ (%)	$\boldsymbol{\mathcal{B}(\overline{B} \to D^{(*)}n\pi\ell\nu)\ (n \geq 1)}$ from [9] (%)
B^-	1.88 ± 0.13	1.88 ± 0.25
$\overline{B}^0$	1.86 ± 0.24	2.3 ± 0.5

Table 8.3: Comparison between the estimated $\mathcal{B}(B^- \to D^{**}\ell^-\overline{\nu}_\ell)$ and $\mathcal{B}(\overline{B}^0 \to D^{**}\ell^-\overline{\nu}_\ell)$ branching fractions and the measurements from [9].

Once the branching fractions for $\overline{B} \to D^{**}\tau^-\overline{\nu}_\tau$ decays are obtained, it is possible to estimate their yields relative to the $B^+ \to \overline{D}^{*0}\tau^+\nu_\tau$ signal,

$$f_{D^{**}/D^{*0}} = \frac{N(\overline{B} \to D^{**}\tau^-\overline{\nu}_\tau)}{N(B^+ \to \overline{D}^{*0}\tau^+\nu_\tau)}, \tag{8.6}$$

in the signal-selection sample. This can be done through the expression:

$$f_{D^{**}/D^{*0}} = \frac{\mathcal{B}(B^- \to D^{**}\tau^-\overline{\nu}_\tau) \times \frac{\varepsilon_{B^- \to D^{**}}}{\varepsilon_{B^- \to D^{*0}}} + \mathcal{B}(\overline{B}^0 \to D^{**}\tau^-\overline{\nu}_\tau) \times \frac{f_d}{f_u} \times \frac{\varepsilon_{\overline{B}^0 \to D^{**}}}{\varepsilon_{B^- \to D^{*0}}} + \mathcal{B}(\overline{B}_s^0 \to D^{**}\tau^-\overline{\nu}_\tau) \times \frac{f_s}{f_u} \times \frac{\varepsilon_{\overline{B}_s^0 \to D^{**}}}{\varepsilon_{B^- \to D^{*0}}}}{\mathcal{B}(B^- \to D^{*0}\tau^-\overline{\nu}_\tau) \times \mathcal{B}(D^{*0} \to D^0X)}, \tag{8.7}$$

where $\varepsilon_{B^- \to D^{**}}/\varepsilon_{B^- \to D^{*0}}$, $\varepsilon_{\overline{B}^0 \to D^{**}}/\varepsilon_{B^- \to D^{*0}}$ and $\varepsilon_{\overline{B}_s^0 \to D^{**}}/\varepsilon_{B^- \to D^{*0}}$ are the relative efficiencies for $B^- \to D^{**}\tau^-\overline{\nu}_\tau$, $\overline{B}^0 \to D^{**}\tau^-\overline{\nu}_\tau$ and $\overline{B}_s^0 \to D^{**}\tau^-\overline{\nu}_\tau$ decays with respect to signal $B^+ \to \overline{D}^{*0}\tau^+\nu_\tau$ decays; f_d/f_u and f_s/f_u are the ratios of fragmentation fractions, where $f_d/f_u = 1$ and f_s/f_u is taken from Ref. [156], and $\mathcal{B}(D^{*0} \to D^0X)$ is taken to be 100%. This results in

$$f_{D^{**}/D^{*0}} = 0.043, \tag{8.8}$$

which is set as a fixed parameter in the signal fit.

Decay	D^{**} decays used in measurement	$\mathcal{B}$ from [9] (%)	Estimated $\mathcal{B}(\overline{B} \to D^{**}\ell\overline{\nu}_\ell)$ (%)	$\mathcal{B}(\overline{B} \to D^{**}\ell\overline{\nu}_\ell)$ estimation from [153] (%)	Estimated $\mathcal{B}(\overline{B} \to D^{**}\ell\overline{\nu}_\ell) \times \mathcal{B}(D^{**} \to D^0X)$ (%)	$\mathcal{R}(D^{**})$ from [153]	Estimated $\mathcal{B}(\overline{B} \to D^{**}\tau\overline{\nu}_\tau) \times \mathcal{B}(D^{**} \to D^0X)$ (%)
$B^- \to D_1^0\ell^-\overline{\nu}_\ell$	$D_1^0 \to D^{*+}\pi^-$	0.303 ± 0.020	0.721 ± 0.048	0.67 ± 0.05	0.55 ± 0.04	0.10 ± 0.01	0.055 ± 0.007
$B^- \to D_2^{*0}\ell^-\overline{\nu}_\ell$	$D_2^{*0} \to D^{*+}\pi^-$	0.101 ± 0.024	0.385 ± 0.044	0.30 ± 0.04	0.194 ± 0.022	0.07 ± 0.01	0.014 ± 0.002
	$D_2^{*0} \to D^+\pi^-$	0.153 ± 0.016					
$B^- \to D_1^{0\prime}\ell^-\overline{\nu}_\ell$	$D_1^{0\prime} \to D^{*+}\pi^-$	0.27 ± 0.06	0.403 ± 0.090	0.20 ± 0.05	0.313 ± 0.070	0.06 ± 0.02	0.019 ± 0.008
$B^- \to D_0^{*0}\ell^-\overline{\nu}_\ell$	$D_0^{*0} \to D^+\pi^-$	0.25 ± 0.05	0.373 ± 0.075	0.44 ± 0.08	0.123 ± 0.025	0.08 ± 0.03	0.010 ± 0.004
$\overline{B}^0 \to D_1^+\ell^-\overline{\nu}_\ell$	$D_1^+ \to D^{*0}\pi^+$	0.280 ± 0.028	0.667 ± 0.067	—	0.525 ± 0.052	0.10 ± 0.01	0.052 ± 0.007
$\overline{B}^0 \to D_2^{*+}\ell^-\overline{\nu}_\ell$	$D_2^{*+} \to D^{*0}\pi^+$	0.068 ± 0.012	0.286 ± 0.053	—	0.214 ± 0.040	0.07 ± 0.01	0.015 ± 0.004
	$D_2^{*+} \to D^0\pi^+$	0.121 ± 0.033		—			
$\overline{B}^0 \to D_1^{0\prime}\ell^-\overline{\nu}_\ell$	$D_1^{0\prime} \to D^{*0}\pi^+$	0.31 ± 0.09	0.463 ± 0.134	—	0.412 ± 0.120	0.06 ± 0.02	0.025 ± 0.011
$\overline{B}^0 \to D_0^{*+}\ell^-\overline{\nu}_\ell$	$D_0^{*+} \to D^0\pi^+$	0.30 ± 0.12	0.448 ± 0.179	—	0.30 ± 0.12	0.08 ± 0.03	0.024 ± 0.013
$\overline{B}_s^0 \to D_{s1}^{0\prime}\ell^-\overline{\nu}_\ell X$	$D_{s1}^{0\prime} \to D^{*0}K^+$	0.44 ± 0.13	0.88 ± 0.26	—	0.73 ± 0.22	$0.09 \pm 0.02^*$	0.066 ± 0.024
$\overline{B}_s^0 \to D_{s2}^{*+}\ell^-\overline{\nu}_\ell X$	$D_{s2}^{*+} \to D^0K^+$	0.27 ± 0.10	0.54 ± 0.20	—	0.27 ± 0.10	$0.07 \pm 0.01^*$	0.019 ± 0.008

Table 8.4: Branching fractions measurements of $\overline{B} \to D^{**}(\to D^{(*)}X)\ell^-\overline{\nu}_\ell$ decays and all other inputs needed to estimate $\mathcal{B}(\overline{B} \to D^{**}\tau^-\overline{\nu}_\tau) \times \mathcal{B}(D^{**} \to D^0X)$ in this work. The estimated $\mathcal{B}(B^- \to D^{**}\tau^-\overline{\nu}_\tau)$ are compared with the results from [153].

8.2.3 Summary on the signal fit model

The model used in the signal fit to data is summarized in the Tab. 8.5. The meaning of the parameters that appear in that table is the following:

- $N(B^+ \to \overline{D}^0\tau^+\nu_\tau)$ is a free parameter accounting for the number of signal $B^+ \to \overline{D}^0\tau^+\nu_\tau$ events.
- $N(B^+ \to \overline{D}^{*0}\tau^+\nu_\tau)$ is a free parameter accounting for the number of signal $B^+ \to \overline{D}^{*0}\tau^+\nu_\tau$ events.
- $f_{3\pi}^{D^0}$ is the fraction of $\tau^+ \to 3\pi\overline{\nu}_\tau$ decays with respect to the sum of $\tau^+ \to 3\pi\overline{\nu}_\tau$ and $\tau^+ \to 3\pi\pi^0\overline{\nu}_\tau$ for $B^+ \to \overline{D}^0\tau^+\nu_\tau$ decays. Its value is fixed to 0.836.
- $f_{3\pi}^{D^{*0}}$ is the fraction of $\tau^+ \to 3\pi\overline{\nu}_\tau$ with respect to to the sum of $\tau^+ \to 3\pi\overline{\nu}_\tau$ and $\tau^+ \to 3\pi\pi^0\overline{\nu}_\tau$ for $\overline{B}^0 \to D^{*-}\tau^+\nu_\tau$ decays. Its value is fixed to 0.844.
- $f_{3\pi}^{D^{*-}}$ is the fraction of $\tau^+ \to 3\pi\overline{\nu}_\tau$ with respect to to the sum of $\tau^+ \to 3\pi\overline{\nu}_\tau$ and $\tau^+ \to 3\pi\pi^0\overline{\nu}_\tau$ in decays with a D^{*-}. The value is fixed to 0.853.
- $f_{D^{*-}/D^{*0}}$ is the amount of $B^0 \to D^{*-}\tau^+\nu_\tau$ decays relative to $B^+ \to \overline{D}^{*0}\tau^+\nu_\tau$ decays. The value is fixed to 0.142.
- $f_{D^{**}/D^{*0}}$ is the amount of $B \to D^{**}\tau^+\nu_\tau$ decays relative to $B^+ \to \overline{D}^{*0}\tau^+\nu_\tau$ decays. It is fixed to 0.043.
- $N(B \to \overline{D}^0 D^0 X)$ is the number of $B \to \overline{D}^0 D^0 X$ events. A Gaussian constraint of 15% is applied on this yield, based on the measurement of the yield of $\overline{D}^0 \to K^+ 3\pi^\pm$ decays.
- $N(B \to \overline{D}^0 D^+ X)$ is the number of $B \to \overline{D}^0 D^+ X$ events. This is a free parameter.
- $N(B \to \overline{D}^0 3\pi X)$ is the number of *prompt* events $B \to \overline{D}^0 3\pi X$. This is a free parameter.
- $N_{comb-bkg}$ is the number of combinatorial events where the D^0 and the three pions come from different decays. This is a fixed parameter, based on the number of events with $m(\overline{D}^0 3\pi)$ invariant mass above the B^+ best-known mass.
- $N_{not\overline{D}^0}$ is the number of combinatorial background events giving a fake $\overline{D}^0$. This yield is fixed to the number of events observed in the $\overline{D}^0$ sidebands.
- $N_{D_s^+}$ is the number of decays involving a D_s^+. This is a free parameter. The D_s^+ model is described in detail in Sec. 7.1.
- F_i is relative yield of a component i with respect to the $B^+ \to \overline{D}^0 D_s^+$ component, so $F_i \equiv \frac{N_i}{N_{B^+ \to \overline{D}^0 D_s^+}}$ (see Sec. 7.1). They are used as constraints.

- F_i^* is relative yield of a component i with respect to the $B^0 \to D^{*-} D_s^+$ component, *i.e.* $F_i^* \equiv \frac{N_i}{N_{B^0 \to D^{*-} D_s^+}}$ (see Sec. 7.1). These parameters are fixed.
- The ϵ_i parameters correspond to the relative efficiencies of a component i between the $B^+ \to \overline{D}^0 D_s^+(X)$ control sample and the signal sample.
- $\sum_i \epsilon_i F_i$ is given by:

$$\begin{aligned}\sum_i \epsilon_i F_i = {} & \epsilon_{B^+ \to \bar{D}^0 D_s^+} \times F_{B^+ \to \bar{D}^0 D_s^+} + \epsilon_{B^+ \to \bar{D}^{*0} D_s^+} \times F_{B^+ \to \bar{D}^{*0} D_s^+} + \epsilon_{B^+ \to \bar{D}^0 D_s^{*+}} \times F_{B^+ \to \bar{D}^0 D_s^{*+}} \\ & + \epsilon_{B^+ \to \bar{D}^{*0} D_s^{*+}} \times F_{B^+ \to \bar{D}^{*0} D_s^{*+}} + \epsilon_{B^+ \to \bar{D}^0 D_{s1}(2460)^+} \times F_{B^+ \to \bar{D}^0 D_{s1}(2460)^+} \\ & + \epsilon_{B^+ \to \bar{D}^{*0} D_{s1}(2460)^+} \times F_{B^+ \to \bar{D}^{*0} D_{s1}(2460)^+} + \epsilon_{B^+ | B_s^0 \to \bar{D}^0 D_s^+(X)} \times F_{B^+ | B_s^0 \to \bar{D}^0 D_s^+(X)} \\ & + \epsilon_{B^0 \to \bar{D}^0 D_s^+ X} \times F_{B^0 \to \bar{D}^0 D_s^+ X} + \epsilon_{B^0 \to D^{*-} D_s^+} \times F_{B^0 \to D^{*-} D_s^+} \\ & + \epsilon_{B^0 \to D^{*-} D_s^{*+}} \times F_{B^0 \to D^{*-} D_s^+} \times F^*_{B^0 \to D^{*-} D_s^{*+}} \\ & + \epsilon_{B^0 \to D^{*-} D_s^+} \times F_{B^0 \to D^{*-} D_s^+} \times F^*_{B^0 \to D^{*-} D^*_{s0}(2317)^+} \\ & + \epsilon_{B^0 \to D^{*-} D_{s1}(2460)^+} \times F_{B^0 \to D^{*-} D_s^+} \times F^*_{B^0 \to D^{*-} D_{s1}(2460)^+},\end{aligned} \tag{8.9}$$

where $F_{B^+ \to \bar{D}^0 D_s^+} = 1$ and $\epsilon_{B^+ \to \bar{D}^0 D_s^+} = 1$.

Component	Yield
$B^+ \to \overline{D}^0\tau^+\nu_\tau$, $\tau^+ \to 3\pi\overline{\nu}_\tau$	$N(B^+ \to \overline{D}^0\tau^+\nu_\tau) \times f_{3\pi}^{D^0}$
$B^+ \to \overline{D}^0\tau^+\nu_\tau$, $\tau^+ \to 3\pi\pi^0\overline{\nu}_\tau$	$N(B^+ \to \overline{D}^0\tau^+\nu_\tau) \times (1 - f_{3\pi}^{D^0})$
$B^+ \to \overline{D}^{*0}\tau^+\nu_\tau$, $\tau^+ \to 3\pi\overline{\nu}_\tau$	$N(B^+ \to \overline{D}^{*0}\tau^+\nu_\tau) \times f_{3\pi}^{D^{*0}}$
$B^+ \to \overline{D}^{*0}\tau^+\nu_\tau$, $\tau^+ \to 3\pi\pi^0\overline{\nu}_\tau$	$N(B^+ \to \overline{D}^{*0}\tau^+\nu_\tau) \times (1 - f_{3\pi}^{D^{*0}})$
$B^0 \to D^{*-}\tau^+\nu_\tau$, $\tau^+ \to 3\pi\overline{\nu}_\tau$	$N(B^0 \to D^{*-}\tau^+\nu_\tau) \times f_{D^{*-}/D^{*0}} \times f_{3\pi}^{D^{*-}}$
$B^0 \to D^{*-}\tau^+\nu_\tau$, $\tau^+ \to 3\pi\pi^0\overline{\nu}_\tau$	$N(B^+ \to \overline{D}^{*0}\tau^+\nu_\tau) \times f_{D^{*-}/D^{*0}} \times (1 - f_{3\pi}^{D^{*-}})$
$B \to D^{**}\tau^+\nu_\tau$	$N(B^+ \to \overline{D}^{*0}\tau^+\nu_\tau) \times f_{D^{**}/D^{*0}}$
$B \to \overline{D}^0 D^0 X$	$N(B \to \overline{D}^0 D^0 X)$
$B \to \overline{D}^0 D^+ X$	$N(B \to \overline{D}^0 D^+ X)$
$B \to \overline{D}^0 3\pi X$	$N(B \to \overline{D}^0 3\pi X)$
Comb. background $\overline{D}^0/3\pi$	$N_{comb-bkg}$
not $\overline{D}^0$	$N_{not\overline{D}^0}$ ($\overline{D}^0$ sideband)
$B^+ \to \overline{D}^0 D_s^+$	$N_{D_s^+} \times \epsilon_{B^+\to\overline{D}^0 D_s^+} \times F_{B^+\to\overline{D}^0 D_s^+} / \sum_i \epsilon_i F_i$
$B^+ \to \overline{D}^{*0} D_s^+$	$N_{D_s^+} \times \epsilon_{B^+\to\overline{D}^{*0} D_s^+} \times F_{B^+\to\overline{D}^{*0} D_s^+} / \sum_i \epsilon_i F_i$
$B^+ \to \overline{D}^0 D_s^{*+}$	$N_{D_s^+} \times \epsilon_{B^+\to\overline{D}^0 D_s^{*+}} \times F_{B^+\to\overline{D}^0 D_s^{*+}} / \sum_i \epsilon_i F_i$
$B^+ \to \overline{D}^{*0} D_s^{*+}$	$N_{D_s^+} \times \epsilon_{B^+\to\overline{D}^{*0} D_s^{*+}} \times F_{B^+\to\overline{D}^{*0} D_s^{*+}} / \sum_i \epsilon_i F_i$
$B^+ \to \overline{D}^0 D_{s1}(2460)^+$	$N_{D_s^+} \times \epsilon_{B^+\to\overline{D}^0 D_{s1}(2460)^+} \times F_{B^+\to\overline{D}^0 D_{s1}(2460)^+} / \sum_i \epsilon_i F_i$
$B^+ \to \overline{D}^{*0} D_{s1}(2460)^+$	$N_{D_s^+} \times \epsilon_{B^+\to\overline{D}^{*0} D_{s1}(2460)^+} \times F_{B^+\to\overline{D}^{*0} D_{s1}(2460)^+} / \sum_i \epsilon_i F_i$
$B^+ \vert B_s^0 \to \overline{D}^0 D_s^+(X)$	$N_{D_s^+} \times \epsilon_{B^+\vert B_s^0\to\overline{D}^0 D_s^+(X)} \times F_{B^+\vert B_s^0\to\overline{D}^0 D_s^+(X)} / \sum_i \epsilon_i F_i$
$B^0 \to \overline{D}^0 D_s^+ X$	$N_{D_s^+} \times \epsilon_{B^0\to\overline{D}^0 D_s^+ X} \times F_{B^0\to\overline{D}^0 D_s^+ X} / \sum_i \epsilon_i F_i$
$B^0 \to D^{*-} D_s^+$	$N_{D_s^+} \times \epsilon_{B^0\to D^{*-} D_s^+} \times F_{B^0\to D^{*-} D_s^+} / \sum_i \epsilon_i F_i$
$B^0 \to D^{*-} D_s^{*+}$	$N_{D_s^+} \times \epsilon_{B^0\to D^{*-} D_s^{*+}} \times F_{B^0\to D^{*-} D_s^+} \times F^*_{B^0\to D^{*-} D_s^{*+}} / \sum_i \epsilon_i F_i$
$B^0 \to D^{*-} D_{s0}^*(2317)^+$	$N_{D_s^+} \times \epsilon_{B^0\to D^{*-} D_{s0}^*(2317)^+} \times F_{B^0\to D^{*-} D_s^+} \times F^*_{B^0\to D^{*-} D_{s0}^*(2317)^+} / \sum_i \epsilon_i F_i$
$B^0 \to D^{*-} D_{s1}(2460)^+$	$N_{D_s^+} \times \epsilon_{B^0\to D^{*-} D_{s1}(2460)^+} \times F_{B^0\to D^{*-} D_s^+} \times F^*_{B^0\to D^{*-} D_{s1}(2460)^+} / \sum_i \epsilon_i F_i$

Table 8.5: Components included in the signal fit and their corresponding yields.

8.2.4 The blinding strategy

The analysis is in a preliminary stage. Therefore, in order to minimize biases, the number of signal events $N(B^+ \to \overline{D}^0\tau^+\nu_\tau)$ and $N(B^+ \to \overline{D}^{*0}\tau^+\nu_\tau)$ are blinded. The strategy followed is to add to each signal yield a random number, x, from a Gaussian distribution, G(μ,σ), with values $\mu = 0$ and $\sigma = 20000$:

$$N_{sig} = N_{sig}^{blind} + x. \tag{8.10}$$

In this way, the uncertainty in the signal yield remains un-blinded and can be monitored, while the relative uncertainty $\sigma_{N_{sig}/N_{sig}}$ is unknown.

At this point, both signal yields are blinded. However, these values could be obtained with the dataset size and all the background yields. In order to prevent this issue, also the largest background component due to $B \to \overline{D}^0 D_s^+(X)$ decays, $M_{D_s^+}$, is blinded, following the same strategy. The blinded $\overline{D}^0 D_s^+$ yield is given by $N_{D_s^+}^{blind} = N_{D_s^+} - x'$. The parameter

x' corresponds to a number from a Gaussian distribution with values $\mu' = 0$ and $\sigma' = 40000$.

The last step of the blinding strategy has to do with the visualisation. We set the area of the $B^+ \to \overline{D}^0\tau^+\nu_\tau$ and $B^+ \to \overline{D}^{*0}\tau^+\nu_\tau$ components to 90000 and 110000, respectively. Also, the area of the D_s^+ component is set to 100000.

8.2.5 Determination of the signal yields

The signal yields of $B^+ \to \overline{D}^0\tau^+\nu_\tau$ and $B^+ \to \overline{D}^{*0}\tau^+\nu_\tau$ are obtained from a 3-dimensional template fit to the τ decay time, q^2 and BDT distributions using the Beeston-Barlow Lite method [157]. The fit results are show in Tab. 8.6 and the fit projections in Fig. 8.6. The correlation between the $B^+ \to \overline{D}^0\tau^+\nu_\tau$ and $B^+ \to \overline{D}^{*0}\tau^+\nu_\tau$ yields provided by the fit is -0.94.

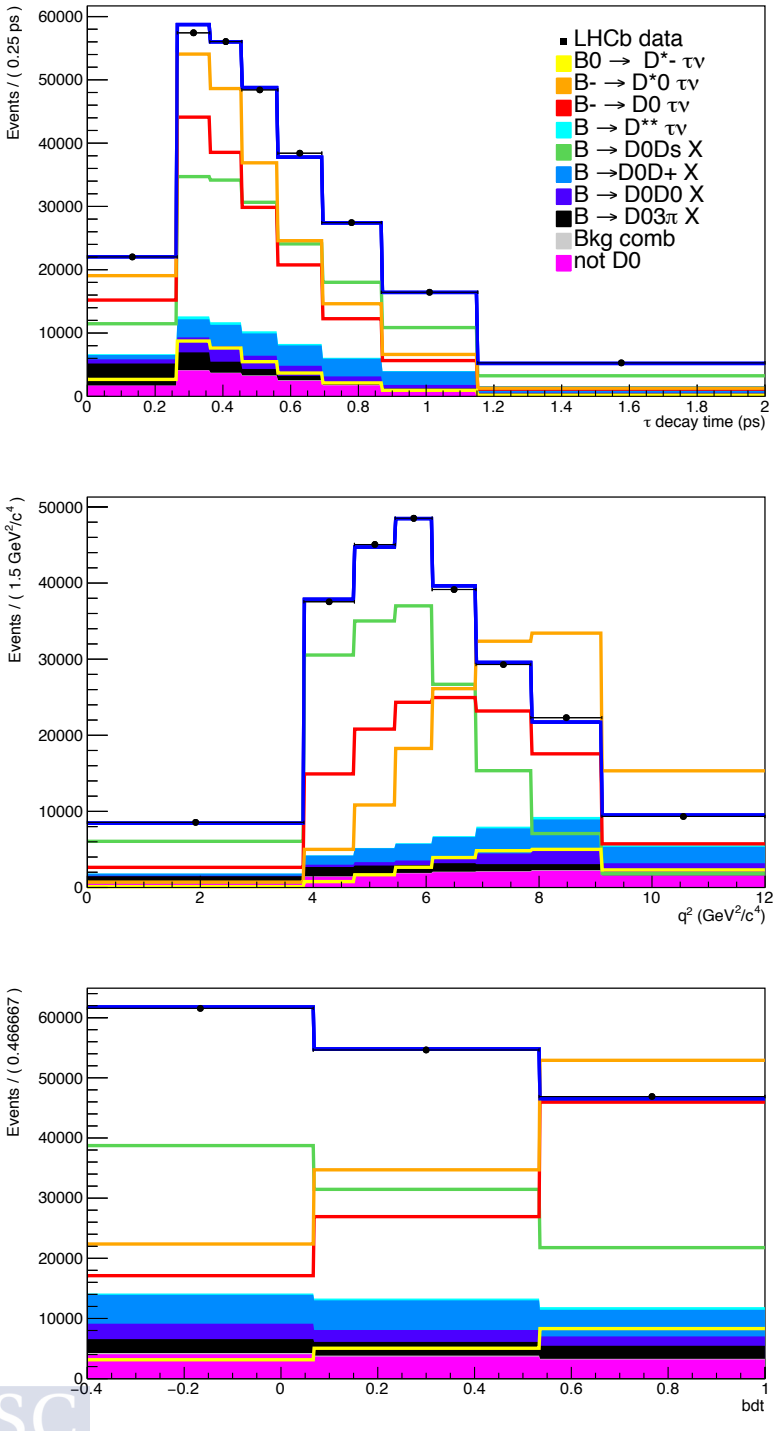

Figure 8.6: Projections of the nominal 3D fit on the τ decay time, q^2 and BDT distributions. The $B^+ \to \overline{D}^0 \tau^+ \nu_\tau$ and $B^+ \to \overline{D}^{*0} \tau^+ \nu_\tau$ signal components and the $B \to \overline{D}^0 D_s^+(X)$ background are blind in the fit and their normalisation is chosen arbitrarily.

Parameter	**Fit result**	**Constraint**
$N(B^+ \to \overline{D}^0 \tau^+ \nu_\tau)$	xxx $\pm$1844	—
$N(B^+ \to \overline{D}^{*0} \tau^+ \nu_\tau)$	xxx $\pm$1096	—
$N(D_s^+)$	xxx $\pm$1068	—
$N(D^0)$	7978 ± 613	6655 ± 998
$N(D^+)$	8606 ± 554	—
N_{Prompt}	6223 ± 306	—
$N_{not-\bar{D}^0}$	10902	10902
$N_{comb.bkg.}$	3286	3286
$F^{\bar{D}^0 D_s^+}_{B^+ \to \bar{D}^{*0} D_s^+}$	0.944 ± 0.037	0.915 ± 0.054
$F_{B^+ \to \bar{D}^0 D_s^{*+}}$	0.870 ± 0.043	0.935 ± 0.056
$F_{B^+ \to \bar{D}^{*0} D_s^{*+}}$	1.847 ± 0.041	1.829 ± 0.047
$F_{B^+ \to \bar{D}^0 D_{s1}(2460)^+}$	0.266 ± 0.033	0.332 ± 0.038
$F_{B^+ \to \bar{D}^{*0} D_{s1}(2460)^+}$	0.805 ± 0.030	0.710 ± 0.040
$F_{B^+ \mid B_s^0 \to \bar{D}^0 D_s^+(X)}$	0.791 ± 0.034	0.817 ± 0.037
$f_{D^{**}/D^{*0}}$	0.043	0.043

Table 8.6: Results of the nominal 3D fit using the Beeston-Barlow Lite method.

8.2.6 Toys studies

The behaviour of the fit model is checked using toys studies. 1000 pseudo-experiments are generated and fitted using the parameter values obtained from the nominal fit. The pull distributions for the fit model parameters are shown in Fig. 8.7. The 100% of the fits converge well.

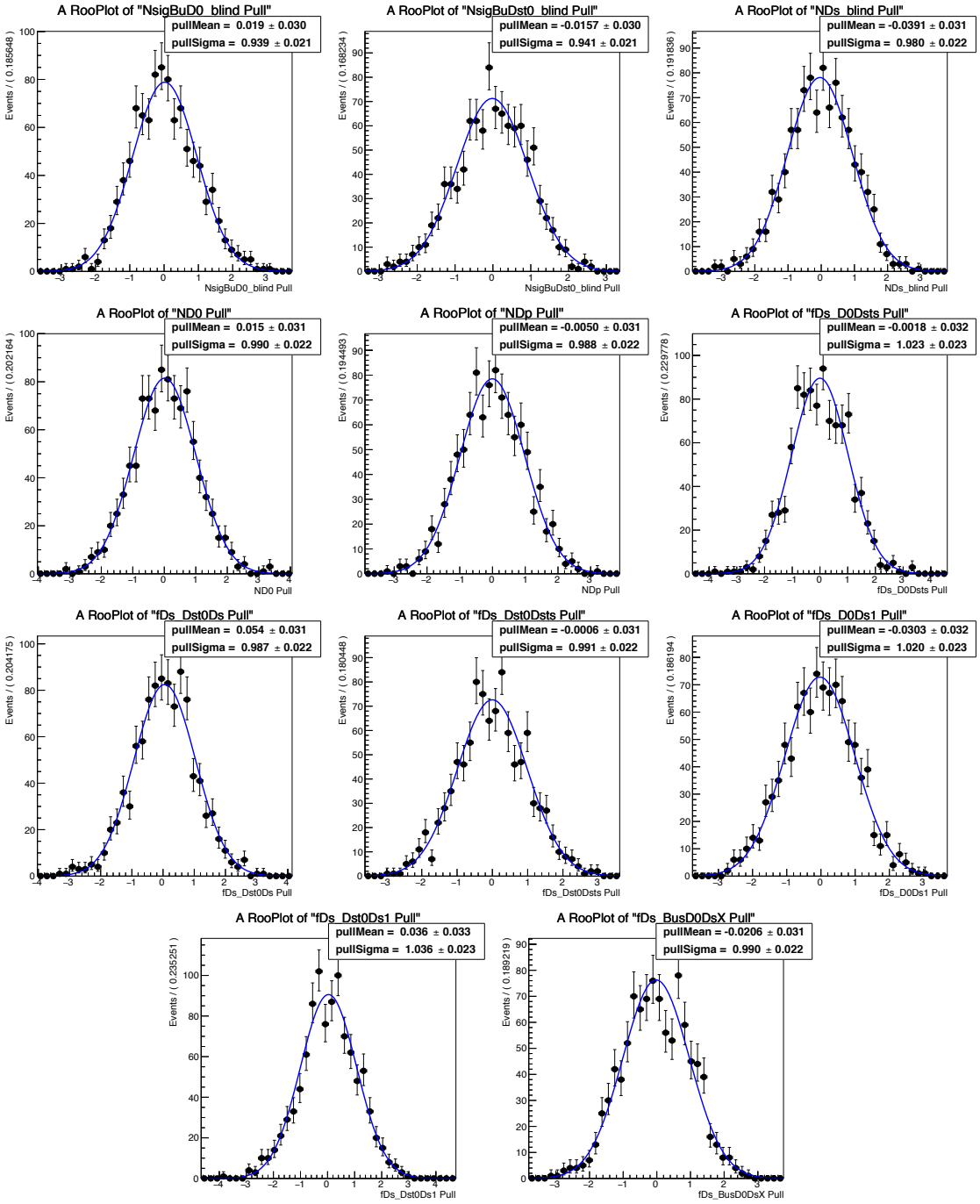

Figure 8.7: Pull distributions of fit parameters obtained from 1000 pseudo-experiments.

Since no significant biases are observed in any of the fit parameters, no corrections are applied.

8.3 Determination of $B^+ \to \overline{D}^0\tau^+\nu_\tau$ and $B^+ \to \overline{D}^{*0}\tau^+\nu_\tau$ branching fractions

The signals (see Sec. 8.2.5) and normalisation (see Sec. 8.1) yields are used to measure the $B^+ \to \overline{D}^0\tau^+\nu_\tau$ and $B^+ \to \overline{D}^{*0}\tau^+\nu_\tau$ branching fractions. From the expression for $\mathcal{K}(D^{(*)0})$ presented in the Sec. 5 (Eq. 5.3):

$$\mathcal{K}(D^{(*)0}) = \frac{\mathcal{B}(B^+ \to \bar{D}^{(*)0}\tau^+\nu_\tau)}{\mathcal{B}(B^+ \to \overline{D}^0 D_s^+) \times \mathcal{B}(D_s^+ \to \pi^+\pi^-\pi^+)}, \tag{8.11}$$

one can obtain, in terms of the signal and normalisation yields:

$$\begin{aligned}\mathcal{K}(D^{(*)0}) &= \frac{N(B^+ \to \bar{D}^{(*)0}\tau^+\nu_\tau)}{N(B^+ \to \overline{D}^0 D_s^+)} \\ &\times \frac{\varepsilon_{B^+\to\overline{D}^0 D_s^+}}{\varepsilon^{\tau\to 3\pi\nu}_{B^+\to\bar{D}^{(*)0}\tau^+\nu_\tau}\mathcal{B}(\tau \to 3\pi\nu)_{\rm PDG} + \varepsilon^{\tau\to 3\pi\pi^0\nu}_{B^+\to\bar{D}^{(*)0}\tau^+\nu_\tau}\mathcal{B}(\tau \to 3\pi\pi^0\nu)_{\rm PDG}}\end{aligned} \tag{8.12}$$

where the efficiencies have been determined in Sec. 6.4, and the branching fractions $\mathcal{B}(B^+ \to \overline{D}^0 D_s^+)_{\rm PDG} = (9.0 \pm 0.9) \times 10^{-3}$, $\mathcal{B}(D_s^+ \to \pi^+\pi^-\pi^+)_{\rm PDG} = (1.08 \pm 0.04) \times 10^{-2}$, $\mathcal{B}(\tau \to 3\pi\nu)_{\rm PDG} = 0.0902 \pm 0.0005$ and $\mathcal{B}(\tau \to 3\pi\pi^0\nu)_{\rm PDG} = 0.0449 \pm 0.0005$ are taken from the PDG [9]. The results are:

$$\mathcal{K}(D^0) = xx \pm 22\ (stat.) \pm 0.35\ (ext.), \tag{8.13}$$
$$\mathcal{K}(D^{*0}) = xx \pm 16\ (stat.) \pm 0.74\ (ext.), \tag{8.14}$$

where the correlation between the statistical uncertainties of $\mathcal{K}(D^0)$ and $\mathcal{K}(D^{*0})$ is -0.91 and between uncertainties due to external measurements is $+1$. The uncertainty from external measurements is negligible in comparison with the statistical one.

Now, from Eqs. 8.11 and 8.12, the branching fractions of $B^+ \to \overline{D}^0\tau^+\nu_\tau$ and $B^+ \to \overline{D}^{*0}\tau^+\nu_\tau$ can be obtained as:

$$\mathcal{B}(B^+ \to \bar{D}^{(*)0}\tau^+\nu_\tau) = \mathcal{K}(D^{(*)0}) \times \mathcal{B}(B^+ \to \overline{D}^0 D_s^+)_{\rm PDG} \times \mathcal{B}(D_s^+ \to \pi^+\pi^-\pi^+)_{\rm PDG}. \tag{8.15}$$

The measured branching fractions are:

$$\mathcal{B}(B^+ \to \overline{D}^0\tau^+\nu_\tau) = xx \pm 0.21\ (stat.) \pm 0.07\ (ext.)\ \%, \tag{8.16}$$
$$\mathcal{B}(B^+ \to \overline{D}^{*0}\tau^+\nu_\tau) = xx \pm 0.15\ (stat.) \pm 0.15\ (ext.)\ \%, \tag{8.17}$$

where the first uncertainties are due to the statistical uncertainty of the signal and normalisation yields, and the second is due to the external inputs. The correlation between

the statistical uncertainties of both branching fractions measurements is -0.91 and between external uncertainties is $+1$. Adding both statistical and external uncertainties, the branching fractions are:

$$\mathcal{B}(B^+ \to \overline{D}^0 \tau^+ \nu_\tau) = xx \pm 0.23\ (stat. + ext.)\ \%, \tag{8.18}$$
$$\mathcal{B}(B^+ \to \overline{D}^{*0} \tau^+ \nu_\tau) = xx \pm 0.22\ (stat. + ext.)\ \%, \tag{8.19}$$

with a correlation of -0.37.

These results can be compared with the world average measurements [9]:

$$\mathcal{B}(B^+ \to \overline{D}^0 \tau^+ \nu_\tau)_{\rm PDG} = 0.77 \pm 0.25\ \%, \tag{8.20}$$
$$\mathcal{B}(B^+ \to \overline{D}^{*0} \tau^+ \nu_\tau)_{\rm PDG} = 1.88 \pm 0.20\ \%. \tag{8.21}$$

These results, before including the systematic uncertainties, are competitive with the world average precision.

9

Determination of $\mathcal{R}(D^0)$ and $\mathcal{R}(D^{*0})$ branching fractions

The LFU ratios:

$$\mathcal{R}(D^0) = \frac{\mathcal{B}(B^+ \to \overline{D}^0 \tau^+ \nu_\tau)}{\mathcal{B}(B^+ \to \overline{D}^0 \ell^+ \nu_\ell)},$$

and

$$\mathcal{R}(D^{*0}) = \frac{\mathcal{B}(B^+ \to \overline{D}^{*0} \tau^+ \nu_\tau)}{\mathcal{B}(B^+ \to \overline{D}^{*0} \ell^+ \nu_\ell)},$$

are determined using the results of the signal branching fractions from Sec. 8 and the branching fractions measurements $\mathcal{B}(B^+ \to \overline{D}^0 \ell^+ \nu_\ell) = 2.30 \pm 0.06\ (stat.) \pm 0.08\ (syst.)$ % and $\mathcal{B}(B^+ \to \overline{D}^{*0} \ell^+ \nu_\ell) = 5.58 \pm 0.07\ (stat.) \pm\ 0.21\ (syst.)$ % as external inputs [47]. The results are:

$$\begin{aligned} \mathcal{R}(D^0) &= xx \pm 0.093\ (stat.) \pm 0.034\ (ext.), \\ \mathcal{R}(D^{*0}) &= xx \pm 0.026\ (stat.) \pm 0.029\ (ext.). \end{aligned}$$

The correlation between the $\mathcal{R}(D^0)$ and $\mathcal{R}(D^{*0})$ statistical uncertainties is -0.91 and between the external uncertainties is $+1$. The results are shown in Fig. 9.1. Being the results still blinded, the ellipse is placed at the SM benchmark. The continuous cyan line is due to the statistical uncertainty only and the dashed cyan line to both statistical and external measurements uncertainties.

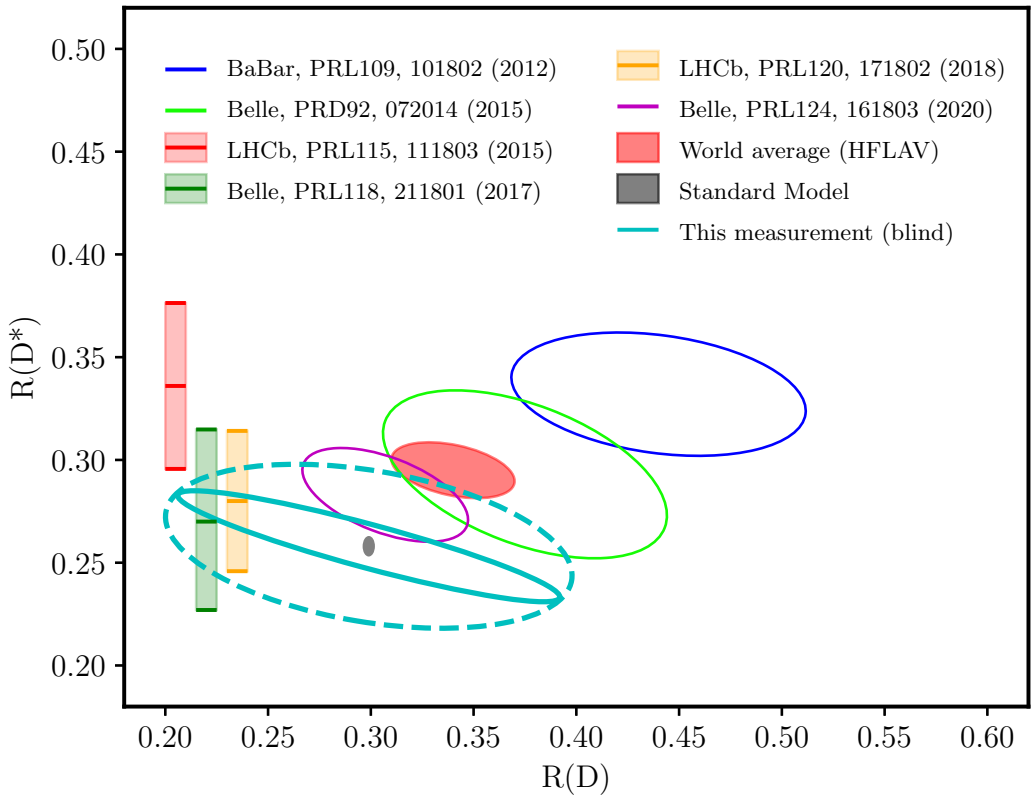

Figure 9.1: $\mathcal{R}(D)$ and $\mathcal{R}(D^*)$ measurements of this work, shown in cyan. Since the result is blinded, the central values are placed at the SM prediction benchmark. The statistical uncertainty is shown with a continuous line, while the total uncertainty, statistical plus external, is shown with a dashed line. The world average is given by the red ellipse, while the SM prediction corresponds to the gray ellipse. Other measurements performed by different experiments are also indicated.

10

Systematic uncertainties

Contents

At the time of writing this thesis, the systematic uncertainties have not been computed. In the following, a description of some of the most important systematic effects are briefly described.

10.1 Monte Carlo statistics

In the previous LHCb measurements of $\mathcal{R}(D^*)$ [42–44] the dominant systematic uncertainty was due to the limited statistics in the simulation. In the nominal signal fit of this work, the Beeston-Barlow [157] "Lite" method was applied. This method treats bin statistical uncertainties introducing a single nuisance parameter per bin that accounts for the overall statistical uncertainty. The strategy to determine the systematic uncertainty due to the templates statistics consists in introducing the Beeston-Barlow method in the

fit, so that each bin of the model is allowed to float. The fit is also repeated with Beeston-Barlow method turned off. The quadrature difference of the signal precision between the two fits is assumed to be due to the template statistics. In addition, a bootstrap technique can be applied. In this technique, the data is fitted with varied templates. Each bin in the templates are fluctuated according to a Poisson distribution and the fit is repeated a sufficiently large number of times. The variation on the signal yields can be assumed to be the systematic uncertainty.

10.2 $B \to D^{**}\tau^+\nu_\tau$ decays events

The feed-down from $B \to D^{**}\tau^+\nu_\tau$ decays is estimated using approximate isospin conservation, together with theoretical calculations. Therefore, the systematic uncertainty derived from this estimation is obtained using information coming from the corresponding theoretical assumptions and experimental measurements of $B \to D^{**}\tau\nu$. Using a bootstrap technique, introducing a large variation of the fraction of $B \to D^{**}\tau^+\nu_\tau$, $f_{D^{**}/D^{*0}}$, will be sufficient to study the systematic effect due to the presence of these decays in the signal sample.

10.3 Form-factors uncertainties

Another source of uncertainty comes from the knowledge of the signal hadronic form-factors. In Sec. 6.3.4, it is shown the BGL parameterisation for the $B \to D\tau^+\nu_\tau$ and $B \to D^*\tau^+\nu_\tau$ decays. A theoretical determination of the BGL parameters is used in order to correct the shape the signal decays. Pseudo-experiments are made varying the form-factor parameters, so that it can be derived the systematic uncertainties arising form the limited knowledge of these parameters.

10.4 Background model uncertainties

The main systematic uncertainties corresponding to the background modelling are due to the double-charm $B \to \overline{D}^0 D(X)$ and the inclusive $D_s^+ \to \pi^+\pi^-\pi^+(X)$ decay models. In order to determine the effect of the model of these decays, in the final fit, different parameters corresponding to each background model can be varied. Applying the bootstrap technique, the systematic uncertainty due to these backgrounds can be estimated.

10.5 Other systematic effects

In addition to the dominant systematic effect, systematic uncertainties must be studied regarding the selection of signal and normalisation events, the trigger lines, the particle identification performance, the decay kinematics and the event multiplicity.

11

Conclusions and prospects

The LHCb detector has been demonstrated as an excellent tool for extending the SM knowledge. However, the physics efforts towards BSM searches remain statistically constrained, which highly motivates an upgrade of the detector during the LS2 of the LHC. The LHCb Upgrade I will allow for an operation luminosity environment of 5 times higher than the previous spectrometer, with a more efficient trigger. A key part of this upgrade is the replacement of the VELO detector by hybrid pixel sensors, consisting of two parts: a planar silicon sensor and a VeloPix readout ASIC. As part of this thesis, the performance of the new VELO sensors was characterised. In particular, sensors consisting of n-on-p triples HPK of 200 µm thick, $55 \times 55\,\mu m^2$ pixels and 39 µm implant size were studied.

Firstly, the IV curve was characterised for a non-irradiated sensor. The scan was carried out in a similar environment to the LHC running conditions, and the results corroborated that the sensor was able to reach the 1000 V required without showing breakdown. Secondly, one of the biggest challenges that the upgraded VELO will face is radiation damage. Therefore, a study was performed in order to determine the dependence of the high-voltage tolerance with temperature for sensors irradiated with different fluence profiles. Sensors irradiated with a uniform profile (at IRRAD facilities) showed a correct behaviour in all the IV scan range. However, all non-uniform irradiated profile sensors (at Birmingham) displayed a very early breakdown voltage. This behaviour drove further research in order to understand the nature of this effect. Several hypotheses were tested at the VELO laboratory, without obtaining a determining conclusion about the mechanism that would trigger the breakdown. Finally, since the effect was not further found in none of the subsequent sensors that were sent to irradiation facilities, it was generally accepted

that some defects in either the cold chain, the manufacturing, the irradiation process or the Parylene damage would cause the early breakdown. As an additional contribution to the VELO upgrade project, two models for the IV curve were proposed for sensors that did not show breakdown voltage. Both parameterisations worked well, being the results compatible among them.

At the time of writing, the new VELO has already been installed in the upgraded LHCb. The first stable beams have occurred, while the first high energy collisions are scheduled for the fifth of July 2022. The work documented in this thesis was part of the project that would ensure a safe operation of the LHCb, guaranteeing a correct and reliable data acquisition.

With respect to data analysis, the second and main work of this thesis is dedicated to Lepton Flavour Universality tests in semitauonic B decays. Several measurements of this kind of observables present long-standing tensions with respect to the SM prediction. In addition, they are sensitive to NP contributions. The measurements of the $\mathcal{R}(D^0)$ and $\mathcal{R}(D^{*0})$ ratios using 2016, 2017 and 2018 data collected by the LHCb experiment are reported in this thesis. The τ lepton is reconstructed in its 3-prong hadronic decay, $\tau^+ \to \pi^+\pi^-\pi^-(\pi^0)\overline{\nu}_\tau$.

The analysis is in an advanced state, and comprehensive documentation of it is reported in this thesis. The steps completed so far consist of the selection and preparation of data and Monte Carlo samples and the study of control samples. The normalisation and signal yields have been determined. The former through an unbinned maximum likelihood fit, and the later by means of a 3D templates-based fit. The method followed for the measurement allows to express the coefficient $\mathcal{K}(D^{(*)0})$, the target of the analysis, in terms of the signal and normalisation yields. The results obtained are:

$$\begin{aligned} \mathcal{K}(D^0) &= xx \pm 22\ (stat.) \pm 0.35\ (ext.), \\ \mathcal{K}(D^{*0}) &= xx \pm 16\ (stat.) \pm 0.74\ (ext.), \end{aligned}$$

where the first uncertainties are due to the statistical uncertainty of the signal and normalisation yields, and the second are due to the external inputs. Introducing these results, the measured branching fractions are found to be:

$$\begin{aligned} \mathcal{B}(B^+ \to \overline{D}^0\tau^+\nu_\tau) &= xx \pm 0.21\ (stat.) \pm 0.07\ (ext.)\ \%, \\ \mathcal{B}(B^+ \to \overline{D}^{*0}\tau^+\nu_\tau) &= xx \pm 0.15\ (stat.) \pm 0.15\ (ext.)\ \%, \end{aligned}$$

being the uncertainties analogous to the previous case. These results can be compared to the world average measurements [9], showing competitive results in terms of precision. Finally, the blinded $\mathcal{R}(D^0)$ and $\mathcal{R}(D^{*0})$ ratios are determined:

$$\begin{aligned} \mathcal{R}(D^0) &= xx \pm 0.093\ (stat.) \pm 0.034\ (ext.), \\ \mathcal{R}(D^{*0}) &= xx \pm 0.026\ (stat.) \pm 0.029\ (ext.), \end{aligned}$$

which are competitive with previous experimental measurements [47].

Based on the work reported in this thesis, the analysis described will undergo an internal LHCb review, along with the subsequent publication. The result will mean a sensitive test of Lepton Flavour Universality, having a significant impact on the $\mathcal{R}(D^{(*)})$ world average. Aiming for clarifying if the open questions related to Lepton Flavour Universality are due to NP effects, different strategies are proposed.

Firstly, the current dataset will be exploited by updating the completed analyses up to now, and performing new analyses. This strategy foresees the measurement of $\mathcal{R}(D^0)$, $\mathcal{R}(D^{*0})$, $\mathcal{R}(D^+)$, $\mathcal{R}(D^{*+})$, $\mathcal{R}(D_s^+)$, $\mathcal{R}(D_s^{*+})$, $\mathcal{R}(\Lambda_c^+)$, $\mathcal{R}(\Lambda_c^{*+})$ or $\mathcal{R}(J/\psi)$ ratios, among others. Besides, decays involving $b \to u\ell\nu_\ell$ transitions are also currently under investigation, such as the ratios $\mathcal{R}(\Lambda_b^0 \to p\tau^-\overline{\nu}_\tau)$ or $\mathcal{R}(B^+ \to p\overline{p}\tau^+\nu_\tau)$.

Moreover, LFU tests will be performed in observables beyond decay rates. Angular analyses, such as the measurement of the D^* longitudinal polarisation fraction, provides an interesting scenario to test NP models.

Finally, new datasets are going to be collected, as it was reported throughout this document. In the near future, LHCb is expected to acquire data corresponding to an integrated luminosity of $25\,\text{fb}^{-1}$ by the end of LHC Run 3, which will scale up to $50\,\text{fb}^{-1}$ after Run 4. With this data sample, it is estimated that the LHCb precision of LFU observables will improve by about a factor of 2-4 [154]. The proposed LHCb upgrade Phase II, would allow to further improve the precision of the presented ratios down to the $0.5 - 2.0\%$ level [154]. In the case of Belle II, the goal for the next decade is to collect $50\,\text{ab}^{-1}$. This would imply that, for different LFU ratios, the precision would range $0.5 - 4\%$, depending on the considered scenario. This means that both experiments will achieve comparable precision.

To summarise, motivated by the intriguing long-standing anomalies in $\mathcal{R}(D^{(*)})$, this thesis documents a new test of Lepton Flavour Universality using semitauonic decays, at the LHCb experiment. This measurement, along with others currently ongoing and planned from both LHCb and Belle II, will contribute to the understanding of the flavour sector puzzle.

Appendices


USC
UNIVERSIDADE
DE SANTIAGO
DE COMPOSTELA

A

Luminosity

One of the most important parameters of an accelerator is the luminosity, $\mathcal{L}$, which is a measurement of the collected data size. In the LHC, the number of events N_{events} produced in a collision depends of the event cross-section σ_{event} and the luminosity as:

$$N_{\text{events}} = \sigma_{\text{event}} \int \mathcal{L} dt, \tag{A.1}$$

where the luminosity depends on the beam parameters as:

$$\mathcal{L} = \frac{N_b^2 n_b f_{\text{rev}} \gamma_r}{4\pi \epsilon_n \beta^*} F, \tag{A.2}$$

being N_b particles per bunch, n_b bunches per beam, f_{rev} the revolution frequency, γ_r the relativistic gamma factor, ϵ_n the normalised transverse beam emittance, β^* the beta function at the collision point and F the geometric luminosity reduction factor due to the crossing angle of the beams at the interaction point.

Fig. A.1 shows a comparison of integrated luminosity recorded by LHCb during different years.

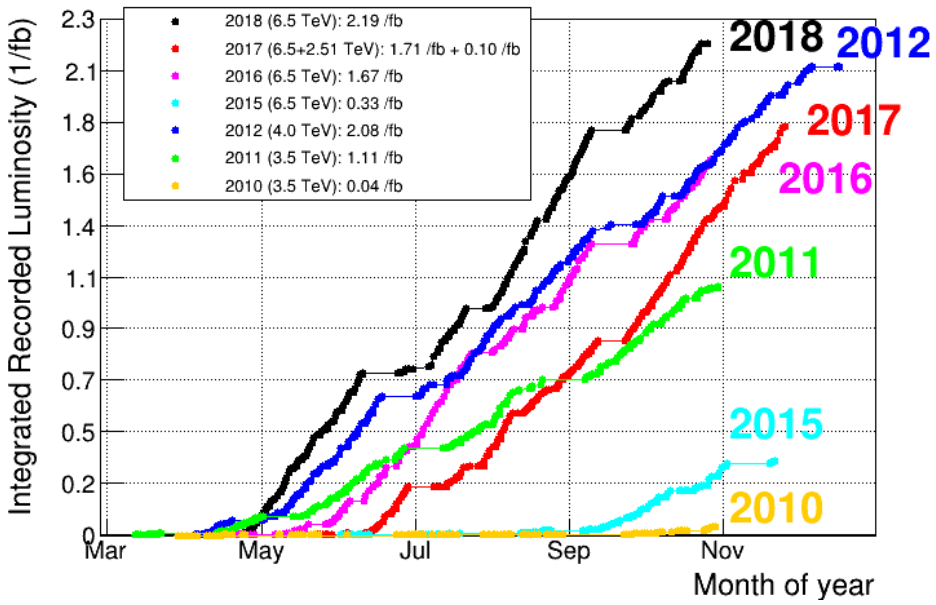

Figure A.1: LHCb Integrated recorded luminosity over Run 1 and Run 2. Obtained from [158].

B

Non-uniform irradiation campaign

The irradiation campaign at Birmingham was carried out following a non-uniform irradiation profile, as it was described in Chap. 4. In order to match different running conditions and therefore study the effect that this difference may have in the sensor response, different irradiation fluences were applied in different regions close to the sensor, or foils. As a result, Birmingham irradiated TILES are a set of different combinations of irradiation fluence in different regions. All the irradiation campaign details can be found in Tabs. B.1, B.2, B.3 and B.4 and Figs. B.1, B.2, B.3 and B.4.

Foil	Fluence (10^{15} 1 MeV n_{eq} cm^{-2})
49	3.16
28	3.14
47	3.09
7	2.29
9	2.05
44	0.760
45	0.350
20	0.0926

Table B.1: Summary of irradiation characteristics to which TILE 4 was subjected.

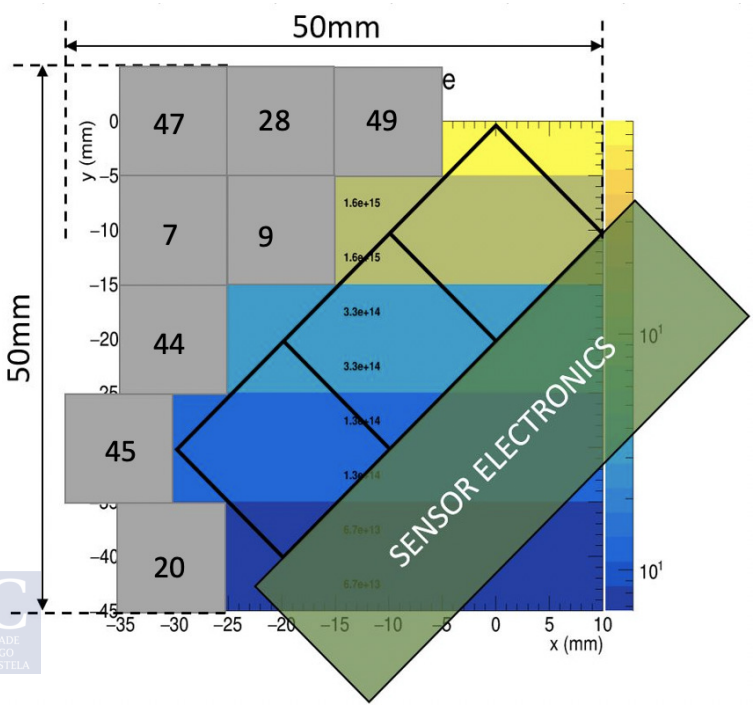

Figure B.1: Irradiation profile for the TILE 4.

Foil	**Fluence** (10^{15} 1 MeV n_{eq} cm^{-2})
37	0.0867
1	0.0966
34	0.181
21	0.582
5	0.671
27	2.93
4	3.50
22W	4.02

Table B.2: Summary of irradiation characteristics to which TILE 5 was subjected.

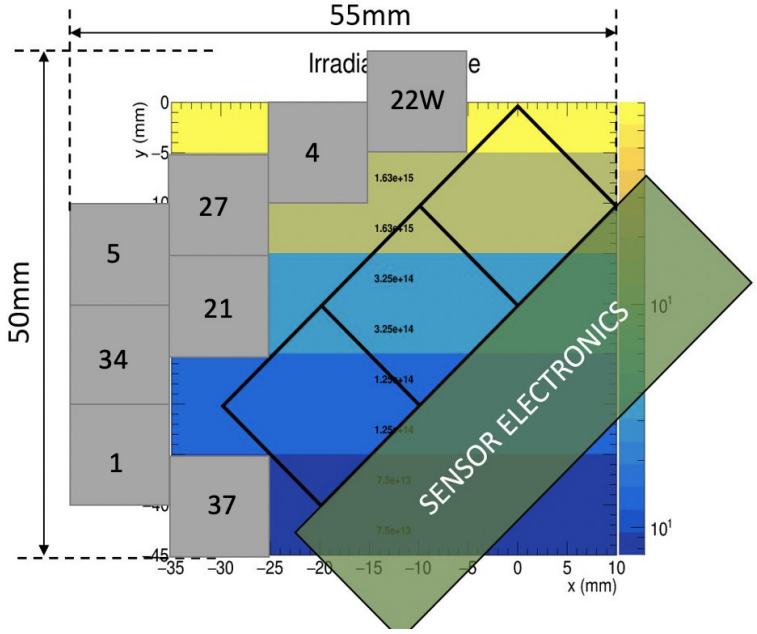

Figure B.2: Irradiation profile for the TILE 5.

Foil	Fluence (10^{15} 1 MeV n_{eq} cm^{-2})
Z1	1.90
Z17	5.90
Z2	0.600
Z18	4.70
Z22	0.350
Z21	0.340
Z	5.90
Z23	0.312

Table B.3: Summary of irradiation characteristics to which TILE 6 was subjected.

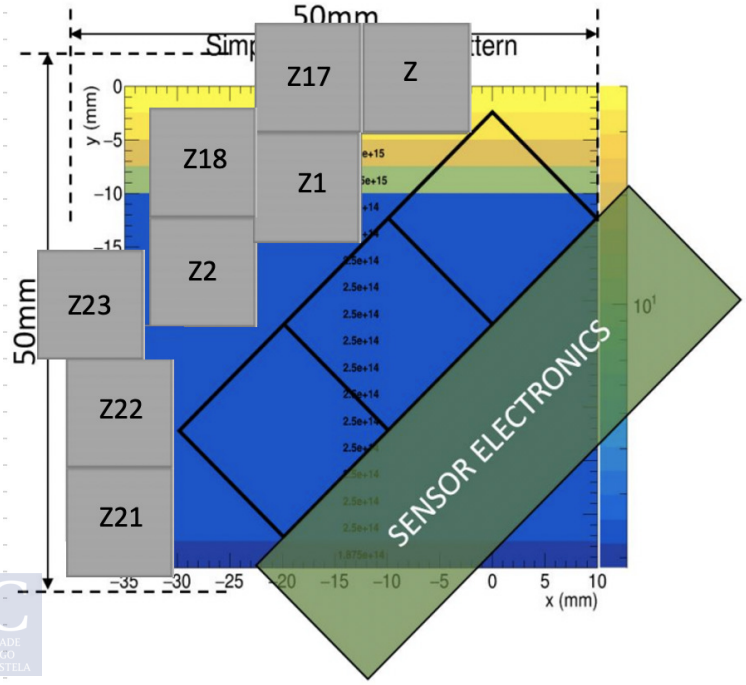

Figure B.3: Irradiation profile for TILE 6.

Foil	**Fluence** (10^{15} 1 MeV n_{eq} cm^{-2})
Z21	2.50
Z8	2.50
Z13	2.20
Z37	1.70
Z36	0.340
Z35	0.300
Z3	0.260

Table B.4: Summary of irradiation characteristics to which TILE 7 was subjected.

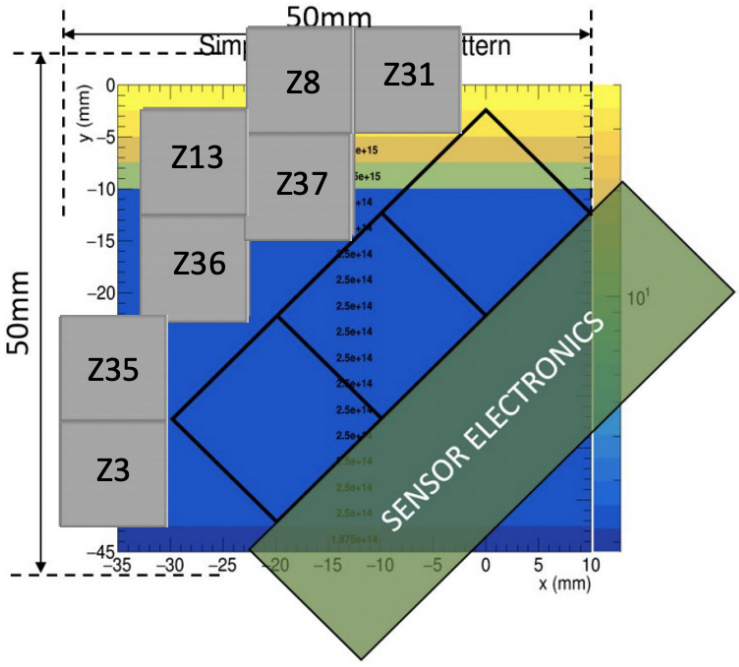

Figure B.4: Irradiation profile for TILE 7.

C

Resumo da tese en Galego

C.1 Motivación teórica e obxetivos

O Modelo Estándar (ME) da Física de Partículas é a teoría que describe os constituíntes fundamentais da materia, as *partículas*, e as interaccións entre elas, as *forzas*. Un dos alicerces nos que se sostén é a chamada Universalidade Leptónica de Sabor (ULS), propiedade que predí que os acoplamentos dos leptóns aos bosóns son independentes da familia leptónica. Dado que este é un dos ingredientes fundamentais da teoría, a súa violación poría en cuestión o ME, abrindo un interesante camiño á Nova Física (NF).

A pesar do éxito de ME predicindo e explicando a meirande parte dos resultados experimentais, hai cuestións abertas que non encaixan no marco teórico, polo que é necesario unha extensión do mesmo. O experimento LHCb foi deseñado primeiramente para medir parámetros da violacion CP en desintegracións de hadróns cun quark b. Sen embargo, nos últimos anos estendeuse ampliamente o programa científico do detector, constituíndose a día de hoxe como unha ferramenta moi potente de cara á NF. A pesar do éxito acadado polo experimento LHCb, os seus resultados atópanse limitados estatisticamente.

Nas últimas décadas a ULS foi minuciosamente medida e estudada, resultando, por unha banda nun patrón de anomalías experimentais; e por outra banda en novos modelos teóricos que xustificarían as medidas obtidas experimentalmente. En concreto, a ULS sométese a proba mediante a comparación das fracción de desintegración (FD) de desintegracións semitauónicas e semimuónicas. Os cocientes $\mathcal{R}(H_c)$ definidos como:

$$\mathcal{R}(H_c) = \frac{H_b \to H_c \tau^+ \nu_\tau}{H_b \to H_c \ell'^+ \nu_{\ell'}},$$

onde H_c (H_b) son hadróns cun quark c (b) e ℓ' un electrón ou un muon, son observables particularmente interesantes, debido á que resultan limpos en virtude de que os efectos hadrónicos cancélanse na fracción, así como as eficiencias e efectos sistemáticos causados polo dispositivo experimental.

As primeiras medicións da ULS leváronse a cabo nas chamadas fábricas de B (BaBar e Belle), ás que seguiron resultados de moi alta precisión do experimento LHCb [42–45]. A media global de todas as medidas experimentais de $\mathcal{R}(D^{(*)0})$ sitúa a anomalía a $3{,}4\sigma$ da predición do SM, o que motiva novas procuras neste eido que poidan esclarecer a presencia de procesos de NF.

Nesta tese preséntase a primeira medida dos cocientes:

$$\mathcal{R}(D^0) = \frac{\mathcal{B}(B^+ \to \overline{D}^0 \tau^+ \nu_\tau)}{\mathcal{B}(B^+ \to \overline{D}^0 \ell^+ \nu_\ell)},$$
$$\mathcal{R}(D^{*0}) = \frac{\mathcal{B}(B^+ \to \overline{D}^{*0} \tau^+ \nu_\tau)}{\mathcal{B}(B^+ \to \overline{D}^{*0} \ell^+ \nu_\ell)},$$

co tau reconstruído nos modos $\tau^+ \to \pi^+\pi^-\pi^+\overline{\nu}_\tau$ e $\tau^+ \to \pi^+\pi^-\pi^+\pi^0\overline{\nu}_\tau$, o $\overline{D}^0$ en $K^+\pi^-$ e o $\overline{D}^{*0}$ desintegrándose ou ben de xeito $\overline{D}^0\pi^0$ (no $64{,}7 \pm 0{,}9\,\%$ [9] dos casos) ou en $\overline{D}^0\gamma$ ($35{,}3 \pm 0{,}9\,\%$ [9]). A análise levouse a cabo con datos do Run 2 recollidos polo experimento LHCb, correspondentes aos anos 2016, 2017 e 2018. Os datos foron obtidos de colisións protón-protón a unha enerxía no centro de masas de 13 TeV, resultando nunha luminosidade total integrada de $5{,}4\,\mathrm{fb}^{-1}$.

C.2 Dispositivo experimental

O Gran Colisor de Hadróns, LHC (*Large Hadron Collider*), é o acelerador de partículas máis potente xamais construído. Sitúase no Laboratorio Europeo para a Física de Partículas (CERN), ubicado en Xenebra. O LHC está instalado nun túnel de case 27 km de circunferencia e unha profundidade media de 100 m.

O proceso de aceleración dos feixes de protóns lévase a cabo mediante varios subaceleradores que, sucesivamente, incrementan a enerxía das partículas. Finalmente, os protóns son inxectados no último acelerador, o LHC, polo que circulan a 6,5 TeV en dous sentidos opostos. Ao mesmo tempo, para curvar a traxectoria dos protóns, é preciso a presencia dun campo magnético duns 8 T, que é creado por imáns superconductores operados a 1,9 K no interior dun criostato.

Os feixes de protóns fanse colidir en catro puntos diferentes do LHC, onde están situados os grandes detectores: ATLAS (*A Toroidal LHC Apparatus*), CMS (*Compact Muon Solenoid*), ALICE (*A Large Ion Collider Experiment*) e LHCb (*Large Hadron Collider beauty*).

Nesta tese, traballouse con datos recollidos polo experimento LHCb. O detector consiste nun espectrómetro dun só brazo cuxa xeometría está especificamente deseñada para

o rango de aceptación de hadróns $b\bar{b}$ que, a altas enerxías, prodúcense nun cono cara diante (e cara atrás) dende o vértice principal. As diferentes compoñentes do detector durante o período de funcionamento 2016-2018, atópanse esquematizadas na Fig. C.1. Listadas en orde dende o punto de interación, correspóndense con:

- Localizador de Vértices (*Vertex Locator*, VELO) que resulta fundamental para reconstruír os vértices de producción e desintegración dos hadróns.
- Imán que proporciona un campo magnético de 4 Tm entre as estacións de trazado para a determinación do momento das partículas cargadas producidas nas colisións.
- Sistema de trazado que se compón dunha estación de silicio situada antes do imán (*Tracker Turicensis*, TT) e de tres estacións de trazado (*T Stations*, T1, T2 e T3) que se atopan despois do imán. Encárganse da reconstrucción das trazas das partículas cargadas que atravesan o detector.
- Detectores de aneis de imáxenes Cherenkov (*Ring Imaging Cherenkov*) situados antes (RICH1) e despois (RICH2) do imán, cuxa función é identificar hadróns cargados nun amplio rango de momento.
- Sistema de calorímetros (*Scintillator Pad Detector*, SPD; *PreShower*, PS; *Electromagnetic CALorimeter*, ECAL e *Hadronic CALorimeter*, HCAL)) que ten como propósito a correcta idenficación de hadróns, electróns e fotóns; mediante a medida da súa enerxía.
- Sistema de muóns para identificar muóns.

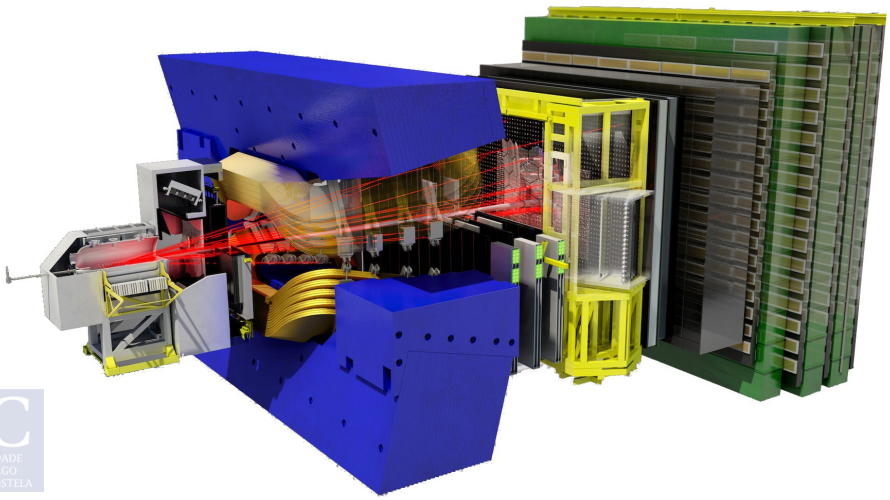

Figura C.1: Representación do detector LHCb, figura de [159] modificada pola autora.

Malia que a análise de datos foi levada a cabo co detector LHCb que se acaba de presentar, no momento de redactar este documento, a nova actualización do LHCb atópase prácticamente finalizada. Na seguinte sección proporcionarase máis información sobre dito proxecto.

C.3 A actualización do VELO do LHCb

Nos períodos que abarcan os anos 2010-2012 (*Run 1*) e 2015-2018 (*Run 2*), LHCb levou a cabo análises que contribuiron notablemente a expandir o noso coñecemento do ME. Partindo desta base, co obxectivo de realizar medidas altamente sensibles aos efectos da NF, apostouse por unha actualización do detector, de xeito que puidera operar as altas condicións de luminosidade do LHC (incremento que comezará no 2022).

A actualización do detector LHCb terá lugar en dúas grandes fases, a primeira, que comezou en 2019; e a segunda, que terá lugar a partir de 2033. Neste traballo, centrarémonos na Fase I, que preparará o experimento para facer fronte a unha luminosidade un factor cinco maior con respecto ao *Run 2*. O programa de física que se propón abrangue dende resolver os problemas que plantexa o sector do sabor (onde se inclúen as anomalías presentadas), ata medidas de desintegracións moi raras ou mesmo extensións do SM. Para acadar estes obxectivos, o sistema de *trigger* será remplazado por un que permita que a selección se leve a cabo exclusivamente a través de *software*. Con respecto aos subdetectores, o VELO será totalmente remplazado, así como o sistema de trazado e o de identificación de partículas, ou ou deseño óptico do RICH1.

Unha das actualizacións fundamentais será reemplazar o VELO por un detector de silicio baseado na tecnoloxía de píxeles, o VeloPix. Os novos módulos do VELO estarán formados por híbridos en forma de L (ver Fig. C.2) colocados perpendicularmente entre eles, de xeito que maximicen o rango de aceptancia á vez que se sitúan o máis preto do feixe posible. Nos híbridos instálanse os sensores, xunto co sistema de refrixeración e a electrónica. Como parte fundamental do proceso de testeado do VELO, é preciso comprobar que cada sensor funciona correctamente replicando unhas condicións similares a aquelas nas que operará. Esta tese documenta parte do traballo relativo ás probas de laboratorio que se levou a cabo como parte do proxecto de actualización do VELO. Unha das técnicas máis empregadas para este traballo foi o estudo de curvas de voltaxe-intensidade (IV), xa que proporcionan unha ferramenta eficaz para determinar o rendemento dos sensores. En primeiro lugar, elaboráronse curvas IV dun sensor sen irradiar, atopando que a resposta coincidia coa esperada. Por outra banda, un dos maiores retos aos que se ten que enfrontar o VELO é ao envellecemento por radiación, xa que ao ser a parte do LHCb que se atopa máis preto do feixe de protóns, esta alcanza valores elevadísimos, e ademáis incide sobre o VELO dun xeito non uniforme.

A segunda parte do traballo organizouse co obxectivo de estudar o efecto que poden ter diferentes tipos de irradiación, uniforme e non uniforme, e caracterizar a resposta dos sensores unha vez sometidos a este proceso. Atopouse que, mentras que os sensores irradia-

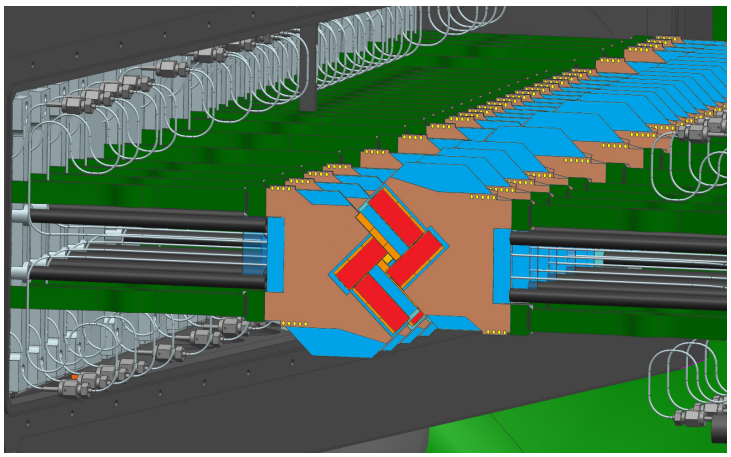

Figura C.2: Ilustración do VELO actualizado, figura de [160].

dos dun xeito uniforme operaban segundo o esperado, aqueles sensores irradiados de xeito non uniforme presentaban un incremento repentino da corrente *breakdown*. Procurando comprender a natureza deste efecto, leváronse a cabo estudos para determinar a relación que podería ter a aparición deste fenómeno coa temperatura do sensor. Por último, proporciónanse dúas parametrizacións para modelar a resposta dos sensores. Aínda que os estudos non foron determinantes, o feito de que o efecto de *breakdown* non se atopara en posteriores sensores, lévanos a conclusión de que durante o proceso de fabricación ou de irradiación provocou algunha imperfección nos sensores.

C.4 Medida de $\mathcal{R}(D^{(*)0})$

Centrándonos agora no traballo de análise de datos, o obxectivo principal desta tese é unha nova medida hadrónica dos cocientes de ULS:

$$\mathcal{R}(D^{(*)0}) = \frac{\mathcal{B}(B^+ \to \overline{D}^{*0}\tau^+\nu_\tau)}{\mathcal{B}(B^+ \to \overline{D}^{*0}\ell^+\nu_\ell)}. \tag{C.1}$$

A análise comeza por un proceso de selección de candidatos, que será aplicado tantos aos datos como ás contribucións xeradas por simulación *Monte Carlo*. Este proceso, á súa vez, divídese en distintas etapas:

- En primeiro lugar os eventos son obtidos a partir duns requerimentos xerais que teñen como obxectivo formar candidatos a B^+ combinando $\overline{D}^0 \to K\pi$ e $\tau \to 3\pi^{\pm}\overline{\nu}$: cortes en distancia de voo, calidade das trazas, ou identificación de partículas.

- A segunda etapa trátase dunha preselección de refinado, que procuran suprimir eventos de fondo: cortes na distancia e calidade dos vértices do B e 3π, momento

ou pseudo-rapidez[1].

- Finalmente aplícanse criterios de selección específicos para os eventos de sinal ou de normalización: corte na distancia entre vértices.

Unha das claves da análise presentada aquí ten que ver coa semellanza entre o estado final reconstruído da sinal e a maior contribución ao fondo. No primeiro caso, procúrase un meson $\overline{D}^0$ e tres pions cargados, mentres que na contribución de fondo os tres pions cargados procúdense no mesmo vértice do B, é dicir, eventos do tipo $B \to \overline{D}^0\pi^+\pi^-\pi^+X$, denominadas desintegracións *inmediatas*. Esto enténdese mellor reparando na topoloxías semellantes entre as dúas sinais da Fig. C.3 e o fondo predominante da Fig. C.4.

Polo tanto, para resolver esta cuestión, é preciso un corte entre os vértices (dividido pola súa incertidume) do τ e do B que permita discernir entre eventos de sinal e de fondo.

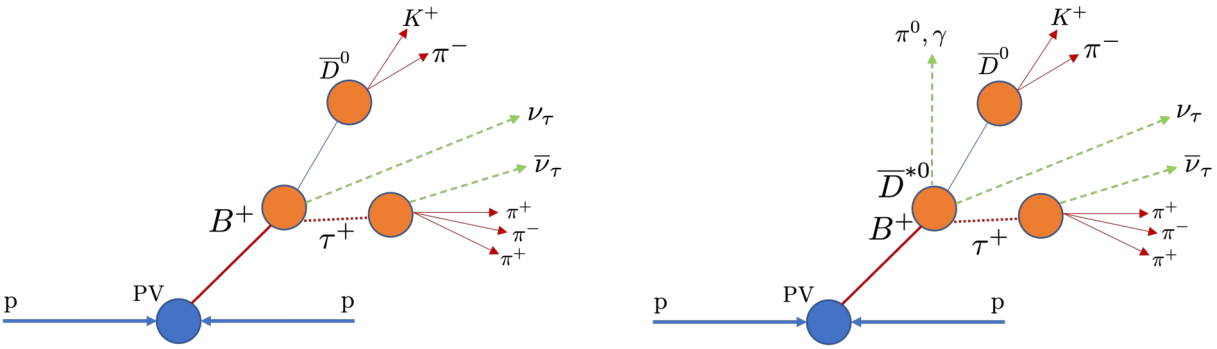

Figura C.3: Topoloxía de eventos de sinal, correspondentes á cadea de desintegración do $\overline{D}^0$ (esquerda) e do $\overline{D}^{*0}$ (dereita).

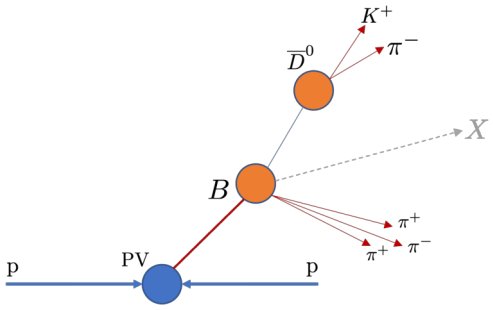

Figura C.4: Topoloxía do fondo máis abundante: a desintegración *inmediata*.

[1]Coordenada espacial que describe o ángulo que forma o momento dunha partícula con respecto á dirección do feixe

Unha vez aplicado o corte na distancia dos vértices, o fondo predominante é o debido a desintegracións con dous mesóns *encanto*, do tipo $B \to \overline{D}^0 D_s^+(X)$. Aplícase a técnica de análise multivariante para producir unha árbore de decisión (*Gradient Boosted Decision Tree*, BDT) que permita diferenciar estas componentes. A saída da BDT é unha variable con moita capacidade discriminadora entre fondo e sinal, e polo tanto empregase no axuste tridimensional, a partir do cal obténse o número de eventos de sinal.

Para levar a cabo a medida proposta, é preciso describir a distribución de datos coa maior exactitude posible, o que require simular de xeito moi preciso as compoñentes de fondo (todas aquelas que non son de sinal). Para isto, créanse plantillas simuladas de todas as compoñentes que aparecen no noso espectro de datos, e aplícanse lixeiras correccións para dar conta das mellores parametrizacións existentes para describir as diferentes compoñentes. Ademáis, créanse mostras de control de eventos reais, enriquecidas en certas compoñentes (por exemplo en desintegracións $B \to \overline{D}^0 D_s^+(X)$ ou *inmediatas*), que permitirán aplicar certas restriccións a un axuste final mediante o cal obteremos a medida obxectivo desta tese.

O cociente $\mathcal{R}(\mathcal{D}^{(*)0})$ pódese dividir en duas partes diferenciadas: o numerador e o denominador. A parte máis sinxela de obter é o denominador, $\mathcal{B}(B^+ \to \bar{D}^{(*)0}\ell^+\nu_\ell)$, xa que se empréga unha combinación de resultados externos de boa precisión, obtidos polos experimentos CLEO, BaBar and Belle [47].

Con respecto ao numerador, $\mathcal{B}(B^+ \to \bar{D}^{(*)0}\tau^+\nu_\tau)$, aplícase a estratexia de introducir unha normalización que comparta o mesmo estado final visible que a sinal, de xeito que moitas das incertidumes sistemáticas e de reconstrucción se cancelan no seu cociente. No presente traballo, escoulleuse $B^+ \to \overline{D}^0 D_s^+$, co $D_s^+ \to \pi^+\pi^-\pi^+$ como canle de normalización. A FD para o $B^+ \to \overline{D}^0 D_s^+$ atópase medida cunha precisión dun 10 % [9], mentres que para o caso de $D_s^+ \to 3\pi^\pm$, a precisión de dita fracción é do 4 % [9].

Tendo en conta o método presentado, o obxectivo da análise é a medida de:

$$\mathcal{K}(D^{(*)0}) = \frac{\mathcal{B}(B^+ \to \bar{D}^{(*)0})\tau^+\nu_\tau)}{\mathcal{B}(B^+ \to \overline{D}^0 D_s^+) \times \mathcal{B}(D_s^+ \to \pi^+\pi^-\pi^+)}, \tag{C.2}$$

que, á súa vez, pode ser expresado en termos do número total de sinal e normalización. Este número de eventos obtense axustando os datos ás plantillas creadas, e correxindo polas respectivas eficiencias, considerando a suma de ambas fraccións de ramificación dos modos de desintegración do τ^+, é dicir:

$$\begin{aligned} \mathcal{K}(D^{(*)0}) &= \frac{N(B^+ \to \bar{D}^{(*)0}\tau^+\nu_\tau)}{N(B^+ \to \overline{D}^0 D_s^+)} \\ &\times \frac{\varepsilon_{B^+ \to \bar{D}^0 D_s^+}}{\varepsilon^{\tau\to 3\pi\nu}_{B^+ \to \bar{D}^{(*)0}\tau^+\nu_\tau}\mathcal{B}(\tau \to 3\pi\nu)_{\text{PDG}} + \varepsilon^{\tau\to 3\pi\pi^0\nu}_{B^+ \to \bar{D}^{(*)0}\tau^+\nu_\tau}\mathcal{B}(\tau \to 3\pi\pi^0\nu)_{\text{PDG}}}, \end{aligned} \tag{C.3}$$

onde as diferentes eficiencias, ε, determínanse na análise e as fraccións de desintegración etiquetadas con PDG son factores externos obtidos de [9].

Séguense dúas estratexias diferentes para determinar o número de eventos de sinal e normalización. Por unha banda, o número de candidatos de normalización,

$N(B^+ \to \overline{D}^0 D_s^+)$, obtense dun axuste á masa do pico do $B^+ \to \overline{D}^0 D_s^+$, resultando nun total de 3047 ± 56 eventos.

Por outra banda, os eventos de sinal $B^+ \to \overline{D}^0 \tau^+ \nu_\tau$ e $B^+ \to \overline{D}^{*0} \tau^+ \nu_\tau$ extráense dun axuste de histogramas en tres dimensións, nos que se empregan as plantillas predifinidas para as diferentes compoñentes. As tres dimensións do axuste son o tempo de desintegración do sistema 3π, a masa do sistema di-leptón ao cadrado, q^2, e a BDT. As variables escóllense de xeito que estén o menos relacionadas entre elas, á vez que se manten a máxima capacidade discriminante entre as compoñentes das plantillas.

O modelo do axuste presenta alta complexidade, requirindo o desenvolvemento dun modelo con 24 compoñentes e restricións previamente estudadas. O axuste final conta con 17 parámetros libres; isto, xunto con todas as dificultades presentadas, implica que a súa converxencia sexa un dos resultados principais do traballo presentado aquí. O resultado da proxección do axuste en tres dimensións nas diferentes distribucións atópase en Fig. C.5.

Debido a que a análise non está rematada, o axuste no momento de redación deste documento é *cego*, o que quere dicir que os resultados atópanse camuflados, co obxectivo de evitar sesgos. Esta estratexia permite, sen embargo, acceder ás incertidumes, tanto estatísticas como externas, xa que as sistemáticas non se atopan calculadas. Polo tanto, introducindo na Eq. C.3 os resultados obtidos para o número de eventos de sinal e normalización, séguese que:

$$\mathcal{K}(D^0) = xx \pm 22\ (stat.) \pm 0{,}35\ (ext.), \tag{C.4}$$
$$\mathcal{K}(D^{*0}) = xx \pm 16\ (stat.) \pm 0{,}74\ (ext.), \tag{C.5}$$

onde a incertidume debido a medidas externas é despreciable comparado coa estatística.

O seguinte paso na análise consiste na obtención das FD de $B^+ \to \overline{D}^0 \tau^+ \nu_\tau$ e $B^+ \to \overline{D}^{*0} \tau^+ \nu_\tau$. Para isto, pártese dos parámetros $\mathcal{K}(D^{(*)}0)$, de forma que:

$$\mathcal{B}(B^+ \to \bar{D}^{(*)0} \tau^+ \nu_\tau) = \mathcal{K}(D^{(*)0}) \times \mathcal{B}(B^+ \to \overline{D}^0 D_s^+)_{\mathrm{PDG}} \times \mathcal{B}(D_s^+ \to \pi^+ \pi^- \pi^+)_{\mathrm{PDG}}, \tag{C.6}$$

onde as fraccións de desintegración etiquetadas con PDG son factores externos obtidos de [9]. Introducindo os resultados previos, chégase ao seguinte resultados das fraccións de desintegración:

$$\mathcal{B}(B^+ \to \overline{D}^0 \tau^+ \nu_\tau) = xx \pm 0{,}21\ (stat.) \pm 0{,}07\ (ext.)\ \%, \tag{C.7}$$
$$\mathcal{B}(B^+ \to \overline{D}^{*0} \tau^+ \nu_\tau) = xx \pm 0{,}15\ (stat.) \pm 0{,}15\ (ext.)\ \%, \tag{C.8}$$

que poden comparase coa media mundial [9], resultado nunha precisión competitiva.

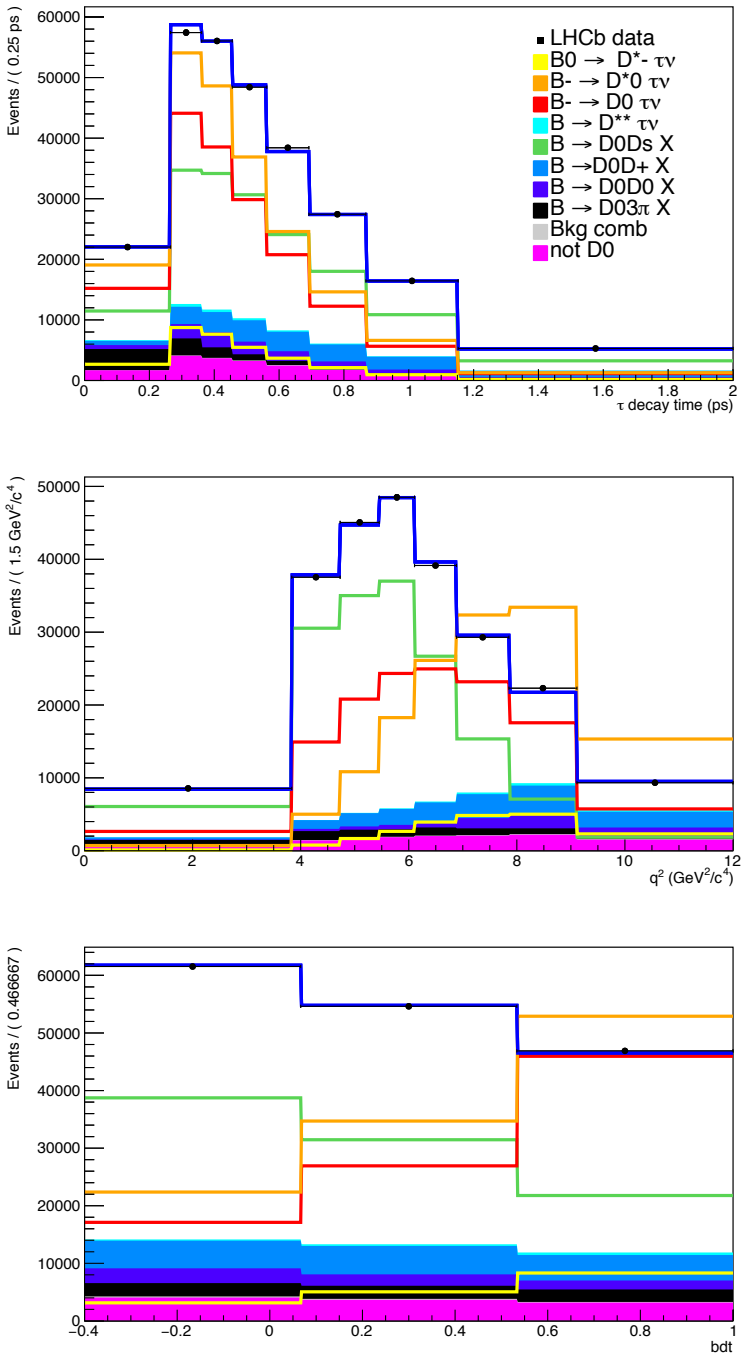

Figura C.5: Proxección do fit en 3D nas distribucións de tempo de desintegración do τ, q^2 e BDT. As compoñentes de sinal $B^+ \to \overline{D}^0\tau^+\nu_\tau$ e $B^+ \to \overline{D}^{*0}\tau^+\nu_\tau$ xunto co fondo $B \to \overline{D}^0 D_s^+(X)$ ocúltanse no axuste.

Finalmente, os cocientes $\mathcal{R}(D^{(*)0})$ obtéñense a partir dos resultados presentados ata agora, mediante a seguinte igualdade:

$$\mathcal{R}(D^{(*)0}) = \mathcal{K}(D^{(*)0}) \left(\frac{\mathcal{B}(B^+ \to \overline{D}^0 D_s^+) \times \mathcal{B}(D_s^+ \to 3\pi^\pm)}{\mathcal{B}(B^+ \to D^{(*)0} \ell^+ \nu_\ell)} \right)_{ext.}, \tag{C.9}$$

sendo as FD etiquetadas, con *ext.*, medidas externas obtidas de [9] e [47]. Deste xeito, acádanse os seguintes resultados:

$$\begin{aligned} \mathcal{R}(D^0) &= xx \pm 0{,}093\ (stat.) \pm 0{,}034\ (ext.), \\ \mathcal{R}(D^{*0}) &= xx \pm 0{,}026\ (stat.) \pm 0{,}029\ (ext.). \end{aligned}$$

Estos valores poden compararse coas anteriores medidas experimentais, como amosa a Fig. C.6. Deste gráfico obtense que a medida é comparable con resultados anteriores, sendo así un resultado moi competitivo.

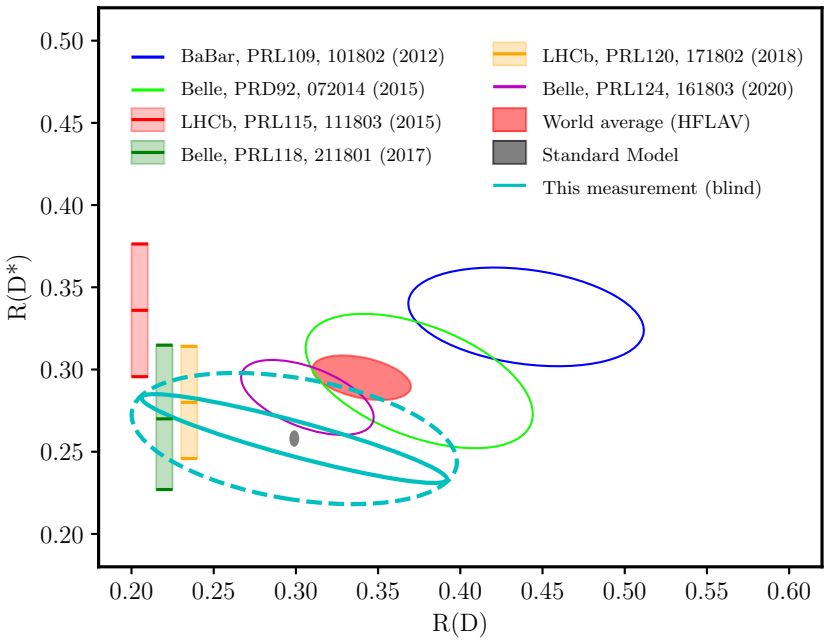

Figura C.6: Medidas de $\mathcal{R}(D)$ e $\mathcal{R}(D^*)$ do presente traballo, en turquesa. Debido a que os resultados son *cegos*, os valores centrales están situados no punto de referencia da predición do ME. A intertidume estatística atópase representada cunha liña continua, mentres que a incertidume total, estatística máis externa, móstrase cunha línea discontinua. O promedio mundial ven dado pola elipse vermella, mentres que a predición do ME correspóndese coa elipse gris. Indícanse a maiores outras medidas realizadas por diferentes experimentos.

C.5 Conclusións

Esta tese documenta parte do procedemento para verificar os prototipos dos sensores do VELO actualizado, baseado en sensores híbridos de tecnoloxía píxel. Esto forma parte do proxecto de actualización do LHCb. Neste documento, foi probado que os sensores funcionaban correctamente, mediante o método de IV. Con este mesmo procedemento, caracterízase o efecto que diferentes irradiacións teñen nos sensores. Despois de atopar un fenómeno de *breakdown* a baixos voltaxes en certos sensores, e investigarse diferentes posibilidades, chégase á conclusión de que un fallo na cadea de frío, na fabricación ou no proceso de irradiación provocou danos nos sensores, que non foron atopados en posteriores prototipos. Conclúese que o traballo documentado aquí contribuiu a asegurar o correcto funcionamento de LHCb, garantizando unha correcta adquisición de datos a partir do *Run 3* do LHC, que prevee as primeiras colisións estables para o cinco de Xuño de 2022.

Con respecto á análise de datos, o segundo e principal traballo desta tese dedícase á medida de observables de ULS. En particular, os cocientes $\mathcal{R}(D^{(*)0})$ mídense empregando datos recollidos polo experimento LHCb nos anos 2016, 2017 e 2018. Nesta análise, o leptón tau reconstrúese na súa forma hadrónica, que consiste nos modos $\tau^+ \to \pi^+\pi^-\pi^-(\pi^0)\overline{\nu}_\tau$. A análise atópase nun estado moi avanzado, onde a selección de datos e Monte Carlo, xunto co estudo de datos de control permitiu a obtención dos número de eventos de normalización e sinal. O primeiro a través dun axuste nunha dimensión e o segundo mediante un axuste en tres dimensións baseado en padróns. Con estos histogramas determínanse, en primeiro lugar os coeficientes $\mathcal{K}(D^{(*)0})$. A partir deste resultado, calcúlanse os cocientes de ramificación de $B^+ \to \overline{D}^0\tau^+\nu_\tau$ e $B^+ \to \overline{D}^{*0}\tau^+\nu_\tau$, cun resultado cuxa precisión é competitiva co actual promedio mundial [9]. Finalmente, obtéñense os cocientes $\mathcal{R}(D^{(*)0})$, cunha incertidume que prevee que o resultado será relevante no promedio mundial [47]. A presente tese contribuirá así á resolución de cuestións aínda abertas no sector do sabor, en particular as debidas á ULS, permitindo así esclarecer a presencia de efectos de NF.

List of Figures

List of Tables

From: **David Galbraith** dgalbraith@gmail.com
Subject: Re: Reuse diagram of Standard Model
Date: 21 March 2022 at 12:10
To: GARCIA PLANA BEATRIZ beatriz.garcia@usc.es

Sure

On Mon 21 Mar 2022 at 12:10, GARCIA PLANA BEATRIZ <beatriz.garcia@usc.es> wrote:

> Dear Sir,
>
> My name is Beatriz García Plana, I am an experimental particle physics PhD student. I am finishing writing the PhD thesis at the University of Santiago de Compostela (Spain). I would like to reuse the Standard Model diagram published in http://davidgalbraith.org/portfolio/ux-standard-model-of-the-standard-model/. Could you grant this permission?
>
> The title of my thesis is "Tests of Lepton Flavour Universality using semitauonic B decays in the LHCb experiment at CERN". Thank you in advance for your help.
>
> King regards,
> Beatriz
> ---
> Beatriz García Plana, PhD student
> Instituto Galego de Física de Altas Enerxías (IGFAE) - Universidade de Santiago de Compostela
>
> Rúa de Xoaquín Díaz de Rábago 2, Campus Vida, Universidade de Santiago de Compostela, Santiago de Compostela, Galicia, 15705, Spain
>
> IGFAE: beatriz.garcia@usc.es Tlf: +34 8818 13983 (ext 13983)
> CERN: beatriz.garcia.plana@cern.ch Tlf: +41 22 76 76585

--
David Galbraith http://davidgalbraith.org us: 415 655 1797 swiss: +41 76 304 41 94 skype: davidwg twitter: @daveg

From: **Ramon Cid** rcidmanzano@gmail.com
Subject: Re: Reuse of LHC dipole figure
Date: 21 March 2022 at 20:44
To: GARCIA PLANA BEATRIZ beatriz.garcia@usc.es

RC

Estimado Beatriz García Plana,
tiene usted el permiso para hacer uso de la imagen a la que se refiere en su email, en las condiciones de acreditación que son usuales.

No obstante, y tal como se dice en la sección AVISO, de nuestro sitio web: https://www.lhc-closer.es/taking_a_closer_look_at_lhc/0.notice:
"Algunos de los datos e informaciones, así como imágenes, has sido tomados de los diferentes websites del CERN, habiendo sido solicitado y concedido el ***correspondente permiso para ello por la administración del CERN. El resto de las imágenes, gráficas, etc., no hechas por nosotros,*** *han sido tomadas como de "****fair use****".*

Por tanto, el permiso que aquí se manifiesta está siempre condicionado, limitado o restringido en los términos del párrafo anterior.
En los más de quince años en los que nuestro sitio web está disponible nunca hemos recibido ningún tipo de queja, reclamación, requerimiento, reproche, etc., sobre esos materiales que han sido utilizados en nuestros contenidos.

Atentamente,
Ramón Cid.
www.lhc-closer.es

El lun., 21 mar. 2022 19:29, GARCIA PLANA BEATRIZ <beatriz.garcia@usc.es> escribió:

> Dear Sir,
>
> My name is Beatriz García Plana, I am an experimental particle physics PhD student. I am finishing writing the PhD thesis at the University of Santiago de Compostela (Spain). I would like to reuse the Standard Model diagram published in https://www.lhc-closer.es/taking_a_closer_look_at_lhc/0.lorentz_force. Could you grant this permission?
>
> The title of my thesis is “Tests of Lepton Flavour Universality using semitauonic B decays in the LHCb experiment at CERN”. Thank you in advance for your help.
>
> King regards,
> Beatriz
> ---
> Beatriz García Plana, PhD student
> Instituto Galego de Física de Altas Enerxías (IGFAE) - Universidade de Santiago de Compostela
>
> Rúa de Xoaquín Díaz de Rábago 2, Campus Vida, Universidade de Santiago de Compostela, Santiago de Compostela, Galicia, 15705, Spain
>
> IGFAE: beatriz.garcia@usc.es Tlf: +34 8818 13983 (ext 13983)
> CERN: beatriz.garcia.plana@cern.ch Tlf: +41 22 76 76585

From: **Permissions** permissions@ioppublishing.org
Subject: Re: Reuse figure from: The LHCb Collaboration et al 2008 JINST 3 S08005
Date: 23 March 2022 at 10:47
To: GARCIA PLANA BEATRIZ beatriz.garcia@usc.es
Cc: jinst-eo jinst-eo@jinst.sissa.it

Dear Beatriz,

Thank you for your request to reproduce material published by IOP Publishing *in your thesis,* ***"Tests of Lepton Flavour Universality using semitauonic B decays in the LHCb experiment at CERN"***

Regarding:

- ***Figures 2.1, 4.1, 5.1,*** *&* ***6.1*** *from* ***"The LHCb Detector at the LHC"***

We are happy to grant permission for the use you request on the terms set out below.

License to publish material published by IOP Publishing

Please provide the below to your new publisher as proof of permission.

Conditions

Non-exclusive, non-transferrable, revocable, worldwide, permission to use the material in print and electronic form will be granted **subject to the following conditions:**

- Permission will be cancelled without notice if you fail to fulfil any of the conditions of this letter.
- You will make reasonable efforts to contact the author(s) to seek consent for your intended use. Contacting one author acting expressly as authorised agent for their co-authors is acceptable.
- You will reproduce the following prominently alongside the material:
  - the source of the material, including author, article title, title of journal, volume number, issue number (if relevant), page range (or first page if this is the only information available) and date of first publication. This information can be contained in a footnote or reference note; or
  - a link back to the article (via DOI); and
  - ***if practical and IN ALL CASES for works published under any of the Creative Commons licences the words "© IOP Publishing Ltd and SISSA . Reproduced by permission of IOP Publishing. All rights reserved"***
- The material will not, without the express permission of the author(s), be used in any way which, in the opinion of IOP Publishing, could distort or alter the author(s)' original intention(s) and meaning, be prejudicial to the honour or reputation of the author(s) and/or imply endorsement by the author(s) and/or IOP Publishing and/or SISSA.
- Payment of £0 is received in full by IOP Publishing prior to use.

This permission does not apply to any material/figure which is credited to another source in our publication or has been obtained from a third party. Express permission for such materials/figures must be obtained from the copyright owner.

Kind regards,

Sophie
Copyright & Permissions Team
Sophie Brittain - Rights & Permissions Assistant
Cameron Wood - Legal & Rights Adviser
Contact Details
E-mail: permissions@ioppublishing.org

For further information about copyright and how to request permission:
https://publishingsupport.iopscience.iop.org/copyright-journals/
See also: https://publishingsupport.iopscience.iop.org/
Please see our Author Rights Policy
https://publishingsupport.iopscience.iop.org/author-rights-policies/
Please note: We do not provide signed permission forms as a separate attachment. Please print this email and provide it to your publisher as proof of permission. **Please note**: Any statements made by IOP Publishing to the effect that authors do not need to get permission to use any content where IOP Publishing is not the publisher is not intended to constitute any sort of legal advice. Authors must make their own decisions as to the suitability of the content they are using and whether they require permission for it to be published within their article.

From: GARCIA PLANA BEATRIZ <beatriz.garcia@usc.es>
Sent: 21 March 2022 12:41
To: Permissions <permissions@ioppublishing.org>
Subject: Reuse figure from: The LHCb Collaboration et al 2008 JINST 3 S08005

Dear Sir or Madam,

My name is Beatriz García Plana, I am an experimental particle physics PhD student. I am finishing writing the PhD thesis at the University of Santiago de Compostela (Spain). I would like to reuse some frigures from the publications:
The LHCb Detector at the LHC, The LHCb Collaboration *et al* 2008 *JINST* **3** S08005
The figures to be reused are:
-Figure 2.1
-Figure 4.1
-Figure 5.1
-Figure 6.1

Could you grant permission for being reused? The title of my thesis is “Tests of Lepton Flavour Universality using semitauonic B decays in the LHCb experiment at CERN”. Thank you in advance for your help.

King regards,
Beatriz

Beatriz García Plana, PhD student
Instituto Galego de Física de Altas Enerxías (IGFAE) - Universidade de Santiago de Compostela

Rúa de Xoaquín Díaz de Rábago 2, Campus Vida, Universidade de Santiago de Compostela, Santiago de Compostela, Galicia, 15705, Spain

IGFAE: beatriz.garcia@usc.es Tlf: +34 8818 13983 (ext 13983)
CERN: beatriz.garcia.plana@cern.ch Tlf: +41 22 76 76585

From: **Vinicius Franco Lima** vinicius.franco.lima@cern.ch
Subject: Re: Reuse figure of CERN-THESIS-2019-28
Date: 4 May 2022 at 13:48
To: GARCIA PLANA BEATRIZ beatriz.garcia@usc.es

VL

Hi Bea,
Of course you can use it!
Sorry, I completely forgot about this email, and I suspect it is a bit too late, but in an case!

Cheers,
Vinicius.

> On 22 Mar 2022, at 10:13, LHCb Secretariat <Lhcb.Secretariat@cern.ch> wrote:
>
> Dear Beatriz,
>
> Thanks for your email, I copy here Vinicius, as this is his thesis you refer to and that he should be the person letting know whether you can use this figure.
>
> Best regards and have a good day,
>
> Kévin Viel
>
> LHCb Secretariat
> EP Department - CERN
> Mailbox J02010
> CH-1211 Geneva 23
> Switzerland
> Phone: 0041 22 767 92 78
>
> ---
>
> **From:** GARCIA PLANA BEATRIZ <beatriz.garcia@usc.es>
> **Sent:** Monday, March 21, 2022 9:04 PM
> **To:** LHCb Secretariat <Lhcb.Secretariat@cern.ch>
> **Subject:** Reuse figure of CERN-THESIS-2019-28
>
> Dear Sir or Madam,
>
> My name is Beatriz García Plana, I am an experimental particle physics PhD student. I am finishing writing the PhD thesis at the University of Santiago de Compostela (Spain). I would like a figure from the publication CERN-THESIS-2019-288, LHCb Vertex Locator Upgrade Development and Rare b-quark Decays in LHCb.
> The figure that I would like to reuse is the figure 7.22 . Could you grant this permission?
>
> The title of my thesis is "Tests of Lepton Flavour Universality using semitauonic B decays in the LHCb experiment at CERN". Thank you in advance for your help.
>
> King regards,
> Beatriz
> ---
> Beatriz García Plana, PhD student
> Instituto Galego de Física de Altas Enerxías (IGFAE) - Universidade de Santiago de Compostela
>
> Rúa de Xoaquín Díaz de Rábago 2, Campus Vida, Universidade de Santiago de Compostela, Santiago de Compostela, Galicia, 15705, Spain

IGFAE: beatriz.garcia@usc.es Tlf: +34 8818 13983 (ext 13983)
CERN: beatriz.garcia.plana@cern.ch Tlf: +41 22 76 76585

From: **Federico Alessio** Federico.Alessio@cern.ch
Subject: Re: Reuse operation plot
Date: 20 April 2022 at 11:59
To: GARCIA PLANA BEATRIZ beatriz.garcia@usc.es
Cc: Richard Jacobsson Richard.Jacobsson@cern.ch, Renaud Le Gac legac@cppm.in2p3.fr

FA

Dear Beatriz,

i'm sorry your mail must have been lost. Please go ahead, the plots are free for use.

Best,
Federico.

> On 20 Apr 2022, at 11:25 AM, GARCIA PLANA BEATRIZ <beatriz.garcia@usc.es> wrote:
>
> Dear all,
>
> sorry for insisting, it is rather urgent that you grant me the permission below, since the deadline for my thesis is approaching.
>
> Cheers,
> Beatriz
> ---
> Beatriz García Plana, PhD student
> Instituto Galego de Física de Altas Enerxías (IGFAE) - Universidade de Santiago de Compostela
>
> Rúa de Xoaquín Díaz de Rábago 2, Campus Vida, Universidade de Santiago de Compostela, Santiago de Compostela, Galicia, 15705, Spain
>
> IGFAE: beatriz.garcia@usc.es Tlf: +34 8818 13983 (ext 13983)
> CERN: beatriz.garcia.plana@cern.ch Tlf: +41 22 76 76585
>
> > On 7 Apr 2022, at 14:57, GARCIA PLANA BEATRIZ <beatriz.garcia@usc.es> wrote:
> >
> > Dear all,
> >
> > I kindly remind to the request below.
> >
> > King regards,
> > Beatriz
> > ---
> > Beatriz García Plana, PhD student
> > Instituto Galego de Física de Altas Enerxías (IGFAE) - Universidade de Santiago de Compostela
> >
> > Rúa de Xoaquín Díaz de Rábago 2, Campus Vida, Universidade de Santiago de Compostela, Santiago de Compostela, Galicia, 15705, Spain
> >
> > IGFAE: beatriz.garcia@usc.es Tlf: +34 8818 13983 (ext 13983)
> > CERN: beatriz.garcia.plana@cern.ch Tlf: +41 22 76 76585
> >
> > USC UNIVERSIDADE DE SANTIAGO DE COMPOSTELA
> >
> > > On 26 Mar 2022, at 18:33, GARCIA PLANA BEATRIZ <beatriz.garcia@usc.es> wrote:
> > >
> > > Dear Sir or Madam,
> > >
> > > My name is Beatriz García Plana, I am an experimental particle physics PhD student. I am finishing writing the PhD thesis at the University of Santiago de Compostela (Spain). I would like a figure from the operation plots webpage: https://lbgroups.cern.ch/online/OperationsPlots/index.htm. The plot that I would like to reuse is the "Integrated Recorded Luminosity" of the years 2010-2018. Could you grant this permission?
> > >
> > > The title of my thesis is "Tests of Lepton Flavour Universality using semitauonic B decays in the LHCb experiment at

CERN". Thank you in advance for your help.

King regards,
Beatriz

Beatriz García Plana, PhD student
Instituto Galego de Física de Altas Enerxías (IGFAE) - Universidade de Santiago de Compostela

Rúa de Xoaquín Díaz de Rábago 2, Campus Vida, Universidade de Santiago de Compostela, Santiago de Compostela, Galicia, 15705, Spain

IGFAE: beatriz.garcia@usc.es Tlf: +34 8818 13983 (ext 13983)
CERN: beatriz.garcia.plana@cern.ch Tlf: +41 22 76 76585

From: **GARCIA PLANA BEATRIZ** beatriz.garcia@usc.es
Subject: Reuse operation plot
Date: 26 March 2022 at 18:33
To: Federico Alessio federico.alessio@cern.ch, richard.jacobsson@cern.ch, legac@cppm.in2p3.fr

BP

Dear Sir or Madam,

My name is Beatriz García Plana, I am an experimental particle physics PhD student. I am finishing writing the PhD thesis at the University of Santiago de Compostela (Spain). I would like a figure from the operation plots webpage: https://lbgroups.cern.ch/online/OperationsPlots/index.htm. The plot that I would like to reuse is the "Integrated Recorded Luminosity" of the years 2010-2018. Could you grant this permission?

The title of my thesis is "Tests of Lepton Flavour Universality using semitauonic B decays in the LHCb experiment at CERN". Thank you in advance for your help.

King regards,
Beatriz

Beatriz García Plana, PhD student
Instituto Galego de Física de Altas Enerxías (IGFAE) - Universidade de Santiago de Compostela

Rúa de Xoaquín Díaz de Rábago 2, Campus Vida, Universidade de Santiago de Compostela, Santiago de Compostela, Galicia, 15705, Spain

IGFAE: beatriz.garcia@usc.es Tlf: +34 8818 13983 (ext 13983)
CERN: beatriz.garcia.plana@cern.ch Tlf: +41 22 76 76585

From: **Permissions** permissions@ioppublishing.org
Subject: Re: Reuse a figure
Date: 8 April 2022 at 12:15
To: GARCIA PLANA BEATRIZ beatriz.garcia@usc.es
Cc: jinst-eo jinst-eo@jinst.sissa.it

Dear Beatriz,

Thank you for your request to reproduce material published by IOP Publishing *in your thesis,* ***"Tests of Lepton Flavour Universality using semitauonic B decays in the LHCb experiment at CERN"***

Regarding:

- ***Figure 2*** *from* ***"The LHCb Vertex Locator (VELO) Pixel Detector Upgrade"***

We are happy to grant permission for the use you request on the terms set out below.

License to publish material published by IOP Publishing

Please provide the below to your new publisher as proof of permission.

Conditions

Non-exclusive, non-transferrable, revocable, worldwide, permission to use the material in print and electronic form will be granted **subject to the following conditions:**

- Permission will be cancelled without notice if you fail to fulfil any of the conditions of this letter.
- You will make reasonable efforts to contact the author(s) to seek consent for your intended use. Contacting one author acting expressly as authorised agent for their co-authors is acceptable.
- You will reproduce the following prominently alongside the material:
  - the source of the material, including author, article title, title of journal, volume number, issue number (if relevant), page range (or first page if this is the only information available) and date of first publication. This information can be contained in a footnote or reference note; or
  - a link back to the article (via DOI); and
  - ***if practical and IN ALL CASES for works published under any of the Creative Commons licences the words "© IOP Publishing Ltd and Sissa Medialab srl. Reproduced by permission of IOP Publishing. All rights reserved"***
- The material will not, without the express permission of the author(s), be used in any way which, in the opinion of IOP Publishing, could distort or alter the author(s)' original intention(s) and meaning, be prejudicial to the honour or reputation of the author(s) and/or imply endorsement by the author(s) and/or IOP Publishing and/or Sissa Medialab srl.
- Payment of £0 is received in full by IOP Publishing prior to use.

This permission does not apply to any material/figure which is credited to another source in our publication or has been obtained from a third party. Express permission for such materials/figures must be obtained from the copyright owner.

Kind regards

Kind regards,

Sophie
Copyright & Permissions Team
Sophie Brittain - Rights & Permissions Assistant
Cameron Wood - Legal & Rights Adviser
Contact Details
E-mail: permissions@ioppublishing.org

For further information about copyright and how to request permission:
https://publishingsupport.iopscience.iop.org/copyright-journals/
See also: https://publishingsupport.iopscience.iop.org/
Please see our Author Rights Policy
https://publishingsupport.iopscience.iop.org/author-rights-policies/
Please note: We do not provide signed permission forms as a separate attachment. Please print this email and provide it to your publisher as proof of permission. **Please note**: Any statements made by IOP Publishing to the effect that authors do not need to get permission to use any content where IOP Publishing is not the publisher is not intended to constitute any sort of legal advice. Authors must make their own decisions as to the suitability of the content they are using and whether they require permission for it to be published within their article.

From: GARCIA PLANA BEATRIZ <beatriz.garcia@usc.es>
Sent: 07 April 2022 13:57
To: Permissions <permissions@ioppublishing.org>
Subject: Reuse a figure

Dear Sir or Madam,

My name is Beatriz García Plana, I am an experimental particle physics PhD student. I am finishing writing the PhD thesis at the University of Santiago de Compostela (Spain). I would like to reuse a figure from:
https://iopscience.iop.org/article/10.1088/1748-0221/12/01/C01013
In particular de figure that I would like to use is the figure 2 (left). Could you grant this permission?

The title of my thesis is “Tests of Lepton Flavour Universality using semitauonic B decays in the LHCb experiment at CERN”.
Thank you in advance for your help.

King regards,
Beatriz

Beatriz García Plana, PhD student
Instituto Galego de Física de Altas Enerxías (IGFAE) - Universidade de Santiago de Compostela

Rúa de Xoaquín Díaz de Rábago 2, Campus Vida, Universidade de Santiago de Compostela, Santiago de Compostela, Galicia, 15705, Spain

IGFAE: beatriz.garcia@usc.es Tlf: +34 8818 13983 (ext 13983)
CERN: beatriz.garcia.plana@cern.ch Tlf: +41 22 76 76585

REFERENCES

[1] ATLAS collaboration, G. Aad *et al.*, *Observation of a new particle in the search for the Standard Model Higgs boson with the ATLAS detector at the LHC*, Phys. Lett. B **716** (2012) 1, arXiv:1207.7214. (Cited on pages 1 and 28.)

[2] CMS collaboration, S. Chatrchyan *et al.*, *Observation of a New Boson at a Mass of 125 GeV with the CMS Experiment at the LHC*, Phys. Lett. B **716** (2012) 30, arXiv:1207.7235. (Cited on pages 1 and 28.)

[3] LHCb collaboration, R. Aaij *et al.*, *Observation of new resonances decaying to $J/\psi K^+$ and $J/\psi\phi$*, arXiv:2103.01803. (Cited on page 4.)

[4] M. I. Eides, V. Y. Petrov, and M. V. Polyakov, *New LHCb pentaquarks as hadrocharmonium states*, Mod. Phys. Lett. A **35** (2020) 2050151, arXiv:1904.11616. (Cited on page 4.)

[5] A. Pich, *The Standard Model of Electroweak Interactions; rev. version*, doi: 10.5170/CERN-2006-003.1. (Cited on page 5.)

[6] David Galbraith, *Standard model of physics*, http://davidgalbraith.org/portfolio/ux-standard-model-of-the-standard-model, 2021. Online; accessed 25 July 2021. (Cited on pages 5 and 181.)

[7] N. Cabibbo, *Unitary symmetry and leptonic decays*, Phys. Rev. Lett. **10** (1963) 531. (Cited on page 5.)

[8] M. Kobayashi and T. Maskawa, *CP-violation in the renormalizable theory of weak interaction*, Prog. Theor. Phys. **49** (1973) 652. (Cited on page 5.)

[9] Particle Data Group, P. A. Zyla *et al.*, *Review of Particle Physics*, PTEP **2020** (2020) 083C01. (Cited on pages 6, 8, 9, 10, 14, 76, 77, 78, 86, 87, 122, 124, 132, 137, 138, 139, 147, 148, 156, 170, 175, 176, 178, and 179.)

[10] S. Descotes-Genon and P. Koppenburg, *The CKM Parameters*, Ann. Rev. Nucl. Part. Sci. **67** (2017) 97, arXiv:1702.08834. (Cited on page 6.)

[11] L. Wolfenstein, *Parametrization of the Kobayashi-Maskawa Matrix*, Phys. Rev. Lett. **51** (1983) 1945. (Cited on page 6.)

[12] S. L. Glashow, J. Iliopoulos, and L. Maiani, *Weak Interactions with Lepton-Hadron Symmetry*, Phys. Rev. D **2** (1970) 1285. (Cited on page 6.)

[13] Z. Maki, M. Nakagawa, and S. Sakata, *Remarks on the unified model of elementary particles*, Prog. Theor. Phys. **28** (1962) 870. (Cited on page 7.)

[14] M. Fael and C. Greub, *Next-to-leading order prediction for the decay $\mu \to e\ (e^+e^-)\ \nu\,\overline{\nu}$*, JHEP **01** (2017) 084, arXiv:1611.03726. (Cited on page 8.)

[15] A. Pich, *Tau physics: theoretical perspective*, Nuclear Physics B - Proceedings Supplements **98** (2001) 385. (Cited on pages 8 and 9.)

[16] W. J. Marciano and A. Sirlin, *Electroweak Radiative Corrections to tau Decay*, Phys. Rev. Lett. **61** (1988) 1815. (Cited on page 9.)

[17] S. de Boer, T. Kitahara, and I. Nisandzic, *Soft-Photon Corrections to $\bar{B} \to D\tau^-\bar{\nu}_\tau$ Relative to $\bar{B} \to D\mu^-\bar{\nu}_\mu$*, Phys. Rev. Lett. **120** (2018) 261804, arXiv:1803.05881. (Cited on page 9.)

[18] S. Calí, S. Klaver, M. Rotondo, and B. Sciascia, *Impacts of radiative corrections on measurements of lepton flavour universality in $B \to D\ell\nu_\ell$ decays*, Eur. Phys. J. C **79** (2019) 744, arXiv:1905.02702. (Cited on page 9.)

[19] M. Thomson, *Modern particle physics*, Cambridge University Press, New York, 2013. (Cited on page 10.)

[20] S. Bifani, S. Descotes-Genon, A. Romero Vidal, and M.-H. Schune, *Review of Lepton Universality tests in B decays*, J. Phys. G **46** (2019) 023001, arXiv:1809.06229. (Cited on pages 10, 11, 14, 15, 18, 20, and 181.)

[21] G. Hiller and M. Schmaltz, *R_K and future $b \to s\ell\ell$ physics beyond the standard model opportunities*, Phys. Rev. D **90** (2014) 054014, arXiv:1408.1627. (Cited on page 12.)

[22] G. Hiller and M. Schmaltz, *Diagnosing lepton-nonuniversality in $b \to s\ell\ell$*, JHEP **02** (2015) 055, arXiv:1411.4773. (Cited on page 12.)

[23] M. Bordone, G. Isidori, and A. Pattori, *On the Standard Model predictions for R_K and R_{K^*}*, Eur. Phys. J. C **76** (2016) 440, arXiv:1605.07633. (Cited on page 12.)

[24] W. Altmannshofer, C. Niehoff, P. Stangl, and D. M. Straub, *Status of the $B \to K^*\mu^+\mu^-$ anomaly after Moriond 2017*, Eur. Phys. J. C **77** (2017) 377, arXiv:1703.09189. (Cited on page 12.)

[25] L.-S. Geng *et al.*, *Towards the discovery of new physics with lepton-universality ratios of $b \to s\ell\ell$ decays*, Phys. Rev. D **96** (2017) 093006, arXiv:1704.05446. (Cited on page 12.)

[26] B. Capdevila *et al.*, *Patterns of New Physics in $b \to s\ell^+\ell^-$ transitions in the light of recent data*, JHEP **01** (2018) 093, arXiv:1704.05340. (Cited on page 12.)

[27] Belle collaboration, J.-T. Wei *et al.*, *Measurement of the Differential Branching Fraction and Forward-Backword Asymmetry for $B \to K^{(*)}\ell^+\ell^-$*, Phys. Rev. Lett. **103** (2009) 171801, arXiv:0904.0770. (Cited on pages 12, 13, and 14.)

[28] BaBar collaboration, J. P. Lees *et al.*, *Measurement of Branching Fractions and Rate Asymmetries in the Rare Decays $B \to K^{(*)}l^+l^-$*, Phys. Rev. D **86** (2012) 032012, arXiv:1204.3933. (Cited on pages 12, 13, and 14.)

[29] Belle collaboration, A. Abdesselam *et al.*, *Test of Lepton-Flavor Universality in $B \to K^*\ell^+\ell^-$ Decays at Belle*, Phys. Rev. Lett. **126** (2021) 161801, arXiv:1904.02440. (Cited on pages 12 and 13.)

[30] Belle collaboration, S. Choudhury *et al.*, *Test of lepton flavor universality and search for lepton flavor violation in $B \to K\ell\ell$ decays*, JHEP **03** (2021) 105, arXiv:1908.01848. (Cited on pages 12, 13, and 14.)

[31] LHCb collaboration, R. Aaij *et al.*, *Test of lepton universality using $B^+ \to K^+\ell^+\ell^-$ decays*, Phys. Rev. Lett. **113** (2014) 151601, arXiv:1406.6482. (Cited on pages 12 and 13.)

[32] LHCb collaboration, R. Aaij *et al.*, *Test of lepton universality with $B^0 \to K^{*0}\ell^+\ell^-$ decays*, JHEP **08** (2017) 055, arXiv:1705.05802. (Cited on pages 12, 13, 14, and 181.)

[33] LHCb collaboration, R. Aaij *et al.*, *Test of lepton universality in beauty-quark decays*, arXiv:2103.11769. (Cited on pages 12, 13, and 14.)

[34] LHCb collaboration, R. Aaij *et al.*, *Search for lepton-universality violation in $B^+ \to K^+\ell^+\ell^-$ decays*, Phys. Rev. Lett. **122** (2019) 191801, arXiv:1903.09252. (Cited on pages 12 and 13.)

[35] Particle Data Group, P. A. Zyla *et al.*, *Review of particle physics*, Prog. Theor. Exp. Phys. **2020** (2020) 083C01. (Cited on page 15.)

[36] BaBar collaboration, J. P. Lees *et al.*, *Evidence for an excess of $\bar{B} \to D^{(*)}\tau^-\bar{\nu}_\tau$ decays*, Phys. Rev. Lett. **109** (2012) 101802, arXiv:1205.5442. (Cited on pages 15 and 16.)

[37] BaBar collaboration, J. P. Lees *et al.*, *Measurement of an Excess of $\bar{B} \to D^{(*)}\tau^-\bar{\nu}_\tau$ Decays and Implications for Charged Higgs Bosons*, Phys. Rev. D **88** (2013) 072012, arXiv:1303.0571. (Cited on pages 15 and 16.)

[38] Belle collaboration, M. Huschle *et al.*, *Measurement of the branching ratio of $\bar{B} \to D^{(*)}\tau^-\bar{\nu}_\tau$ relative to $\bar{B} \to D^{(*)}\ell^-\bar{\nu}_\ell$ decays with hadronic tagging at Belle*, Phys. Rev. D **92** (2015) 072014, arXiv:1507.03233. (Cited on pages 15 and 16.)

[39] Belle collaboration, S. Hirose *et al.*, *Measurement of the τ lepton polarization and $R(D^*)$ in the decay $\bar{B} \to D^* \tau^- \bar{\nu}_\tau$*, Phys. Rev. Lett. **118** (2017) 211801, arXiv:1612.00529. (Cited on page 16.)

[40] Belle collaboration, Y. Sato *et al.*, *Measurement of the branching ratio of $\bar{B}^0 \to D^{*+} \tau^- \bar{\nu}_\tau$ relative to $\bar{B}^0 \to D^{*+} \ell^- \bar{\nu}_\ell$ decays with a semileptonic tagging method*, Phys. Rev. D **94** (2016) 072007, arXiv:1607.07923. (Cited on page 16.)

[41] Belle collaboration, G. Caria *et al.*, *Measurement of $\mathcal{R}(D)$ and $\mathcal{R}(D^*)$ with a semileptonic tagging method*, Phys. Rev. Lett. **124** (2020) 161803, arXiv:1910.05864. (Cited on page 16.)

[42] LHCb collaboration, R. Aaij *et al.*, *Measurement of the ratio of branching fractions $\mathcal{B}(\bar{B}^0 \to D^{*+} \tau^- \bar{\nu}_\tau)/\mathcal{B}(\bar{B}^0 \to D^{*+} \mu^- \bar{\nu}_\mu)$*, Phys. Rev. Lett. **115** (2015) 111803, arXiv:1506.08614, [Erratum: Phys.Rev.Lett. 115, 159901 (2015)]. (Cited on pages 16, 17, 151, and 170.)

[43] LHCb collaboration, R. Aaij *et al.*, *Measurement of the ratio of the $B^0 \to D^{*-} \tau^+ \nu_\tau$ and $B^0 \to D^{*-} \mu^+ \nu_\mu$ branching fractions using three-prong τ-lepton decays*, Phys. Rev. Lett. **120** (2018) 171802, arXiv:1708.08856. (Cited on pages 16, 17, 90, 91, 107, 151, and 170.)

[44] LHCb collaboration, R. Aaij *et al.*, *Test of Lepton Flavor Universality by the measurement of the $B^0 \to D^{*-} \tau^+ \nu_\tau$ branching fraction using three-prong τ decays*, Phys. Rev. D **97** (2018) 072013, arXiv:1711.02505. (Cited on pages 16, 17, 90, 91, 107, 151, and 170.)

[45] LHCb collaboration, R. Aaij *et al.*, *Measurement of the ratio of branching fractions $\mathcal{B}(B_c^+ \to J/\psi \tau^+ \nu_\tau)/\mathcal{B}(B_c^+ \to J/\psi \mu^+ \nu_\mu)$*, Phys. Rev. Lett. **120** (2018) 121801, arXiv:1711.05623. (Cited on pages 16, 17, and 170.)

[46] LHCb collaboration, R. Aaij *et al.*, *Observation of the decay $\Lambda_b^0 \to \Lambda_c^+ \tau^- \overline{\nu}_\tau$*, arXiv:2201.03497. (Cited on pages 16 and 17.)

[47] HFLAV collaboration, Y. S. Amhis *et al.*, *Averages of b-hadron, c-hadron, and τ-lepton properties as of 2018*, Eur. Phys. J. **C81** (2021) 226, arXiv:1909.12524, updated results and plots available at https://hflav.web.cern.ch/. (Cited on pages 17, 18, 19, 22, 23, 75, 78, 149, 156, 175, 178, 179, and 181.)

[48] G. Buchalla, A. J. Buras, and M. E. Lautenbacher, *Weak decays beyond leading logarithms*, Rev. Mod. Phys. **68** (1996) 1125, arXiv:hep-ph/9512380. (Cited on page 17.)

[49] A. J. Buras, *Weak Hamiltonian, CP violation and rare decays*, in *Les Houches Summer School in Theoretical Physics, Session 68: Probing the Standard Model of Particle Interactions*, 1998, arXiv:hep-ph/9806471. (Cited on page 17.)

[50] O. Antipin, *Applications of effective field theories within and beyond the Standard Model*, master thesis, Iowa State U., 2008. (Cited on page 17.)

[51] M. Neubert, *Heavy quark effective theory*, Subnucl. Ser. **34** (1997) 98, arXiv:hep-ph/9610266. (Cited on page 17.)

[52] S. Fajfer, J. F. Kamenik, and I. Nisandzic, *On the $B \to D^* \tau \bar{\nu}_\tau$ Sensitivity to New Physics*, Phys. Rev. D **85** (2012) 094025, arXiv:1203.2654. (Cited on pages 17, 19, and 23.)

[53] I. Caprini, L. Lellouch, and M. Neubert, *Dispersive bounds on the shape of anti-B —> D(*) lepton anti-neutrino form-factors*, Nucl. Phys. B **530** (1998) 153, arXiv:hep-ph/9712417. (Cited on page 21.)

[54] D. Bigi and P. Gambino, *Revisiting $B \to D\ell\nu$*, Phys. Rev. D **94** (2016) 094008, arXiv:1606.08030. (Cited on pages 21, 24, and 120.)

[55] C. G. Boyd, B. Grinstein, and R. F. Lebed, *Constraints on form-factors for exclusive semileptonic heavy to light meson decays*, Phys. Rev. Lett. **74** (1995) 4603, arXiv:hep-ph/9412324. (Cited on page 22.)

[56] C. G. Boyd, B. Grinstein, and R. F. Lebed, *Model independent determinations of anti-B —> D (lepton), D* (lepton) anti-neutrino form-factors*, Nucl. Phys. B **461** (1996) 493, arXiv:hep-ph/9508211. (Cited on page 22.)

[57] C. G. Boyd, B. Grinstein, and R. F. Lebed, *Precision corrections to dispersive bounds on form-factors*, Phys. Rev. D **56** (1997) 6895, arXiv:hep-ph/9705252. (Cited on page 22.)

[58] Flavour Lattice Averaging Group, S. Aoki *et al.*, *FLAG Review 2019: Flavour Lattice Averaging Group (FLAG)*, Eur. Phys. J. C **80** (2020) 113, arXiv:1902.08191. (Cited on page 23.)

[59] F. U. Bernlochner, Z. Ligeti, M. Papucci, and D. J. Robinson, *Combined analysis of semileptonic B decays to D and D*: $R(D^{(*)})$, $|V_{cb}|$, and new physics*, Phys. Rev. D **95** (2017) 115008, arXiv:1703.05330, [Erratum: Phys.Rev.D 97, 059902 (2018)]. (Cited on pages 23 and 24.)

[60] Belle collaboration, A. Abdesselam *et al.*, *Precise determination of the CKM matrix element $|V_{cb}|$ with $\bar{B}^0 \to D^{*+} \ell^- \bar{\nu}_\ell$ decays with hadronic tagging at Belle*, arXiv:1702.01521. (Cited on page 23.)

[61] BaBar collaboration, B. Aubert *et al.*, *Measurement of —V(cb)— and the Form-Factor Slope in anti-B —> D l- anti-nu Decays in Events Tagged by a Fully Reconstructed B Meson*, Phys. Rev. Lett. **104** (2010) 011802, arXiv:0904.4063. (Cited on pages 23 and 77.)

[62] Belle collaboration, R. Glattauer *et al.*, *Measurement of the decay $B \to D\ell\nu_\ell$ in fully reconstructed events and determination of the Cabibbo-Kobayashi-Maskawa matrix element $|V_{cb}|$*, Phys. Rev. D **93** (2016) 032006, arXiv:1510.03657. (Cited on pages 23 and 77.)

[63] MILC collaboration, J. A. Bailey *et al.*, *$B \to D\ell\nu$ form factors at nonzero recoil and $-V_{cb}-$ from 2+1-flavor lattice QCD*, Phys. Rev. D **92** (2015) 034506, arXiv:1503.07237. (Cited on page 23.)

[64] HPQCD collaboration, H. Na *et al.*, *$B \to Dl\nu$ form factors at nonzero recoil and extraction of $|V_{cb}|$*, Phys. Rev. D **92** (2015) 054510, arXiv:1505.03925, [Erratum: Phys.Rev.D 93, 119906 (2016)]. (Cited on page 23.)

[65] D. Bigi, P. Gambino, and S. Schacht, *$R(D^*)$, $|V_{cb}|$, and the Heavy Quark Symmetry relations between form factors*, JHEP **11** (2017) 061, arXiv:1707.09509. (Cited on pages 24 and 121.)

[66] S. Jaiswal, S. Nandi, and S. K. Patra, *Extraction of $|V_{cb}|$ from $B \to D^{(*)}\ell\nu_\ell$ and the Standard Model predictions of $R(D^{(*)})$*, JHEP **12** (2017) 060, arXiv:1707.09977. (Cited on page 24.)

[67] P. Asadi, M. R. Buckley, and D. Shih, *It's all right(-handed neutrinos): a new W' model for the $R_{D^{(*)}}$ anomaly*, JHEP **09** (2018) 010, arXiv:1804.04135. (Cited on page 24.)

[68] A. Greljo, D. J. Robinson, B. Shakya, and J. Zupan, *$R(D^{(*)})$ from W' and right-handed neutrinos*, JHEP **09** (2018) 169, arXiv:1804.04642. (Cited on page 24.)

[69] D. J. Robinson, B. Shakya, and J. Zupan, *Right-handed neutrinos and $R(D^{(*)})$*, JHEP **02** (2019) 119, arXiv:1807.04753. (Cited on page 24.)

[70] K. S. Babu, B. Dutta, and R. N. Mohapatra, *A theory of $R(D^*, D)$ anomaly with right-handed currents*, JHEP **01** (2019) 168, arXiv:1811.04496. (Cited on page 24.)

[71] R. Mandal, C. Murgui, A. Peñuelas, and A. Pich, *The role of right-handed neutrinos in $b \to c\tau\bar{\nu}$ anomalies*, JHEP **08** (2020) 022, arXiv:2004.06726. (Cited on page 24.)

[72] Y. Sakaki, M. Tanaka, A. Tayduganov, and R. Watanabe, *Testing leptoquark models in $\bar{B} \to D^{(*)}\tau\bar{\nu}$*, Phys. Rev. D **88** (2013) 094012, arXiv:1309.0301. (Cited on page 24.)

[73] X.-Q. Li, Y.-D. Yang, and X. Zhang, *Revisiting the one leptoquark solution to the $R(D^{(*)})$ anomalies and its phenomenological implications*, JHEP **08** (2016) 054, arXiv:1605.09308. (Cited on page 24.)

[74] S. Bansal, R. M. Capdevilla, and C. Kolda, *Constraining the minimal flavor violating leptoquark explanation of the $R_{D^{(*)}}$ anomaly*, Phys. Rev. D **99** (2019) 035047, arXiv:1810.11588. (Cited on page 24.)

[75] U. Aydemir, T. Mandal, and S. Mitra, *Addressing the $\mathbf{R}_{D^{(*)}}$ anomalies with an $\mathbf{S}_1$ leptoquark from $\mathbf{SO(10)}$ grand unification*, Phys. Rev. D **101** (2020) 015011, arXiv:1902.08108. (Cited on page 24.)

[76] A. Crivellin, C. Greub, and A. Kokulu, *Explaining $B \to D\tau\nu$, $B \to D^*\tau\nu$ and $B \to \tau\nu$ in a 2HDM of type III*, Phys. Rev. D **86** (2012) 054014, arXiv:1206.2634. (Cited on page 24.)

[77] A. Celis, M. Jung, X.-Q. Li, and A. Pich, *Sensitivity to charged scalars in $\boldsymbol{B \to D^{(*)}\tau\nu_\tau}$ and $\boldsymbol{B \to \tau\nu_\tau}$ decays*, JHEP **01** (2013) 054, arXiv:1210.8443. (Cited on page 24.)

[78] R. Martinez, C. F. Sierra, and G. Valencia, *Beyond $\mathcal{R}(D^{(*)})$ with the general type-III 2HDM for $b \to c\tau\nu$*, Phys. Rev. D **98** (2018) 115012, arXiv:1805.04098. (Cited on page 24.)

[79] S. Iguro and K. Tobe, *$R(D^{(*)})$ in a general two Higgs doublet model*, Nucl. Phys. B **925** (2017) 560, arXiv:1708.06176. (Cited on page 24.)

[80] D. London and J. Matias, *B Flavour Anomalies: 2021 Theoretical Status Report*, doi: 10.1146/annurev-nucl-102020-090209 arXiv:2110.13270. (Cited on page 24.)

[81] L. Evans and P. Bryant, *LHC Machine*, JINST **3** (2008) S08001. (Cited on page 25.)

[82] E. Mobs, *The CERN accelerator complex - 2019. Complexe des accélérateurs du CERN - 2019*, https://cds.cern.ch/record/2684277, 2021. Online, accessed 27 July 2021. (Cited on pages 27 and 181.)

[83] R. Cid Manzano and X. Cid Vidal, *Taking a closer look at lhc*, https://www.lhc-closer.es/taking_a_closer_look_at_lhc/0.lorentz_force. Online, accessed 3 September 2021. (Cited on pages 27 and 181.)

[84] ATLAS collaboration, G. Aad *et al.*, *The ATLAS Experiment at the CERN Large Hadron Collider*, JINST **3** (2008) S08003. (Cited on page 28.)

[85] CMS collaboration, S. Chatrchyan *et al.*, *The CMS Experiment at the CERN LHC*, JINST **3** (2008) S08004. (Cited on page 28.)

[86] ALICE collaboration, K. Aamodt *et al.*, *The ALICE experiment at the CERN LHC*, JINST **3** (2008) S08002. (Cited on page 28.)

[87] LHCb collaboration, A. A. Alves Jr *et al.*, *The LHCb Detector at the LHC*, JINST **3** (2008) S08005. (Cited on pages 28, 32, 35, 36, 38, 41, and 43.)

[88] LHCb collaboration, R. Aaij *et al.*, *LHCb Detector Performance*, Int. J. Mod. Phys. A **30** (2015) 1530022, arXiv:1412.6352. (Cited on pages 28, 33, 35, and 181.)

[89] LHCb collaboration, R. Aaij *et al.*, *Measurement of the W boson mass*, JHEP **01** (2022) 036, arXiv:2109.01113. (Cited on page 28.)

[90] *CERN home page*, https://home.cern. Online, accessed 6 October 2021. (Cited on pages 29 and 181.)

[91] LHCb collaboration, C. Elsässer, *$\bar{b}b$ production angle plots*, https://lhcb.web.cern.ch/lhcb/speakersbureau/html/bb_ProductionAngles.html. Online, accessed 27 July 2021. (Cited on pages 30 and 181.)

[92] LHCb collaboration, *Nu, Mu and Pile-Up. The LHCb definitions of what we see and what we don't see*, https://twiki.cern.ch/twiki/bin/view/LHCb/NuMuPileUp, 2021. Online; accessed 6 May 2021. (Cited on page 29.)

[93] R. Alemany-Fernandez, F. Follin, and R. Jacobsson, *The LHCb Online Luminosity Control and Monitoring*, in *4th International Particle Accelerator Conference*, TUPFI010, 2013. (Cited on page 30.)

[94] LHCb collaboration, A. A. Alves Jr *et al.*, *The LHCb Detector at the LHC*, JINST **3** (2008) S08005. (Cited on pages 31, 32, 36, 38, and 39.)

[95] LHCb collaboration, P. R. Barbosa-Marinho *et al.*, *LHCb VELO (VErtex LOcator): Technical Design Report*, CERN-LHCC-2001-011, 2001. (Cited on page 32.)

[96] LHCb collaboration, R. Aaij *et al.*, *Performance of the LHCb Vertex Locator*, JINST **9** (2014) P09007, arXiv:1405.7808. (Cited on pages 33, 34, 35, and 181.)

[97] LHCb VELO Group, H. L. Snoek, *The LHCb VELO: Performance and radiation damage*, Nucl. Instrum. Meth. A **765** (2014) 35. (Cited on pages 34 and 35.)

[98] LHCb Collaboration, S. Amato *et al.*, *LHCb magnet: Technical Design Report*, Technical design report. LHCb, CERN, Geneva, 2000. (Cited on page 35.)

[99] M. Losasso *et al.*, *Tests and Field Map of LHCb Dipole Magnet*, IEEE Trans. Appl. Supercond. **16** (2006) 1700. (Cited on page 36.)

[100] W. Baldini *et al.*, *Overview of lhcb alignment*, Proceedings of the 1st LHC Detector Alignment Workshop (2007). (Cited on pages 37 and 181.)

[101] L. S. T. group, *LHCb Silicon Tracker - Material for Publications* , https://lhcb.physik.uzh.ch/ST/public/material/index.php. Online, accessed 10 September 2021. (Cited on pages 37 and 181.)

[102] J. Gassner, M. Needham, and O. Steinkamp, *Layout and Expected Performance of the LHCb TT Station*, LHCb-2003-140, CERN, Geneva, 2004. (Cited on page 38.)

[103] LHCb collaboration, P. R. Barbosa-Marinho *et al.*, *LHCb inner tracker: Technical Design Report*, Technical design report. LHCb, CERN, Geneva, 2002. revised version number 1 submitted on 2002-11-13 14:14:34. (Cited on page 38.)

[104] LHCb collaboration, P. R. Barbosa-Marinho *et al.*, *LHCb outer tracker: Technical Design Report*, Technical design report. LHCb, CERN, Geneva, 2001. (Cited on page 38.)

[105] LHCb collaboration, M. Adinolfi *et al.*, *Performance of the LHCb RICH detector at the LHC*, Eur. Phys. J. C **73** (2013) 2431, arXiv:1211.6759. (Cited on page 38.)

[106] LHCb collaboration, S. Amato *et al.*, *LHCb RICH: Technical Design Report*, CERN-LHCC-2000-037, 2000. (Cited on pages 40, 41, and 181.)

[107] LHCb collaboration, S. Amato *et al.*, *LHCb calorimeters: Technical Design Report*, CERN-LHCC-2000-036, 2000. (Cited on page 41.)

[108] LHCb collaboration, C. Abellán Beteta *et al.*, *Calibration and performance of the LHCb calorimeters in Run 1 and 2 at the LHC*, arXiv:2008.11556. (Cited on pages 41, 43, and 181.)

[109] LHCb collaboration, F. Archilli *et al.*, *Performance of the Muon Identification at LHCb*, JINST **8** (2013) P10020, arXiv:1306.0249. (Cited on pages 43, 44, and 181.)

[110] LHCb collaboration, R. Aaij *et al.*, *Design and performance of the LHCb trigger and full real-time reconstruction in Run 2 of the LHC*, JINST **14** (2019) P04013, arXiv:1812.10790. (Cited on pages 43, 45, and 181.)

[111] S. Benson, V. V. Gligorov, M. A. Vesterinen, and M. Williams, *The LHCb Turbo Stream*, J. Phys. Conf. Ser. **664** (2015) 082004. (Cited on page 45.)

[112] LHCb starterkit group, *The LHCb data flow*, https://lhcb.github.io/starterkit-lessons/first-analysis-steps/dataflow.html. Online, accessed 5 October 2021. (Cited on pages 46, 48, and 181.)

[113] LHCb collaboration, M. Clemencic *et al.*, *The LHCb simulation application, Gauss: Design, evolution and experience*, J. Phys. Conf. Ser. **331** (2011) 032023. (Cited on page 46.)

[114] T. Sjöstrand, S. Mrenna, and P. Skands, *PYTHIA 6.4 physics and manual*, JHEP **05** (2006) 026, arXiv:hep-ph/0603175. (Cited on page 46.)

[115] D. J. Lange, *The EvtGen particle decay simulation package*, Nucl. Instrum. Meth. **A462** (2001) 152. (Cited on page 46.)

[116] P. Golonka and Z. Was, *PHOTOS Monte Carlo: A precision tool for QED corrections in Z and W decays*, Eur. Phys. J. **C45** (2006) 97, arXiv:hep-ph/0506026. (Cited on page 46.)

[117] GEANT4 collaboration, S. Agostinelli *et al.*, *GEANT4–a simulation toolkit*, Nucl. Instrum. Meth. A **506** (2003) 250. (Cited on page 46.)

[118] LHCb collaboration, R. Aaij *et al.*, *Letter of Intent for the LHCb Upgrade*, CERN-LHCC-2011-001, LHCC-I-018, CERN, Geneva, 2011. (Cited on page 50.)

[119] LHCb collaboration, I. Bediaga *et al.*, *Framework TDR for the LHCb Upgrade: Technical Design Report*, CERN-LHCC-2012-007, 2012. (Cited on pages 50 and 52.)

[120] LHCb collaboration, J. Baptista Leite *et al.*, *Framework TDR for the LHCb Upgrade II*
- Opportunities in flavour physics, and beyond, in the HL-LHC era
, CERN-LHCC-2021-012, LHCB-TDR-023, CERN, Geneva, 2021. (Cited on pages 50, 51, and 181.)

[121] LHCb collaboration, R. Aaij *et al.*, *Expression of Interest for a Phase-II LHCb Upgrade: Opportunities in flavour physics, and beyond, in the HL-LHC era*, CERN-LHCC-2017-003, 2017. (Cited on page 50.)

[122] LHCb collaboration, I. Bediaga *et al.*, *Physics case for an LHCb Upgrade II — Opportunities in flavour physics, and beyond, in the HL-LHC era*, arXiv:1808.08865. (Cited on page 50.)

[123] LHCb collaboration, A. A. Alves Jr *et al.*, *LHCb Tracker Upgrade Technical Design Report*, CERN-LHCC-2014-001, 2014. (Cited on pages 51, 52, 53, and 181.)

[124] LHCb collaboration, A. A. Alves Jr *et al.*, *Expression of interest for an LHCb upgrade*, CERN-LHCB-2008-019, CERN-LHCC-2008-007, CERN, Geneva, 2008. revised version submitted on 2008-05-07 12:08:45. (Cited on page 52.)

[125] LHCb collaboration, I. Bediaga *et al.*, *LHCb Trigger and Online Upgrade Technical Design Report*, CERN-LHCC-2014-016, 2014. (Cited on page 52.)

[126] LHCb collaboration, A. A. Alves Jr *et al.*, *LHCb VELO Upgrade Technical Design Report*, CERN-LHCC-2013-021, 2013. (Cited on pages 52, 53, 55, 56, 57, and 181.)

[127] LHCb collaboration, A. A. Alves Jr *et al.*, *LHCb PID Upgrade Technical Design Report*, CERN-LHCC-2013-022, 2013. (Cited on page 53.)

[128] A. Piucci, *The LHCb Upgrade*, J. Phys. Conf. Ser. **878** (2017) 012012. (Cited on page 53.)

[129] K. Hennessy, *LHCb VELO Upgrade*, Nucl. Instrum. Meth. A **845** (2017) 97, arXiv:1604.05045. (Cited on pages 54, 56, and 182.)

[130] J. Visser *et al.*, *SPIDR: a read-out system for Medipix3 & Timepix3*, JINST **10** (2015) C12028. (Cited on page 58.)

[131] B. van der Heijden *et al.*, *SPIDR, a general-purpose readout system for pixel ASICs*, JINST **12** (2017) C02040. (Cited on page 58.)

[132] R. Bitter, T. Mohiuddin, and M. Nawrocki, *LabVIEW: Advanced programming techniques*, Crc Press, 2006. (Cited on page 58.)

[133] G. Lutz, *Semiconductor Radiation Detectors: Device Physics*, Springer Berlin Heidelberg, 2007. (Cited on page 61.)

[134] S. M. Sze, Y. Li, and K. K. Ng, *Physics of Semiconductor Devices*, Wiley, 2021. (Cited on page 61.)

[135] V. Franco Lima, *LHCb Vertex Locator Upgrade Development and Rare b-quark Decays in LHCb*, PhD thesis, U. Liverpool (main), 2019, doi: 10.17638/03061928. (Cited on pages 61, 69, 70, 72, and 182.)

[136] *PS-IRRAD Proton Facility*, https://ps-irrad.web.cern.ch/ps-irrad/, 2022. Online; accessed 4 April 2022. (Cited on page 61.)

[137] E. Dall'Occo *et al.*, *Temporal characterisation of silicon sensors on Timepix3 ASICs*, arXiv:2102.06088. (Cited on pages 61, 62, and 182.)

[138] P. Allport *et al.*, *Recent results and experience with the Birmingham MC40 irradiation facility*, JINST **12** (2017) C03075. (Cited on page 63.)

[139] R. Wunstorf *et al.*, *Results on radiation hardness of silicon detectors up to neutron fluences of 10**15-n/cm**2*, Nucl. Instrum. Meth. A **315** (1992) 149. (Cited on page 64.)

[140] CLICdp collaboration, M. Benoit, *Pixel detector R&D for the Compact Linear Collider*, JINST **14** (2019) C06003, arXiv:1902.08752. (Cited on page 69.)

[141] Å. Folkestad *et al.*, *Development of a silicon bulk radiation damage model for Sentaurus TCAD*, Nucl. Instrum. Meth. A **874** (2017) 94. (Cited on page 69.)

[142] *Proton Irradiation*, https://www.etp.kit.edu/english/264.php, 2022. Online; accessed 4 April 2022. (Cited on page 69.)

[143] CLEO collaboration, J. E. Bartelt *et al.*, *Measurement of the B —> D lepton neutrino branching fractions and form-factor*, Phys. Rev. Lett. **82** (1999) 3746, arXiv:hep-ex/9811042. (Cited on page 77.)

[144] CLEO collaboration, N. E. Adam *et al.*, *Determination of the anti-B —> D* l anti-nu decay width and —V(cb)—*, Phys. Rev. D **67** (2003) 032001, arXiv:hep-ex/0210040. (Cited on page 77.)

[145] BaBar collaboration, B. Aubert *et al.*, *A Measurement of the branching fractions of exclusive $\bar{B} \to D^{(*)}$ (π) $\ell^- \bar{\nu}$(ℓ) decays in events with a fully reconstructed B meson*, Phys. Rev. Lett. **100** (2008) 151802, arXiv:0712.3503. (Cited on page 77.)

[146] BaBar collaboration, B. Aubert *et al.*, *Measurement of the Decay $B^- \to$ D*0 $e^- \bar{\nu}$(e)*, Phys. Rev. Lett. **100** (2008) 231803, arXiv:0712.3493. (Cited on page 77.)

[147] LHCb collaboration, D. Müller, M. Clemencic, G. Corti, and M. Gersabeck, *ReDecay: A novel approach to speed up the simulation at LHCb*, Eur. Phys. J. C **78** (2018) 1009, arXiv:1810.10362. (Cited on page 82.)

[148] LHCb collaboration, L. Anderlini *et al.*, *The PIDCalib package*, LHCb-PUB-2016-021, CERN-LHCb-PUB-2016-021, CERN, Geneva, 2016. (Cited on pages 87 and 107.)

[149] LHCb collaboration, M. Williams *et al.*, *The HLT2 Topological Lines*, LHCb-PUB-2011-002, CERN-LHCb-PUB-2011-002, CERN, Geneva, 2011. (Cited on page 88.)

[150] H. Voss, A. Hoecker, J. Stelzer, and F. Tegenfeldt, *TMVA - Toolkit for Multivariate Data Analysis with ROOT*, PoS **ACAT** (2007) 040. (Cited on page 101.)

[151] F. U. Bernlochner *et al.*, *Das ist der HAMMER: Consistent new physics interpretations of semileptonic decays*, The European Physical Journal C **80** (2020) . (Cited on page 120.)

[152] S. Faller, A. Khodjamirian, C. Klein, and T. Mannel, *B —> D(*) Form Factors from QCD Light-Cone Sum Rules*, Eur. Phys. J. C **60** (2009) 603, arXiv:0809.0222. (Cited on page 121.)

[153] F. U. Bernlochner and Z. Ligeti, *Semileptonic $B_{(s)}$ decays to excited charmed mesons with e, μ, τ and searching for new physics with $R(D^{**})$*, Phys. Rev. D **95** (2017) 014022, arXiv:1606.09300. (Cited on pages 136, 137, and 139.)

[154] F. U. Bernlochner, M. F. Sevilla, D. J. Robinson, and G. Wormser, *Semitauonic b-hadron decays: A lepton flavor universality laboratory*, arXiv:2101.08326. (Cited on pages 137 and 157.)

[155] LHCb collaboration, R. Aaij *et al.*, *Measurements of the Branching fractions for $B_{(s)} \to D_{(s)}\pi\pi\pi$ and $\Lambda_b^0 \to \Lambda_c^+\pi\pi\pi$*, Phys. Rev. D **84** (2011) 092001, arXiv:1109.6831, [Erratum: Phys.Rev.D 85, 039904 (2012)]. (Cited on page 137.)

[156] LHCb collaboration, R. Aaij *et al.*, *Precise measurement of the f_s/f_d ratio of fragmentation fractions and of B^0_s decay branching fractions*, Phys. Rev. D **104** (2021) 032005, arXiv:2103.06810. (Cited on page 138.)

[157] R. J. Barlow and C. Beeston, *Fitting using finite Monte Carlo samples*, Comput. Phys. Commun. **77** (1993) 219. (Cited on pages 143 and 151.)

[158] LHCb collaboration, F. Alessio, R. Jacobsson, and R. Le Gac, *LHCb Operations Plots Webpage*, http://lbgroups.cern.ch/online/OperationsPlots/index.htm. Online, accessed 26 March 2022. (Cited on pages 162 and 183.)

[159] *LHCb Material for Presentations*, https://lhcb.web.cern.ch/speakersbureau/html/Material_for_Presentations_130424.html, 2022. Online; accessed 6 April 2022. (Cited on pages 171 and 183.)

[160] LHCb collaboration, E. Buchanan, *The LHCb Vertex Locator (VELO) Pixel Detector Upgrade*, JINST **12** (2017) C01013. (Cited on pages 173 and 183.)

The LHCb experiment foresees a new era of high luminosity, aiming to clarify persistent tensions between experiments and the SM predictions, such as those related to the flavour sector. This thesis is devoted to the measurement of the LFU ratios R(D0) and R(D*0), with the 3-prong hadronic tau decay modes, using LHCb Run 2 data. Even though the final result is blinded and the systematics uncertainties need to be computed, the signal branching fraction are obtained with a competitive precision. Moreover, the computation of the statistical and external uncertainties of the R(D(*)0) ratios hints that the analysis documented here will be a relevant contribution to the LFU sector.
Furthermore, a contribution to the LHCb detector upgrade is documented, based on testing the new hybrid pixel VELO sensors' performance.